Resolving Nonlinear Inverse Heat Conduction Problem by the Property Transformed Calibration Integral Equation Method Utilizing Novel Sequential and Phase Plane Strategies for Optimization

A Dissertation Presented for the

Doctor of Philosophy

Degree

The University of Tennessee, Knoxville

Hongchu Chen

December 2017

Acknowledgement

First of all, I would express my sincere gratitude to my major advisor Dr. Jay Frankel, for his support, mentorship and encouragement. Dr. Frankel is an extraordinary scholar, professor and friend. He not only taught me a lot of invaluable knowledge, but also influenced me by his scientific spirit, academic standard and the way he uses mathematical tools for handling engineering problems.

I would thank Dr. Majid Keyhani, for his valuable advice and insights during my doctoral study and the important material conveyed during his teaching of the convective heat transfer course. I am also grateful to my committee members Dr. Zhili Zhang and Dr. Fangxing Li, for their insightful suggestions on my dissertation. I would also thank my fellow students for their assistance and friendship.

I am grateful to the Mechanical, Aerospace and Biomedical Engineering Department for the GTA position during my doctoral study as well as the financial support from by Dr. Frankel through National Science Foundation cooperative agreement NSF-CBET 1703442.

Personally, I would like to thank my parents Weijian Chen and Lijuan Hong for their love, support and encouragement.

Abstract

A systematic "parameter free" calibration integral equation method is proposed for estimating the surface temperature and surface heat flux in the context of one-dimensional, transient, nonlinear inverse heat conduction problems. The calibration integral equation method can be formulated in terms of various probes arrangements. Temperature-dependent thermophysical properties and probe locations are not specified a priori but are implicitly accounted through the calibration campaigns. The final mathematical formulations involve Volterra integral equations of the first kind for the unknown surface temperature or surface heat flux. A first kind Chebyshev expansion possessing undetermined coefficients is applied for approximating the introduced property transform function. The undetermined expansion coefficients associated with the Chebyshev expansion are then estimated through calibration tests with known surface thermal conditions and probe responses. A time sequential testing procedure is illustrated and demonstrated for the model building process leading to the optimal truncation for the Chebyshev expansion. A future-time method is applied for stabilizing the ill-posed first kind Volterra integral equations. Phase plane and cross-correlation analyses are employed for estimating the optimal regularization parameter (i.e., the future-time parameter) from a spectrum of chosen values. The feasibility and robustness of the proposed approach are verified by numerical simulations. The effectiveness of using phase plane and cross-correlation analyses as a statistical tool for estimating optimal regularization parameters is also verified in the "parameter required" space marching method. This additional study demonstrates the universal nature of phase plane and cross-correlation analyses for

estimating the optimal regularization parameter necessary for alternative numerical implementations.

Table of Contents

List of Tables

List of Figures

List of Symbols

a_n^N = n^{th} undetermined coefficient in N^{th} order first kind Chebyshev expansion

b_1, b_2 = in-depth thermocouple probe positions, m

c = specific heat capacity, J/(kgK)

C_n = power spectral density

E_n = first kind Chebyshev polynomial of n^{th} order based on mapped temperature

f, f_c = cut-off frequency, Hz

$f_{c, DFT}$ = cut-off frequency determined by DFT, Hz

$f_{sampling}$ = sampling frequency, Hz

f_n = n^{th} chosen cut-off frequency, Hz

k = thermal conductivity, W/(mK)

L = thickness of the one-dimensional geometry, m

m = a positive integer

M = total number of spatial nodes in the space marching region $x \in [0, b_1]$ minus 1

M_f = multiplication factor

N = total number of temporal nodes past the initial condition

N^* = number of data points cut in predicted surface heat flux and heat flux rate for phase plane and the cross-correlation investigation

P = total number of chosen cut-off frequencies

q'' = heat flux, W/m^2

q''_f = predicted surface heat flux under specific cut-off frequency f, W/m^2

q''_{f_n} = predicted surface heat flux under nth chosen cut-off frequency f_n, W/m^2

$\dot{q}''_{f_n}$ = predicted surface heat flux rate under nth chosen cut-off frequency f_n, W/(m^{2}s)

q_i^j = discrete heat flux at $x_i = i\Delta x$, $t_j = j\Delta t$ in the space marching region $x \in [0, b_1]$, W/m^2

q_0^j = $q''_{tc}(b_1, t_j)$, which is heat flux at $x = b_1$ obtained by solving direct problem in $x \in [b_1, b_2]$ using "thermocouple" data, W/m^2

q''_0 = front surface heat flux, W/m^2

$q''_{\max}$ = maximum value of the double Gaussian heat flux, W/m^2

q''_s = surface heat flux, W/m^2

q''_{tc} = heat flux obtained by solving direct problem in $x \in [b_1, b_2]$ using "thermocouple" data, W/m^2

$q''_{tc, f_{c,DFT}}$ = heat flux obtained by solving direct problem in $x \in [b_1, b_2]$ using filtered "thermocouple" data by cut-off frequency $f_{c,\,DFT}$ determined by DFT, W/m^2

r_j = jth random number in the interval [-1,1]

r_N = least-squares residual function

R_N = sum of the least-squares residual function

R_q = heat flux cross-correlation coefficient

$R_{\dot{q}}$, $R_{dq/dt}$ = heat flux rate cross-correlation coefficient

R_T = temperature cross-correlation coefficient

$R_{\dot{T}}$, $R_{dT/dt}$ = temperature rate cross-correlation coefficient

t = time, s

t_k = k^{th} temporal node, s

$t_{\max}$ = maximum data collection time, s

t_j = j^{th} temporal node, s

T = temperature, K

T_f = predicted surface temperature under chosen cut-off frequency f, W/m^2

T_0 = initial temperature, K

T_0^j = $T_{tc}(b_1, t_j)$, which is the "thermocouple" temperature at $x = b_1$, K

T_i^j = discrete temperature at $x_i = i\Delta x$, $t_j = j\Delta t$ in the space marching region $x \in [0, b_1]$, K

T_s = surface temperature, K

T_{tc} = "thermocouple" temperature, K

T_{tc,f_c} = filtered "thermocouple" temperature by cut-off frequency denoted by f_c, K

$T_{tc,f_{c,DFT}}$ = filtered "thermocouple" temperature by cut-off frequency $f_{c,\ DFT}$ determined by DFT, K

T_{tc,f_n} = filtered "thermocouple" temperature by n^{th} chosen cut-off frequency f_n determined by DFT, K

T^* = dimensionless mapped temperature in the range [-1, 1]

u = dummy time variable, s

v = dummy time variable, s

x = spatial coordinate, m

x_i = x^{th} spatial node, m

x_0 = first spatial nodes at $x = b_1$ in the space marching region $x \in [0, b_1]$

x_M = last spatial nodes at $x = 0$ in the space marching region $x \in [0, b_1]$

Δf = the stepping frequency for forming a finite set of predictions, Hz

Δt = time step, s

Δx = space step, m

Greek Symbols

α = thermal diffusivity, m^2/s

β_1 = parameter in the double Gauss function, s

β_2 = parameter in the double Gauss function, s

γ = future-time parameter, s

ε = noise factor

θ = reduced temperature, K

κ = a constant number used in the derivation

ρ = density, kg/m^3

σ_1 = parameter in the double Gauss function, s

σ_2 = parameter in the double Gauss function, s

φ = transformed variable

ϕ = reduced transformed variable

ω_c = circular cut-off frequency, Hz

Subscripts

c = calibration test

r = reconstruction test

s = surface

tc = thermocouple

Chapter 1: Introduction and Literature Review

1.1 Introduction to inverse heat conduction problems

Inverse heat conduction problems involve predicting the surface thermal conditions in severely hostile thermal environments based on in-depth or backside measurements. Such environments appear in high-speed flights, combustion, brakes, nuclear reactors, arc jets, shock tunnels, furnaces, fires, etc. Under such harsh thermal conditions, sensors cannot directly be mounted onto the surface of interest. Instead, information collected by in-depth sensors is employed for predicting the surface thermal conditions. Projecting in-depth temperature data to surface defines the inverse heat conduction problem which is ill-posed [1]. That is, significant error magnification occurs when projecting unregularized in-depth noisy temperature data to the surface. In other words, small errors in the in-depth temperature data cause substantial error growth in the prediction of both the surface temperature and heat flux. This can be explained by the physics of heat diffusion as high-frequency oscillations are damped as heat conducts through a body. In the opposite direction, any noise (high-frequency oscillations) contained in the in-depth measurements are amplified when projecting to the surface. For this reason, regularization [1] is necessary for stabilizing all numerical schemes used for resolving inverse heat conduction problems (IHCP's). In most transient studies, the sensor's temperature is assumed to be identical to the positional temperature at the sensor site. Sensor characterization is often neglected in properly accounting capacitance, conductive lead losses and contact resistance [2-4]. The omission of these physical effects can potentially lead to a time-lagged and attenuated surface prediction.

Inverse heat conduction problems were initially considered in hypersonic flight applications [5]. Inverse problems can be defined in combustion [6-8], brakes [9, 10], solidification [11], quenching [12], nuclear reactor components [13], etc. After an inverse heat conduction problem is established and formulated, a projection scheme and a regularization method must be employed for predicting the surface thermal conditions (surface heat flux or surface temperature or both) using discrete in-depth measured temperature data. Regularization can be an external process independent of the projection scheme or incorporated into the projection scheme itself [14].

1.2 Projection schemes for inverse heat conduction problems

A variety of projection methods have been proposed for resolving inverse heat conduction problems. These include exact solution [15], space marching and finite difference methods [16-20], function specification method [21-23], global time method [24], conjugate gradient method [25, 26], Laplace transform method [27, 28], boundary-element method [29, 30], and an iteration method [31]. All aforementioned inverse heat conduction methods are "parameter required" methods that need accurate knowledge of the thermophysical properties of the host material, probe locations as well as sensor parameters (sensor capacitance, lead losses, thermal contact, etc). Uncertainties are inherent to parameter measurements. However, the uncertainty associated with these parameters are often neglected. The lack of uncertainty analysis for the "parameter required" methods [32] can potentially cause inaccuracies in the surface prediction. In addition, the entire measurement process is both financially expensive and time-consuming.

Burggraf [15] formed an exact solution to a one-dimensional transient inverse heat conduction problem in a slab where the time-dependent temperature and heat flux was known at an embedded sensor site. Continuity was assumed in the derivation prior to viewing data as discrete. An infinite series was expressed involving time derivatives of the temperature and heat flux data are truncated to two terms for estimating the surface heat flux. The time derivatives of temperature and heat flux were found by differentiating a polynomial representation of the simulated input data. While this method provides a clear investigation using errorless data, measurement error analysis was not included. In addition, accuracy was limited since only two terms of the infinite series were used. Greater accuracy would require additional higher time derivatives of the data which would become problematic since the data were approximated by polynomials.

Space marching [16-20, 24, 33-35] is one of the simplest and physically easiest numerical methods to visualize and implement for resolving inverse heat conduction problems. In the space-marching method, the spatial and temporal domains are discretized by finite difference approximations [16-20, 33, 34]. Temperature data from thermocouple sensors are commonly used and imposed as known in-depth boundary conditions in the direct region. Finite difference approximations are sensitive to high-frequency measurement errors [18]. Various methods have been proposed for damping noise in measurements. Al-Khalidy [33] and Taler [20] applied least squares fit based on a polynomial representation for smoothing the noise in the measured temperatures. Notwithstanding, least-squares fitting cannot guarantee the optimum representation of the time derivatives of the filtered function [36]. Hills and Hensel [19] utilized a stabilizing matrix as a digital filter to handle the noisy temperature data. Carraso [17] developed a space marching scheme coupled with Tikhonov regularization to resolve an inverse heat conduction problem. However, determining the value of the "regularization parameter" is problematic as it does not have a clear physical interpretation. Taler and Duda [34] studied two space marching methods. One involved discretizing the space derivative in the heat equation while the other one discretized the time derivative. Solution stability and accuracy of both methods depend on the time step size. Standard deviations based on the calculated surface conditions and exact surface conditions were used for determining the optimum time step. This is not a feasible approach for determining the optimal regularization parameter as the exact surface conditions are unknown in a field experiment.

In the function specification method [1], the transient surface heat flux with time is assumed to be of a functional form. The regularization parameter in this approach involves specifying the number of future time steps required for stabilizing the approximation. At present, no a priori rule exists for estimating this regularization parameter. The function specification method is computationally efficient since it is sequential in time. The difficulty of this method lies defining the number of future time steps since it depends on the unknown surface heat flux. Osman et al. [37] combined the function specification and Tikhonov regularization methods to resolve an inverse heat conduction problem. A piecewise polynomial function is used for the parameterization of the spatial distribution of the unknown surface heat flux while "stair-wise" steps on the time approximation are used at each discretized spatial location. A sequential-in-time procedure is used for predicting the surface heat flux. The objective function combines the function specification and regularization. This function is then minimized in the least-squares sense.

Elkins et al. [24] presented a global time and discrete space formulation of an inverse heat conduction problem. In contrast with conventional techniques for solving inverse heat conduction problem, the heating rate and higher time derivatives of the temperature data are directly measured by a rate-based sensor [38]. This is done in lieu of using a finite difference representation for the time derivatives of the measured temperature data. The rate-based sensor concept involves analog filtering prior to enter the voltage rate circuit. This concept uses the cut-off frequency as the regularization parameter. In Ref. [39], a Gauss low-pass filter with a physically based cut-off frequency is used for regularization in resolving the null point equation associated with arcjet testing. The Gauss filter removes high-frequency noise from the collected temperature data as a processor. Data interrogation by discrete Fourier transform produces a power spectrum that leads itself to weight filtering concepts designed for estimating the cut-off frequency. Robustness has been shown using this principle. The Gauss filter maintains smoothness in higher time derivatives unlike most low pass digital filters. The robustness of global time method [24] lies in its accuracy to predict the surface heat flux as the sampling rate increases. This contrasts many traditional inverse methods.

The conjugate gradient method has also been widely used to resolve inverse heat conduction problems. Zhou et al. [26] studied a one-sided inverse heat conduction problem where both the temperature and heat flux are specified at the back boundary. Temperature data are used as the back surface boundary condition and the heat flux is adopted as the objective function to be minimized. The inverse heat conduction problem formulation was shown to possess good stability in the parameter range considered in that study. However, the conjugate gradient method is computationally expensive and requires a large amount of computer memory.

Monde and Mitsutake [27], and Monde et al. [28] developed a Laplace transformed analytical method for both one-dimensional and two-dimensional inverse heat conduction problems. A polynomial power series in time with Fourier series expansion in space was performed for approximating the temperature changes in the body. The spatial resolution of this method is limited by the sensor spacing, probe depth placement and the accuracy of the sensor.

Iterative methods are necessary for resolving complex nonlinear inverse heat conduction problems. A Gauss method [40] is one of the iterative procedures proposed for solving a nonlinear inverse heat conduction problem. In the Gauss method, the next estimation is represented by a first order Taylor series expansion of the current estimation. The sensitivity matrix needs to be determined at the current estimation state and assumed invariant until the next iterative step. This linearization allows for updating the parameter of interest. The iterative procedure of this method is repeated until a stopping criterion is satisfied. However, when the columns of its corresponding sensitivity matrix are not linearly independent, the Gauss method is not able to ensure the existence of a unique solution.

The Levenberg-Marquardt method [41] modifies the ordinary least-squares norm with a penalty term that limits the parameter set variation at each step. The Levenberg-Marquardt method possesses a major advantage over the Gauss method as it can reduce the ill-conditioned sensitivity matrix effects [42]. Historically, the Levenberg-Marquardt method was conceived for nonlinear parameter estimation problems and successfully demonstrated and applied to both linear and nonlinear inverse heat conduction problems [43].

1.3 Regularization methods for inverse heat conduction problems

As inverse heat conduction problems are ill-posed [1], some sort of “regularization" technique [1] is required for stabilizing the ill-posed effects. Many regularization methods have been developed for this purpose, such as future-time method [1], Tikhonov regularization [44], digital filtering [33, 39], Singular-Value Decomposition (SVD) [45, 46] and so on. Inverse analysis leading to predictions can be highly sensitive to the choice of the regularization parameter.

A local future-time method has been proposed by Lamm [47] for regularizing ill-posed problems formulated by integral equations. By introducing and future-time parameter, the method will recast the ill-posed Volterra integral equation of the first kind into a well-posed Volterra integral equation of the second kind. The regularization parameter in the local future-time method is the future-time parameter. A local future-time method has been applied as regularization scheme for the calibration integral equation method proposed by Frankel, et al. [3, 48] and Elkins et al. [48]. Accurate surface heat flux predictions are achieved without pre-filtering the in-depth temperature data in both numerical [3] and experimental [48] tests.

Classical Tikhonov regularization stabilizes the ill-posed problem by adding the product of a “regularization parameter” with a semi-norm involving some function. Often this semi-norm involves the heat flux [44]. However, determining the value of the “regularization parameter” is often problematic as it does not have a clear physical interpretation. There are several approaches available for estimating the optimal Tikhonov regularization parameter. These approaches include the Morozov’s discrepancy principle [49, 50], the L-curve method [51-53], and the maximum likelihood method [50]. These methods have their limitations. Thus, determining the suitable Tikhonov regularization parameter is still under intensive research.

Digital filtering is an effective regularization approach for inverse heat conduction problems. Al-Khalidy [33] used a Savitzky-Gollary digital filter in a space marching method for resolving an inverse heat conduction problem. This approach essentially uses a least squares fitting, based on a polynomial representation, for filtering the noise in the measured temperatures. However, the least-squares fitting cannot guarantee the optimal representation of the time derivative of the filtered function [36]. A Gauss filter [39] removes high frequencies signal while maintains smoothness in higher time derivative. The Gauss low-pass filter function possesses the unique self-reciprocating characteristic of retaining the Gauss functional behavior in both time and frequency thereby substantially reducing ringing effects in time. Ringing effects are amplified when time differentiation is involved. The regularization parameter in this approach is defined as the cut-off frequency that appears in the construction of the Gauss low-pass filter. The effectiveness of using a Gauss filter as the regularization method for resolving inverse heat conduction problems has been verified based on a global time method [24] and a space marching method [54].

Singular value decomposition (SVD) is a regularization approach used in resolving inverse heat conduction problems based on matrix manipulations. The dependency of the surface heat flux and temperature response at the thermocouple site can be obtained by Duhamel's principle [45, 46, 55]. The ill-conditioned matrix is decomposed into two orthonormal matrices and a diagonal matrix that contains its singular values in descending order. Elements in the diagonal matrix after a certain row number can be set to zero in order to remove noise. Singular-value decomposition can also be viewed as a digital filter. The row number serves as the regularization parameter in this method. Again, the key to this method is the determination of optimal row number. Garcia et al. [55] considered a sequential SVD method for the two-dimensional nonlinear inverse heat conduction problem in an irregular-shaped body. The nonlinearity is due to temperature dependent thermophysical properties. The finite-element method is applied to solve the direct problem. Test cases were presented verifying the stability of the method. An overall error estimation was defined in order to find the optimal estimation of the two-dimensional inverse heat conduction problem. In addition, the accuracy of the method was evaluated by comparison with the function specification method [1]. The sequential SVD method provides a slightly more accurate result than the function specification method in most cases.

As noted earlier, the most fundamental and crucial element of any proposed inverse method ultimately involves acquiring the optimal regularization parameter that produces the “best” prediction from a spectrum of solutions. Therefore, establishing a means for estimating this crucial optimal regularization parameter is the key to achieve optimal surface prediction for inverse heat conduction problems. Phase-plane and cross-correlation analysis [56] will be applied in this context as a systematic methodology for estimating the optimum regularization parameter in both the visual and quantitative senses.

1.4 Sensor characterization

As mentioned earlier, in most transient investigations discussed in the literature, the thermocouple temperature is assumed to be identical to the positional temperature that is required by the modeled heat equation. In some situations, both attenuation and lag effects are observed if adjustments are not made that correctly account for the causes of the observed effects. As a basis for understanding their appearance, a simplified lumped analysis about the bead can be performed that account for capacitance/contact resistance and conductive lead losses. Some investigations have considered these occurrences [2-4]. Woodbury [4] investigated the effect of thermocouple time constant on the inverse projection using the function specification method. As expected, increasing the value of thermocouple time constant leads to greater attenuation and lag in the surface heat flux prediction.

1.5 System calibration methodology for inverse heat conduction problems

System calibration is a “parameter free” methodology for resolving inverse heat conduction problems. In this framework, the thermophysical, geometrical and transducer properties are not explicitly required for resolving the surface thermal conditions. These parameters are replaced by calibration data acquired through a well-designed and carefully orchestrated series of experiments. It is, of course, assumed that the system properties remain consistent throughout the life cycle of the test article.

The non-integer system identification (NISI) method [57-62] is a calibration method that requires the accurate extraction of the impulse function based on a fractional derivative formulation [63] of the heat equation. A known net surface source is used as a calibration source for obtaining the relationship between net surface heat flux and temperature response at the sensor site. The sensor characteristics, depth of sensor, and thermophysical properties of the host material are accounted in the calibration coefficients that are determined by a least-squares method. The unknown surface heat flux can be estimated by the corresponding sensor response and the calibration coefficients.

An alternative calibration methodology based on the calibration integral equation method (CIEM) has been developed at the University of Tennessee [3, 48, 64-66]. The calibration integral equation method inherently contains sensor positioning, sensor characteristics and thermophysical properties of the host material in the final mathematical expression that relates the in-depth measured temperature data to the surface temperature or net heat flux. The final mathematical expression is presented in terms of a Volterra integral equation of the first kind [67, 68] which is inherently ill-posed. Hence, regularization is required for stabilizing the integral equation. The calibration integral equation method is derived in a unified mathematical framework that can be applied to inverse heat conduction problems with higher dimensions [64], finite width domains [64, 65] and temperature-dependent thermophysical properties [65].

For the calibration integral equation method, one-probe (one in-depth thermocouple) [3, 48, 65, 66] or two-probe (two in-depth thermocouples) [69, 70] can be used. In the one-probe calibration integral equation method, the boundary condition for the back surface should be imposed as either adiabatic or a convective condition where the heat transfer coefficient remains unchanged between the calibration and reconstruction tests. The two-probe calibration integral equation method removes this limitation on the back surface boundary condition. With well-designed and executed front surface and back surface boundary conditions in the calibration tests, the two-probe calibration integral equation method can be applied for estimating front surface heat flux in a reconstruction test without considering the corresponding back surface boundary condition. The calibration integral equation method can be formulated in terms of both linear and nonlinear models. The linear calibration integral equation method requires the assumption of constant thermophysical properties. The nonlinear calibration integral equation method accounts for the temperature-dependent thermophysical properties in the model equation.

1.6 Identified gaps and scope for the proposed dissertation

The linear one-probe [3, 48, 66] and two-probe [69, 71] calibration integral equation methods have been experimentally validated with excellent accuracy at low temperatures. However, for applications involving large temperature variations, the temperature-dependency of thermophysical properties requires consideration. This leads to the development of a nonlinear calibration integral equation method. A new nonlinear calibration method based on Kirchhoff transform and rescaling principles has been proposed for one-probe [72] and two-probe [70] formulations. The nonlinear one-probe calibration integral equation method described in Ref. [72] has been experimentally verified [73, 74] at elevated temperatures in excess of 700^{o}C using the 0.91 μm Laserline laser facility (500W) at UTK. Probe positioning is not required in this rescaling approach but the thermal conductivity and thermal diffusivity of the host material are required. In contrast, Frankel and Keyhani [65] developed a nonlinear one-probe calibration integral equation method for estimating surface heat flux based on linearizing the nonlinear heat equation by a property transform. Compared to the rescaling approach, this method does not require the input of any thermophysical properties as well as probe locations. Instead, the temperature-dependent thermophysical properties are represented as a property transform function in the final mathematical formulation of a Volterra integral equation of the first kind. Excellent results are reported in Ref. [65] illustrating a potential new avenue for research.

This dissertation focuses on extending and developing new physical formulations, numerical analyses and mathematical means for assuring the best model expansion required in the property transform for the calibration integral equation method. The proposed novel calibration approach to inverse heat conduction creates the basic analytic and numerical tools, and framework for extending the approach to other areas such as vibrations and fluid mechanics.

Chapter 2 begins the study by illustrating the universal nature of phase-plane analysis for estimating the optimal regularization parameter. This demonstration is performed using a classical space marching method based on filtered in-depth temperature data for a nonlinear inverse heat conduction problem. In this case, the regularization parameter is defined as the cut-off frequency. The phase plane approach described in Ref. [56, 75, 76] is re-formulated for this problem and shown to demonstrate the universal nature of the methodology for extracting the optimal regularization parameter. This chapter is based on a published archival paper appearing in Numerical Heat Transfer, Part B: Fundamentals, Vol. 72, Issue 2, pp. 109-129, 2017.

Chapter 3 generalizes the previously described property transformed calibration integral equation based methodology described in Ref. [65]. In Chapter 3, Chebyshev polynomials of the first kind are introduced for a nonlinear, one-probe problem. In this investigation, the focus of the study involves resolving the surface temperature. This chapter demonstrates that is it possible to use the property transform formulation for resolving the nonlinear problem where no thermophysical properties are specified. Again, the probe position is not required. Two novel concepts are introduced in this chapter. First, a Chebyshev expansion is proposed unlike the power series approach described in the original derivation [65]. It is demonstrated that this basis is now the preferred building block for the expansion. Second, a novel sequential study is introduced for defining the optimal number of terms in the expansion based on parameter estimation principles. A high degree of accuracy is produced in this fundamental study providing confidence in the methodology. This study has been performed and an archival paper has been submitted to ZAMM journal.

Chapter 4 presents a nonlinear two-probe calibration integral equation method for surface heat flux prediction based on the linear two-probe calibration integral equation method [69, 71] and the nonlinear one-probe calibration integral equation method using a property transform for linearization [65]. The final mathematical formulation of this two-probe calibration integral equation method is expressed as a complicated nonlinear Volterra integral equation of the first kind for net surface heat flux with a property transform function that accounts for the temperature-dependent thermophysical properties and probe positioning. Again, the property transform function is approximated using a Chebyshev expansion of the first kind possessing undetermined coefficients. Three well-defined calibration tests are applied for estimating the undetermined coefficients associated with the Chebyshev expansion of the first kind. Results from this chapter generated an archival paper which is presently under review at the International Journal of Heat and Mass Transfer.

Chapter 5 is based on a “to be” submitted paper (to the journal: Applied Mathematical Modelling) that describes the results obtained from investigating a two-probe calibration integral equation method involving estimation of surface temperature in a one-dimensional, transient nonlinear heat conduction model. Again, phase plane and cross-correlation analyses are employed for estimating the optimal future-time parameter from a spectrum of chosen values. Numerical simulations using stainless steel as the host material produces excellent surface temperature predictions.

Finally, Chapter 6 presents concluding remarks and suggestions for future research.

Chapter 2: Nonlinear Inverse Heat Conduction: Digitally Filtered Space Marching with Phase-Plane and Cross-Correlation Analysis

This chapter is based on the paper: H. Chen, J. I. Frankel, and M. Keyhani, "Nonlinear inverse heat conduction: digitally filtered space marching with phase-plane and cross-correlation analysis", Numerical Heat Transfer, Part B: Fundamentals, Vol. 72, Issue 2, pp. 109-129, 2017.

2.1 Introduction

High-temperature and high-heat flux applications are abundant in combustion [6-8], brakes [9, 10] and hypersonic flight [5] as well as in many other industrial and commercial processes. Severely hostile thermal environments often preclude surface mounting of sensors. In-depth temperature measurements, based on thermocouples, are coupled to an inverse analysis for recovering the surface condition. In this way, the health and integrity of the sensors remain true and reliable. Through an inverse analysis, reconstruction of the surface condition is appropriated in an approximate sense. This projection process is ill-posed and requires special methods for recapturing stability in the resolution of the surface condition. As all propagated information in a numerical analysis is predicated by the heat equation, the first time derivative of temperature clearly indicates the physical dilemma in the numerical process when noisy discrete data are present. In most transient investigations discussed in the literature, the thermocouple temperature is assumed to be identical to the positional temperature required by the modeled heat equation. In some situations, both attenuation and lag effects will be observed if adjustments are not made that correctly account for the causes of the observed effects. As a basis for understanding their appearance, a simplified lumped analysis about the bead can be performed that account for capacitance/contact resistance and conductive lead losses. Some investigations have considered these occurrences [2-4].

Over the past 50-60 years, numerous numerical schemes have been proposed for resolving inverse heat conduction problems. Inverse heat conduction methods can be divided into two primary groups; namely, "parameter required" [1, 2, 7, 15-20, 23, 34, 45, 46] or "parameter free" methods [3, 48, 62, 64]. If the scheme requires the specification of thermophysical properties, geometric properties (thickness, probe positions) and sensor characteristics then it is a "parameter required" approach. On the other hand, if a system identification point of view is taken then a system calibration(s) eliminates the specification of the aforementioned parameters. This defines a "parameter free" approach; nonetheless, both views define an inverse problem as regularization is required for introducing stability.

Inverse heat conduction problems are ill-posed [1]. That is, interior measurements possessing noise, inherent to any measurement, are amplified in the projection process to the desired surface [1]. Therefore, some sort of "regularization" technique [1] is required for reducing the ill-posed effects caused by the presence of discrete noisy data. Many regularization methods have been developed for this purpose, such as future-time method [47], Tikhonov regularization [44], digital filtering [33, 39], singular value decomposition (SVD) [45, 46] and so on. Inverse analysis leading to predictions can be highly sensitive to the choice of the regularization parameter. Hence, the determination of optimum regularization parameter is fundamental and crucial for all inverse heat conduction problems. Techniques such as L-curve [51-53], Morozov's discrepancy principle [49] and other approaches have been used to resolve the optimality condition.

Space marching [16-20, 24, 33-35] is one of the simplest and physically easiest numerical methods to visualize and implement for resolving inverse heat conduction problems. In the space marching method, the spatial and temporal domains are discretized by finite difference approximations [16-20, 33, 34]. Temperature data from thermocouple sensors are commonly used and imposed as known in-depth boundary conditions in the direct region. Finite difference approximations are sensitive to high-frequency measurement errors [18]. Various methods have been proposed for damping noise in measurements. Al-Khalidy [33] and Taler [20] applied least-squares fitting based on a polynomial representation for smoothing the noise in the measured temperatures. Notwithstanding, least-squares fitting cannot guarantee the optimum representation of the time derivatives of the filtered function [36]. Hills and Hensel [19] utilized a stabilizing matrix as a digital filter to handle the noisy temperature data. Carraso [17] developed a space marching scheme coupled with Tikhonov regularization to resolve an inverse heat conduction problem. However, determining the value of the "regularization parameter" is problematic as it does not have a clear physical interpretation. Taler and Duda [34] studied two space marching methods. One involves discretizing the space derivative in the heat equation while the other one uses the discretization of the time derivative. The solution stability and accuracy of both methods depend on the time step size. Standard deviations based on calculated surface conditions and exact surface conditions are used for determining the optimum size of the time step. This is not a feasible approach for determining the optimal regularization parameter as the exact surface conditions are unknown in a field experiment.

As noted earlier, the most fundamental and crucial element of any proposed inverse method ultimately involves acquiring the optimal regularization or tuning parameter that produces the best solution from the predicted spectrum of solutions. Here, the spectral variable is the regularization parameter. Establishing a means for estimating this crucial tuning variable is the focus of the present chapter in the context of a “parameter required” method. In this context, a backward time differencing space marching scheme [16] using a low-pass Gauss filter [39] is employed as the projection scheme and regularization method, respectively. Unlike most low-pass digital filters, the Gauss filter maintains smoothness in higher time derivatives in both the frequency and time domains. This filter function possesses the unique self-reciprocating characteristic of retaining the Gaussian functional behavior in both time and frequency thereby substantially reducing ringing effects in time. Ringing effects are amplified when time differentiation is involved. The regularization parameter in this approach is defined as the cut-off frequency that appears in the construction of the Gauss low-pass filter. Phase-plane and cross-correlation analysis [56] will be extended in this note for estimating the optimum cut-off frequency (i.e., optimum regularization parameter) in both the visual and quantitative senses. This chapter focuses on demonstrating that the phase-plane and cross-correlation concepts have merit beyond its original application involving the future-time method [56] as the base numerical scheme.

2.2 Problem statement

Consider the one-dimensional body, shown in Fig. A-2.1 (all the figures and tables in this dissertation are placed in Appendix), subject to surface heating at $x = 0$. The net conductive heat flux is given as $q''(0, t)$ while the surface temperature is defined as $T(0, t)$. The thickness of the one-dimensional geometry is L such that $x \in [0, L]$. The host material is composed of a material with temperature-dependent thermophysical properties; namely thermal conductivity, $k(T)$ and heat capacitance $\rho c(T)$. The initial temperature distribution is assumed uniform at T_0 in $x \in [0, L]$. For simplicity but without loss of generality, the back surface boundary condition at $x = L$ is assumed adiabatic implying $q''(L, t) = 0$. The proposed approach works equally well for arbitrary back surface boundary conditions as the projection will be based on the two, in-depth thermocouples ($x = b_1$, $x = b_2$). This problem definition is merely used to generate the temperature data at the two, in-depth positions in order to emulate a typical experimental setup.

Assume that two thermocouples are embedded at $x = b_1$ and $x = b_2$, respectively such that $0 < b_1 < b_2 \leq L$. For the moment, additionally assume that the data collected from these sensors are ideal (both noiseless and representative of the positional temperature). In this case, we assign $T(b_1, t) = T_{tc}(b_1, t)$ and $T(b_2, t) = T_{tc}(b_2, t)$ while no apparent information is provided describing the physical boundary conditions at $x = 0, L$. Here, the thermocouple is denoted by "TC". At this idealized junction in the analysis, the data are assumed continuous as indicated by the notation. The mathematical (inverse) formulation for the problem is now stated as

$$\rho c(T)\frac{\partial T}{\partial t}(x,t)=\frac{\partial}{\partial x}\left[k(T)\frac{\partial T}{\partial x}(x,t)\right],\ \ x\in[0,L],\ \ t\geq 0 \tag{2.1a}$$

subject to unknown boundary condition at the front surface (x = 0)

$$\begin{aligned}&T_s(t)=T(0,t)=?\\&q_s''(t)=q''(0,t)\equiv -k\left(T(0,t)\right)\frac{\partial T}{\partial x}(0,t)=?,\ \ t>0\end{aligned} \tag{2.1b}$$

where the term $q_s''(t)$ consists of different heat transfer modes and/or sources; however, it leads to the net conductive heat flux, $q''(0, t)$ as previously noted. The two in-depth thermocouples producing transient temperature data are defined as

$$\begin{aligned}&T(b_1,t)=T_{tc}(b_1,t),\\&T(b_2,t)=T_{tc}(b_2,t),\ \ \ t>0\end{aligned} \tag{2.1c,d}$$

where the initial condition is given as

$$T(x,0)=T_0,\ \ x\in[0,L] \tag{2.1e}$$

In this formulation, the goal is to determine the active side net surface heat flux, $q''(0, t)$ and surface temperature, $T(0, t)$. Physically, it is evident that a direct, well-posed region exists in $x\in[b_1,b_2]$ while the inverse region of interest lies in $x\in[0,b_1]$.

2.3 Simulated data collection

In this study, a numerical simulation is performed for demonstrating the concepts. This analysis provides a forum for error analysis. The data sampling frequency is defined as $f_{sampling}$ while the total simulation time is given as $t_{\max}$. As a numerical and demonstrative study, data must be generated for emulating the two in-depth "thermocouple sites" for defining the direct problem in the region $x\in[b_1,b_2]$. For the inverse region, $x\in[0,b_1]$, an over-specified condition at $x = b_1$ must be provided for resolving the surface thermal condition at $x = 0$ using a space marching approach.

To generate the desired temperature data at $x = b_1$ and $x = b_2$, the heat flux boundary condition at $x = 0$ for the net surface heat flux, $q''(t)$ is provided. Using this condition and the adiabatic condition at $x = L$ with a constant initial condition permits the numerical solution for $T(x, t)$, $x \in [0, L]$, $0 < t \leq t_{\max}$ to be obtained. A conventional implicit finite difference method is implemented where the thermophysical properties are evaluated based on one-time step lag for simplicity. The, to be discussed, inverse method will be based on space marching and will require knowledge of both $T(b_1, t)$ and $q''(b_1, t)$ to initiate the process. For this chapter, the intent is to emulate a physical experiment based on two in-depth temperature measurements. Further, it is assumed that the positional temperatures acquired at $x = b_1$, b_2 are representative of the in-depth thermocouple temperatures (i.e., neglecting attenuation and lag effects introduced by an intrusive sensor).

With these "ideal" thermocouple data sets at $x = b_1$ and $x = b_2$, artificial noise can be added in accordance to

$$T_{tc}(b_1, t_j) = T(b_1, t_j)(1 + \varepsilon_T r_j), \quad j = 0, 1, \ldots, N \tag{2.2a}$$

$$T_{tc}(b_2, t_j) = T(b_2, t_j)(1 + \varepsilon_T r_j), \quad j = 0, 1, \ldots, N \tag{2.2b}$$

with $t_j = j\Delta t = j/f_{sampling}$, $j = 0, 1, \ldots, N$ where N represents the total number of data utilized in the simulation past the initial condition. In other words, the total time span for the simulation is $t_{\max} = N\Delta t$. Here, ε_T denotes the temperature noise factor, r_j denotes the j^{th}

random number in the interval [-1,1]. The entire simulation is performed using MATLAB R2016a on a Lenovo Thinkpad T530 laptop. As such, the MATLAB command "2(*rand*-0.5)" is used for acquiring the random numbers**.**

2.4 Inverse heat conduction formulation based on two in-depth thermocouples

In space marching methods [16-20, 33, 34], both the temperature and heat flux, at the single thermocouple site $x = b_1$, are needed by the algorithm as spatial marching begins from $x = b_1$ to the front surface at $x = 0$. Hence, the local heat flux based on the measured temperature data at the first thermocouple site $q''_{tc}(b_1,t)$ requires calculation. The heat flux $q''_{tc}(b_1,t)$ is numerically acquired from the solution of the direct problem in $x \in [b_1, b_2]$ using the discrete "thermocouple" data at $x = b_1$, b_2. Again, it is noted that the notation intentionally uses functions as a continuous "state estimation" [40] view offers another approach applicable in the direct region for acquiring $q''_{tc}(b_1,t)$. There are several permutations of the probe with known back surface boundary condition that can be utilized by this approach. It should be remarked that if the back surface boundary condition is known and a single in-depth thermocouple is available then a direct region exists between the thermocouple (TC) and the back surface, $x \in [b_1, L]$. Often it is difficult to precisely quantify an exposed boundary condition; and, hence using two in-depth thermocouples form a compelling and practical compromise.

A well-known, backward time differencing space marching scheme [11] is proposed that requires regularization in the spatial region, $x \in [0, b_1]$. The spatial, x_i and temporal, t_j nodes are represented using the indices i and j, respectively. The first spatial node at i = 0 is given as $x_0 = b_1$ while the last spatial node, M is at the front surface and denoted as. Observe that the spatial march is from $x = b_1$ to $x = 0$ and hence the rationale for the spatial nodal sequencing. In this spatial span, $M + 1$ points are defined. As remarked earlier, the march from $x = b_1$ toward the active surface of interest requires over-specification (or one-sided) conditions; namely, both temperature and heat flux. In the following discretization, we define and for notational simplicity. Following Carasso [16], we have

$$. q_{i+1}^{j} = q_i^j + \frac{\rho c(T_i^j)\Delta x}{\Delta t}\left(T_i^j - T_i^{j-1}\right), \quad i = 0, 1, \ldots, M-1; \quad j = 1, 2, \ldots, N . \tag{2.3a}$$

$$T_{i+1}^{j} = T_i^j + q_i^j \frac{\Delta x}{k(T_i^j)}, \quad i = 0, 1, \ldots, M-1; \quad j = 1, 2, \ldots, N \tag{2.3b}$$

where

$$\Delta x = \frac{b_1}{M} \tag{2.3c}$$

$$\Delta t = \frac{t_{\max}}{N} \tag{2.3d}$$

$$. x_i = b_1 - i\Delta x, \; i = 0, 1, \ldots, M \tag{2.3e}$$

$$t_j = j\Delta t, \;\; j = 1, 2, \ldots, N \tag{2.3f}$$

The discrete initial condition for temperature and heat flux are given by

$$T_i^0 = T_0, \quad i = 0, 1, \ldots, M \tag{2.3g}$$

$$q_i^0 = 0, \;\; i = 0, 1, \ldots, M \tag{2.3h}$$

respectively, with the one-sided boundary conditions $T_0^j, q_0^j, j = 1, 2, ..., N$. The truncation order of this scheme is O(Δx, Δt). At the present stage, the numerical method is doomed to fail owing to instability brought about by the imperfect data $T_{tc}(b_1, t)$ and $q''_{tc}(b_1, t)$.

2.5 Regularization by digital filtering

As noted earlier, regularization must be introduced for stabilization. Stabilization can lead to over-smoothness as less frequency content is permitted to be propagated to the active surface at $x = 0$. Filtering involves pre-processing the data by removing a certain level of high-frequency content from the signal. In this way, three basic prediction regimes are formed; namely, (i) unstable which contains too much high-frequency content, (ii) transition where the optimal regularization parameter exists, and (iii) over-smoothed where insufficient high frequencies are kept. It is well known that diffusion damps high frequencies as one propagates spatially further away from the source. For this study, a global Gauss filter is chosen that is defined as [39]

$$T_{tc,f_c}(b_1, t) = \frac{\sum_{j=0}^{N} T_{tc}(b_1, t_j)\, e^{-\omega_c^2 (t-t_j)^2/4}}{\sum_{j=0}^{N} e^{-\omega_c^2 (t-t_j)^2/4}}, \ t \in [0, t_{\max}] \tag{2.4}$$

where $\omega_c = 2\pi f_c$. Here, the circular cut-off frequency is given as ω_c while the cut-off frequency is given as f_c. At this junction, it is evident that the cut-off frequency, f_c defines the regularization parameter. Other filtering methods can be chosen and applied to inverse heat conduction. Additionally, observe that Eq. (2.4) returns a function in time, t that allows for resampling if required by a numerical method. In this way, it is possible to change from the experimental sampling times to a convenient numerical time discretization. Hence, the optimal regularization parameter involves determining the optimal "cut-off" frequency, f_c. Alternatively, a so-called "running" filter could be defined that involves the local data at the discrete time point t_k. Details on a running Gauss filter can be found in Ref. [77]. A "running" filter will substantially reduce the computational effort as a clear influence region is produced.

A physically formulated method for estimating the "cut-off" frequency utilizes the power spectrum of the signal [78] as generated by a Discrete Fourier Transfer (DFT) [78]. The spectral details the contributing frequencies in the acquired signal. Weiner filtering [79] suggests a qualitative test for estimating this value based on signal-to-noise (**S/N**) ratio. The **S/N** consideration makes physical sense for inverse problems. The power spectrum provides guidance for forming an initial estimation of f_c. However, tuning this value for estimating the optimal regularization parameter is unclear based solely on the DFT. This approach relies on pre-processing the data from the transducer sites for estimating the cut-off frequency, f_c. The next section offers an alternative approach for estimating the cut-off frequency, f_c based on the projected predictions over a predefined cut-off frequency, f_n (n = 1, 2, …, P) spectrum.

2.6 Phase plane and cross-correlation for estimating optimum cut-off frequency, f_c

Recently, a combined dynamical system viewpoint involving phase-plane and a pattern recognition technique involving cross-correlation has been successfully applied for estimating the optimal regularization parameter associated with the future-time method

[56]. For the present study, phase-plane analysis and cross-correlation [56] are used for identifying the optimal cut-off frequency of the digital filter given in Eq. (2.4) based on the projected predictions for fixed f_c. In the present context, phase-plane analysis [56] involves the desired surface quantity for the heat flux. In applied mathematics, the phase plane often involves the time parameterized plot of velocity versus displacement. By analogy, we define the phase plane as the heat flux rate, dq''/dt versus q'' where time is parameterized. Specifically, the predicted surface heat flux rate and heat flux under specifically chosen cut-off frequency is represented by $\dot{q}''_{f_n}(0,t_j)$ and $q''_{f_n}(0,t_j)$, respectively. Here, n is the n^{th} chosen value of cut-off frequency. Hence, the cut-off frequency defines the spectrum involving the calculated predictions of surface heat flux and heat flux rate. Here, the focus is on the surface heat flux as this property is normally more difficult to resolve than the corresponding surface temperature.

The heat flux cross-correlation coefficient is defined as [56]

$$R_q(q''_{f_n}, q''_{f_{n+1}}) = \frac{\sum_{j=N'}^{N} q''_{f_n}(0,t_j) q''_{f_{n+1}}(0,t_j)}{\sqrt{\sum_{j=N'}^{N}\left(q''_{f_n}(0,t_j)\right)^2 \sum_{j=N'}^{N}\left(q''_{f_{n+1}}(0,t_j)\right)^2}},$$

$$j = N^*, N^*+1, \ldots, N;\ n = 1, 2, \ldots, P-1 \quad (2.5a)$$

while the heat flux rate cross-correlation coefficient is given as [56]

$$R_{\dot{q}}(\dot{q}''_{f_n}, \dot{q}''_{f_{n+1}}) = \frac{\sum_{j=N'}^{N} \dot{q}''_{f_n}(0,t_j) \dot{q}''_{f_{n+1}}(0,t_j)}{\sqrt{\sum_{j=N'}^{N}\left(\dot{q}''_{f_n}(0,t_j)\right)^2 \sum_{j=N'}^{N}\left(\dot{q}''_{f_{n+1}}(0,t_j)\right)^2}},$$

$$j = N^*, N^*+1, \ldots, N;\ n = 1, 2, \ldots, P-1 \quad (2.5b)$$

where $f_n = n\Delta f$ (Hz), $n = 1, 2, \dots, P$. Here, Δf is the stepping frequency for forming a finite set of predictions. When the cross-correlation coefficient approaches unity it implies correlation or linear dependency or formation of a pattern. This can be seen by the discussion given in Ref. [76] based on the inner product (1 = identical direction, 0 = orthogonal, -1 = opposite direct). When the cross-correlation coefficient is near zero it implies a lack of correlation or closeness.

For the space marching projection, the prediction of surface thermal conditions at first few discrete data points is meaningless due to the signal delay by thermal penetration and the intrinsic delay effects introduced by an intrusive transducer. Therefore, N^* is introduced in Eqs. (2.5a, b) as an additional parameter to be considered. That is, can one set $N^* = 0$ or should one set it to some small value based on an observation associated with **S/N**? How do these choices affect the interpretation of the phase plane?

With the filtered thermocouple data at both $x = b_1$ and $x = b_2$ given as $T_{tc,\,fn}(b_1, t_j)$ and $T_{tc,\,fn}(b_2, t_j)$, the direct problem is solved between $x = b_1$ and $x = b_2$ to obtain the desired heat flux at $x = b_1$ as needed by the space marching method described in Section 2.4. Observe that though two sets of temperature data are required in the direct region. However, it is convenient to use a single cut-off frequency. In fact, as both b_1 and b_2 are in proximity to each other, nearly identical cut-off frequencies for these two sets of temperature data are expected. With regard to the notation provided in Section 2.4 involving the space marching method, the noisy thermocouple data $T_{tc}(b_1, t_j)$ are now replaced by $T_{tc,\,fn}(b_1, t_j)$ whose notation now reflects the filtering process for fixed cut-off frequency. Therefore,

$T_0^j = T_{tc,f_n}(b_1, t_j)$ and $q_0^j = q''_{f_n}(b_1, t_j)$, j = 1, 2, … , N are used in the specified space marching scheme.

2.7 Numerical algorithm

The algorithm is as follows:

1) Filter raw thermocouple (TC) temperatures at $x = b_1$ and $x = b_2$ using the Gauss low-pass filter for fixed cut-off frequency, f_n per Eq. (2.4).

2) Solve the direct heat conduction problem for the defined spatial domain between $x = b_1$ and $x = b_2$ using the filtered TC temperatures obtained in Step 1 as boundary conditions in the assigned direct region. Assuming a sufficiently high sampling frequency, use the identical sampling rate in the finite difference scheme.

3) Calculate the local heat flux at $x = b_1$ by a control volume assessment. This provides the second condition at $x = b_1$ for defining the one-sided problem ready for space marching to the axis origin, $x = 0$.

4) Using the local heat flux calculated by Step 3 and filtered TC temperature at $x = b_1$ from Step 1 march to the front surface for obtaining the surface heat flux and surface temperature. Eqs. (2.3a-h) in Section 2.2 describe the backward time differencing space marching scheme.

5) For fixed cut-off frequency, the surface temperature and heat flux are calculated in Step 4. Next, use simple finite difference representation for the first time derivative of heat flux to obtain the heat flux rate, dq''/dt for the phase-plane and cross-correlation analysis. Central differences are used for internal nodes while forward and backward differences are used at end points.

6) Perform Steps 1-5 for each chosen cut-off frequency, f_n, n = 1, 2, … , P and store for later use in phase-plane and cross-correlation analysis.

7) Perform phase-plane and cross-correlation studies per Section 2.6 and identify optimal regularization parameter, f_n (opt) based on observed outputs.

2.8 Results

This section provides fruitful results indicating the merit of the combined space-marching and filtering method where the optimal regularization parameter is estimated by phase-plane and cross-correlation analysis. Table A-2.1 contains the thermophysical properties of stainless steel 304 [80] as well as the geometrical properties of the study. Figures A-2.2a, b present the temperature dependent behavior of the thermal conductivity, $k(T)$ and specific heat, $c(T)$ over a large temperature range. The simulation will cover a gamut of temperature ranges to ensure the nonlinear effects are significant and observable. The widths of spatial and temporal nodes in the finite difference scheme for solving the direct problem in the region $x \in [0, L]$ are denoted by Δx and Δt, respectively. The values for Δx and Δt are kept fixed in this context for both direct calculations in $x \in [0, L]$ and $x \in [b_1, b_2]$ as well as the inverse calculation region in $x \in [0, b_1]$.

Figure A-2.3 presents the chosen surface heat flux to be re-constructed that is defined as

$$q_s''(t) = q''(0,t) = q''_{\max}\left(e^{-\frac{(t-\beta_1)^2}{\sigma_1^2}} + 0.75e^{-\frac{(t-\beta_2)^2}{\sigma_2^2}}\right), \quad t > 0 \tag{2.6}$$

This surface heat flux also identified as the boundary condition for generating in-depth positional temperatures at $x = b_1$, b_2. The values of the parameters $q''_{\max}, \beta_1, \sigma_1, \beta_2, \sigma_2$ are listed in Table A-2.1. The double Gauss function possesses a characteristic temporal history seen in some aerospace heating applications.

Figure A-2.4 displays the corresponding ideal temperature histories at $x = 0$, b_1, b_2, L. Here, ideal represents noiseless and numerically "exact" values or converged numerical results to some predefined convergence criteria. As this is a nonlinear study, it is apparent that exactness is defined as numerical convergence to some physically reasonable value commensurate with experimental accuracy. Convergence is given in terms of a Cauchy sense (comparison upon splitting intervals) and with a relative difference not to exceed some value. Figure A-2.5 illustrates the convergence of the finite difference scheme for solving the direct heat conduction problem in the region $x \in [0, L]$ for the forward probe location (nearest the active surface). As shown in Fig. A-2.5, convergence is achieved by plotting $T(b_1, t)$ obtained by $(\Delta x, \Delta t)$ and $(\Delta x/2, \Delta t/2)$, respectively. The maximum percentage difference between the two temperature curves is only 0.088%. Figure A-2.6 presents the positional temperature at the thermocouple sites, $x = b_1$ and b_2 given as $T(b_1, t_j)$ and $T(b_2, t_j)$ as well as the discrete noisy "thermocouple" data now defined as $T_{tc}(b_1, t_j)$ and $T_{tc}(b_2, t_j)$, $j = 1, 2, \dots, N$. These data are generated per Eqs. (2.2a, b) at 10 Hz. This chosen sampling frequency is common for high-speed ground flight testing undertaken due to the length of time and number of data sets that must be collected. It is evident that significant noise is introduced into the temperature data with the choice of parameters given in Table A-2.1.

Figure A-2.7 compares the numerically "exact" (no noise added to the temperature data) heat fluxes $q''(b_1, t_j)$, $q''(b_2, t_j)$, $j = 0, 1, 2, \ldots, N$, with heat fluxes $q''_{tc}(b_1, t_j)$, $q''_{tc}(b_2, t_j)$ that result from the simulation of the direct problem in $x \in [b_1, b_2]$ using the discrete unfiltered noisy "thermocouple" data at the two defined measurement sites. As illustrated in Fig. A-2.7, the heat fluxes $q''_{tc}(b_1, t_j)$, $q''_{tc}(b_2, t_j)$, $j = 0, 1, \ldots, N$ are contaminated with noise illustrating the intrinsic amplification effect due to using noisy TC data. The numerically acquired, noisy heat flux $q''_{tc}(b_1, t_j)$ used with the raw "thermocouple" temperature $T_{tc}(b_1, t_j)$ will prevent the success of the space marching algorithm in the inverse region $x \in [0, b_1]$. As the sampling frequency increases the oscillation magnitude will correspondingly increase.

Figures A-2.8a, b display the power spectrums of $T_{tc}(b_1, t_j)$ and $T_{tc}(b_2, t_j)$, $j = 0, 1, \ldots, N$. The power spectral density is defined as C_n and acquired by the Discrete Fourier Transform [78]. These figures provide guidance for forming an initial estimation of f_c. Figure A-2.8a shows the full frequency range (based on sampling frequency) where the y-axis is the $\log_{10}$ scale of power spectrum density C_n. Normally only half of the frequency range is presented owing to the Nyquist criterion. The power spectrum densities C_n for $T_{tc}(b_1, t_j)$ and $T_{tc}(b_2, t_j)$ are numerically obtained by MATLAB code "sqrt(fft(TCb1).*conj(fft(TCb1))/N)" and "sqrt(fft(TCb2).*conj(fft(TCb2))/N)", where $TCb1$ and $TCb2$ represent $T_{tc}(b_1, t_j)$ and $T_{tc}(b_2, t_j)$, respectively. The power spectrums of the "thermocouple" temperatures $T_{tc}(b_1, t_j)$ and $T_{tc}(b_2, t_j)$ are similar as displayed in Figs. A-2.8a,b due to both proximity and induced noise generation. Figure A-2.8b narrows the frequency range for focusing on the determination of the cut-off frequency. Two tangent lines are drawn in Fig. A-2.8b so that the Weiner filtering concept involving signal-to-noise (**S/N**) can be qualitatively visualized. The large f tangent line represents the extrapolated noise, **N** line. The small f tangent line is an estimate of the deduced signal, **S** line. The frequency value at the intersection of the two tangent lines in Fig. A-2.8b provides an initial estimate for defining the minimum cut-off frequency f_c as we wish to retain as many of the higher frequencies as possible. This estimate is now denoted as $f_{c,\,DFT} \in [0.075, 0.25]$ Hz as the "noise line" leaves the data at about 0.25 Hz. As an initial estimate, the upper limit in the interval is chosen; hence, leading to $f_{c,\,DFT} = 0.25$ Hz. The sensitivity of surface predictions to small perturbations of this estimate should always be considered. Again, it should be remarked that diffusion damps out higher frequency as the thermal penetration depth increases. High frequencies then become interpreted as a source of noise. Figure A-2.9 illustrates the effect of the preconditioning the TC data using the Gauss filter and selected cut-off frequency, $f_{c,\,DFT}$. This figure shows the positional temperatures $T(b_1, t_j)$, $T(b_2, t_j)$, $j = 0, 1, 2, \dots, N$ and filtered "thermocouple" temperatures $T_{tc,f_{c,DFT}}(b_1,t_j)$, $T_{tc,f_{c,DFT}}(b_2,t_j)$, $j = 0, 1, \dots, N$. The unadulterated and filtered data curves are indistinguishable when $f_{c,\,DFT} = 0.25$ Hz. Figure A-2.10 displays both the numerically "exact" heat fluxes $q''(b_1, t_j)$, $q''(b_2, t_j)$, $j = 0, 1, \dots, N$ and the heat fluxes resulting from filtered "thermocouple" data, based on Eq. (2.4), are denoted as $q''_{tc,f_{c,DFT}}(b_1,t_j)$, $q''_{tc,f_{c,DFT}}(b_2,t_j)$, $j = 0, 1, \dots, N$. This illustrates the effect of preconditioning the data, based on Weiner filtering concepts, as an initial estimator for the cut-off frequency of the Gauss filter at the TC sites. Comparing Fig. A-2.7 with Fig. A-2.10 illustrates an immediate benefit.

The one-sided projection using both the temperature and heat flux from the position $x = b_1$ is next addressed as this is the inverse problem. In this calculation, stability plays an important role in arriving at a reasonable estimation of the surface condition. The following discussion is based on resolving the optimal regularization parameter based on the projected heat flux at $x = 0$ (not the TC data from $x = b_1$).

As discussed in Section 2.6, the phase plane and cross-correlation phase plane are now used for estimating the optimum cut-off frequency (regularization parameter). Figure A-2.11a provides the predicted heat flux, $q''_{f_n}(0,t_j)$, $j = N^*, N^*+1, \dots, N$; $n = 1, 2, \dots, 10$ and heat flux rate, $\dot{q}''_{f_n}(0,t_j)$, $j = N^*, N^*+1, \dots, N$; $n = 1, 2, \dots, 10$ over 10 incrementally chosen cut-off frequencies ranging from 0.05 Hz to 0.50 Hz. Figure A-2.11b reduces the number of phase-plane results by focusing on the frequency range of 0. 15 to 0.35 Hz. As indicated in Figs. A-2.11a and A-2.11b, large cut-off frequencies produce basically random predictions. As the cut-off frequencies decrease from 0.5 Hz to 0.05 Hz, the corresponding phase planes take on a distinctive pattern as loss of randomness is observed. Again, this initial estimator is based on a qualitative measure (the heat flux and heat flux rate phase plane). The initiation of a pattern in the surface heat flux and heat flux rate phase plane defines the optimal regularization parameter as randomness is removed from both heat flux and more importantly, the heat flux rate. Both temperature rate, $\partial T/\partial t$ and heat flux rate, $\partial q''/\partial t$ carry ingredients for defining the best estimation as noted by their heat equation formulations. From Fig. A-2.11b, we can observe that the onset of a repeatable or "settled" pattern begins to occur in the range of f_c = 0.20 - 0.25 Hz. Furthermore, highly smoothed results are observed for $f_c \leq 0.1$ Hz. In fact, it is desired to retain as many high-frequency components in the signal for recovering small temporal changes in the predicted surface thermal conditions. Hence, predictions using $f_c \leq 0.1$ Hz are removed from consideration as over-smoothing dominates.

The phase planes involving the predicted surface heat flux and heat flux rate cross-correlation coefficients denoted by $R_q(q''_{f_n}, q''_{f_{n+1}})$ and $R_{\dot{q}}(\dot{q}''_{f_n}, \dot{q}''_{f_{n+1}})$, reveal additional interpretable features. Physically, three regimes exist; namely, 1) instability region, 2) transition region, and 3) over-smoothing region. Figure A-2.12a is the constructed cross-correlation coefficient phase plane using $N^* = 0$ while Fig. A-2.12b uses $N^* = 20$ for the indicated pairs of cut-off frequencies. Here, $N^* = 20$ is chosen as 20 time steps (2 seconds) are necessary for removing the random, large amplitude oscillates appearing at early times in the heat flux predictions shown in Fig. A-2.13. This is physically due to the insufficient change in the signal at the TC sites (low signal-to-noise ratio). That is, the TC measurement has yet to move out of the initial condition, background noise band. A reasonable heat flux begins to follow after the oscillatory predictions at early times (Fig. A-2.13). Interpretation of the cross-correlation coefficient phase-plane results using (a) $N^* = 0$ and (b) $N^* = 20$ are now discussed. Figure A-2.12a ($N^* = 0$) illustrates the appearance of the three regions defined as unstable, transition and over-smoothed. From cut-off frequency pairs (0.50, 0.45) Hz to (0.40, 0.35) Hz, instability is observed due to the drastic changes in the values of the corresponding heat flux rate cross-correlation coefficients $R_{\dot{q}}(\dot{q}''_{f_n}, \dot{q}''_{f_{n+1}})$ (Fig. A-2.12a), which correspond to randomness in the predicted heat flux and heat flux rate phase plane plot when f = 0.50 Hz, 0.45 Hz, 0.40 Hz, 0.35 Hz (see Fig. A-2.11a). As the values of the frequency pair decrease to (0.30, 0.25) Hz, the corresponding heat flux rate cross-correlation coefficient $R_{\dot{q}}(\dot{q}''_{f_n}, \dot{q}''_{f_{n+1}})$ approaches 1. In addition, as the values of frequency pairs further decrease, $R_{\dot{q}}(\dot{q}''_{f_n}, \dot{q}''_{f_{n+1}})$ remain at unity. This implies the occurrence of over-smoothness.

Figure A-2.12b (N^* = 20) displays the three regions previously described. It is important to view the actual axis values for both the heat flux and heat flux rate. This figure has different characteristics compared to Fig. A-2.12a since the highly oscillatory early-time data are removed. It is expected that $R_q(q''_{f_n}, q''_{f_{n+1}}) \to 1$ but physically $R_{\dot{q}}(\dot{q}''_{f_n}, \dot{q}''_{f_{n+1}})$ should not approach unity as this implies too much smoothness in its construction based on non-smooth data. Taking the temporal derivative of non-smooth data represents the most fundamental inverse problem. From repeatability studies based on a variety of sources and sampling rates, it is found that the indicated minimum produces the best reconstruction of both the surface heat flux and temperature. As sufficient robustness exists, and a pairing is defined, it would be appropriate and acceptable to use a value in pairing set [0.20, 0.25] Hz.

Figures A-2.13 and A-2.14 display the resulting surface heat flux, $q''_f(0, t_j)$ and temperature, $T_f(0, t_j)$, j = 0, 1, 2, … , N predictions using cut-off frequencies of f_c = 0.05, 0.10, 0.15, 0.20, 0.25, 0.30, 0.35 Hz. Based on the cross-correlation phase plane and its ensuing discussion, the favorable cut-off frequency, f_c (see Fig. A-2.12b) is chosen as f_c =

0.25 Hz. Figures A-2.15 and A-2.16 display the predicted surface heat flux, $q''_f(0,t)$ and surface temperature, $T_f(0, t)$ predictions using f_c = 0.25 Hz. These results are highly encouraging. As the probes are moved closer to the surface of interest, the delay in the prediction becomes less apparent. This is not evident in the present set of results due to the timescale. The shift in time is approximately the width of the region shown in Fig. A-2.13. The feasibility of the technique for short time duration and high sampling frequency studies is now discussed. In a nutshell, the simulation results using stainless steel domain in 5 seconds time duration with data collection as 300 Hz are shown in Figs. A-2.17 and A-2.18. Figure A-2.17 displays the predicted surface heat flux, $q''_f(0,t)$ while Fig. A-2.18 displays the surface temperature, $T_f(0, t)$ using f = 4.0 Hz. This value is obtained by phase plane and cross-correlation analysis following the previously outlined approach. The parameters used in the short time duration simulation are listed in Table A-2.2.

2.9 Conclusions

In this chapter, it was demonstrated that a heat-flux phase plane and cross-correlation coefficient phase plane can assist in identifying the optimal regularization parameter for resolving an inverse heat conduction problem by space marching. In this study, the identification of the low-pass Gauss filter's cut-off frequency is required at the data collection sites while the surface condition is sought. Numerical results indicate the robustness of the Gauss filter and the viability of the phase plane and cross-correlation analysis for extracting the optimum cut-off frequency. The phase plane and cross-correlation provide an additional analytical tool for estimating the optimum regularization parameter.

Chapter 3: Nonlinear Inverse Heat Conduction Problem of Surface Temperature Estimation by Calibration Integral Equation Method

This chapter is based on the paper: H. Chen, J. I. Frankel, and M. Keyhani, "Nonlinear inverse heat conduction problem of surface temperature estimation by calibration integral equation method", ZAMM – Journal of applied mathematics and mechanics / Zeitschrift für angewandte Mathematik und Mechanik (in review).

3.1 Introduction

This chapter addresses a universal need in heat transfer community for accurately determining the surface temperature in severely hostile thermal environments. Such environments appear in high-speed flights, combustion, brakes, nuclear reactors, arc jets, shock tunnels, furnaces, fires, etc. Under such harsh thermal conditions, surface mounted sensors can be damaged or produce dubious results. Instead, information collected by in-depth sensors are employed for predicting the surface thermal conditions. Projecting in-depth temperature data to surface involves an inverse heat conduction problem which is ill-posed [1]. That is, significant error magnification occurs when projecting unregularized in-depth noisy temperature data to the surface. In other words, small errors in the in-depth temperature data can cause substantial error growth in the prediction of both the surface temperature and heat flux. For this reason, regularization methods [1] are introduced for stabilizing all numerical schemes used for resolving inverse heat conduction problems. In most transient studies, the sensor's temperature is assumed to be identical to the positional temperature at the defined sensor site. Neglecting sensor characteristics involves omitting the effects of thermal capacitance, conductive lead losses and contact resistance [2-4]. The omission of these physical effects can potentially lead to a time-lagged and attenuated surface prediction.

Inverse heat conduction solution techniques have been applied to combustion [7, 8], brakes [9, 10], solidification [11], and quenching studies [12]. Various methods have been proposed for resolving inverse heat conduction problems over the past several decades, among them are the function specification method [21-23], space marching and finite difference methods [16-20], global time method [24, 81], exact solutions [15], conjugate gradient method [25, 26], boundary-element method [29, 30], and an iteration approach [31]. For all aforementioned inverse heat conduction methods, explicit knowledge of the thermophysical properties, and probe locations is required. Furthermore, the parameters associated with the temperature sensor model [3, 4] require quantification. Hence, these numerically inspired methods require significant and accurate parameter inputs and are presently termed as "parameter required" methods. Uncertainties are inherent to parameter measurements. Additionally, the measurement process is both financially expensive and time-consuming. System calibration is a "parameter free" methodology for resolving inverse heat conduction problems. In this framework, the thermophysical, geometrical and temperature sensor properties are not explicitly required for resolving the surface thermal conditions. These parameters are replaced by calibration data acquired through a well-designed and carefully implemented experiments. It is, of course, assumed that the system properties remain consistent for the life cycle of the test article.

The non-integer system identification (NISI) method [57-62] is a calibration method that requires the accurate extraction of the impulse function based on the fractional derivative formulation [63] of the heat equation. A known net surface heating source is used in the calibration test for obtaining the relationship between net surface heat flux and temperature response at the sensor site. The sensor characteristics, depth of sensor, and thermophysical properties of the host material are accounted in the calibration coefficients that are determined by a least-squares method. The unknown surface heat flux can be estimated by the corresponding sensor response and the calibration coefficients.

An alternative calibration methodology based on calibration integral equation is under development at the University of Tennessee [3, 48, 64-66]. The calibration integral equation method inherently contains sensor positioning, sensor characteristics and thermophysical properties of the host material in the final mathematical expression that relates the in-depth measured temperature data to the surface temperature or heat flux. The final mathematical expression is presented in terms of a Volterra integral equation of the first kind [67, 68] for the desired surface thermal condition. This integral statement is inherently ill-posed. Hence, regularization is required for stabilizing the integral equation. The calibration integral equation method was derived in a unified mathematical framework that can be applied to inverse heat conduction problems with higher dimensions [64], finite width domains [64, 65] and temperature-dependent thermophysical properties [65, 70, 72].

The linear (constant thermophysical properties) one-probe [3, 48, 66] and two-probe [69, 71] calibration integral equation methods for predicting surface heat flux have been numerically verified and experimentally validated with excellent accuracy at low temperatures. However, in aerospace applications, a large temperature variation is expected due to aerothermal heating effect [82]. Accounting for temperature-dependent thermophysical properties leads to a fully nonlinear physical formulation of the required physics. This is nontrivial and requires a substantial amount of consideration. A new nonlinear surface heat flux calibration method, based on Kirchhoff transformation and rescaling principles, was proposed and numerically investigated [70, 72]. This rescaling approach does not require specification of the probe locations. The rescaling and Kirchhoff transformation methods have been verified using high-temperature experimental data [73, 74]. However, both the thermal conductivity and thermal diffusivity for the host material are required for this approach. Frankel and Keyhani [65] proposed a nonlinear calibration integral equation method for predicting the surface heat flux through property physics linearization. This alternative approach does not require the specification of any thermophysical properties and probe locations.

For many aerospace and industrial applications, estimating the surface temperature using an inverse method can be as important as estimating surface heat flux [83]. The purpose of this chapter is to develop an effective calibration integral equation method for predicting surface temperature that accounts for the unknown temperature-dependent thermophysical properties. The mathematical formulation of the temperature calibration method is expressed in terms of a nonlinear Volterra integral equation of the first kind involving the surface temperature. This functional equation possesses a small set of undetermined coefficients associated with the chosen expansion. Data from the two calibration tests are used for obtaining the undetermined coefficients. The order of truncation is determined by checking the equality of the integral equation and a sequential time study whereby coefficient stability is sought. A local future-time method [47] is implemented as regularization scheme for the Volterra integral equation of the first kind. This regularization method retains causality while producing a second kind Volterra integral equation for discretization. A phase plane and cross-correlation analyses [56, 75, 76] are then employed for estimating the optimal regularization parameter. In the present context, the optimal future-time parameter is estimated. The results illustrate the merit and accuracy of the nonlinear temperature calibration method as well as the effectiveness of the phase plane and cross-correlation analyses for determining the optimal future-time parameter.

3.2 Problem statement and background

Consider the one-dimensional slab displayed in Fig. A-3.1. The front surface at $x = 0$ is subjected to surface heating denoted as $q_0''(t)$ with the net conductive heat flux denoted as $q''(0, t)$ while the surface temperature is denoted as $T(0, t)$. The thickness of the one-dimensional geometry is L such that $x \in [0, L]$ and a temperature sensor is embedded at position $x = b$. The one-dimensional slab is composed of a material with temperature-dependent thermal conductivitαy, $k(T)$ and heat capacitance, $\rho c(T)$. The αitial temperature distribution is assumed uniforαm at T_0 in $x \in [0, L]$. For simplicity but without loss of generality, the back surface boundary condition at $x = L$ is assumed adiabatic ($q''(L, t) = 0$). By assuming an adiabatic back surface boundary condition, it is convenient for formulating the calibration integral equation that requires only one in-depth temperature sensor [64, 73, 84]. The calibration integral equation method that considers arbitrary back surface boundary conditions which change between the calibration and reconstruction tests can be formulated by introducing a second in-depth temperature sensor. The two-probe linear calibration integral equation method [69] and two-probe nonlinear calibration integral equation method with given thermal conductivity and thermal diffusivity [70] have been investigated. The two-probe nonlinear calibration integral equation method that accounts for unknown temperature-dependent thermophysical properties is the subject of Chapters 4 and 5.

3.3 Formulation of the nonlinear temperature calibration integral equation

3.3.1 Background: the linear temperature calibration integral equation

The linear one-dimensional temperature calibration integral equation has been derived based on frequency domain analysis of the linear heat equation [3]. The linear temperature calibration integral equation is

$$\int_{u=0}^{t} \theta_r(0,u)\theta_c(b,t-u)du = \int_{u=0}^{t} \theta_c(0,u)\theta_r(b,t-u)du, \;\; t \geq 0 \tag{3.1}$$

where $\theta(x, t) = T(x, t) - T_0$ denotes the reduced temperature and "u" is a dummy time variable. Here, the probe is located at $x = b$ and the reduced surface temperature is sought at $x = 0$. The numerical value for probe position of $x = b$ is not required in Eq. (3.1). The subscript "c" and "r" represent calibration and reconstruction tests. The goal is to resolve Eq. (3.1) for the unknown reduced surface temperature, $\theta_r(0, t)$ as all other functions can be expressed in terms of data collected over time.

3.3.2 Derivation of the nonlinear temperature calibration integral equation

Consider the transient one-dimensional nonlinear heat equation [85] given as

$$\rho c(T)\frac{\partial T}{\partial t}(x,t)=\frac{\partial}{\partial x}\left[k(T)\frac{\partial T}{\partial x}(x,t)\right],\ \ x\in[0,L],\ \ t\geq 0 \tag{3.2a}$$

subject to the boundary conditions

$$q_0''(t)=q''(0,t)\equiv -k\left(T(0,t)\right)\frac{\partial T}{\partial x}(0,t),\ \ t>0 \tag{3.2b}$$

$$\frac{\partial T}{\partial x}(L,t)=0,\ \ t>0 \tag{3.2c}$$

and initial condition

$$T(x,0)=T_0,\ \ x\in[0,L] \tag{3.2d}$$

where T is the temperature-dependent variable, x and t are the independent spatial and temporal variables, ρ is the density, c is the specific heat capacity, k is the thermal conductivity. Here, $q''(0, t)$ denotes the conductive (net) heat flux at $x = 0$ while $q_0''(t)$ can be composed of source and/or other modes of heat transfer. In Ref. [65], the concept of a generalized property transforms for linearization was introduced in the context of an unknown heat flux boundary condition on the active heating side. In a nutshell, it was demonstrated that the heat equation can be decomposed as

$$\rho c(T)\frac{dT}{d\varphi}\frac{\partial \varphi}{\partial t}(x,t)=\frac{\partial}{\partial x}\left(k(T)\frac{dT}{d\varphi}\frac{\partial \varphi}{\partial x}(x,t)\right),\ \ x\in[0,L],\ \ t\geq 0 \tag{3.3}$$

where the transformed variable $\varphi(x, t)$ can be thermal conductivity, thermal capacity, thermal diffusivity, thermal effusivity, etc [65]. The assumption that inverse function of φ (T) exists is made that permits a single valued $dT/d\varphi$. Actually, the inverse function of temperature-dependent thermophysical properties $k(T)$, $c(T)$, $\alpha(T)$, $\beta(T)$ exist for almost all practical materials [85]. Assuming there exists a combination that produces

$$k(T)\frac{dT}{d\varphi} = \kappa \approx \text{constant} \tag{3.4}$$

then we can alternatively express the transformed heat equation in terms of the transformed variable, $\varphi(x, t)$ as

$$\frac{1}{\alpha(T)}\frac{\partial\varphi}{\partial t}(x,t) = \frac{\partial^2\varphi}{\partial x^2}(x,t), \;\; x \in [0, L], \;\; t \geq 0 \tag{3.5}$$

By further assuming the thermal diffusivity $\alpha(T)$ is a constant value denoted as α_0. We can write the linearized heat equation as

$$\frac{1}{\alpha_0}\frac{\partial\varphi}{\partial t}(x,t) = \frac{\partial^2\varphi}{\partial x^2}(x,t), \;\; x \in [0, L], \;\; t \geq 0 \tag{3.6a}$$

with respect to the transformed boundary conditions as

$$q''(0,t) \equiv -\kappa\frac{\partial\varphi}{\partial x}(0,t), \;\; t > 0 \tag{3.6b}$$

$$\frac{\partial\varphi}{\partial x}(L,t) = 0, \;\; t > 0 \tag{3.6c}$$

and the transformed initial condition as

$$\varphi(x,0) = \varphi(T_0), \;\; x \in [0, L] \tag{3.6d}$$

Let us now define $\phi(T) = \varphi(T) - \varphi(T_0)$, then Eqs. (3.6a-d) become

$$\frac{1}{\alpha_0}\frac{\partial\phi}{\partial t}(x,t) = \frac{\partial^2\phi}{\partial x^2}(x,t), \;\; x \in [0, L] \tag{3.7a}$$

subject to the transformed boundary conditions

$$q''(0,t) \equiv -\kappa\frac{\partial\phi}{\partial x}(0,t), \;\; t > 0 \tag{3.7b}$$

$$\frac{\partial \phi}{\partial x}(L,t) = 0, \;\; t > 0 \tag{3.7c}$$

and the transformed initial condition

$$\phi(x,0) = 0, \;\; x \in [0, L] \tag{3.7d}$$

The calibration integral equation for the linearized model system given in Eqs. (3.7a-d) become

$$\int_{u=0}^{t} \phi_r(0,u)\, \phi_c(b,t-u)du = \int_{u=0}^{t} \phi_c(0,u)\, \phi_r(b,t-u)du, \;\; t \geq 0 \tag{3.8}$$

Equation (3.8) is the model equation under examination for the present study. The approach taken here is based on representing the transform functions in terms of Chebyshev expansion of the first kind [86-90] for mapped temperature in the range [-1, 1] defined as

$$T^*(x,t) = \frac{2T(x,t) - T_L - T_U}{T_U - T_L}, \;\; T^* \in [-1, 1] \tag{3.9}$$

where "T_L" and "T_U" represent the lower and upper temperature bound, respectively. The values of "T_L" and "T_U" can be properly set to ensure that the temperature ranges for all calibration and reconstruction tests are in the domain [T_L, T_U]. The coefficients of the Chebyshev expansion are determined by an ordinary least-squares (OLS) method [91, 92] involving two well-defined calibration tests [65] with known surface temperatures and correspondently measured in-depth temperatures at the fixed location, $x = b$. Using the Chebyshev expansion of the first kind for the mapped temperature to represent the transformed variable $\phi(x, t)$ in Eq. (3.8) as

$$\phi(x,t) = \sum_{n=0}^{\infty} a_n E_n(T^*(x,t)) = \sum_{n=0}^{\infty} a_n E_n(x,t) \approx \phi_N(x,t) = \sum_{n=0}^{N} a_n^N E_n(x,t), \tag{3.10a}$$

where E_n is the n^{th} Chebyshev polynomial of the first kind. Further, it is clear that

$$E_n(T^*(x,t)) = E_n(x,t),\ \ n = 0, 1, 2, ... \tag{3.10b}$$

Table A-3.1 presents several Chebyshev polynomials of the first kind conforming to the notation used in this context. Chebyshev polynomials are mutually orthogonal in the domain [-1, 1] with respect to the weight function $(1-T^{*2})^{-1/2}$ and it is highly efficient for approximating functions [79, 91, 92]. The monomial basis T^n, n = 0, 1, …, are not well suited to the present analysis as they are susceptible to excessive round-off [91]. Hence, using the monomial basis $\boldsymbol{T}^n$ is a poor choice for approximating a function in the present ill-posed problem.

In Eq. (3.10a), the transformed variable ϕ is a function of temperature but with the understanding that the units of the coefficients $\{a_0, a_1, a_2, ...\}$ are unknown. Substituting the expansion given in Eq. (3.10a) into Eq. (3.8) produces

$$\begin{aligned}
&\int_{u=0}^{t} \left(a_0 E_0 + a_1 E_{1,\,r}(0,u) + a_2 E_{2,\,r}(0,u) + a_3 E_{3,\,r}(0,u) + ...\right)\times \\
&\quad \left(a_0 E_0 + a_1 E_{1,\,c}(0,t-u) + a_2 E_{2,\,c}(0,t-u) + a_3 E_{3,\,c}(0,t-u) + ...\right) du \\
&= \int_{u=0}^{t} \left(a_0 E_0 + a_1 E_{1,\,c}(0,u) + a_2 E_{2,\,c}(0,u) + a_3 E_{3,\,c}(0,u) + ...\right)\times \\
&\quad \left(a_0 E_0 + a_1 E_{1,\,r}(0,t-u) + a_2 E_{2,\,r}(0,t-u) + a_3 E_{3,\,r}(0,t-u) + ...\right) du,\ \ t \ge 0
\end{aligned} \tag{3.11a}$$

By comparing Eq. (3.11a) to the linear temperature calibration given in Eq. (3.1), we can set $a_1 = 1$. Hence, the truncated version of Eq. (3.11a) is expressible as

$$\int_{u=0}^{t}\left(a_0^N E_0+E_{1,r}(0,u)+a_2^N E_{2,r}(0,u)+a_3^N E_{3,r}(0,u)+...+a_N^N E_{N,r}(0,u)\right)\times$$
$$\left(a_0^N E_0+E_{1,c}(0,t-u)+a_2^N E_{2,c}(0,t-u)+a_3^N E_{3,c}(0,t-u)+...+a_N^N E_{N,c}(0,t-u)\right)du$$
$$\approx\int_{u=0}^{t}\left(a_0^N E_0+E_{1,c}(0,u)+a_2^N E_{2,c}(0,u)+a_3^N E_{3,c}(0,u)+...+a_N^N E_{N,c}(0,u)\right)\times$$
$$\left(a_0^N E_0+E_{1,r}(0,t-u)+a_2^N E_{2,r}(0,t-u)+a_3^N E_{3,r}(0,t-u)+...+a_N^N E_{N,r}(0,t-u)\right)du,\ \ t\geq 0.$$

(3.11b)

which now involves a finite number of undetermined coefficients $\{a_0^N, a_2^N, a_3^N, ..., a_N^N\}$. If N is sufficiently large then $a_j^N \to a_j$ for j = 0, 2, 3, … , N, and the required balance of Eq. (3.11b) is given as

$$\int_{u=0}^{t}\left(a_0^N E_0+E_{1,r}(0,u)+a_2^N E_{2,r}(0,u)+a_3^N E_{3,r}(0,u)+...+a_N^N E_{N,r}(0,u)\right)\times$$
$$\left(a_0^N E_0+E_{1,c}(0,t-u)+a_2^N E_{2,c}(0,t-u)+a_3^N E_{3,c}(0,t-u)+...+a_N^N E_{N,c}(0,t-u)\right)du$$
$$=\int_{u=0}^{t}\left(a_0^N E_0+E_{1,c}(0,u)+a_2^N E_{2,c}(0,u)+a_3^N E_{3,c}(0,u)+...+a_N^N E_{N,c}(0,u)\right)\times$$
$$\left(a_0^N E_0+E_{1,r}(0,t-u)+a_2^N E_{2,r}(0,t-u)+a_3^N E_{3,r}(0,t-u)+...+a_N^N E_{N,r}(0,t-u)\right)du,\ \ t\geq 0.$$

(3.11c)

(An alternative mathematical development based on residuals is presented in Chapter 5. This chapter emphasizes physics over mathematical rigor). Two well-defined calibration tests are required for estimating the undetermined coefficients $\{a_0^N, a_2^N, a_3^N, ..., a_N^N\}$ presented in Eq. (3.11c). The two well-defined calibration tests are denoted with the subscripts “c1” and “c2” for notational convenience. Therefore, Eq. (3.11c) can be written as

$$
\begin{aligned}
&\int_{u=0}^{t}\left(a_0^N E_0+E_{1,\,c1}(0,u)+a_2^N E_{2,\,c1}(0,u)+a_3^N E_{3,\,c1}(0,u)+\ldots+a_N^N E_{N,\,c1}(0,u)\right)\times\\
&\quad\left(a_0^N E_0+E_{1,\,c2}(0,t-u)+a_2^N E_{2,\,c2}(0,t-u)+a_3^N E_{3,\,c2}(0,t-u)+\ldots+a_N^N E_{N,\,c2}(0,t-u)\right)du\\
&=\int_{u=0}^{t}\left(a_0^N E_0+E_{1,\,c2}(0,u)+a_2^N E_{2,\,c2}(0,u)+a_3^N E_{3,\,c2}(0,u)+\ldots+a_N^N E_{N,\,c2}(0,u)\right)\times\\
&\quad\left(a_0^N E_0+E_{1,\,c1}(0,t-u)+a_2^N E_{2,\,c1}(0,t-u)+a_3^N E_{3,\,c1}(0,t-u)+\ldots+a_N^N E_{N,\,c1}(0,t-u)\right)du
\end{aligned}
\tag{3.12}
$$

Equation (3.12) possesses N unknown coefficients explicitly given by the set $\{a_0^N, a_2^N, a_3^N, ..., a_N^N\}$ that can be determined using a nonlinear least-squares method based on the temperature data collected from the time set, $\{t_i\}_{i=1}^{M}$, where $t_i = i\Delta t$, $i = 1, 2, 3, \ldots,$ M, with $\Delta t \triangleq t_{\max} / M$. The least-squares residual is expressed as

$$
\begin{aligned}
&r_N\left(t_i;\{a_0^N, a_2^N, a_3^N, ..., a_N^N\}\right)\\
&=\int_{u=0}^{t_i}\left(a_0^N E_0+E_{1,\,c1}(0,u)+a_2^N E_{2,\,c1}(0,u)+a_3^N E_{3,\,c1}(0,u)+\ldots+a_N^N E_{N,\,c1}(0,u)\right)\times\\
&\quad\left(a_0^N E_0+E_{1,\,c2}(0,t_i-u)+a_2^N E_{2,\,c2}(0,t_i-u)+a_3^N E_{3,\,c2}(0,t_i-u)+\ldots+a_N^N E_{N,\,c2}(0,t_i-u)\right)du\\
&-\int_{u=0}^{t_i}\left(a_0^N E_0+E_{1,\,c2}(0,u)+a_2^N E_{2,\,c2}(0,u)+a_3^N E_{3,\,c2}(0,u)+\ldots+a_N^N E_{N,\,c2}(0,u)\right)\times\\
&\quad\left(a_0^N E_0+E_{1,\,c1}(0,t_i-u)+a_2^N E_{2,\,c1}(0,t_i-u)+a_3^N E_{3,\,c1}(0,t_i-u)+\ldots+a_N^N E_{N,\,c1}(0,t_i-u)\right)du
\end{aligned}
$$

$$
i = 1, 2, 3, \ldots, M \tag{3.13}
$$

Forming the sum of the squares of $r_N\left(t_i;\{a_0^N, a_2^N, a_3^N, ..., a_N^N\}\right)$ produces

$$
\begin{aligned}
&R_N\left(\{a_0^N, a_2^N, a_3^N, ..., a_N^N\}\right)=\sum_{i=1}^{M} r_N^2\left(t_i;\{a_0^N, a_2^N, a_3^N, ..., a_N^N\}\right)\\
&=\sum_{i=1}^{M}\left(\begin{aligned}
&\int_{u=0}^{t_i}\left(a_0^N E_0+E_{1,\,c1}(0,u)+a_2^N E_{2,\,c1}(0,u)+a_3^N E_{3,\,c1}(0,u)+\ldots+a_N^N E_{N,\,c1}(0,u)\right)\times\\
&\quad\left(a_0^N E_0+E_{1,\,c2}(0,t_i-u)+a_2^N E_{2,\,c2}(0,t_i-u)+a_3^N E_{3,\,c2}(0,t_i-u)+\ldots+a_N^N E_{N,\,c2}(0,t_i-u)\right)du\\
&-\int_{u=0}^{t_i}\left(a_0^N E_0+E_{1,\,c2}(0,u)+a_2^N E_{2,\,c2}(0,u)+a_3^N E_{3,\,c2}(0,u)+\ldots+a_N^N E_{N,\,c2}(0,u)\right)\times\\
&\quad\left(a_0^N E_0+E_{1,\,c1}(0,t_i-u)+a_2^N E_{2,\,c1}(0,t_i-u)+a_3^N E_{3,\,c1}(0,t_i-u)+\ldots+a_N^N E_{N,\,c1}(0,t_i-u)\right)du
\end{aligned}\right)^2
\end{aligned}
$$

$$
i = 1, 2, 3, \ldots, M \tag{3.14}
$$

and then formally minimize, with respect to each undetermined coefficient in the set, per

$$\frac{\partial R_N}{\partial a_n^N}(\{a_0^N, a_2^N, a_3^N, ..., a_N^N\}) = 0, \quad n = 0, 2, 3, ..., N \tag{3.15}$$

for producing a closed system of nonlinear equations involving N unknown expansion coefficients. An appropriate numerical analysis is performed for obtaining the N unknown expansion coefficients. Once the coefficients are calculated, Eq. (3.11c) can be used to find the reconstruction prediction for a given calibration test. An appropriate regularization scheme is required for recovering the transformed surface temperature $\phi_r(0, t_i)$ at each time step t_i, i = 1, 2, 3, …, M, as needed in Eq. (3.11c). Section 3.4 addresses this issue in Eq. (3.11c) after the expansion coefficients are obtained. A nonlinear root-finder is required for determining $T_r^*(0, t_i)$, i = 1, 2, 3, … , M. Subsequently $T_r(0, t_i)$ are obtained by inverting Eq. (3.9).

It is worth noting that although the thermal diffusivity $\alpha(T)$ is assumed as a constant value denoted as α_0 in Eq. (3.6a), the proposed approach will be shortly shown to work well for stainless steel and carbon-carbon. Both materials possess considerable thermal diffusivity variations from room temperature to high temperatures [84]. Furthermore, this concept will potentially work well for ultra-high-temperature ceramics (UHTCs) being considered for some thermal protection systems (TPS).

3.4 Regularization by the future-time method

Equations (3.8) and (3.11c) are Volterra integral equations of the first kind [67, 68] that are ill-posed. A local future-time method [3, 47, 64] is utilized as the regularization scheme for stabilizing the ill-posed first kind Volterra integral equation. The future-time method recasts the Volterra integral equation of the first kind into a Volterra integral equation of the second kind that is well-posed [67, 68]. It also maintains causality that makes it easy to program. The major technical issue regarding all regularization methods is the estimation of the optimal regularization parameter as some techniques are highly sensitive to its choice. Section 3.5 addresses this issue and provides insight into means for extracting the optimal choice with the aid of a phase plane and cross-correlation analyses. The calibration integral equation given in Eq. (3.8) can be alternatively expressed as

$$\int_{u=0}^{t} \phi_r(0,u)\, \phi_c(b,t-u)du = F(t), \;\; t \geq 0 \tag{3.16a}$$

where

$$F(t) = \int_{u=0}^{t} \phi_c(0,u)\, \phi_r(b,t-u)du, \;\; t \geq 0 \tag{3.16b}$$

Observe that the integrand in Eq. (3.16b) is completely known in the discrete sense after the expansion coefficients in Eq. (3.12) are calculated. Time is now advanced by introducing future-time parameter γ, through letting $t \rightarrow t + \gamma$, Eq. (3.16a) becomes

$$\int_{u=0}^{t+\gamma} \phi_r(0,u)\, \phi_c(b,t+\gamma-u)du = F(t+\gamma), \;\; t \in [0, t_{\max} - \gamma] \tag{3.17}$$

Observe that the recoverable time domain is reduced by γ as noted by $t \in [0, t_{\max} - \gamma]$. The integral given in Eq. (3.17) can be expressed as

$$\int_{u=0}^{t} \phi_r(0,u)\, \phi_c(b,t+\gamma-u)du + \int_{u=t}^{t+\gamma} \phi_r(0,u)\, \phi_c(b,t+\gamma-u)du = F(t+\gamma), \;\; t \in [0, t_{\max} - \gamma] \tag{3.18}$$

where the region $u \in [t, t + \gamma]$ is now isolated for further manipulations. The reader is reminded that γ should be a represent a short period of time that accounts for physical contributions involving penetration time and temperature sensor characteristics effects. Next, define $v = u - t$ for use in the second integral in Eq. (3.18). Therefore, Eq. (3.18) can be written as

$$\int_{u=0}^{t} \phi_r(0,u)\, \phi_c(b,t+\gamma-u)du + \int_{v=0}^{\gamma} \phi_r(0,v+t)\, \phi_c(b,\gamma-v)dv = F(t+\gamma),\ \ t \in [0, t_{\max} - \gamma] \tag{3.19}$$

If γ is sufficiently small then $\phi_r(0,v+t) \approx \phi_r(0,t)$ since $v \in [0,\gamma]$. If this is the case then Eq. (3.19) can be written as

$$\int_{u=0}^{t} \phi_r(0,u)\, \phi_c(b,t+\gamma-u)du + \phi_r(0,t)\int_{v=0}^{\gamma} \phi_c(b,\gamma-v)dv \approx F(t+\gamma),\ \ t \in [0, t_{\max} - \gamma] \tag{3.20a}$$

In order to recover the equality, Eq. (3.20a) can be written as

$$\int_{u=0}^{t} \phi_{r,\gamma}(0,u)\, \phi_c(b,t+\gamma-u)du + \phi_{r,\gamma}(0,t)\int_{v=0}^{\gamma} \phi_c(b,\gamma-v)dv = F(t+\gamma),\ \ t \in [0, t_{\max} - \gamma] \tag{3.20b}$$

where $\phi_{r,\gamma}(0,t) \approx \phi_r(0,t)$. Equation (3.20b) is a Volterra integral equation of the second kind for the unknown transformed surface temperature denoted by $\phi_{r,\gamma}(0, t)$. Note: if $\int_{v=0}^{\gamma} \phi_c(b,\gamma-v)dv \to 0$ then Eq. (3.20b) reduces to a first kind equation for $\phi_{r,\gamma}(0, t)$. Hence, this term has to be sufficiently large to introduce stability. Here, $\phi_{r,\gamma}(0, t)$ is an approximation to $\phi_r(0, t)$ as it depends on the future-time parameter γ and permits the return of the equal sign as shown in Eq. (3.20b). Data are collected up to a specific time denoted as $t_{\max}$. The predicted transformed surface temperature $\phi_{r,\gamma}(0, t)$ can only be resolved in temporal domain $t \in [0, t_{\max} - \gamma]$ due to the inclusion of future data for stabilizing the numerical implementation.

Discretization of Eq. (3.20b) can be performed by a variety numerical integration rules [79]. However, low-order rules are preferred for inverse problems. A right-hand rectangular rule is employed in this context. The discrete values for $\phi_{r,\gamma}(0, t_i)$ can be obtained in the time-marching form where $\gamma \rightarrow \gamma_m = mM_f\Delta t$. Here, m is a positive integer and Δt is given as $\Delta t = t_{\max}/M$. The constant M is the number of segments (or samples) in the discretized temporal domain, and M_f is a convenient multiplying factor introduced to time-advance in multiples of Δt. Discretizing Eq. (3.20b) based on a product integration rule [67] produces

$$\sum_{j=1}^{i}\phi_{r,\gamma_m}(0,t_j)\int_{u=t_{j-1}}^{t_j}\phi_c(b,t_i+\gamma_m-u)du+\phi_{r,\gamma_m}(0,t_i)\sum_{j=1}^{mM_f}\int_{u=t_{j-1}}^{t_j}\phi_c(b,\gamma_m-u)du=F(t_i+\gamma_m),$$

$$i = 1, 2, 3, \ldots, M - mM_f \quad (3.21a)$$

The equal sign in Eq. (3.21a) should produce a change in notation as the truncation error is not explicitly displayed. However, for notational simplicity, this change is omitted with the understanding that an additional approximation has been incurred. Next, extracting the desired transformed surface temperature at $t = t_i$ produces

$$\phi_{r,\gamma_m}(0,t_i)=\frac{F(t_i+\gamma_m)-\sum_{j=1}^{i-1}\phi_{r,\gamma_m}(0,t_j)\int_{u=t_{j-1}}^{t_j}\phi_c(b,t_i+\gamma_m-u)du}{\int_{u=t_i-1}^{t_i}\phi_c(b,t_i+\gamma_m-u)du+\sum_{j=1}^{mM_f}\int_{u=t_{j-1}}^{t_j}\phi_c(b,\gamma_m-u)du},$$

$$i = 1, 2, 3, \ldots, M - mM_f \quad (3.21b)$$

with

$$F(t_i+\gamma_m)=\sum_{j=1}^{i+mM_f}\phi_c(0,u)\phi_r(b,t_i+\gamma_m-u)\Delta t,\;\; i=1,2,3,\ldots,M-mM_f \qquad (3.21c)$$

The future-time parameter γ_m must be specified over a range of values and then interrogated until an optimal value is determined based on some metric or other physics based criteria.

In this chapter, both a phase plane (qualitative) and cross-correlation (quantitative) analyses [56, 75, 76] are performed for estimating the optimal future-time parameter.

In this context, Eqs. (3.16a,b) are the exact formulations for the chosen model being considered for the temperature calibration integral equation. Equation (3.20a) represents the approximation as the chosen stabilization scheme modifies the transformed surface temperature calibration integral equation. The introduction of the future-time method converts the ill-posed first kind Volterra integral equation into a well-posed second kind Volterra integral equation for sufficiently large γ. If the future-time parameter, γ is too small then the prediction via Eq. (3.21b) is unstable. In the opposite sense, if the future-time parameter γ is too large then the prediction results are over-smoothed (highly attenuated) since too many high frequencies in the signal are removed. Hence, significant surface physics will be lost. Compromise should be maintained between stability and accuracy. From this, it is evident that these regions exist; namely, instability, transition, and over-smoothed. The optimal regularization parameter lies in the transition region. Further, inverse problems should first involve an exclusionary process unlike direct problems where the solution can be concluded by an inclusionary process. That is, a significant amount of work can be reduced by defining the best solution when removing the instability and over-smoothed predictions.

3.5 Phase plane and cross-correlation analyses for estimating the optimal future-time parameter

Recently, a metric involving phase plane and cross-correlation analyses have been successfully applied for estimating the optimal future-time parameter associated with the future-time method [56, 75, 76]. In vibration studies, the phase plane often involves the time parameterized plot of velocity versus displacement [93]. By analogy, one can define the thermal phase plane as the temperature rate, *dT/dt* versus temperature, *T* where time is parameterized. The predicted surface temperature rate and temperature for a specifically chosen future-time parameter are now represented as $\dot{T}_{r,\gamma_m}(0,t_i)$ and $T_{r,\gamma_m}(0,t_i)$, respectively. If surface heat flux is sought then a heat flux phase plane would be applied [56, 75, 76]. Loss of randomness indicates the formation of a pattern in the phase plane and assists in establishing the optimal future-time parameter. Varying the discrete γ_m spectrum provides a visual basis for estimating γ_{opt} in this parameterized setting. Therefore, the desired range for the optimal future-time parameter can be visually estimated when a loss of randomness or onset of a pattern formation occurs in the phase plane.

The surface temperature cross-correlation coefficient is defined as [56, 75, 76]

$$R_T(T_{r,\gamma_m},T_{r,\gamma_{m+1}}) = \frac{\sum_{i=1}^{M-PM_f} T_{r,\gamma_m}(0,t_i)T_{r,\gamma_{m+1}}(0,t_i)}{\sqrt{\sum_{i=1}^{M-PM_f}\left(T_{r,\gamma_m}(0,t_i)\right)^2 \sum_{i=1}^{M-PM_f}\left(T_{r,\gamma_{m+1}}(0,t_i)\right)^2}},$$

$$i = 1, 2, 3, \ldots, M - PM_f;\, m = p,\ p+1,\ p+2, \ldots, p-2+P \quad (3.22a)$$

while the surface temperature rate cross-correlation coefficient is defined as [56, 75, 76]

$$R_{\dot{T}}(\dot{T}_{r,\gamma_m},\dot{T}_{r,\gamma_{m+1}}) = \frac{\sum_{i=1}^{M-PM_f} \dot{T}_{r,\gamma_m}(0,t_i)\dot{T}_{r,\gamma_{m+1}}(0,t_i)}{\sqrt{\sum_{i=1}^{M-PM_f}\left(\dot{T}_{r,\gamma_m}(0,t_i)\right)^2 \sum_{i=1}^{M-PM_f}\left(\dot{T}_{r,\gamma_{m+1}}(0,t_i)\right)^2}},$$

$$i = 1, 2, 3, \ldots, M - PM_f; m = p, p+1, p+2, \ldots, p-2+P \quad (3.22b)$$

where $\gamma_m = mM_f\Delta t$ (s), $m = p, p+1, p+2, \ldots, p-2+P$, p is the 1st m value and P is the number of values in γ spectrum. Here, $M_f\Delta t$ is the stepping time for forming a finite set of predictions. Dependency (closeness) is indicated when the cross-correlation coefficient approaches unity. In other words, linear dependency is achieved by using two adjacent future-time parameters (γ_m and γ_{m+1}) for predicting surface temperature. It has been illustrated that driving the surface temperature cross-correlation coefficient $R_T(T_{r,\gamma_m},T_{r,\gamma_{m+1}})$ to unity would meet expectation while it is inappropriate to drive the surface temperature rate cross-correlation coefficient $R_{\dot{T}}(\dot{T}_{r,\gamma_m},\dot{T}_{r,\gamma_{m+1}})$ to unity as noise is amplified in the numerical differentiation process. Hence, the fundamental key for identifying the transition between an unstable surface prediction and an over-smoothed surface prediction is the magnitude of surface temperature rate cross-correlation coefficient $R_{\dot{T}}(\dot{T}_{r,\gamma_m},\dot{T}_{r,\gamma_{m+1}})$. As $R_{\dot{T}}(\dot{T}_{r,\gamma_m},\dot{T}_{r,\gamma_{m+1}}) \to 1$, over-smoothing of the predicted surface temperature will be observed. As remarked earlier, a compromise between stability and accuracy must be maintained. Thus, the transition region between instability and over-smoothness is where the optimum future-time parameter lies.

3.6 Results

3.6.1 Simulated data collection

A purely numerical simulation is performed for demonstrating the viability of the proposed nonlinear temperature calibration integral equation method. The geometry for simulation is displayed in Fig. A-3.1. An in-depth “thermocouple” is embedded at position $x = b$ and a thin film “thermocouple” is mounted at the surface ($x = 0$) as illustrated in Fig. A-3.1. In Fig. A-3.1, the in-depth “thermocouple” and the surface “thermocouple” are denoted as “TC” and “TF”, respectively. An idealized TF “thermocouple” is visualized for measuring the surface temperature in the calibration tests. Surface temperatures should be accurately quantified in the context of calibration tests. The host material of the one-dimensional geometry shown in Fig. A-3.1 for the numerical simulation presented in this chapter is stainless steel 304. The thermophysical properties of the stainless steel 304 [80] and the geometrical properties for this study are given in Table A-3.2. Figures A-3.2a-c display the temperature-dependent thermal conductivity, $k(T)$, specific heat, $c(T)$ and thermal diffusivity, $\alpha(T) = k(T)/(\rho c(T))$ over a large temperature range. For the nonlinear effects to be significant, this simulation will cover a large temperature range.

As all data for the present study are simulated, a direct heat conduction problem must be initially solved for generating the required temperature data for the calibration and reconstruction tests. To create surface and in-depth temperature data, the net surface heat flux, $q''(0,t)$ is specified for the calibration and reconstruction tests. This condition along with the adiabatic back boundary at $x = L$ permit direct finite difference modeling. The initial condition for each test can be different but should be constant in the spatial domain. An implicit finite difference method is implemented where the thermophysical properties are evaluated based on one-time step lag for simplicity [94]. In this numerical study, two calibration tests with known temperature at $x = 0$ and $x = b$ are used for calculating the undetermined coefficients $a_0^N, a_2^N, a_3^N, \ldots, a_N^N$ in Eq. (3.12). A reconstruction test with unknown surface temperature ($x = 0$) and known temperature at in-depth thermocouple site ($x = b$) is used for verifying the surface temperature prediction approach. Calibration test 1 involves a constant surface heat flux given as $q''_{c1}(0,t) = q''_{c1,\max}$ in $t \in [0, t_{\max}]$. Calibration test 2 uses a step change surface heat flux as $q''_{c2}(0,t) = q''_{c2,\max}$ in $t \in [0, t_{\max}/2]$ and $q''_{c2}(0,t) = 0$ in $t \in (t_{\max}/2, t_{\max}]$. The reconstruction test involves a double Gaussian surface heat flux defined as

$$q''_s(t) = q''(0,t) = q''_{r,\max}\left(e^{-\frac{(t-\beta_1)^2}{\sigma_1^2}} + 0.75e^{-\frac{(t-\beta_2)^2}{\sigma_2^2}}\right), \ t \in [0, t_{\max}]. \tag{3.23}$$

Table A-3.2 contains the values used for the parameters in all test runs. The double Gauss function possesses a characteristic temporal history seen in some aerospace heating applications. Figure A-3.3 displays the surface heat fluxes for calibration test 1, $q''_{c1}(0,t)$; calibration test 2, $q''_{c2}(0,t)$; and, reconstruction test, $q''_r(0,t)$. The implicit finite difference scheme used for solving the direct heat conduction problem in the region $x \in [0, L]$ has spatial and temporal widths denoted by Δx and Δt, respectively. The number of temporal segments in the implicit finite difference scheme is denoted as M. The positional temperatures at $x = 0$, $x = b$ and $x = L$ under calibration test 1, calibration test 2 and reconstruction test obtained by the implicit finite difference scheme are displayed in Figs. A-3.4a, b, c, respectively. Those positional temperatures are denotes as $\{T_{c1}(0, t_i), T_{c1}(b, t_i), T_{c1}(L, t_i)\}$, $\{T_{c2}(0, t_i), T_{c2}(b, t_i), T_{c2}(L, t_i)\}$, and $\{T_r(0, t_i), T_r(b, t_i), T_r(L, t_i)\}$, where $t_i =$

$i\Delta t$, i = 1, 2, 3, … , M. Convergence of the implicit finite difference scheme is verified by grid halving. Convergence is achieved as shown in Fig. A-3.5. The maximum percentage difference between the two temperature curves is less than 0.1%.

The sampling frequency is denoted as $f_{sampling}$ (time step Δt = 1/$f_{sampling}$) for the emulated surface mounted "thermocouple" and in-depth "thermocouple" data used in this study, In other words, the discrete data at $t_i = i\Delta t$, i = 1, 2, 3, … , M, obtained by the implicit finite difference scheme are used. Artificial noise is added to the positional temperatures $\{T_{c1}(0, t_i), T_{c1}(b, t_i)\}$, $\{T_{c2}(0, t_i), T_{c2}(b, t_i)\}$, *and* $\{T_r(b, t_i)\}$ for mimicking "thermocouple" data in accordance to

$$T_{tc,\,c1}(0,t_i) = T_{c1}(0,t_i)(1+\varepsilon_T r_{i,\,c1,\,0}),\;\; t_i = i\Delta t, i = 0, 1, \ldots, M \qquad (3.24a)$$

$$T_{tc,\,c1}(b,t_i) = T_{c1}(b,t_i)(1+\varepsilon_T r_{i,\,c1,\,b}),\;\; t_i = i\Delta t, i = 0, 1, \ldots, M \qquad (3.24b)$$

$$T_{tc,\,c2}(0,t_i) = T_{c2}(0,t_i)(1+\varepsilon_T r_{i,\,c2,\,0}),\;\; t_i = i\Delta t, i = 0, 1, \ldots, M \qquad (3.24c)$$

$$T_{tc,\,c2}(b,t_i) = T_{c2}(b,t_i)(1+\varepsilon_T r_{i,\,c2,\,b}),\;\; t_i = i\Delta t, i = 0, 1, \ldots, M \qquad (3.24d)$$

$$T_{tc,\,r}(b,t_i) = T_r(b,t_i)(1+\varepsilon_T r_{i,\,r,\,b}),\;\; t_i = i\Delta t, i = 0, 1, \ldots, M \qquad (3.24e)$$

with $t_i = i\Delta t = i/f_{sampling}$, i = 0, 1, …, M where M represents the total number of data utilized in the simulation beyond the initial condition. It is evident that $t_{\max} = M\Delta t$ with these definitions. Here, ε_T denotes the temperature noise factor, r_i denotes the i^{th} random number generated from the interval [-1,1]. The entire simulation is performed using MATLAB R2016a on a Lenovo Thinkpad T530 laptop.

Figure A-3.6 illustrates the positional temperatures $\{T_{c1}(0, t_i), T_{c1}(b, t_i)\}$, $\{T_{c2}(0, t_i), T_{c2}(b, t_i)\}$, $\{T_r(b, t_i)\}$ and noisy temperatures $\{T_{tc,\,c1}(0, t_i), T_{tc,\,c1}(b, t_i)\}$, $\{T_{tc,\,c2}(0, t_i), T_{tc,\,c2}(b, t_i)\}$, $\{T_{tc,\,r}(\mathrm{b}, t_i)\}$ under the calibration tests 1, 2 and reconstruction test at the surface ($x = 0$) and in-depth "thermocouple" site ($x = b$), $i = 1, 2, 3, \ldots, M$. The noisy "thermocouple" data are generated per Eqs. (3.24a- e) at the previously noted sampling frequency, $f_{sampling}$. The value of the temperature noise factor used is $\varepsilon_T = 0.01$, which implies 1% noise. This noise factor is greater than the values provided in the thermocouple accuracy chart by OMEGA Engineering [95]. It is obvious that a significant amount of noise is introduced into the data displayed in Fig. A-3.6. It is important to mention that the positional temperature at the surface ($x = 0$) during reconstruction test is unknown. However, in numerical simulations and laboratory experiments, the surface temperature during the reconstruction test can be quantified and serve as a comparison with the estimated surface temperature by the inverse analysis. Again, all parameters used in the numerical simulation are listed in Table A-3.2.

3.6.2 Simulation using noiseless data

Ideal data allow for the evaluation of the numerical methods without consideration to the instability produced by noise. The emulated "thermocouple" data are generated according to Section 3.6.1. The nonlinear surface temperature calibration integral equation method has sufficient data to generate preliminary predictions. In this section, ideal positional temperatures at the front surface ($x = 0$) and the in-depth sensor site ($x = b$) are used to evaluate the numerical implementation of the calibration inverse method.

To begin, the expansion coefficients given in Eq. (3.12) are calculated by the least-squares method discussed in Section 3.3. Therefore, the noiseless "thermocouple" data in the calibration test 1 and calibration test 2 denoted as $T_{c1}(0, t_i)$ and $T_{c1}(b, t_i)$, $T_{c2}(0, t_i)$ and $T_{c2}(b, t_i)$, i = 1, 2, 3, … , M, are mapped onto the domain [-1, 1] by Eq. (3.9) for obtaining $T^*_{c1}(0,t_i), T^*_{c1}(b,t_i); T^*_{c2}(0,t_i)$ and $T^*_{c2}(b,t_i)$, i = 1, 2, 3, … , M. The T_L and T_U values required in Eq. (3.9) are assigned in Table A-3.2. Next, $T^*_{c1}(0,t_i), T^*_{c1}(b,t_i); T^*_{c2}(0,t_i)$ and $T^*_{c2}(b,t_i)$ are substituted into Eq. (3.10b), leading to the Chebyshev polynomials based on the mapped temperatures denoted as $E_n(T^*_{c1}(0,t_i)), E_n(T^*_{c1}(b,t_i)), E_n(T^*_{c2}(0,t_i))$ and $E_n(T^*_{c2}(b,t_i))$, or $E_{n,c1}(0,t_i), E_{n,c1}(b,t_i), E_{n,c1}(0,t_i)$ and $E_{n,c1}(b,t_i)$, n = 0, 2, 3, … , N, i = 1, 2, 3, … , M. Finally, the Chebyshev polynomials based on the mapped temperatures are substituted into Eqs. (3.13-15) for forming the proposed least-squares minimization needed for calculating the undetermined coefficients $\{a_0^N, a_2^N, a_3^N, ..., a_N^N\}$. In this chapter, trapezoidal integration [79] is applied for numerically integrating the integrals in Eq. (3.13) to obtain the discrete residual data as $r_N\left(t_i; \{a_0^N, a_2^N, a_3^N, ..., a_N^N\}\right)$, i = 1, 2, 3, … , M. The MATLAB command for solving nonlinear least squares problems "*lsqnonlin*" is used for symbolically calculating the undetermined coefficients $\{a_0^N, a_2^N, a_3^N, ..., a_N^N\}$. For the MATLAB command "*lsqnonlin*", an initial guess for the undetermined coefficients $\{a_0^N, a_2^N, a_3^N, ..., a_N^N\}$ is required. In this chapter, the initial guess is 0 for all undetermined coefficients $\{a_0^N, a_2^N, a_3^N, ..., a_N^N\}$. Before continuing further, the balancing of Eq. (3.12) should be checked for verifying the calculated coefficients $\{a_0^N, a_2^N, a_3^N, ..., a_N^N\}$. The balancing check of Eq. (3.12) is performed by plotting left-hand side and right-hand side of Eq. (3.12) as a function of discrete time $t_i = i\Delta t$, i = 1, 2, 3, … , M, in the same figure. For notational convenience, Eq. (3.12) can be rewritten as

$$G_{LHS,N}(t_i) = G_{RHS,N}(t_i)\,,\ \ t_i = i\Delta t,\ i = 1, 2, 3, \ldots, M \qquad (3.25a)$$

where

$$\begin{aligned} &G_{LHS,N}(t_i) \\ &= \int_{u=0}^{t_i} \left(a_0^N E_0 + E_{1,c1}(0,u) + a_2^N E_{2,c1}(0,u) + a_3^N E_{3,c1}(0,u) + \ldots + a_N^N E_{N,c1}(0,u)\right)\times \\ &\qquad \left(a_0^N E_0 + E_{1,c2}(0,t_i-u) + a_2^N E_{2,c2}(0,t_i-u) + a_3^N E_{3,c2}(0,t_i-u) + \ldots + a_N^N E_{N,c2}(0,t_i-u)\right)du \end{aligned}$$

$$i = 1, 2, 3, \ldots, M \qquad (3.25b)$$

and

$$\begin{aligned} &G_{RHS,N}(t_i) \\ &= \int_{u=0}^{t_i} \left(a_0^N E_0 + E_{1,c2}(0,u) + a_2^N E_{2,c2}(0,u) + a_3^N E_{3,c2}(0,u) + \ldots + a_N^N E_{N,c2}(0,u)\right)\times \\ &\qquad \left(a_0^N E_0 + E_{1,c1}(0,t_i-u) + a_2^N E_{2,c1}(0,t_i-u) + a_3^N E_{3,c1}(0,t_i-u) + \ldots + a_N^N E_{N,c1}(0,t_i-u)\right)du \end{aligned}$$

$$i = 1, 2, 3, \ldots, M \qquad (3.25c)$$

The undetermined coefficients $\{a_0^N, a_2^N, a_3^N, \ldots, a_N^N\}$ are obtained using "c1" and "c2" heating profiles displayed in Fig. A-3.3. At this junction in the analysis, it is evident that the value of N is a key factor before proceeding. Further, visualizing this portion of the study as a parameter estimation problem provides insight into the choice of N. To initiate, a Chebyshev expansion of 7$^{\text{th}}$ order (N = 7) is initially used for representing the transformed variable $\phi(x, t)$ in Eq. (3.10). The undetermined coefficients $\{a_0^7, a_2^7, a_3^7, \ldots, a_7^7\}$ are calculated and listed in column 2 of Table A-3.3. Figure A-3.7 displays $G_{\text{LHS},7}(t_i)$ and $G_{\text{RHS},7}(t_i)$ defined in Eqs. (3.25b, c) using noiseless temperatures at x = 0, b based on calibration test 1 and calibration test 2 as previously defined. As clearly shown in Fig. A-3.7, Eq.

(3.25a) does not balance using the calculated coefficients $\{a_0^7, a_2^7, a_3^7, ..., a_7^7\}$. It can also be observed that the magnitude of the functions $G_{\mathrm{LHS},\,7}(t_i)$ and $G_{\mathrm{RHS},\,7}(t_i)$ shown in Fig. A-3.7 are small (O(10^{-4})). This can be considered as a trivial solution and discarded. Next, consider the 6th order Chebyshev expansion for representing the transformed variable $\phi(x, t)$ in Eq. (3.10). The expansion coefficients $\{a_0^6, a_2^6, a_3^6, ..., a_6^6\}$ are calculated and listed in column 3 of Table A-3.3. The $G_{\mathrm{LHS},\,6}(t_i)$ and $G_{\mathrm{RHS},\,6}(t_i)$ are compared and displayed in Fig. A-3.8. In this case, balance is achieved and the magnitude is substantially larger than the results from $N = 7$.

Table A-3.3 lists the values of the coefficients $\{a_0^N, a_2^N, a_3^N, ..., a_N^N\}$ under various orders of Chebyshev expansions for approximating the property transform $\phi(T)$ As can be observed from Table A-3.3, there is one order of magnitude decrease from a_0^N to a_2^N when $N = 2$, 3, … , 6. However, for $N = 7$, from a_0^7 to a_2^7, the coefficient values increase from 0.5274 to 0.8452. This strongly contrasts the behavior indicated when $N = 2$, 3, … , 6. Figure A-3.9 displays the transformed variable $\phi(T)$ as a function of temperature defined in Eq. (3.9) and Eqs. (3.10a, b) in the temperature range [293.15, 1400] K using the calculated coefficients $\{a_0^N, a_2^N, a_3^N, ..., a_N^N\}$ under the six N values listed in Table A-3.3. It is clear that the $\phi(T)$ corresponding to $N = 7$ produces a contrasting behavior when compared to the $\phi(T)$ solutions corresponding to $N = 2$, 3, … , 6. It can also be observed that the $\phi(T)$ corresponding to $N = 3$, 4, 5 coalesce. In model building for parameter estimation, often a sequential study is performed using subsets of the total available data in the time interval $t \in [0, t_{\max}]$. That is, it is important to sequentially demonstrate coefficient stability. As discussed earlier, the expansion coefficients are determined by an ordinary least-square method using the complete data span $t \in [0, t_{\max}]$. Often, "best" model can be illustrated by sequentially viewing the coefficients constructed by using an ordinary least-square method at increasing time step. For convenience and to demonstrate the concept, the times of 14 s, 16 s, 18 s, 20 s seconds are studied to see if the expansion coefficients are replicated on the partial interval. Table A-3.4 displays the calculated coefficients $\{a_0^6, a_2^6, a_3^6, ..., a_6^6\}$ based on the indicated collection times. Observe that using a data collection time of 18 s produces contrasting coefficients when compared to data collection times of 20 s, 16 s and 14 s. In addition, the 18 s collected coefficients $\{a_0^6, a_2^6, a_3^6, ..., a_6^6\}$ in column 3 of Table A-3.4 are similar to the coefficients $\{a_0^7, a_2^7, a_3^7, ..., a_7^7\}$ listed in column 2 of Table A-3.3. Earlier, it was noted that this result leads to a trivial solution. The inconsistency in the calculated coefficients $\{a_0^6, a_2^6, a_3^6, ..., a_6^6\}$ under different data collection times shown in Table A-3.4 indicates that the 6$^{\text{th}}$ order for the Chebyshev expansion is not appropriate. Next, consider the numerically calculated coefficients $\{a_0^5, a_2^5, a_3^5, a_4^5, a_5^5\}$ when $N = 5$. In this case, observe consistency under different data collection times as shown in Table A-3.5. The balance between $G_{\text{LHS},\,5}(t_i)$ and $G_{\text{RHS},\,5}(t_i)$ is also verified as illustrated in Fig. A-3.10. Therefore, the 5$^{\text{th}}$ order Chebyshev expansion is chosen for representing the transformed variable $\phi(x, t)$ in Eq. (3.10) and the corresponding calculated coefficients $\{a_0^5, a_2^5, a_3^5, a_4^5, a_5^5\}$ listed in column 4 of Table A-3.3 (or column 2 of Table A-3.5) are used in this portion (noiseless) of the study.

Now that the expansion coefficients have been established, the inverse problem defined in Eq. (3.11c) can be resolved. In this chapter, calibration test 1 is chosen as calibration test for the inverse problem. By the same manner discussed above, the Chebyshev polynomials $E_{n,r}(b,t_i)$, $n = 0, 2, 3, \dots, N$, $t_i = i\Delta t$, $i = 1, 2, 3, \dots, M$ can be calculated based on the noiseless in-depth ($x = b$) temperature $T_r(b, t_i)$, $t_i = i\Delta t$, $i = 1, 2, 3, \dots, M$ in the context of reconstruction test. Meanwhile, the Chebyshev polynomials $E_{n,r}(0,t_i)$ and the corresponding unknown surface temperature at $x = 0$ in the reconstruction test require estimation. Steps are now described for estimating the surface temperature at $x = 0$ in the reconstruction test. The first step involves calculating the transformed variable in the context of reconstruction test denoted as $\phi_{r,\gamma_m}(0,t_i)$, $t_i = i\Delta t$, $i = 0, 1, \dots, M - mM_f$ using Eq. (3.21b) over future-time parameter spectrum γ_m. A numerical roots-finder is applied for obtaining the surface temperature at $x = 0$ in the reconstruction test denoted as $T_{r,\gamma_m}(0,t_i)$ using $\phi_{r,\gamma_m}(0,t_i)$, $t_i = i\Delta t$, $i = 0, 1, \dots, M - mM_f$ through Eq. (3.9) and Eqs. (3.10a, b). More specifically, common order terms in the Chebyshev expansion shown in Eq. (3.10a) are collected by the calculated coefficients $\{a_0^N, a_2^N, a_3^N, \dots, a_N^N\}$ with $a_1^N = 1$ for forming a monomial based polynomial based on the order of the predicted mapped surface temperature denoted as $T^*_{r,\gamma_m}(0,t_i)$, $t_i = i\Delta t$, $i = 0, 1, \dots, M - mM_f$. The MATLAB function "*roots*" for finding roots of monomial based polynomials is applied for calculating $T^*_{r,\gamma_m}(0,t_i)$, $t_i = i\Delta t$, $i = 0, 1, \dots, M - mM_f$. Multiple roots including complex numbers can be observed. The unfavorable roots are eliminated by setting the limit range of roots as $T^*_{r,\gamma_m}(0,t_i) \in [-1,1]$. In the end, the surface temperature in the reconstruction test denoted as $T_{r,\gamma_m}(0,t_i)$ can be obtained by inverting $T^*_{r,\gamma_m}(0,t_i)$, $t_i = i\Delta t$, $i = 0, 1, \ldots, M - mM_f$, per Eq. (3.9).

Following the procedure discussed above, the predicted transform variable in the reconstruction test $\phi_{r,\gamma_m}(0,t_i)$, $t_i = i\Delta t$, $i = 0, 1, \ldots, M - mM_f$, can be resolved over a spectrum of future-time parameters γ_m. Figures A-3.11a, b display $\phi_{r,\gamma_m}(0,t_i)$ from resolving Eq. (3.20b) when $\gamma_m = 0.1$ s and 0.2 s, respectively. It is clear that $\gamma_m = 0.1$ s leads to an unstable surface prediction as shown in Fig. A-3.11a. In contrast, when $\gamma_m = 0.2$ s, the predicted transform variable $\phi_{r,\gamma_m}(0,t_i)$ shown in Fig. A-3.11b provides an excellent reconstruction of the intermediate variable $\phi_{r,\gamma_m}(0,t_i)$. Figure A-3.12 displays the corresponding predicted surface temperature $T_{r,\gamma_m}(0,t_i)$ upon inverting the predicted transform variable in the reconstruction test $\phi_{r,\gamma_m}(0,t_i)$ given in Fig. A-3.11b. The predicted surface temperature $T_{r,\gamma_m}(0,t_i)$ nearly replicates the exact surface temperature $T_r(0, t)$. In contrast, Fig. A-3.12 also displays the surface temperature prediction $T_{r,\gamma_m}(0,t_i)$ with $\gamma_m = 0.2$ s, $i = 1, 2, 3, \ldots, M - mM_f$, using the temperature calibration integral equation (i.e. fully linear model developed under a constant property assumption) given in Eq. (3.1) and the exact surface temperature $T_r(0, t)$ in the reconstruction test. In Fig. A-3.12, the surface temperature prediction from the linear analysis [3] produces a biasing effect as observed in the two peaks being shifted. This is due to the fact that the linear temperature calibration integral equation given in Eq. (3.1) does not sufficiently account for temperature dependency of the thermophysical properties. Figure A-3.13 illustrates the absolute error of surface temperature prediction using the nonlinear model discussed in this chapter and the linear model given in Eq. (3.1). As shown in Fig. A-3.13, the nonlinear model yields a significantly smaller surface temperature prediction error when compared to the linear model except at early times. The temperature of the slab stays at room temperature at early times of the reconstruction test (see Fig. A-3.4c). In this region, the nonlinear heat equation given in Eqs. (3.2) becomes linear, hence the linear model leads to better surface temperature prediction.

The purpose of this section involved demonstrating a viable numerical procedure without consideration to non-ideal data. As demonstrated, the prediction quickly and nearly recovers the exact solution for small γ. At this junction, discussion for determining γ_{opt} is postponed until non-ideal data are imposed. This additional consideration and its effect on the inverse method is of paramount importance.

3.6.3 Simulation using noisy data

In this section, the noisy "thermocouple" data $\{T_{tc,\,c1}(0, t_i), T_{tc,\,c1}(b, t_i)\}$, $\{T_{tc,\,c2}(0, t_i), T_{tc,\,c2}(b, t_i)\}$ and $\{T_{tc,\,r}(b, t_i)\}$, $i = 1, 2, \ldots, M$ are generated via Eqs. (3.24a-e) as input to recover the surface temperature history in the reconstruction test. In addition, the phase plane and cross-correlation analyses are employed for estimating the optimal future-time parameter, γ_{opt}. The calculated expansion coefficients $\{a_0^N, a_2^N, a_3^N, \ldots, a_N^N\}$ based on noisy data are listed in Tables A-3.6~A-3.8 corresponding to the noisy data sets, "c1" and "c2" shown in Fig. A-3.6. Table A-3.6 displays the calculated expansion coefficients for $N = 2$ through $N = 6$ in the presence of noisy data per Fig. A-3.6 whose parameters are described in Table A-

3.2. Tables A-3.7 and A-3.8 illustrate a sequential time study exposing the most stable coefficients from a parameter estimation viewpoint. Again, the Chebyshev expansion of 5^{th} order is used for representing the transformed variable $\phi(x, t)$ in Eq. (3.10) as it displays consistency in the coefficients. The calculated coefficients $\{a_0^5, a_2^5, a_3^5, a_4^5, a_5^5\}$ based on noisy data are listed in column 4 of Table A-3.6 (or column 2 of Table A-3.8) and will be used in reconstructing the surface temperature, $T_{r,\gamma}(0, t)$ of the reconstruction case.

Figure A-3.14 shows that balancing of Eq. (3.25a) is achieved as $G_{\mathrm{LHS},\,5}(t_i)$ and $G_{\mathrm{RHS},\,5}(t_i)$ are nearly identical. Figure A-3.15 displays the transformed variable $\phi(T)$ as a function of temperature given by Eq. (3.9) and Eqs. (3.10a, b) in the temperature range [293.15, 1400] K using the calculated coefficients $\{a_0^5, a_2^5, a_3^5, a_4^5, a_5^5\}$ listed in column 4 of Table A-3.6.

The optimal regularization parameter, γ_{opt} now requires estimation. The phase plane and cross-correlation analyses discussed in Section 3.5 are employed for estimating the optimal future-time parameter γ_{opt} in the chosen spectrum $\gamma_m = M_f m \Delta t$, $m = 2 - 8$, $M_f = 10$, $\Delta t = 0.01$ s. Figure A-3.16a provides the predicted surface temperature rate, $\dot{T}_{r,\gamma}(0, t_i)$ and temperature, phase plane over future parameter spectrum γ_m, $m = 2 - 8$ while Fig. A-3.16b gives the zoomed in version of Fig. A-3.16a using the future parameter spectrum $\gamma_m = M_f m\Delta t$, $m = 5 - 8$, $M_f = 10$, $\Delta t = 0.01$ s. As indicated in Fig. A-3.16a, small γ's produce a largely random pattern of immense magnitude. As future-time parameters γ's increase from 0.5 s to 0.6 s, their corresponding phase plane takes on a distinctive pattern as loss of randomness is observed. The initiation of a pattern in the surface temperature rate and temperature phase plane defines the optimal regularization parameter as both temperature and more importantly, the temperature rate stabilizes. From Fig. A-3.16b, the onset of an overlapping or “settled” pattern begins to occur in the range $\gamma \in [0.6, 0.7]$ s . Furthermore, highly smoothed results are observed for $\gamma \in 0.8$ s as shown in Fig. A-3.16b. In fact, it is desired to retain as many high-frequency components in the signal for recovering small temporal changes in the predicted surface thermal conditions. Hence, predictions using $\gamma \in [0.7, 0.8]$ s are removed from consideration as over-smoothing dominates. This is the initial qualitative/physical perspective for understanding the optimal regularization parameter.

Figure A-3.17 describes the cross-correlation coefficients phase plane, Eqs. (3.20a, b) illustrating the appearance of the three regions. These regions are defined as 1) unstable, 2) transition and 3) over-smoothed. From γ pairs (0.2, 0.3) s to (0.3, 0.4) s, instability is correlated to the phase plane figure displayed in Fig. A-3.16a. As γ increases to 0.7 s, the corresponding surface temperature rate cross-correlation coefficient $R_{\dot{T}}(\dot{T}_{r,\gamma_m}, \dot{T}_{r,\gamma_{m+1}})$ climbs toward 1. Unity on the vertical axis ($R_{\dot{T}}(\dot{T}_{r,\gamma_m}, \dot{T}_{r,\gamma_{m+1}})$) implies the occurrence of over-smoothness as more smoothness than possibly available due to noisy data is suggested. The γ pair (0.5, 0.6) s in the transition region indicates that the optimum γ lies in the range [0.5, 0.6] s.

Figure A-3.18 displays the predicted surface temperature, $T_{r,\gamma}(0,t_i)$ over the future-time spectrum $\gamma_m = M_f m \Delta t$, $m = 2 - 8$, $M_f = 10$, Δt =0.01 s. Based on the phase plane plot shown in Fig. A-3.16a and cross-correlation coefficient phase plane plot given in Fig. A-3.17, it would be appropriate and acceptable to choose the estimated optimal γ_{opt} as 0.5 s. Figure A-3.19 compares the surface temperature, $T_{r,\gamma}(0,t_i)$ to the exact $T_r(0, t)$ using γ_{opt} = 0.5 s. Highly favorable results are produced in light of the significant amount of noise contained in the "thermocouple" data for both the calibration tests and reconstruction test.

3.7 Conclusions

A calibration integral equation method has been demonstrated for estimating the surface temperature for resolving a one-dimensional nonlinear inverse heat conduction problem. The nonlinear calibration integral equation method is a "parameter free" approach where the temperature-dependent thermophysical properties are inherently contained in a Volterra integral equation of the first kind. A temperature-dependent property transform has been proposed for linearizing the nonlinear heat equation. The unknown property transform is represented by a Chebyshev expansion of the first kind possessing undetermined coefficients. Two well-defined calibration tests are applied for calculating the undetermined coefficients. A time sequential investigation and balance verification of the expansion coefficients provide a means for determining the order of the Chebyshev expansion. The future-time method is used for stabilizing the ill-posed Volterra integral equation of the first kind for the reconstruction effort. The regularization parameter for the nonlinear inverse problem in this chapter is the future-time parameter. A spectrum of future-time parameters is studied from which the optimal values emerges through a phase plane analysis. A systematic phase plane and cross-correlation phase plane analyses are applied for extracting the optimal future-time parameter. Numerical simulation for stainless steel is performed yielding highly encouraging surface temperature predictions. Though not presented here, numerical simulations using carbon-carbon as the host material also yields excellent surface temperature predictions.

Chapter 4: Two-Probe Calibration Integral Equation Method for Nonlinear Inverse Heat Conduction Problem of Surface Heat Flux Estimation

This chapter is based on the paper: H. Chen, J. I. Frankel, and M. Keyhani, "Two-probe calibration integral equation method for nonlinear inverse heat conduction problem of surface heat flux estimation", International Journal of Heat and Mass Transfer (in review).

4.1 Introduction

Nonlinear inverse heat conduction problems involve predicting the surface thermal condition based on in-depth measurements within a host material possessing temperature-dependent thermophysical properties. In-depth installed sensors protect the integrity of the collected data when severely hostile thermal environments are encountered. Such severe thermal conditions appear in hypersonic reentry vehicles, shock tunnels, arc jets, brakes, nuclear reactors, combustions, etc.

Inverse heat conduction problems are ill-posed [1]. This implies that any errors from in-depth measurements will lead to error amplification in the prediction process leading to the boundary condition. Normally, this occurrence is exacerbated as the sampling rate increases. This can be explained by the physics of heat diffusion [42]. Diffusion damps out high frequencies as heat conducts through the body. However, reversing the direction also reverses this attenuation/amplification effect. Therefore, regularization methods must be introduced to all inverse heat conduction problems for recapturing stability [1].

A variety of techniques have been proposed for resolving inverse heat conduction problems. These include exact solutions [15], space marching and finite difference methods [16-20], function specification method [21-23], conjugate gradient method [25, 26], boundary-element method [29, 30], and iteration method [31]. All aforementioned inverse heat conduction methods are "parameter required" methods that require accurate knowledge of thermophysical properties, probe locations as well as sensor parameters (sensor capacitance, lead losses, thermal contact). These properties introduce uncertainties that are often neglected. The lack of uncertainty analysis for "parameter required" methods [32] can potentially lead to inaccuracies and misunderstandings of the prediction.

A "parameter free" methodology for resolving inverse heat conduction problems involves system calibration principles. The main advantage of a system calibration over a "parameter required" method lies in a reduction of systematic errors introduced by the uncertainties in the thermophysical properties, probe locations and sensor parameters. For a system calibration approach, well-designed laboratory calibration tests are required using an accurately defined boundary condition at the surface of interest. The non-integer system identification (NISI) method [57-62] is a calibration method that uses an impulsive surface flux for obtaining the relationship between net surface heat flux and temperature response at the sensor site. The NISI method requires the accurate extraction of the impulse function based on a fractional derivative [63] formulation of the linear, semi-infinite domain heat equation. Undetermined calibration coefficients are used for accounting the sensor characteristics, depth of sensor, and thermophysical properties of the host material. A least-squares method is then applied for estimating the undetermined coefficients. Regularization is still required for reducing stabilities. The unknown surface heat flux in reconstruction test can be predicted by the corresponding sensor response and the calibration coefficients previously described. An alternative calibration methodology that substantially reduces the unknown parameter set has been developed at the University of Tennessee [3, 48, 64-66]. In addition, the fractional derivative formulation is removed while additional clarity is developed in the contrasting formulation. In the calibration integral equation method, the sensor positioning, sensor characteristics and thermophysical properties of the host material are inherently contained in the final mathematical expression [67, 68].

For the calibration integral equation method, one-probe [3, 48, 65, 66] and two-probe [69-71] formulations have been developed. In the one-probe calibration integral equation method, the boundary condition for the back surface should remain unchanged between calibration and reconstruction tests. The two-probe calibration integral equation method will be shown to remove this restriction on the back surface boundary condition. The two-probe calibration integral equation method can be applied for estimating front surface heat flux in a reconstruction test without the need to quantify the corresponding back surface boundary condition. This is a benefit and an advantage of the two-probe approach as the formulation is developed based on the region defined between the front surface to the furthest in-depth sensor.

The linear one-probe [3] and two-probe [69] calibration integral equation methods have been experimentally validated [48, 71] with excellent accuracy at low temperatures. However, for applications involving large temperature variations, the temperature-dependency of thermophysical properties need to be considered. This leads to the development of the nonlinear calibration integral equation method. More recently, an alternative calibration integral equation method based on knowledge of the thermophysical properties and Kirchhoff transform [70, 72] has been experimentally validated [73, 74] yielding highly favorable results at elevated temperatures using a 500 W laser test facility at the University of Tennessee. In contrast, Frankel and Keyhani [65], Chen et al. [96] developed a nonlinear one-probe calibration integral equation method for estimating surface heat flux and temperature based on linearizing the nonlinear heat equation by a property transform formulation. Compared to the rescaling approach [70, 72], this method does not require knowledge of any thermophysical properties. Instead, the temperature-dependent thermophysical properties are represented as a property transform function embedded into the final mathematical formulation of a first kind Volterra integral equation for the desired surface boundary condition. Chen et al. [96] use a first kind Chebyshev expansion with unknown coefficients for approximating the property transform function. The undetermined coefficients are then estimated by using two well-defined calibration tests.

The goal of this chapter is expand the nonlinear two-probe calibration integral equation method [96] for predicting the surface heat flux based on the linear two-probe CIEM [69, 71] and the recently proposed nonlinear one-probe CIEM using property transform for linearization [65, 96]. The final mathematical formulation of this nonlinear two-probe calibration integral equation method is expressed as a complicated nonlinear Volterra integral equation of the first kind in terms of surface heat flux with a property transform function that accounts the temperature-dependent thermophysical properties. Again, the property transform function is approximated using a Chebyshev expansion of the first kind possessing undetermined coefficients. Three well-defined calibration tests are applied for estimating the undetermined coefficients associated with the Chebyshev expansion of the first kind. Section 4.2 presents the derivation of the nonlinear two-probe calibration integral equation as well as the least-square methods for estimating the undetermined coefficients associated with the Chebyshev expansion. Section 4.3 presents the implementation of a local future-time method [3, 47] for stabilizing the Volterra integral equation of the first kind for predicting the surface heat flux in reconstruction test. The local future-time method [3], as well as the numerical methods required for estimating the surface heat flux in reconstruction test, are described in this section. Section 4.4 presents the phase plane and cross-correlation analyses [56, 75, 76] for estimating the optimal future-time parameter. Section 4.5 presents numerical simulation results based on stainless steel involving both noiseless and noisy data. Section 4.6 provides some concluding remarks on the proposed nonlinear two-probe calibration integral equation method.

4.2 Formulation of the nonlinear two-probe calibration integral equation method

The nonlinear two-probe surface heat flux calibration integral equation is derived based on the linear two-probe surface heat flux calibration integral equation [69]. Hence, the linear two-probe surface heat flux calibration integral equation is briefly reviewed in Section

4.2.1 for future clarity. Figure A-4.1 displays the schematic for one-dimensional heat conduction in a slab with thickness of L. Two in-depth thermocouples are located at $x = b$ and $x = w$ $(0 < b < w < L)$. The thermocouples (TC's) are additionally subscripted by "TC1" and "TC2", respectively. The heat fluxes at the front and back surfaces are denoted by $q''_0(t)$ and $q''_L(t)$, respectively. The introduction of the second probe at $x = w$ removes the need to specify the back surface boundary condition in the proposed methodology.

4.2.1 Background: linear two-probe surface heat flux calibration integral equation

The linear two-probe surface heat flux calibration integral equation is derived based on frequency domain analysis of the one-dimensional linear heat equation [85] defined as

$$\frac{1}{\alpha}\frac{\partial T}{\partial t}(x,t) = \frac{\partial^2 T}{\partial x^2}(x,t), \quad x \in [0, L], \quad t \ge 0 \tag{4.1a}$$

subject to the time-varying boundary conditions

$$q''_0(t) = q''(0,t) \equiv -k\frac{\partial T}{\partial x}(0,t), \quad t > 0 \tag{4.1b}$$

$$q''_L(t) = -q''(L,t) \equiv k\frac{\partial T}{\partial x}(L,t), \quad t > 0 \tag{4.1c}$$

and uniform initial condition

$$T(x,0) = T_0, \quad x \in [0, L] \tag{4.1d}$$

Here, T denotes temperature, x and t denote spatial and temporal variable, respectively, α denotes thermal diffusivity, k denotes thermal conductivity, and denote the conductive (net) heat fluxes at $x = 0$ and L, respectively, while and denote the imposed heat fluxes composed of external sources and other modes of heat transfer. The linear two-probe surface heat flux calibration integral equation [69] is given as

$$\int_{u=0}^{t} q_r''(0,u)\int_{v=0}^{t-u}\big(\theta_{c1}(b,v)\theta_{c2}(w,t-u-v)-\theta_{c2}(b,v)\theta_{c1}(w,t-u-v)\big)dvdu$$
$$=\int_{u=0}^{t}\theta_r(b,u)\int_{v=0}^{t-u}\big(q_{c1}''(0,v)\theta_{c2}(w,t-u-v)-q_{c2}''(0,v)\theta_{c1}(w,t-u-v)\big)dvdu \tag{4.2}$$
$$-\int_{u=0}^{t}\theta_r(w,u)\int_{v=0}^{t-u}\big(q_{c1}''(0,v)\theta_{c2}(b,t-u-v)-q_{c2}''(0,v)\theta_{c1}(b,t-u-v)\big)dvdu, \quad t\geq 0$$

where θ denotes the excess temperature defined as $\theta = T - T_0$. The subscripts "c1", "c2" and "r" denote calibration test 1, calibration test 2 and reconstruction test, respectively. Equation (4.2) can be compactly expressed as

$$\int_{u=0}^{t} q_r''(0,u)K_l(t-u)du = F_l(t),\ \ t\geq 0 \tag{4.3a}$$

where the subscript "l" denotes linear. The forcing function $F_l\,(t)$ and the convolution kernel $K_l\,(t - u)$ are defined as

$$\begin{aligned}F_l(t)=&\int_{u=0}^{t}\theta_r(b,u)\int_{v=0}^{t-u}\big(q_{c1}''(0,v)\theta_{c2}(w,t-u-v)-q_{c2}''(0,v)\theta_{c1}(w,t-u-v)\big)dvdu\\&-\int_{u=0}^{t}\theta_r(w,u)\int_{v=0}^{t-u}\big(q_{c1}''(0,v)\theta_{c2}(b,t-u-v)-q_{c2}''(0,v)\theta_{c1}(b,t-u-v)\big)dvdu, \quad t\geq 0\end{aligned} \tag{4.3b}$$

and

$$K_l(t-u)=\int_{v=0}^{t-u}\big(\theta_{c1}(b,v)\theta_{c2}(w,t-u-v)-\theta_{c2}(b,v)\theta_{c1}(w,t-u-v)\big)dv,\ \ (t-u)\geq 0 \tag{4.3c}$$

respectively. Note that $F_l\,(t)$ is composed of experimental data and is well defined (i.e., known).

4.2.2 Derivation of the nonlinear two-probe surface heat flux calibration integral equation

Consider the transient one-dimensional nonlinear heat equation [85] given as

$$\rho c(T)\frac{\partial T}{\partial t}(x,t)=\frac{\partial}{\partial x}\left[k(T)\frac{\partial T}{\partial x}(x,t)\right],\ \ x\in[0,L],\ \ t\geq 0 \tag{4.4a}$$

where ρ denotes density and c denotes specific heat. Equation (4.4a) is subject to the time-varying boundary conditions

$$q_0''(t)=q''(0,t)\equiv -k\left(T(0,t)\right)\frac{\partial T}{\partial x}(0,t),\ \ t>0 \tag{4.4b}$$

$$q_L''(t)=-q''(L,t)\equiv k\left(T(L,t)\right)\frac{\partial T}{\partial x}(L,t),\ \ t>0 \tag{4.4c}$$

and uniform initial condition

$$T(x,0)=T_0,\ \ x\in[0,L] \tag{4.4d}$$

The generalized property transform technique [65, 96] is used for linearizing the nonlinear heat equation shown in Eqs. (4.4a-d). In a nutshell, Eq. (4.4a) can be decomposed by property transform as

$$\rho c(T)\frac{dT}{d\varphi}\frac{\partial \varphi}{\partial t}(x,t)=\frac{\partial}{\partial x}\left(k(T)\frac{dT}{d\varphi}\frac{\partial \varphi}{\partial x}(x,t)\right),\ \ x\in[0,L],\ \ t\geq 0 \tag{4.5}$$

where $\varphi(x, t)$ denotes the property transform function, which can be thermal conductivity, specific heat, thermal diffusivity, thermal effusivity, etc [65, 96]. The implicit assumption that $\varphi(T)$ is single valued is required. Actually, the temperature-dependent thermophysical properties $k(T)$, $c(T)$, $\alpha(T)$, $\beta(T)$ (thermal effusivity) are single valued for almost all practical engineering materials [85]. Assuming there exists a combination that produces

$$k(T)\frac{dT}{d\varphi}=\kappa\approx \text{constant} \tag{4.6}$$

then the transformed heat equation can be expressed in terms of the transformed variable, $\varphi(x, t)$ as

$$\frac{1}{\alpha(T)}\frac{\partial\varphi}{\partial t}(x,t)=\frac{\partial^2\varphi}{\partial x^2}(x,t),\;\; x\in[0,L],\;\; t\geq 0 \tag{4.7}$$

Further, assume that the thermal diffusivity $\alpha(T)$ is a constant denoted by α_0. The linearized heat equation can be written as

$$\frac{1}{\alpha_0}\frac{\partial\varphi}{\partial t}(x,t)=\frac{\partial^2\varphi}{\partial x^2}(x,t),\;\; x\in[0,L],\;\; t\geq 0 \tag{4.8a}$$

with the transformed boundary conditions as

$$q''(0,t)\equiv-\kappa\frac{\partial\varphi}{\partial x}(0,t),\;\; t>0 \tag{4.8b}$$

$$q''(L,t)\equiv-\kappa\frac{\partial\varphi}{\partial x}(L,t),\;\; t>0 \tag{4.8c}$$

and the transformed initial condition as

$$\varphi(x,0)=\varphi(T_0),\;\; x\in[0,L] \tag{4.8d}$$

Though this formulation assumes $\alpha(T)\rightarrow\alpha_0$, it will be shown later that this formulation introduces system flexibility as the property transform is represented by a first kind Chebyshev expansion possessing undetermined coefficients using calibration data. This flexible formulation accommodates the unbalance of the final calibration integral equation introduced by the temperature-dependency of thermal diffusivity in engineering practices.

Let us now define $\phi(T) = \varphi(T) - \varphi(T_0)$. Equation (4.8) now becomes

$$\frac{1}{\alpha_0}\frac{\partial\phi}{\partial t}(x,t)=\frac{\partial^2\phi}{\partial x^2}(x,t),\;\; x\in[0,L],\;\; t\geq 0 \tag{4.9a}$$

subject to the transformed boundary conditions

$$q''(0,t) \equiv -\kappa \frac{\partial \phi}{\partial x}(0,t), \ \ t > 0 \tag{4.9b}$$

$$q''(L,t) \equiv -\kappa \frac{\partial \phi}{\partial x}(L,t), \ \ t > 0 \tag{4.9c}$$

and the transformed initial condition

$$\phi(x,0) = 0, \ \ x \in [0,L] \tag{4.9d}$$

The two-probe calibration integral equation for the linearized nonlinear heat equation given in Eqs. (4.9) can be derived by following the same procedure as deriving the linear two-probe calibration integral equation given in Ref. [69]. In a nutshell, the two-probe calibration integral equation for the linearized system given in Eqs. (4.9) can be written as

$$\begin{aligned}
&\int_{u=0}^{t} q_r''(0,u) \int_{v=0}^{t-u} \left(\phi_{c1}(b,v)\phi_{c2}(w,t-u-v) - \phi_{c2}(b,v)\phi_{c1}(w,t-u-v) \right) dv du \\
&= \int_{u=0}^{t} \phi_r(b,u) \int_{v=0}^{t-u} \left(q_{c1}''(0,v)\phi_{c2}(w,t-u-v) - q_{c2}''(0,v)\phi_{c1}(w,t-u-v) \right) dv du \\
&- \int_{u=0}^{t} \phi_r(w,u) \int_{v=0}^{t-u} \left(q_{c1}''(0,v)\phi_{c2}(b,t-u-v) - q_{c2}''(0,v)\phi_{c1}(b,t-u-v) \right) dv du, \quad t \geq 0
\end{aligned} \tag{4.10}$$

or in compact mathematical form as

$$\int_{u=0}^{t} q_r''(0,u) K(t-u) du = F(t), \ \ t \geq 0 \tag{4.11a}$$

where the forcing function $F(t)$ and the convolution kernel $K(t-u)$ are defined as

$$\begin{aligned}
F(t) &= \int_{u=0}^{t} \phi_r(b,u) \int_{v=0}^{t-u} \left(q_{c1}''(0,v)\phi_{c2}(w,t-u-v) - q_{c2}''(0,v)\phi_{c1}(w,t-u-v) \right) dv du \\
&- \int_{u=0}^{t} \phi_r(w,u) \int_{v=0}^{t-u} \left(q_{c1}''(0,v)\phi_{c2}(b,t-u-v) - q_{c2}''(0,v)\phi_{c1}(b,t-u-v) \right) dv du, \quad t \geq 0
\end{aligned} \tag{4.11b}$$

and

$$K(t-u) = \int_{v=0}^{t-u} \left(\phi_{c1}(b,v)\phi_{c2}(w,t-u-v) - \phi_{c2}(b,v)\phi_{c1}(w,t-u-v) \right) dv, \ \ (t-u) \geq 0 \tag{4.11c}$$

respectively. The property transform $\phi(x, t)$ can be represented as an infinite series using first kind Chebyshev polynomials as the expansion basis. In order to use the proposed Chebyshev expansion, the temperatures are mapped onto the range [-1, 1] as

$$T^*(x,t) = \frac{2T(x,t) - T_L - T_U}{T_U - T_L} \in [-1, 1] \tag{4.12}$$

where "T_L" and "T_U" represent the temperature of lower bound and upper bound, respectively. The values of "T_L" and "T_U" can be properly set based on physical temperature limits for ensuring that the temperature range for all calibration and reconstruction tests are in the domain [T_L, T_U]. After the temperatures are mapped onto [-1, 1], the Chebyshev expansion for approximating the property transform function $\phi(x, t)$ can be formulated as

$$\phi(x,t) = \sum_{n=0}^{\infty} a_n E_n(x,t) \approx \phi_N(x,t) = \sum_{n=0}^{N} a_n^N E_n(x,t) \tag{4.13a}$$

where

$$E_n(x,t) = E_n\left(T^*(x,t)\right), \ n = 0, 1, 2, ... \tag{4.13b}$$

Equation (4.13b) denotes the n^{th} order first kind Chebyshev polynomial for the mapped temperature. For notational clarity, several first kind Chebyshev polynomials conforming to the notation used in this chapter are listed in Table A-4.1. Chebyshev expansions are well known for their ability to converge more rapidly than other basis functions as well as maintaining low condition numbers. Chebyshev polynomials are mutually orthogonal in the domain [-1, 1] with respect to the weight function $(1 - T^{*2})^{-1/2}$ [79, 91, 92]. Note that in Eq. (4.13a), the transformed variable ϕ is a function of temperature but the units of the undetermined coefficients $\{a_0^N, a_1^N, a_2^N, ..., a_N^N\}$ are unknown.

Substituting the Chebyshev expansion given in Eq. (4.13a) into Eq. (4.10) produces

$$\begin{aligned}
&\int_{u=0}^{t} q_r''(0,u)\int_{v=0}^{t-u}[(a_0^N E_0 + a_1^N E_{1,\,c1}(b,v) + a_2^N E_{2,\,c1}(b,v) + ... + a_N^N E_{N,\,c1}(b,v))\\
&(a_0^N E_0 + a_1^N E_{1,\,c2}(w,t-u-v) + a_2^N E_{2,\,c2}(w,t-u-v) + ... + a_N^N E_{N,\,c2}(w,t-u-v))\\
&-(a_0^N E_0 + a_1^N E_{1,\,c2}(b,v) + a_2^N E_{2,\,c2}(b,v) + ... + a_N^N E_{N,\,c2}(b,v))\\
&\ (a_0^N E_0 + a_1^N E_{1,\,c1}(w,t-u-v) + a_2^N E_{2,\,c1}(w,t-u-v) + ... + a_N^N E_{N,\,c1}(w,t-u-v))]dvdu\\
&\approx \int_{u=0}^{t}(a_0^N E_0 + a_1^N E_{1,\,r}(b,u) + a_2^N E_{2,\,r}(b,u) + ... + a_N^N E_{N,\,r}(b,u))\\
&\int_{v=0}^{t-u}[q_{c1}''(0,v)(a_0^N E_0 + a_1^N E_{1,\,c2}(w,t-u-v) + a_2^N E_{2,\,c2}(w,t-u-v) + ... + a_N^N E_{N,\,c2}(w,t-u-v))\\
&-q_{c2}''(0,v)(a_0^N E_0 + a_1^N E_{1,\,c1}(w,t-u-v) + a_2^N E_{2,\,c1}(w,t-u-v) + ... + a_N^N E_{N,\,c1}(w,t-u-v))]dvdu\\
&-\int_{u=0}^{t}(a_0^N E_0 + a_1^N E_{1,\,r}(w,u) + a_2^N E_{2,\,r}(w,u) + ... + a_N^N E_{N,\,r}(w,u))\\
&\int_{v=0}^{t-u}[q_{c1}''(0,v)(a_0^N E_0 + a_1^N E_{1,\,c2}(b,t-u-v) + a_2^N E_{2,\,c2}(b,t-u-v) + ... + a_N^N E_{N,\,c2}(b,t-u-v))\\
&-q_{c2}''(0,v)(a_0^N E_0 + a_1^N E_{1,\,c1}(b,t-u-v) + a_2^N E_{2,\,c1}(b,t-u-v) + ... + a_N^N E_{N,\,c1}(b,t-u-v))]dvdu,\ \ t \ge 0
\end{aligned}$$

(4.14a)

which involves a finite number of undetermined coefficients $\{a_0^N, a_1^N, a_2^N, ..., a_N^N\}$. If N is sufficiently large then Eq. (4.14a) should be well-balanced. In order to recover the equal sign, we introduce the residual function, $r_N(t)$ as

$$\begin{aligned}
&\int_{u=0}^{t} q_r''(0,u)\int_{v=0}^{t-u}[(a_0^N E_0 + a_1^N E_{1,\,c1}(b,v) + a_2^N E_{2,\,c1}(b,v) + ... + a_N^N E_{N,\,c1}(b,v))\\
&(a_0^N E_0 + a_1^N E_{1,\,c2}(w,t-u-v) + a_2^N E_{2,\,c2}(w,t-u-v) + ... + a_N^N E_{N,\,c2}(w,t-u-v))\\
&-(a_0^N E_0 + a_1^N E_{1,\,c2}(b,v) + a_2^N E_{2,\,c2}(b,v) + ... + a_N^N E_{N,\,c2}(b,v))\\
&\ (a_0^N E_0 + a_1^N E_{1,\,c1}(w,t-u-v) + a_2^N E_{2,\,c1}(w,t-u-v) + ... + a_N^N E_{N,\,c1}(w,t-u-v))]dvdu\\
&= \int_{u=0}^{t}(a_0^N E_0 + a_1^N E_{1,\,r}(b,u) + a_2^N E_{2,\,r}(b,u) + ... + a_N^N E_{N,\,r}(b,u))\\
&\int_{v=0}^{t-u}[q_{c1}''(0,v)(a_0^N E_0 + a_1^N E_{1,\,c2}(w,t-u-v) + a_2^N E_{2,\,c2}(w,t-u-v) + ... + a_N^N E_{N,\,c2}(w,t-u-v))\\
&-q_{c2}''(0,v)(a_0^N E_0 + a_1^N E_{1,\,c1}(w,t-u-v) + a_2^N E_{2,\,c1}(w,t-u-v) + ... + a_N^N E_{N,\,c1}(w,t-u-v))]dvdu\\
&-\int_{u=0}^{t}(a_0^N E_0 + a_1^N E_{1,\,r}(w,u) + a_2^N E_{2,\,r}(w,u) + ... + a_N^N E_{N,\,r}(w,u))\\
&\int_{v=0}^{t-u}[q_{c1}''(0,v)(a_0^N E_0 + a_1^N E_{1,\,c2}(b,t-u-v) + a_2^N E_{2,\,c2}(b,t-u-v) + ... + a_N^N E_{N,\,c2}(b,t-u-v))\\
&-q_{c2}''(0,v)(a_0^N E_0 + a_1^N E_{1,\,c1}(b,t-u-v) + a_2^N E_{2,\,c1}(b,t-u-v) + ... + a_N^N E_{N,\,c1}(b,t-u-v))]dvdu\\
&+r_N(t),\ \ t \ge 0
\end{aligned} \tag{4.14b}$$

when $\{a_j^N\}_{j=0}^N$ are assumed known. At this stage, observe the introduction of additional mathematical rigor into the formulation (recall Chapter 3). This formulation requires two calibration tests for estimating the reconstruction heat flux case, $q_r''(0,t)$. By comparing Eq. (4.14b) to the linear two-probe surface heat flux calibration given in Eq. (4.2), we can set $a_1^N = 1$ (or divide by $(a_1^N)^2$ on both sides of Eq. (4.14b). Thus Eq. (4.14b) can be written as

$$
\begin{aligned}
&\int_{u=0}^{t} q_r''(0,u)\int_{v=0}^{t-u}[(a_0^N E_0 + E_{1,c1}(b,v) + a_2^N E_{2,c1}(b,v) + ... + a_N^N E_{N,c1}(b,v)) \\
&(a_0^N E_0 + E_{1,c2}(w,t-u-v) + a_2^N E_{2,c2}(w,t-u-v) + ... + a_N^N E_{N,c2}(w,t-u-v)) \\
&-(a_0^N E_0 + E_{1,c2}(b,v) + a_2^N E_{2,c2}(b,v) + ... + a_N^N E_{N,c2}(b,v)) \\
&\quad (a_0^N E_0 + E_{1,c1}(w,t-u-v) + a_2^N E_{2,c1}(w,t-u-v) + ... + a_N^N E_{N,c1}(w,t-u-v))]dvdu \\
&= \int_{u=0}^{t} (a_0^N E_0 + E_{1,r}(b,u) + a_2^N E_{2,r}(b,u) + ... + a_N^N E_{N,r}(b,u)) \\
&\int_{v=0}^{t-u}[q_{c1}''(0,v)(a_0^N E_0 + E_{1,c2}(w,t-u-v) + a_2^N E_{2,c2}(w,t-u-v) + ... + a_N^N E_{N,c2}(w,t-u-v)) \\
&- q_{c2}''(0,v)(a_0^N E_0 + E_{1,c1}(w,t-u-v) + a_2^N E_{2,c1}(w,t-u-v) + ... + a_N^N E_{N,c1}(w,t-u-v))]dvdu \\
&- \int_{u=0}^{t} (a_0^N E_0 + E_{1,r}(w,u) + a_2^N E_{2,r}(w,u) + ... + a_N^N E_{N,r}(w,u)) \\
&\int_{v=0}^{t-u}[q_{c1}''(0,v)(a_0^N E_0 + E_{1,c2}(b,t-u-v) + a_2^N E_{2,c2}(b,t-u-v) + ... + a_N^N E_{N,c2}(b,t-u-v)) \\
&- q_{c2}''(0,v)(a_0^N E_0 + E_{1,c1}(b,t-u-v) + a_2^N E_{2,c1}(b,t-u-v) + ... + a_N^N E_{N,c1}(b,t-u-v))]dvdu \\
&+ r_N(t),\ \ t \ge 0
\end{aligned}
\tag{4.14c}
$$

In order to estimate the undetermined coefficients $\{a_0^N, a_2^N, a_3^N, ..., a_N^N\}$ in Eq. (4.14c), we must introduce a third calibration test whereby the subscript notation changes as r → c3. Three well-defined calibration tests are now defined. Thus Eq. (4.14c) can be written as

$$
\begin{aligned}
&\int_{u=0}^{t} q''_{c3}(0,u)\int_{v=0}^{t-u}[(a_0^N E_0 + E_{1,c1}(b,v)+a_2^N E_{2,c1}(b,v)+...+a_N^N E_{N,c1}(b,v))\\
&(a_0^N E_0 + E_{1,c2}(w,t-u-v)+a_2^N E_{2,c2}(w,t-u-v)+...+a_N^N E_{N,c2}(w,t-u-v))\\
&-(a_0^N E_0 + E_{1,c2}(b,v)+a_2^N E_{2,c2}(b,v)+...+a_N^N E_{N,c2}(b,v))\\
&\ (a_0^N E_0 + E_{1,c1}(w,t-u-v)+a_2^N E_{2,c1}(w,t-u-v)+...+a_N^N E_{N,c1}(w,t-u-v))]dvdu\\
&=\int_{u=0}^{t}(a_0^N E_0 + E_{1,c3}(b,u)+a_2^N E_{2,c3}(b,u)+...+a_N^N E_{N,c3}(b,u))\\
&\int_{v=0}^{t-u}[q''_{c1}(0,v)(a_0^N E_0 + E_{1,c2}(w,t-u-v)+a_2^N E_{2,c2}(w,t-u-v)+...+a_N^N E_{N,c2}(w,t-u-v))\\
&-q''_{c2}(0,v)(a_0^N E_0 + E_{1,c1}(w,t-u-v)+a_2^N E_{2,c1}(w,t-u-v)+...+a_N^N E_{N,c1}(w,t-u-v))]dvdu\\
&-\int_{u=0}^{t}(a_0^N E_0 + E_{1,c3}(w,u)+a_2^N E_{2,c3}(w,u)+...+a_N^N E_{N,c3}(w,u))\\
&\int_{v=0}^{t-u}[q''_{c1}(0,v)(a_0^N E_0 + E_{1,c2}(b,t-u-v)+a_2^N E_{2,c2}(b,t-u-v)+...+a_N^N E_{N,c2}(b,t-u-v))\\
&-q''_{c2}(0,v)(a_0^N E_0 + E_{1,c1}(b,t-u-v)+a_2^N E_{2,c1}(b,t-u-v)+...+a_N^N E_{N,c1}(b,t-u-v))]dvdu\\
&+\tilde{r}_N\left(t;\{a_0^N,a_2^N,a_3^N,...,a_N^N\}\right),\ t\ge 0
\end{aligned}
\tag{4.15}
$$

In Eq. (4.15), all the variables are known except the N undetermined coefficients $\{a_0^N, a_2^N, a_3^N, ..., a_N^N\}$. A nonlinear least-squares method based on residual $\tilde{r}_N\left(t;\{a_0^N, a_2^N, a_3^N, ..., a_N^N\}\right)$ can be used for estimating the N undetermined coefficients $\{a_0^N, a_2^N, a_3^N, ..., a_N^N\}$. The least-squares method is expressed as

$$
\begin{aligned}
&\tilde{r}_N\left(t_i;\{a_0^N,a_2^N,a_3^N,...,a_N^N\}\right)\\
&=\int_{u=0}^{t_i} q''_{c3}(0,u)\int_{v=0}^{t_i-u}[(a_0^N E_0 + E_{1,c1}(b,v)+a_2^N E_{2,c1}(b,v)+...+a_N^N E_{N,c1}(b,v))\\
&(a_0^N E_0 + E_{1,c2}(w,t_i-u-v)+a_2^N E_{2,c2}(w,t_i-u-v)+...+a_N^N E_{N,c2}(w,t_i-u-v))\\
&-(a_0^N E_0 + E_{1,c2}(b,v)+a_2^N E_{2,c2}(b,v)+...+a_N^N E_{N,c2}(b,v))\\
&\ (a_0^N E_0 + E_{1,c1}(w,t_i-u-v)+a_2^N E_{2,c1}(w,t_i-u-v)+...+a_N^N E_{N,c1}(w,t_i-u-v))]dvdu\\
&-\{\int_{u=0}^{t_i}(a_0^N E_0 + E_{1,c3}(b,u)+a_2^N E_{2,c3}(b,u)+...+a_N^N E_{N,c3}(b,u))\\
&\int_{v=0}^{t_i-u}[q''_{c1}(0,v)(a_0^N E_0 + E_{1,c2}(w,t_i-u-v)+a_2^N E_{2,c2}(w,t_i-u-v)+...+a_N^N E_{N,c2}(w,t_i-u-v))\\
&-q''_{c2}(0,v)(a_0^N E_0 + E_{1,c1}(w,t_i-u-v)+a_2^N E_{2,c1}(w,t_i-u-v)+...+a_N^N E_{N,c1}(w,t_i-u-v))]dvdu\\
&-\int_{u=0}^{t_i}(a_0^N E_0 + E_{1,c3}(w,u)+a_2^N E_{2,c3}(w,u)+...+a_N^N E_{N,c3}(w,u))\\
&\int_{v=0}^{t_i-u}[q''_{c1}(0,v)(a_0^N E_0 + E_{1,c2}(b,t_i-u-v)+a_2^N E_{2,c2}(b,t_i-u-v)+...+a_N^N E_{N,c2}(b,t_i-u-v))\\
&-q''_{c2}(0,v)(a_0^N E_0 + E_{1,c1}(b,t_i-u-v)+a_2^N E_{2,c1}(b,t_i-u-v)+...+a_N^N E_{N,c1}(b,t_i-u-v))]dvdu\}
\end{aligned}
$$

$$i = 1, 2, \dots, M \qquad (4.16)$$

where $\{t_i\}_{i=1}^{M}$ denotes the discrete sampling time, and M is the number of data points in the discretized temporal domain beyond the initial condition. The sum of the squares of $\tilde{r}_N\left(t_i;\{a_0^N, a_2^N, a_3^N, ..., a_N^N\}\right)$ can be formed as

$$R_N\left(\{a_0^N, a_2^N, \dots, a_N^N\}\right) = \sum_{i=1}^{M} \tilde{r}_N^{\,2}\left(t_i;\{a_0^N, a_2^N, a_3^N, ..., a_N^N\}\right)$$

$$= \sum_{i=1}^{M} \left(\begin{array}{l} \int_{u=0}^{t_i} q''_{c3}(0,u) \int_{v=0}^{t_i-u} [(a_0^N E_0 + E_{1,c1}(b,v) + a_2^N E_{2,c1}(b,v) + ... + a_N^N E_{N,c1}(b,v)) \\ (a_0^N E_0 + E_{1,c2}(w,t_i-u-v) + a_2^N E_{2,c2}(w,t_i-u-v) + ... + a_N^N E_{N,c2}(w,t_i-u-v)) \\ -(a_0^N E_0 + E_{1,c2}(b,v) + a_2^N E_{2,c2}(b,v) + ... + a_N^N E_{N,c2}(b,v)) \\ \quad (a_0^N E_0 + E_{1,c1}(w,t_i-u-v) + a_2^N E_{2,c1}(w,t_i-u-v) + ... + a_N^N E_{N,c1}(w,t_i-u-v))] dvdu \\ -\{\int_{u=0}^{t_i} (a_0^N E_0 + E_{1,c3}(b,u) + a_2^N E_{2,c3}(b,u) + ... + a_N^N E_{N,c3}(b,u)) \\ \int_{v=0}^{t_i-u} [q''_{c1}(0,v)(a_0^N E_0 + E_{1,c2}(w,t_i-u-v) + a_2^N E_{2,c2}(w,t_i-u-v) + ... + a_N^N E_{N,c2}(w,t_i-u-v)) \\ -q''_{c2}(0,v)(a_0^N E_0 + E_{1,c1}(w,t_i-u-v) + a_2^N E_{2,c1}(w,t_i-u-v) + ... + a_N^N E_{N,c1}(w,t_i-u-v))] dvdu \\ -\int_{u=0}^{t_i} (a_0^N E_0 + E_{1,c3}(w,u) + a_2^N E_{2,c3}(w,u) + ... + a_N^N E_{N,c3}(w,u)) \\ \int_{v=0}^{t_i-u} [q''_{c1}(0,v)(a_0^N E_0 + E_{1,c2}(b,t_i-u-v) + a_2^N E_{2,c2}(b,t_i-u-v) + ... + a_N^N E_{N,c2}(b,t_i-u-v)) \\ -q''_{c2}(0,v)(a_0^N E_0 + E_{1,c1}(b,t_i-u-v) + a_2^N E_{2,c1}(b,t_i-u-v) + ... + a_N^N E_{N,c1}(b,t_i-u-v))] dvdu\} \end{array} \right)^2$$

$$i = 1, 2, \dots, M \qquad (4.17)$$

and we formally minimize with respect to each undetermined coefficient in the set as

$$\frac{\partial R_N}{\partial a_n^N}(\{a_0^N, a_2^N, a_3^N, ..., a_N^N\}) = 0, \quad n = 0, 2, 3, ..., N \qquad (4.18)$$

Equation (4.18) forms a closed system of nonlinear equations involving N undetermined coefficients. An appropriate numerical method can be applied for solving the N nonlinear system of equations for obtaining the N unknown coefficients. After the N undetermined coefficients $\{a_0^N, a_2^N, a_3^N, ..., a_N^N\}$ are obtained, one can return to Eq. (4.14c) for the inverse heat conduction analysis. Two well-defined calibration tests are used in Eq. (4.14c) using the calculated coefficients $\{a_0^N, a_2^N, a_3^N, ..., a_N^N\}$ for predicting the front surface heat flux in the reconstruction test denoted as $q_r''(0,t)$. It is important to note that Eq. (4.14c) is a Volterra integral equation of the first kind for $q_r''(0,t)$ which is ill-posed [67, 68]. In this chapter, a future-time method [47] is used for stabilizing the first kind Volterra integral equation for $q_r''(0,t)$ given in Eq. (4.14c). The implementation of the future-time [47] and numerical methods for predicting the front surface heat flux in reconstruction test, $q_r''(0,t)$ is discussed in Section 4.3.

4.3 Regularization and numerical methods

For notational convenience, the implementation of the future-time [3, 47, 64] and numerical methods for estimating the front surface heat flux in reconstruction test are illustrated by the calibration integral equation in the compact form given in Eq. (4.11a), namely

$$\int_{u=0}^{t} q_r''(0,u)K(t-u)du = F(t), \ \ t \geq 0 \tag{4.19a}$$

where the forcing function $F(t)$ and the convolution kernel $K(t-u)$ are defined as

$$\begin{aligned} F(t) = & \int_{u=0}^{t} \phi_r(b,u) \int_{v=0}^{t-u} \left(q_{c1}''(0,v)\phi_{c2}(w,t-u-v) - q_{c2}''(0,v)\phi_{c1}(w,t-u-v) \right) dv du \\ & - \int_{u=0}^{t} \phi_r(w,u) \int_{v=0}^{t-u} \left(q_{c1}''(0,v)\phi_{c2}(b,t-u-v) - q_{c2}''(0,v)\phi_{c1}(b,t-u-v) \right) dv du, \quad t \geq 0 \end{aligned} \tag{4.19b}$$

and

$$K(t-u) = \int_{v=0}^{t-u} \left(\phi_{c1}(b,v)\phi_{c2}(w,t-u-v) - \phi_{c2}(b,v)\phi_{c1}(w,t-u-v) \right) dv, \ \ (t-u) \geq 0 \tag{4.19c}$$

respectively. Introduction of the future-time parameter γ, time is performed by letting $t \rightarrow t + \gamma$. Equation (4.19a) then becomes

$$\int_{u=0}^{t+\gamma} q_r''(0,u)K(t+\gamma-u)du = F(t+\gamma),\ \ t\in[0,t_{\max}-\gamma] \tag{4.20}$$

where $t_{\max}$ denotes the total time of data collection. As can be observed in Eq. (4.20), the recoverable time domain is reduced by γ. Equation (4.20) can be written as

$$\int_{u=0}^{t} q_r''(0,u)K(t+\gamma-u)du + \int_{u=t}^{t+\gamma} q_r''(0,u)K(t+\gamma-u)du = F(t+\gamma),\ \ t\in[0,t_{\max}-\gamma] \tag{4.21}$$

by the basic definition of integration. The second integral on the left-hand side of the Eq. (4.21) can be manipulated in order to convert the first kind Volterra integral equation to the second kind. Let $u' = u - t$ in the second integral on the left-hand side of the Eq. (4.21). Therefore, we obtain

$$\int_{u=0}^{t} q_r''(0,u)K(t+\gamma-u)du + \int_{u'=0}^{\gamma} q_r''(0,u'+t)K(\gamma-u')du' = F(t+\gamma),\ \ t\in[0,t_{\max}-\gamma] \tag{4.22}$$

If γ is sufficiently small then $q_r''(0,u'+t) \approx q_r''(0,t)$ since $u' \in [0,\gamma]$. If this is the case then Eq. (4.22) can be written as

$$\int_{u=0}^{t} q_r''(0,u)K(t+\gamma-u)du + q_r''(0,t)\int_{u'=0}^{\gamma} K(\gamma-u')du' \approx F(t+\gamma),\ \ t\in[0,t_{\max}-\gamma] \tag{4.23a}$$

or

$$\int_{u=0}^{t} q_{r,\gamma}''(0,u)K(t+\gamma-u)du + q_{r,\gamma}''(0,t)\int_{u=0}^{\gamma} K(\gamma-u)du = F(t+\gamma),\ \ t\in[0,t_{\max}-\gamma] \tag{4.23b}$$

where $q_{r,\gamma}''(0,t) \approx q_r''(0,t)$ and denotes the predicted front surface heat flux in the reconstruction test indicating its dependence on γ. The dummy variable u' in the second term of the left-hand side of Eq. (4.23a) is returned to u for cosmetic purposes. Now, the ill-posed Volterra integral equation of the first kind for $q_r''(0,t)$ given in Eq. (4.19a) has been recast into the well-posed Volterra integral equation of the second kind for $q_r''(0,t)$

presented in Eq. (4.23b), but its solution clearly depends on the choice of the regularization parameter, γ.

Various numerical integration rules [79] can be applied for discretizing Eq. (4.23b). For inverse problems, low-order rules are preferred. A right-hand rectangular rule is used in this context. Discretizing Eq. (4.23b) using a right-handed rectangular product rule yields

$$\sum_{j=1}^{i} q''_{r,\gamma_m}(0,t_j)\int_{u=t_{j-1}}^{t_j} K(b,t_i+\gamma_m-u)du + q''_{r,\gamma_m}(0,t_i)\int_{u=0}^{\gamma_m} K(b,\gamma_m-u)du = F(t_i+\gamma_m),$$

$$i = 1, 2, \ldots, M - mM_f \quad (4.24a)$$

where $\gamma \rightarrow \gamma_m$ now represents a discrete value from a finite set (spectrum) of choices. Notice that $q''_{r,\gamma}(0,t)$ has been re-written in terms of a discrete value of γ; namely γ_m, leading to $q''_{r,\gamma_m}(0,t)$. The desired front surface heat flux prediction $q''_{r,\gamma_m}(0,t)$ can be explicitly extracted as

$$q''_{r,\gamma_m}(0,t_i) = \frac{F(t_i+\gamma_m) - \sum_{j=1}^{i-1} q''_{r,\gamma_m}(0,t_j)\int_{u=t_{j-1}}^{t_j} K(b,t_i+\gamma_m-u)du}{\int_{u=t_i-1}^{t_i} K(b,t_i+\gamma_m-u)du + \int_{u=0}^{\gamma_m} K(b,\gamma_m-u)du},$$

$$i = 1, 2, \ldots, M - mM_f \quad (4.24b)$$

The additional numerical approximation introduced through the numerical integration is not indicated in the notation (i.e.: $q''_{r,\gamma_m,M}(0,t) \approx q''_{r,\gamma_m}(0,t)$) for notational simplicity though it is well understood to exist. As shown in Eq. (4.24b), discrete values of the predicted front surface heat flux prediction $q''_{r,\gamma_m}(0,t_i)$ are obtained by time marching. The future-time parameter is chosen as $\gamma \rightarrow \gamma_m = mM_f\Delta t$ where m is a positive integer, and Δt is given as $\Delta t = t_{max}/M$. Here, M is the number of data in the discretized time domain beyond the initial condition, and M_f is a convenient multiplying factor that allows for computational flexibility. A chosen spectrum for the future-time parameter γ_m is defined from which the optimal value is extracted based on some optimization rule. Small γ's will lead to unstable predictions as $\int_{u=0}^{\gamma_m} K(b,\gamma_m - u)du$ becomes small. In contrast, large values of γ cause an over-smoothing effect. Compromise should be maintained between instability and over-smoothness. In Section 4.4, phase plane and cross-correlation analyses are discussed as a means for defining the optimization rule for estimating the optimal future-time parameter.

4.4 Phase plane and cross-correlation analyses for estimating the optimal future-time parameter

Phase plane and cross-correlation analyses have been illustrated as effective metrics for estimating the optimal regularization parameter in the future-time method [56, 75, 76, 96]. Further, this approach was used for estimating the optimal cut-off frequency in a digital filter for preprocessing data in a space marching method [54] (Chapter 2). The phase plane is often used in vibration studies involving velocity versus displacement [93] where time is parameterized. In the study of inverse heat conduction problems, the corresponding analogy involves plotting the time derivative of the predicted front surface heat flux versus the predicted front surface heat flux. This produces the heat flux phase plane. In this context, various parameterized curves of $\dot{q}''_{r,\gamma_m}(0,t_i)$ versus $q''_{r,\gamma_m}(0,t_i)$ with respect to different future-time parameters $\gamma_m = mM_f\Delta t$ (s) ($m = p, p + 1, \ldots, p - 1 + P$, ($p$ is the 1st m value and P is the number of elements in the γ spectrum) are plotted for investigating stability characteristics. Here, m is the m^{th} chosen value from a finite spectrum of P choices for the future-time parameter. If the future-time parameter γ_m is too small then the high degree of roughness (randomness) in the surface heat flux rate $\dot{q}''_{r,\gamma_m}(0,t_i)$ and the surface heat flux $q''_{r,\gamma_m}(0,t_i)$ phase plane corresponds significant instability in the prediction of front surface heat flux. As the future-time parameter, γ_m nears the optimal value, the surface heat flux rate $\dot{q}''_{r,\gamma_m}(0,t_i)$ and the surface heat flux $q''_{r,\gamma_m}(0,t_i)$ phase plane plot begins to produce an identifiable shape. As the future-time parameter γ_m further increases in magnitude, a highly smoothed pattern will form in the phase plane plot. The transition between loss of randomness and pattern forming is considered the region where the optimal future-time parameter γ_{opt} lies.

Cross-correlation is a statistical metric between two sets of data. In this chapter, the front surface heat flux cross-correlation coefficient is defined as [56, 75, 76]

$$R_q(q''_{r,\gamma_m}, q''_{r,\gamma_{m+1}}) = \frac{\sum_{i=1}^{M-PM_f} q''_{r,\gamma_m}(0,t_i) q''_{r,\gamma_{m+1}}(0,t_i)}{\sqrt{\sum_{i=1}^{M-PM_f}\left(q''_{r,\gamma_m}(0,t_i)\right)^2 \sum_{i=1}^{M-PM_f}\left(q''_{r,\gamma_{m+1}}(0,t_i)\right)^2}},$$

$$i = 1, 2, \ldots, M - PM_f;\ m = p,\ p+1, \ldots, p-1+P \qquad (4.25a)$$

while the front surface heat flux rate cross-correlation coefficient is defined as [56, 75, 76]

$$R_{\dot{q}}(\dot{q}''_{r,\gamma_m}, \dot{q}''_{r,\gamma_{m+1}}) = \frac{\sum_{i=1}^{M-PM_f} \dot{q}''_{r,\gamma_m}(0,t_i) \dot{q}''_{r,\gamma_{m+1}}(0,t_i)}{\sqrt{\sum_{i=1}^{M-PM_f}\left(\dot{q}''_{r,\gamma_m}(0,t_i)\right)^2 \sum_{i=1}^{M-PM_f}\left(\dot{q}''_{r,\gamma_{m+1}}(0,t_i)\right)^2}},$$

$$i = 1, 2, \ldots, M - PM_f;\ m = p,\ p+1, \ldots, p-1+P \qquad (4.25b)$$

where $\gamma_m = mM_f\Delta t$ (s), $m = p, p + 1, \ldots, p - 1 + P$, p is the 1st m value and P is the number of values in γ spectrum. Here, $M_f\,\Delta t$ is the stepping time for forming a finite set of predictions since Δt is the sampling time.

The value of the cross-correlation coefficient indicates the similarity level between the two front surface heat flux predictions $q''_{r,\gamma_m}(0,t_i)$ and $q''_{r,\gamma_{m+1}}(0,t_i)$ with respect to two adjacent future-time parameters (γ_m and γ_{m+1}). As the cross-correlation coefficients $R_q(q''_{r,\gamma_m}, q''_{r,\gamma_{m+1}})$, $R_{\dot{q}}(\dot{q}''_{r,\gamma_m}, \dot{q}''_{r,\gamma_{m+1}})$ approach unity, the linear dependency between $q''_{r,\gamma_m}(0,t_i)$ and $q''_{r,\gamma_{m+1}}(0,t_i)$, as well as $\dot{q}''_{r,\gamma_m}(0,t_i)$ and $\dot{q}''_{r,\gamma_{m+1}}(0,t_i)$ are recognized.

The front surface heat flux rate cross-correlation $R_{\dot{q}}(\dot{q}''_{r,\gamma_m}, \dot{q}''_{r,\gamma_{m+1}})$ has difficulty approaching unity because numerical differentiation of discrete data amplifies noise. In fact, achieving unity in a noisy environment makes little sense. Therefore, a criterion for identifying the transition between an unstable and an over-smoothed front surface heat flux prediction involves defining the magnitude of the surface heat flux rate cross-correlation coefficient $R_{\dot{q}}(\dot{q}''_{r,\gamma_m}, \dot{q}''_{r,\gamma_{m+1}})$. This will be illustrated in Section 4.5.3.

4.5 Results

4.5.1 Data collection for inverse simulation

Numerical simulation is employed for generating experimental data. To do this, a direct nonlinear heat conduction problem is solved based on given auxiliary conditions. This allows for in-depth probe data to be obtained. The schematic for the one-dimensional heat conduction with two in-depth thermocouples is displayed in Fig. A-4.1. The thickness of the one-dimensional slab is L, and the two in-depth thermocouples are located at $x = b$ and $x = w$, respectively. The front ($x = 0$) and back ($x = L$) surfaces of the slab are subjected to heat fluxes denoted as $q_0''(t)$ and $q_L''(t)$, respectively. The imposed heat fluxes $q_0''(t)$ and $q_L''(t)$ can be composed of various heat transfer modes involving conduction, convection, radiation. For this chapter, the conductive (net) heat fluxes at front and back surfaces are assumed equal to the imposing heat fluxes, as $q''(0,t) = q_0''(t)$ and $q''(L,t) = q_L''(t)$. The host material of the one-dimensional slab for simulation is again stainless steel 304. The thermophysical properties of the stainless steel 304 [80], as well as the geometrical properties for the simulation, are given in Table A-4.2. Figures A-4.2a-c display the temperature-dependent thermal conductivity, $k(T)$, specific heat, $c(T)$ and thermal diffusivity, $\alpha(T) = k(T)/(\rho c(T))$ over a large temperature range. In order to emulate nonlinear effects in a surface heating experiment, the simulation covers a large temperature range. The numerical simulation presented in this chapter are performed using MATLAB R2016a on a Lenovo Thinkpad T530 laptop.

The two-probe calibration equation is used in situations where the back surface can influence the overall heat transfer or when the back surface boundary condition changes drastically between the calibration campaign and reconstruction test. This example involves stainless steel 304 with the thermophysical and geometrical properties shown in Table A-4.2. The thermal penetration time from the front to the back surface based on the temperature response on the back surface is about 2 seconds. The simulations provided in this study run to 60 seconds indicating that the back surface boundary condition influences the system. In this context, three calibration tests denoted as "c1", "c2" and "c3" are required for estimating the undetermined coefficients $\{a_0^N, a_2^N, a_3^N, ..., a_N^N\}$ in Eq. (4.15). The calculated coefficients $\{a_0^N, a_2^N, a_3^N, ..., a_N^N\}$ together with the data in calibration test 1 ("c1") and test 2 ("c2") are incorporated into Eq. (4.14c) for the inverse analysis to predict the front surface heat flux $q_r''(0,t)$ in the reconstruction test denoted as "r". In calibration test 1, the front and back surface heat fluxes are fixed at constant values denoted as $q''_{0,c1,\max}$ and $q''_{L,c1,\max}$. In calibration test 2, the front surface heat flux is $q''_{0,c2,\max}$ at $t \in [0, t_{\max}/2]$ s and $q''_{0,c2,\max}/2$ at $t \in (t_{\max}/2, t_{\max}]$ s while the back surface boundary condition is adiabatic. In calibration test 3, the front surface heat flux is $q''_{0,c3,\max}$ at $t \in [0, t_{\max}/5]$ s and $q''_{0,c3,\max}/2$ at $t \in (t_{\max}/5, t_{\max}]$ s while the back surface boundary condition is a constant value at $q''_{L,c3,\max}$. The front surface heat flux in the reconstruction test is a double Gaussian function defined as

$$q_s''(t) = q''(0,t) = q''_{r,\max}\left(e^{-\frac{(t-\beta_1)^2}{\sigma_1^2}} + 0.75e^{-\frac{(t-\beta_2)^2}{\sigma_2^2}}\right),\ t \in [0, t_{\max}] \qquad (4.26)$$

while the back surface heat flux in the reconstruction test is a linear decay from $q''_{L,r,\max}$ to 0 at $t \in [0, t_{\max}]$ s. The values for the parameters, β_1, β_2, σ_1, σ_2 are given in Table A-4.2. The imposed front and back surface heat fluxes for the calibration tests "c1", "c2", "c3" and the reconstruction test "r" are shown in Figs. A-4.3a, b. An implicit finite difference method, using a one-time step lag evaluation of the thermophysical properties, is applied for numerically solving the direct heat conduction problems. The transient temperature responses at $x = 0$, b, w and L in the calibration tests "c1", "c2", "c3" and the reconstruction test "r" are obtained and displayed in Figs. A-4.4a-d. The convergence of the implicit finite difference method has been verified and shown by plotting the positional temperature at $x = b$, $T_r(b, t_i)$ in the reconstruction test obtained by (Δx, Δt) and ($\Delta x/2$, $\Delta t/2$), respectively. The convergence plot is displayed in Fig. A-4.5. The maximum relative difference between $T_r(b, t_i)$ obtained by (Δx, Δt) and ($\Delta x/2$, $\Delta t/2$) is only 0.0627%. In this chapter, all the data used are obtained by the proposed finite difference method with the temporal and spatial widths given by (Δx, Δt).

Artificial noise is added to the imposed front surface heat fluxes in the three calibration tests as well as the positional temperatures at $x = b$ and $x = w$ obtained by the finite difference method in the three calibration tests and the reconstruction test. Noisy data for surface heat flux and in-depth temperatures are generated through

$$q''_{noise,c}(0,t_i) = q''_c(0,t_i)(1+\varepsilon_q r_{i,j}),\ \ t_i = i\Delta t,\, i = 0,1,\ldots,M \tag{4.27a}$$

$$T_{tc,c}(b,t_i) = T_c(b,t_i)(1+\varepsilon_T r_{i,j}),\ \ t_i = i\Delta t,\, i = 0,1,\ldots,M \tag{4.27b}$$

$$T_{tc,c}(w,t_i) = T_c(w,t_i)(1+\varepsilon_T r_{i,j}),\ \ t_i = i\Delta t,\, i = 0,1,\ldots,M \tag{4.27c}$$

$$T_{tc,r}(b,t_i) = T_r(b,t_i)(1+\varepsilon_T r_{i,j}),\ \ t_i = i\Delta t,\, i = 0,1,\ldots,M \tag{4.27d}$$

$$T_{tc,r}(w,t_i) = T_r(w,t_i)(1+\varepsilon_T r_{i,j}),\ \ t_i = i\Delta t,\, i = 0,1,\ldots,M \tag{4.27e}$$

where ε_q and ε_T denote noise factors, subscript "c" denotes the three calibration tests in general, and $r_{i,j}$, $i = 0, 1, \ldots, M$ are random numbers drawn from the interval [-1,1] obtained by the MATLAB command "2(*rand*-0.5)" for each noise addition case of surface heat flux and temperature (subscript "j" is used to denote these cases). Equations (4.27a-e) indicate independently generated noisy data sets for all tests. The values for the noise factors ε_q and ε_T are given in Table A-4.2. Figure A-4.6 shows the exact imposed front surface heat fluxes $q''_{c1}(0,t)$, $q''_{c2}(0,t)$, $q''_{c3}(0,t)$ and noise added front surface heat fluxes $q''_{noise,\,c1}(0,t)$, $q''_{noise,\,c2}(0,t)$, $q''_{noise,\,c3}(0,t)$ for calibration tests 1, 2, 3. The uncorrupted positional and noise added temperature data at $x = b$ and $x = w$ in the calibration tests 1, 2, 3 and the reconstruction test are displayed in Figs. A-4.7a-d, respectively. The values for noise factor ε_q and ε_T are set as 0.01 which implies 1% relative noise. All parameters used for the numerical simulation are listed in Table A-4.2.

4.5.2 Inverse simulation using noiseless data

In this section, the noiseless front surface heat fluxes in the three calibration tests displayed in Fig. A-4.3 and the noiseless positional temperatures at two in-depth sensor locations ($x = b$ and $x = w$) are used for verifying the proposed numerical procedure for the two-probe calibration integral equation method. Using noiseless data permits evaluating the numerical methods without considering the instability effects introduced by a simulated noisy sensor. To begin, the undetermined expansion coefficients $\{a_0^N, a_2^N, a_3^N, \ldots, a_N^N\}$ in Eq. (4.15) are estimated by the nonlinear least-squares method discussed in Section 4.2. The noiseless front surface heat fluxes in the three calibration tests denoted as $q''_{c1}(0,t_i)$, $q''_{c2}(0,t_i)$ and $q''_{c3}(0,t_i)$ as well as the noiseless "thermocouple" data (positional temperature at $x = b$ and $x = w$ as calculated by the finite difference method) denoted as $T_{c1}(b, t_i)$, $T_{c2}(b, t_i)$, $T_{c3}(b, t_i)$, $T_{c1}(w, t_i)$, $T_{c2}(w, t_i)$ and $T_{c3}(w, t_i)$, $t_i = i\Delta t$, $i = 1, 2, \ldots, M$ are substituted into Eq. (4.15). In this study, the positional temperatures and noiseless thermocouple temperatures are assumed identical implying that sensor delay and attenuation effects are not considered in the numerical simulation. The chosen sampling frequency is 50 Hz which indicates Δt = 0.02 s. Next, the discrete residual function $\tilde{r}_N\left(t_i;\{a_0^N, a_2^N, a_3^N, ..., a_N^N\}\right)$, i = 1, 2, … , M in Eq. (4.16) is obtained using a trapezoidal integration rule [79]. The undetermined coefficients $\{a_0^N, a_2^N, a_3^N, ..., a_N^N\}$ are symbolically calculated by the MATLAB function "*lsqnonlin*". An initial guess for the undetermined coefficients $\{a_0^N, a_2^N, a_3^N, ..., a_N^N\}$ is required for the MATLAB command "*lsqnonlin*". In this chapter, the trivial value of 0 is used as the initial guess for all undetermined coefficients.

It is apparent that the number of the undetermined coefficients N needs to be chosen in some manner. In addition, after determining the coefficients $\{a_0^N, a_2^N, a_3^N, ..., a_N^N\}$ by the least-squares method, the balance of Eq. (4.15) needs to be verified. The left-hand side and first term on the right-hand side of Eq. (4.15) as a function of discrete time $t_i = i\Delta t$, i = 1, 2, … , M can be plotted in the same figure. The discrete version of Eq. (4.15) can be expressed as

$$G_{LHS,N}(t_i) = G_{RHS,N}(t_i) + \tilde{r}_N\left(t_i;\{a_0^N, a_2^N, a_3^N, ..., a_N^N\}\right), \quad t_i = i\Delta t,\ i = 1, 2, \dots, M \tag{4.28a}$$

where

$$\begin{aligned}
&G_{LHS,N}(t_i) \\
&= \int_{u=0}^{t_i} q''_{c3}(0,u) \int_{v=0}^{t_i-u} [(a_0^N E_0 + E_{1,c1}(b,v) + a_2^N E_{2,c1}(b,v) + ... + a_N^N E_{N,c1}(b,v)) \\
&(a_0^N E_0 + E_{1,c2}(w,t_i-u-v) + a_2^N E_{2,c2}(w,t_i-u-v) + ... + a_N^N E_{N,c2}(w,t_i-u-v)) \\
&-(a_0^N E_0 + E_{1,c2}(b,v) + a_2^N E_{2,c2}(b,v) + ... + a_N^N E_{N,c2}(b,v)) \\
&\ (a_0^N E_0 + E_{1,c1}(w,t_i-u-v) + a_2^N E_{2,c1}(w,t_i-u-v) + ... + a_N^N E_{N,c1}(w,t_i-u-v))] dv du
\end{aligned}$$

$$i = 1, 2, \ldots, M \quad (4.28b)$$

and

$$\begin{aligned}
&G_{RHS,\,N}(t_i) \\
&= \int_{u=0}^{t_i} (a_0^N E_0 + E_{1,c3}(b,u) + a_2^N E_{2,c3}(b,u) + \ldots + a_N^N E_{N,c3}(b,u)) \\
&\int_{v=0}^{t_i-u} [q''_{c1}(0,v)(a_0^N E_0 + E_{1,c2}(w,t_i-u-v) + a_2^N E_{2,c2}(w,t_i-u-v) + \ldots + a_N^N E_{N,c2}(w,t_i-u-v)) \\
&-q''_{c2}(0,v)(a_0^N E_0 + E_{1,c1}(w,t_i-u-v) + a_2^N E_{2,c1}(w,t_i-u-v) + \ldots + a_N^N E_{N,c1}(w,t_i-u-v))]dvdu \\
&-\int_{u=0}^{t_i} (a_0^N E_0 + E_{1,c3}(w,u) + a_2^N E_{2,c3}(w,u) + \ldots + a_N^N E_{N,c3}(w,u)) \\
&\int_{v=0}^{t_i-u} [q''_{c1}(0,v)(a_0^N E_0 + E_{1,c2}(b,t_i-u-v) + a_2^N E_{2,c2}(b,t_i-u-v) + \ldots + a_N^N E_{N,c2}(b,t_i-u-v)) \\
&-q''_{c2}(0,v)(a_0^N E_0 + E_{1,c1}(b,t_i-u-v) + a_2^N E_{2,c1}(b,t_i-u-v) + \ldots + a_N^N E_{N,c1}(b,t_i-u-v))]dvdu
\end{aligned}$$

$$i = 1, 2, \ldots, M \quad (4.28c)$$

The balance can be visualized by plotting $G_{LHS,\,N}(t_i)$ and $G_{RHS,\,N}(t_i)$ over time. This effectively illustrates the smallness of the residual $\tilde{r}_N\left(t_i; \{a_0^N, a_2^N, a_3^N, \ldots, a_N^N\}\right)$ in Eq. (4.28a).

To illustrate, let us begin by using a 7th order (N = 7) Chebyshev expansion. The undetermined coefficients $\{a_0^7, a_2^7, a_3^7, \ldots, a_7^7\}$ are calculated by the least-squares method and listed in column 2 of Table A-4.3. Figure A-4.8a shows $G_{LHS,\,7}(t_i)$ and $G_{RHS,\,7}(t_i)$ as defined in Eqs. (4.28b, c) using noiseless data. As displayed in Fig. A-4.8, the balance between $G_{LHS,\,7}(t_i)$ and $G_{RHS,\,7}(t_i)$ is achieved (implying a small residual). Next, a sequential study using subsets of the total available data in the time interval $t \in [0, t_{\max}]$ is performed for demonstrating the stability of the coefficients [96]. The times 54s, 48s and 42s as well as the total data collection time t_{max} = 60s are used in the sequential study for checking whether the expansion coefficients calculated by the least-squares method are replicated.

Table A-4.4 provides the calculated expansion coefficients $\{a_0^7, a_2^7, a_3^7, ..., a_7^7\}$ based on the data collection times 60s, 54s, 48s and 42s. Observe the contrasting behavior among the expansion coefficients obtained by 60s and that obtained by 54s, 48s, 42s. For the expansion coefficients obtained using 60s, a_0^N is much greater than a_2^N. However, for the expansion coefficients obtained by 54s, 48s and 42s, a_2^N is greater than a_0^N. The inconsistency in the calculation of the expansion coefficients $\{a_0^7, a_2^7, a_3^7, ..., a_7^7\}$ under different data collection times indicates the sequential instability when choosing the 7th order (N = 7) Chebyshev expansion.

Next, consider using a 6th order (N = 6) Chebyshev expansion. The calculated expansion coefficients $\{a_0^6, a_2^6, a_3^6, ..., a_6^6\}$ are listed in column 3 of Table A-4.3. Observe that the coefficients $\{a_0^6, a_2^6, a_3^6, ..., a_6^6\}$ have the unfavorable behavior as a_2^N is greater than a_0^N. This unfavorable behavior causes an unbalance between $G_{\text{LHS}, 6}(t_i)$ and $G_{\text{RHS}, 6}(t_i)$ which is illustrated in Fig. A-4.8b. For N = 6 using noiseless data, a sequential study is not needed as indicated in Fig. A-4.8b due to the poor balance. Next, consider a 5th order (N = 5) Chebyshev expansion. In this case, both sequential consistency and balance are achieved between $G_{\text{LHS}, 5}(t_i)$ and $G_{\text{RHS}, 5}(t_i)$. Sequential consistency is demonstrated in Table A-4.5 while the balance between $G_{\text{LHS}, 5}(t_i)$ and $G_{\text{RHS}, 5}(t_i)$ is illustrated in Fig. A-4.8c. Figure A-4.9 displays the transformed variable $\phi(T)$ as a function of temperature defined in Eq. (4.13a) within the temperature range [293.15, 1400] K using the calculated coefficients $\{a_0^N, a_2^N, a_3^N, ..., a_N^N\}$ under the six imposed values of N with noiseless data. The calculated coefficients under different values of N are listed in Table A-4.3. It is observed that $\phi(T)$

corresponding to $N = 2, 3, 4, 5$ coalesce. In addition, $\phi(T)$ corresponding to $N = 6$ is nearly zero until about 1050 K, which is not physically reasonable. From the results of this section, the 5th order ($N = 5$) Chebyshev expansion is chosen for representing $\phi(T)$ as defined in Eq. (4.13a). The corresponding coefficients $\{a_0^5, a_2^5, a_3^5, a_4^5, a_5^5\}$ are listed in column 4 of Table A-4.3.

The front surface heat flux $q_r''(0,t)$ can now be calculated using the inverse heat conduction problem formulated in Eq. (4.24b). The calibration tests are designated as c1 and c2, which are displayed in Fig. A-4.3a. These two cases are chosen as the calibration tests for the inverse study. The front and back surface heat fluxes in the reconstruction test are shown in Fig. A-4.3b. Following the procedure discussed in Section 4.3, the predicted front surface heat flux $q_{r,\gamma_m}''(0,t_i)$ can be calculated by Eq. (4.24b) for each fixed future-time parameter γ_m. Figures A-4.10a-c display the predicted front surface heat flux $q_{r,\gamma_m}''(0,t_i)$ when γ_m = 0.5 s, 1.0 s and 1.5 s, respectively. The predicted front surface heat flux $q_{r,\gamma_m}''(0,t_i)$ when γ_m = 0.5 s displays some oscillatory behavior as time increases indicating system instability. When γ_m = 1.0 s and 1.5 s, excellent predictions are indicated that nearly replicate the exact front surface heat flux $q_r''(0,t)$.

Figure A-4.11 displays a comparison between the surface heat flux prediction $q_{r,\gamma_m}''(0,t_i)$ using the nonlinear model discussed in this chapter (shown in Fig. A-4.10c) and the surface heat flux prediction $q_{r,\gamma_m}''(0,t_i)$ based on the linear two-probe calibration integral equation given in Eq. (4.2). The future-time parameter used for both the nonlinear and the linear model is γ_m = 1.5 s. As can be observed in Fig. A-4.11, the surface heat flux prediction, using the linear model, introduces significant errors due to the lack of accounting for the temperature dependency of the thermophysical properties. Figure A-4.12 illustrates the comparison of the absolute error between surface heat flux prediction $q''_{r,\gamma_m}(0,t_i)$ by the nonlinear model and the linear model given in Eq. (4.2) when γ_m = 1.5 s. It is clear that the nonlinear model developed in this context substantially reduces the absolute error in the front surface heat flux prediction.

In this section, a feasible numerical method for resolving the nonlinear inverse heat conduction problem has been demonstrated for the two-probe problem based on noiseless data. Discussion on how to determine the optimal future-time parameter γ_{opt} is postponed at this junction until the noisy data are introduced. In fact, choosing the optimal regularization parameter is of paramount significance to all inverse methods.

4.5.3 Inverse simulation using noisy data

In this section, noise is added to the front surface heat fluxes $q''_{noise,c1}(0,t_i)$, $q''_{noise,c2}(0,t_i)$, as shown in Fig. A-4.6. Figures A-4.7a-d display the noisy "thermocouple" data $\{T_{tc,c1}(b, t_i), T_{tc,c1}(w, t_i)\}$, $\{T_{tc,c2}(b, t_i), T_{tc,c2}(w, t_i)\}$, $\{T_{tc,c3}(b, t_i), T_{tc,c3}(w, t_i)\}$, $\{T_{tc,r}(b, t_i), T_{tc,r}(w, t_i)\}$ that will be used in the numerical simulation. Heat flux phase plane and cross-correlation analyses per Eqs. (4.25a, b) are applied for estimating the optimal future-time parameter, γ_{opt}. Table A-4.6 lists the numerically calculated expansion coefficients for various N based on noisy data that are acquired using a 50 Hz sampling frequency. Tables A-4.7 through A-4.9 show the sequential time study for the calculated expansion coefficients $\{a_0^N, a_2^N, a_3^N, ..., a_N^N\}$ when N = 7, 6 and 5, respectively. As shown in Tables A-4.7 and A-4.8, the calculated expansion coefficients $\{a_0^N, a_2^N, a_3^N, ..., a_N^N\}$ using different data collection times do not achieve the desired stability for the leading terms when using N = 7 and 6. In contrast, expansion coefficients $\{a_0^N, a_2^N, a_3^N, ..., a_N^N\}$ when N = 5 displays consistency at leading order terms over the various time segments. Figure A-4.13 displays $G_{\text{LHS, 5}}(t_i)$ and $G_{\text{RHS, 5}}(t_i)$ as defined in Eqs. (4.28b, c) while are listed in column 4 of Table A-4.6. It is obvious that the balance of Eq. (4.28a) is achieved as $G_{\text{LHS, 5}}(t_i)$ and $G_{\text{RHS, 5}}(t_i)$ overlap. Therefore, the 5$^{\text{th}}$ order (N = 5) Chebyshev expansion and their calculated expansion coefficients are used in this section for representing the transformed variable $\phi(T)$ defined in Eq. (4.13a). Figure A-4.14 displays the transformed variable $\phi(T)$ defined in Eq. (4.13a) in the temperature range [293.15, 1400] K using the calculated coefficients. The front surface heat flux in the reconstruction test can be estimated by the procedure discussed in Section 4.3 with a chosen future-time parameter γ leading to the approximation. A spectrum of future-time parameters γ_m's are developed and the phase plane and cross-correlation analyses discussed in Section 4.4 are applied for estimating the optimal future-time parameter γ_{opt}. Figure A-4.15a shows the predicted surface heat flux rate and predicted surface heat flux phase plane when $\gamma_m = M_f m\Delta t$ for m = 6, 7, … , 13, M_f = 10, Δt =0.02 s while Fig. A-4.15b displays a zoomed in version of Fig. A-4.15a with m = 9, 10, … , 13.

In Fig. A-4.15a, a significant random pattern is observed for small γ's (γ < 1.45 s). As future-time parameter γ_m increases to 2.2 s, randomness is substantially reduced and the corresponding phase plane exhibits a distinctive pattern formation that is similar to two concentric ellipses. The onset of a pattern defines the transition region where the balance between stability and accuracy is achieved in the heat flux prediction. Returning to Fig. A-4.15b, one can qualitatively see that the onset of a pattern occurs when $\gamma \in [2.0, 2.2]\,\mathrm{s}$. Highly smoothed surface heat flux rate and surface heat flux predictions are observed when $\gamma \in [2.4, 2{,}6]\,\mathrm{s}$. In order to recover small temporal changes in the predicted heat flux, it is favorable to retain as many high-frequency components in the signal. Therefore, surface heat flux predictions using $\gamma \in [2.4, 2{,}6]\,\mathrm{s}$ or greater are removed from further consideration due to over-smoothing. The surface heat flux rate and surface heat flux phase plane in Figs. A-4.15a, b provide the initial qualitative perspective for extracting the optimal future-time parameter.

Figure A-4.16 illustrates the cross-correlation coefficients phase plane. This phase plane is defined in terms of the surface heat flux cross-correlation coefficient $R_q(q''_{r,\gamma_m}, q''_{r,\gamma_{m+1}})$ and surface heat flux rate cross-correlation coefficient $R_{\dot{q}}(\dot{q}''_{r,\gamma_m}, \dot{q}''_{r,\gamma_{m+1}})$ as given in Eqs. (4.25a, b). The three defined regions (unstable, transition and over-smoothed) that are discussed in the Figs. A-4.15a, b are described in an alternative way in Fig. A-4.16. In Fig. A-4.16, γ pairs (1.2, 1.4) s to (1.4, 1.6) s are defined. Small values of $R_q(q''_{r,\gamma_m}, q''_{r,\gamma_{m+1}})$ and $R_{\dot{q}}(\dot{q}''_{r,\gamma_m}, \dot{q}''_{r,\gamma_{m+1}})$ equate to highly random predictions or uncorrelated predictions. As γ increases to 2, $R_{\dot{q}}(\dot{q}''_{r,\gamma_m}, \dot{q}''_{r,\gamma_{m+1}})$ climbs toward unity. Unity on the $R_q(q''_{r,\gamma_m}, q''_{r,\gamma_{m+1}})$ is more readily available or desirable than the. Approaching unity on the vertical axis should be physically avoided as numerical differentiation is a roughening operation. In this study, γ = 2.0s is chosen as the γ pair (2.0, 2.2) s lies closest to the experienced-based, cut-off line. This choice of γ_{opt} = 2.0s retains sufficient high-frequency content in the signal that balances stability and accuracy. The cut-off line could also be placed at $R_{\dot{q}}(\dot{q}''_{r,\gamma_m}, \dot{q}''_{r,\gamma_{m+1}}) \approx 0.7$ as indicated by experiments. Figure A-4.17 displays the predicted surface heat flux, $q''_{r,\gamma_m}(0,t_i)$ over the future-time spectrum $\gamma_m = M_f m\Delta t$, m = 6 – 13, M_f = 10, Δt =0.02 s. Figure A-4.18 compares the surface heat flux, $q''_{r,\gamma}(0,t_i)$ to the exact when γ_{opt} = 2.0 s. Highly favorable results are produced in light of the significant amount of noise contained in the surface heat fluxes for the calibration tests (Fig. A-4.6) and in the "thermocouple" data for both the calibration tests and reconstruction test (Figs. A-4.7a-d). It is worth noting that the two-probe calibration integral equation method developed in this chapter not only works for predicting the front surface heat flux in case of back surface heating, but also works in case of back surface cooling. With well-designed calibration tests, this method is capable of estimating the front surface heat flux in reconstruction test in terms of an arbitrary back surface boundary condition.

4.6 Conclusions

A new two-probe calibration integral equation method (CIEM) is proposed and numerically verified for estimating the front surface heat flux in the context of a one-dimensional nonlinear inverse heat conduction problem with a time-varying back surface boundary condition. In contrast to one-probe CIEM that requires certain types of boundary conditions on the back surface, the two-probe CIEM can be used for estimating the front surface heat flux in the case of arbitrary back surface boundary conditions. The temperature-dependent thermophysical properties and probe positions are inherently contained in the formulated Volterra integral equation of the first kind for reconstructed surface heat flux. Three well-defined calibration tests are used for estimating the undetermined coefficients associated with the Chebyshev expansion by a least-squares method. A time sequential investigation of the expansion coefficients provides a means for estimating the order of the Chebyshev expansion. A local future-time method is employed as the regularization scheme for stabilizing the ill-posed first kind Volterra integral equation. Phase plane and cross-correlation analyses are applied for estimating the optimal future-time parameter from a spectrum of chosen values. Numerical simulations for stainless steel yield highly favorable surface heat flux predictions. Overall, this "parameter free" inverse method produces highly favorable results that remove the need to accurately quantify the thermophysical properties and probe locations. This advancement is significant to many engineering applications.

Chapter 5: Two-Probe Calibration Integral Equation Method for Nonlinear Inverse Heat Conduction Problem of Surface Temperature Estimation

This chapter is based on the paper: H. Chen, J. I. Frankel, and M. Keyhani, "Two-probe calibration integral equation method for nonlinear inverse heat conduction problem of surface temperature estimation", Applied Mathematical Modelling (to be submitted).

5.1 Introduction

In Chapter 4, the two-probe calibration integral equation method for resolving a nonlinear inverse heat conduction problem involving surface heat flux estimation is demonstrated and numerically verified. In this chapter, the two-probe calibration integral equation method is described for resolving inverse heat conduction problem involving surface temperature estimation.

5.2 Formulation of the nonlinear two-probe surface temperature calibration integral equation method

The two-probe surface temperature calibration integral equation is derived in a similar manner as described in Chapter 4 involving the reconstruction of the surface heat flux. Figure A-5.1 describes the physical problem to be considered in this chapter. Figure A-5.1 shows an idealized thin film (TF) surface thermocouple and two in-depth thermocouples. An instrumentation challenge is presented for surface temperature measurements as it is well known to be notoriously difficult for assuring accuracy. The thickness of the one-dimensional slab is L. For physical understanding, consider a thermocouple located at x = 0, and the two in-depth thermocouples located at $x = b$ and $x = w$. The three thermocouples are denoted by "TF", "TC1" and "TC2", respectively. The net heat fluxes at the front surface (x = 0) and at the back surface ($x = L$) are denoted by $q''_0(t)$ and $q''_L(t)$, respectively. The front surface temperature is denoted by $T(0, t)$. The introduction of the second probe at $x = w$ removes the requirement of imposing specific boundary condition at the back surface.

5.2.1 Background: linear two-probe surface temperature calibration integral equation

The linear two-probe surface temperature calibration integral equation is derived based on frequency domain analysis of the one-dimensional linear heat equation [85] defined as

$$\frac{1}{\alpha}\frac{\partial T}{\partial t}(x,t) = \frac{\partial^2 T}{\partial x^2}(x,t), \quad x \in [0, L], \quad t \ge 0 \tag{5.1a}$$

subject to the boundary conditions

$$q''_0(t) = q''(0,t) \equiv -k\frac{\partial T}{\partial x}(0,t), \quad t > 0 \tag{5.1b}$$

$$q''_L(t) = -q''(L,t) \equiv k\frac{\partial T}{\partial x}(L,t), \quad t > 0 \tag{5.1c}$$

and initial condition

$$T(x,0) = T_0, \quad x \in [0, L] \tag{5.1d}$$

In Eqs. (5.1), T denotes temperature, x and t denote spatial and temporal variable, respectively, α denotes thermal diffusivity, k denotes thermal conductivity, $q''(0,t)$ and

$q''(0,L)$ denote the conductive (net) heat fluxes at x = 0 and L, respectively, while $q_0''(t)$ and $q_L''(t)$ denote the imposed heat fluxes from external sources and other modes of heat transfer. The linear two-probe surface temperature calibration integral equation [69] is given as

$$\begin{aligned}&\int_{u=0}^{t}\theta_r(0,u)\int_{v=0}^{t-u}\left(\theta_{c1}(b,v)\theta_{c2}(w,t-u-v)-\theta_{c2}(b,v)\theta_{c1}(w,t-u-v)\right)dvdu\\&=\int_{u=0}^{t}\theta_r(b,u)\int_{v=0}^{t-u}\left(\theta_{c1}(0,v)\theta_{c2}(w,t-u-v)-\theta_{c2}(0,v)\theta_{c1}(w,t-u-v)\right)dvdu\\&-\int_{u=0}^{t}\theta_r(w,u)\int_{v=0}^{t-u}\left(\theta_{c1}(0,v)\theta_{c2}(b,t-u-v)-\theta_{c2}(0,v)\theta_{c1}(b,t-u-v)\right)dvdu,\quad t\geq 0\end{aligned} \tag{5.2}$$

where θ denotes excess temperature defined as $\theta = T - T_0$. The subscripts "c1", "c2" and "r" denote calibration test 1, calibration test 2 and reconstruction test, respectively. Equation (5.2) can be expressed in compact mathematical form as

$$\int_{u=0}^{t}\theta_r(0,u)K_l(t-u)du = F_l(t),\ t\geq 0 \tag{5.3a}$$

where the subscript "l" denotes linear. The forcing function $F_L(t)$ and the convolution kernel $K_l\,(t - u)$ in Eq. (5.3a) are defined as

$$\begin{aligned}F_l(t)=&\int_{u=0}^{t}\theta_r(b,u)\int_{v=0}^{t-u}\left(\theta_{c1}(0,v)\theta_{c2}(w,t-u-v)-\theta_{c2}(0,v)\theta_{c1}(w,t-u-v)\right)dvdu\\&-\int_{u=0}^{t}\theta_r(w,u)\int_{v=0}^{t-u}\left(\theta_{c1}(0,v)\theta_{c2}(b,t-u-v)-\theta_{c2}(0,v)\theta_{c1}(b,t-u-v)\right)dvdu,\quad t\geq 0\end{aligned} \tag{5.3b}$$

$$K_l(t-u)=\int_{v=0}^{t-u}\left(\theta_{c1}(b,v)\theta_{c2}(w,t-u-v)-\theta_{c2}(b,v)\theta_{c1}(w,t-u-v)\right)dv,\ (t-u)\geq 0 \tag{5.3c}$$

5.2.2 Derivation of the nonlinear two-probe surface temperature calibration integral equation

To begin, consider the transient one-dimensional nonlinear heat equation [85] given as

$$\rho c(T)\frac{\partial T}{\partial t}(x,t)=\frac{\partial}{\partial x}\left[k(T)\frac{\partial T}{\partial x}(x,t)\right],\ \ x\in[0,L],\ \ t\geq 0 \tag{5.4a}$$

subject to the boundary conditions

$$q_0''(t)=q''(0,t)\equiv -k\left(T(0,t)\right)\frac{\partial T}{\partial x}(0,t),\ \ t>0 \tag{5.4b}$$

$$q_L''(t)=-q''(L,t)\equiv k\left(T(L,t)\right)\frac{\partial T}{\partial x}(L,t),\ \ t>0 \tag{5.4c}$$

and initial condition

$$T(x,0)=T_0,\ \ x\in[0,L] \tag{5.4d}$$

The generalized property transform technique [65, 96] is applied for linearizing the nonlinear heat equation shown in Eqs. (5.4), the. In a nutshell, Eq. (5.4a) can be decomposed by property transform as

$$\rho c(T)\frac{dT}{d\varphi}\frac{\partial \varphi}{\partial t}(x,t)=\frac{\partial}{\partial x}\left(k(T)\frac{dT}{d\varphi}\frac{\partial \varphi}{\partial x}(x,t)\right),\ \ x\in[0,L],\ \ t\geq 0, \tag{5.5}$$

where $\varphi(x, t)$ denotes the property transfer function, which can be thermal conductivity, specific heat, thermal diffusivity, thermal effusivity, etc [65]. The implicit assumption that inverse function of $\varphi(T)$ exists is made, which permits us to write $dT/d\varphi$. Assuming there exists a combination that produces

$$k(T)\frac{dT}{d\varphi}=\kappa\approx \text{constant} \tag{5.6}$$

then the transformed heat equation can be expressed in terms of the transformed variable, $\varphi(x, t)$ as

$$\frac{1}{\alpha(T)}\frac{\partial \varphi}{\partial t}(x,t)=\frac{\partial^2 \varphi}{\partial x^2}(x,t),\ \ x\in[0,L],\ \ t\geq 0. \tag{5.7}$$

In addition, it is assumed that the thermal diffusivity $\alpha(T)$ remains constant and now denoted as α_0. The linearized heat equation can then be written as

$$\frac{1}{\alpha_0}\frac{\partial \varphi}{\partial t}(x,t) = \frac{\partial^2 \varphi}{\partial x^2}(x,t), \;\; x \in [0,L], \;\; t \geq 0, \qquad (5.8a)$$

with respect to the transformed boundary conditions as

$$q''(0,t) \equiv -\kappa \frac{\partial \varphi}{\partial x}(0,t), \;\; t > 0, \qquad (5.8b)$$

$$q''(L,t) \equiv -\kappa \frac{\partial \varphi}{\partial x}(L,t), \;\; t > 0, \qquad (5.8c)$$

with the transformed initial condition as

$$\varphi(x,0) = \varphi(T_0), \;\; x \in [0,L]. \qquad (5.8d)$$

Let us now define $\phi(T) = \varphi(T) - \varphi(T_0)$, then Eqs. (5.8a-d) become

$$\frac{1}{\alpha_0}\frac{\partial \phi}{\partial t}(x,t) = \frac{\partial^2 \phi}{\partial x^2}(x,t), \;\; x \in [0,L], \;\; t \geq 0, \qquad (5.9a)$$

subject to the transformed boundary conditions

$$q''(0,t) \equiv -\kappa \frac{\partial \phi}{\partial x}(0,t), \;\; t > 0, \qquad (5.9b)$$

$$q''(L,t) \equiv -\kappa \frac{\partial \phi}{\partial x}(L,t), \;\; t > 0, \qquad (5.9c)$$

and the transformed initial condition

$$\phi(x,0) = 0, \;\; x \in [0,L]. \qquad (5.9d)$$

The two-probe calibration integral equation for the linearized nonlinear heat equation given in Eqs. (5.9) can be derived in the same manner as deriving the linear two-probe calibration integral equation [69]. In a nutshell, the two-probe surface temperature calibration integral equation for the linearized system given in Eqs. (5.9) can be written as

$$\begin{aligned}
&\int_{u=0}^{t}\phi_r(0,u)\int_{v=0}^{t-u}\left(\phi_{c1}(b,v)\phi_{c2}(w,t-u-v)-\phi_{c2}(b,v)\phi_{c1}(w,t-u-v)\right)dv\,du \\
&=\int_{u=0}^{t}\phi_r(b,u)\int_{v=0}^{t-u}\left(\phi_{c1}(0,v)\phi_{c2}(w,t-u-v)-\phi_{c2}(0,v)\phi_{c1}(w,t-u-v)\right)dv\,du \\
&-\int_{u=0}^{t}\phi_r(w,u)\int_{v=0}^{t-u}\left(\phi_{c1}(0,v)\phi_{c2}(b,t-u-v)-\phi_{c2}(0,v)\phi_{c1}(b,t-u-v)\right)dv\,du, \quad t\geq 0
\end{aligned} \tag{5.10}$$

or in the compact mathematical form as

$$\int_{u=0}^{t}\phi_r(0,u)K(t-u)du=F(t),\ \ t\geq 0 \tag{5.11a}$$

where the forcing function $F(t)$ and the convolution kernel $K(t-u)$ are defined as

$$\begin{aligned}
F(t)=&\int_{u=0}^{t}\phi_r(b,u)\int_{v=0}^{t-u}\left(\phi_{c1}(0,v)\phi_{c2}(w,t-u-v)-\phi_{c2}(0,v)\phi_{c1}(w,t-u-v)\right)dv\,du \\
&-\int_{u=0}^{t}\phi_r(w,u)\int_{v=0}^{t-u}\left(\phi_{c1}(0,v)\phi_{c2}(b,t-u-v)-\phi_{c2}(0,v)\phi_{c1}(b,t-u-v)\right)dv\,du, \quad t\geq 0
\end{aligned} \tag{5.11b}$$

$$K(t-u)=\int_{v=0}^{t-u}\left(\phi_{c1}(b,v)\phi_{c2}(w,t-u-v)-\phi_{c2}(b,v)\phi_{c1}(w,t-u-v)\right)dv,\ \ (t-u)\geq 0 \tag{5.11c}$$

respectively. A first kind Chebyshev expansion is used for representing the property transform function $\phi(x, t)$. In order to implement a Chebyshev expansion, the temperatures are mapped into the range [-1, 1] as

$$T^*(x,t)=\frac{2T(x,t)-T_L-T_U}{T_U-T_L}\in[-1,1] \tag{5.12}$$

where "T_L" and "T_U" represent the temperature of lower bound and upper bound, respectively. The values of "T_L" and "T_U" can be properly selected to ensure that the temperature ranges for all calibration tests and reconstruction test are in the domain [T_L,

T_U]. After the temperatures are mapped in the [-1, 1], the Chebyshev expansion for approximating the property transform function $\phi(x, t)$ can be formulated as

$$\phi(x,t) = \sum_{n=0}^{\infty} a_n E_n(x,t) \approx \phi_N(x,t) = \sum_{n=0}^{N} a_n^N E_n(x,t) \tag{5.13a}$$

where

$$E_n(x,t) = E_n\left(T^*(x,t)\right), \; n = 0, 1, 2, \ldots \tag{5.13b}$$

Equation (5.13b) denotes the n^{th} order first kind Chebyshev polynomial for the mapped temperature. For notational clarity, several first kind Chebyshev polynomials conforming to the notation used in this context are listed in Table A-5.1. Note that in Eq. (5.13a), the transformed variable ϕ is a function of temperature but the units of the undetermined coefficients $\{a_0^N, a_1^N, a_2^N, \ldots, a_N^N\}$ remain unknown.

Substituting the Chebyshev expansion given in Eq. (5.13a) into Eq. (5.10) produces the explicit expression

$$
\begin{aligned}
&\int_{u=0}^{t}(a_0^N E_0 + a_1^N E_{1,r}(0,u) + a_2^N E_{2,r}(0,u) + ... + a_N^N E_{N,r}(0,u)) \\
&\int_{v=0}^{t-u}[(a_0^N E_0 + a_1^N E_{1,c1}(b,v) + a_2^N E_{2,c1}(b,v) + ... + a_N^N E_{N,c1}(b,v)) \\
&(a_0^N E_0 + a_1^N E_{1,c2}(w,t-u-v) + a_2^N E_{2,c2}(w,t-u-v) + ... + a_N^N E_{N,c2}(w,t-u-v)) \\
&-(a_0^N E_0 + a_1^N E_{1,c2}(b,v) + a_2^N E_{2,c2}(b,v) + ... + a_N^N E_{N,c2}(b,v)) \\
&\ (a_0^N E_0 + a_1^N E_{1,c1}(w,t-u-v) + a_2^N E_{2,c1}(w,t-u-v) + ... + a_N^N E_{N,c1}(w,t-u-v))]dvdu \\
&\approx \int_{u=0}^{t}(a_0^N E_0 + a_1^N E_{1,r}(b,u) + a_2^N E_{2,r}(b,u) + ... + a_N^N E_{N,r}(b,u)) \\
&\int_{v=0}^{t-u}[(a_0^N E_0 + a_1^N E_{1,c1}(0,v) + a_2^N E_{2,c1}(0,v) + ... + a_N^N E_{N,c1}(0,v)) \\
&(a_0^N E_0 + a_1^N E_{1,c2}(w,t-u-v) + a_2^N E_{2,c2}(w,t-u-v) + ... + a_N^N E_{N,c2}(w,t-u-v)) \\
&-(a_0^N E_0 + a_1^N E_{1,c2}(0,v) + a_2^N E_{2,c2}(0,v) + ... + a_N^N E_{N,c2}(0,v)) \\
&(a_0^N E_0 + a_1^N E_{1,c1}(w,t-u-v) + a_2^N E_{2,c1}(w,t-u-v) + ... + a_N^N E_{N,c1}(w,t-u-v))]dvdu \\
&-\int_{u=0}^{t}(a_0^N E_0 + a_1^N E_{1,r}(w,u) + a_2^N E_{2,r}(w,u) + ... + a_N^N E_{N,r}(w,u)) \\
&\int_{v=0}^{t-u}[(a_0^N E_0 + a_1^N E_{1,c1}(0,v) + a_2^N E_{2,c1}(0,v) + ... + a_N^N E_{N,c1}(0,v))) \\
&(a_0^N E_0 + a_1^N E_{1,c2}(b,t-u-v) + a_2^N E_{2,c2}(b,t-u-v) + ... + a_N^N E_{N,c2}(b,t-u-v) \\
&-(a_0^N E_0 + a_1^N E_{1,c2}(0,v) + a_2^N E_{2,c2}(0,v) + ... + a_N^N E_{N,c2}(0,v)) \\
&(a_0^N E_0 + a_1^N E_{1,c1}(b,t-u-v) + a_2^N E_{2,c1}(b,t-u-v) + ... + a_N^N E_{N,c1}(b,t-u-v))]dvdu,\ t \geq 0
\end{aligned}
\tag{5.14a}
$$

which involves a finite number of undetermined coefficients $\{a_0^N, a_2^N, a_3^N, ..., a_N^N\}$. If N is sufficiently large then Eq. (5.14a) should be well-balanced. In order to proceed with the analysis, we introduce the residual function, $r_N(t)$ as

$$
\begin{aligned}
&\int_{u=0}^{t}(a_0^N E_0 + a_1^N E_{1,r}(0,u) + a_2^N E_{2,r}(0,u) + ... + a_N^N E_{N,r}(0,u)) \\
&\int_{v=0}^{t-u}[(a_0^N E_0 + a_1^N E_{1,c1}(b,v) + a_2^N E_{2,c1}(b,v) + ... + a_N^N E_{N,c1}(b,v)) \\
&(a_0^N E_0 + a_1^N E_{1,c2}(w,t-u-v) + a_2^N E_{2,c2}(w,t-u-v) + ... + a_N^N E_{N,c2}(w,t-u-v)) \\
&-(a_0^N E_0 + a_1^N E_{1,c2}(b,v) + a_2^N E_{2,c2}(b,v) + ... + a_N^N E_{N,c2}(b,v)) \\
&\ (a_0^N E_0 + a_1^N E_{1,c1}(w,t-u-v) + a_2^N E_{2,c1}(w,t-u-v) + ... + a_N^N E_{N,c1}(w,t-u-v))]dvdu \\
&= \int_{u=0}^{t}(a_0^N E_0 + a_1^N E_{1,r}(b,u) + a_2^N E_{2,r}(b,u) + ... + a_N^N E_{N,r}(b,u)) \\
&\int_{v=0}^{t-u}[(a_0^N E_0 + a_1^N E_{1,c1}(0,v) + a_2^N E_{2,c1}(0,v) + ... + a_N^N E_{N,c1}(0,v)) \\
&(a_0^N E_0 + a_1^N E_{1,c2}(w,t-u-v) + a_2^N E_{2,c2}(w,t-u-v) + ... + a_N^N E_{N,c2}(w,t-u-v)) \\
&-(a_0^N E_0 + a_1^N E_{1,c2}(0,v) + a_2^N E_{2,c2}(0,v) + ... + a_N^N E_{N,c2}(0,v)) \\
&(a_0^N E_0 + a_1^N E_{1,c1}(w,t-u-v) + a_2^N E_{2,c1}(w,t-u-v) + ... + a_N^N E_{N,c1}(w,t-u-v))]dvdu \\
&-\int_{u=0}^{t}(a_0^N E_0 + a_1^N E_{1,r}(w,u) + a_2^N E_{2,r}(w,u) + ... + a_N^N E_{N,r}(w,u)) \\
&\int_{v=0}^{t-u}[(a_0^N E_0 + a_1^N E_{1,c1}(0,v) + a_2^N E_{2,c1}(0,v) + ... + a_N^N E_{N,c1}(0,v))) \\
&(a_0^N E_0 + a_1^N E_{1,c2}(b,t-u-v) + a_2^N E_{2,c2}(b,t-u-v) + ... + a_N^N E_{N,c2}(b,t-u-v) \\
&-(a_0^N E_0 + a_1^N E_{1,c2}(0,v) + a_2^N E_{2,c2}(0,v) + ... + a_N^N E_{N,c2}(0,v)) \\
&(a_0^N E_0 + a_1^N E_{1,c1}(b,t-u-v) + a_2^N E_{2,c1}(b,t-u-v) + ... + a_N^N E_{N,c1}(b,t-u-v))]dvdu \\
&+ r_N(t),\ \ t \ge 0
\end{aligned}
\tag{5.14b}
$$

where $\{a_j^N\}_{j=0}^N$ are momentarily assumed known. At this junction, the formulation requires two calibration tests for estimating the surface temperature in reconstruction test. By comparing Eq. (5.14b) to the two-probe surface temperature calibration equation for a constant thermophysical property thermal model given in Eq. (5.2), we can set $a_1^N = 1$ (or divide by $(a_1^N)^2$ on both sides of Eq. (5.14b). Thus Eq. (5.14b) can be written as

$$
\begin{aligned}
&\int_{u=0}^{t}(a_0^N E_0 + E_{1,r}(0,u) + a_2^N E_{2,r}(0,u) + \ldots + a_N^N E_{N,r}(0,u)) \\
&\int_{v=0}^{t-u}[(a_0^N E_0 + E_{1,c1}(b,v) + a_2^N E_{2,c1}(b,v) + \ldots + a_N^N E_{N,c1}(b,v)) \\
&(a_0^N E_0 + E_{1,c2}(w,t-u-v) + a_2^N E_{2,c2}(w,t-u-v) + \ldots + a_N^N E_{N,c2}(w,t-u-v)) \\
&-(a_0^N E_0 + E_{1,c2}(b,v) + a_2^N E_{2,c2}(b,v) + \ldots + a_N^N E_{N,c2}(b,v)) \\
&\ (a_0^N E_0 + E_{1,c1}(w,t-u-v) + a_2^N E_{2,c1}(w,t-u-v) + \ldots + a_N^N E_{N,c1}(w,t-u-v))]dvdu \\
&= \int_{u=0}^{t}(a_0^N E_0 + E_{1,r}(b,u) + a_2^N E_{2,r}(b,u) + \ldots + a_N^N E_{N,r}(b,u)) \\
&\int_{v=0}^{t-u}[(a_0^N E_0 + E_{1,c1}(0,v) + a_2^N E_{2,c1}(0,v) + \ldots + a_N^N E_{N,c1}(0,v)) \\
&(a_0^N E_0 + E_{1,c2}(w,t-u-v) + a_2^N E_{2,c2}(w,t-u-v) + \ldots + a_N^N E_{N,c2}(w,t-u-v)) \\
&-(a_0^N E_0 + E_{1,c2}(0,v) + a_2^N E_{2,c2}(0,v) + \ldots + a_N^N E_{N,c2}(0,v)) \\
&(a_0^N E_0 + E_{1,c1}(w,t-u-v) + a_2^N E_{2,c1}(w,t-u-v) + \ldots + a_N^N E_{N,c1}(w,t-u-v))]dvdu \\
&-\int_{u=0}^{t}(a_0^N E_0 + E_{1,r}(w,u) + a_2^N E_{2,r}(w,u) + \ldots + a_N^N E_{N,r}(w,u)) \\
&\int_{v=0}^{t-u}[(a_0^N E_0 + E_{1,c1}(0,v) + a_2^N E_{2,c1}(0,v) + \ldots + a_N^N E_{N,c1}(0,v))) \\
&(a_0^N E_0 + E_{1,c2}(b,t-u-v) + a_2^N E_{2,c2}(b,t-u-v) + \ldots + a_N^N E_{N,c2}(b,t-u-v) \\
&-(a_0^N E_0 + E_{1,c2}(0,v) + a_2^N E_{2,c2}(0,v) + \ldots + a_N^N E_{N,c2}(0,v)) \\
&(a_0^N E_0 + E_{1,c1}(b,t-u-v) + a_2^N E_{2,c1}(b,t-u-v) + \ldots + a_N^N E_{N,c1}(b,t-u-v))]dvdu \\
&+ r_N(t), \ \ t \geq 0
\end{aligned}
\tag{5.14c}
$$

In order to estimate the undetermined coefficients $\{a_0^N, a_2^N, a_3^N, \ldots, a_N^N\}$ in Eq. (5.14c), we must introduce a third calibration test whereby the subscript notation changes as r → c3. Three well-defined calibration tests are now defined. Thus Eq. (5.14c) can be written as

$$
\begin{aligned}
&\int_{u=0}^{t}(a_0^N E_0 + E_{1,c3}(0,u) + a_2^N E_{2,c3}(0,u) + ... + a_N^N E_{N,c3}(0,u))\\
&\int_{v=0}^{t-u}[(a_0^N E_0 + E_{1,c1}(b,v) + a_2^N E_{2,c1}(b,v) + ... + a_N^N E_{N,c1}(b,v))\\
&(a_0^N E_0 + E_{1,c2}(w,t-u-v) + a_2^N E_{2,c2}(w,t-u-v) + ... + a_N^N E_{N,c2}(w,t-u-v))\\
&-(a_0^N E_0 + E_{1,c2}(b,v) + a_2^N E_{2,c2}(b,v) + ... + a_N^N E_{N,c2}(b,v))\\
&\quad(a_0^N E_0 + E_{1,c1}(w,t-u-v) + a_2^N E_{2,c1}(w,t-u-v) + ... + a_N^N E_{N,c1}(w,t-u-v))]dvdu\\
&= \int_{u=0}^{t}(a_0^N E_0 + E_{1,c3}(b,u) + a_2^N E_{2,c3}(b,u) + ... + a_N^N E_{N,c3}(b,u))\\
&\int_{v=0}^{t-u}[(a_0^N E_0 + E_{1,c1}(0,v) + a_2^N E_{2,c1}(0,v) + ... + a_N^N E_{N,c1}(0,v))\\
&(a_0^N E_0 + E_{1,c2}(w,t-u-v) + a_2^N E_{2,c2}(w,t-u-v) + ... + a_N^N E_{N,c2}(w,t-u-v))\\
&-(a_0^N E_0 + E_{1,c2}(0,v) + a_2^N E_{2,c2}(0,v) + ... + a_N^N E_{N,c2}(0,v))\\
&(a_0^N E_0 + E_{1,c1}(w,t-u-v) + a_2^N E_{2,c1}(w,t-u-v) + ... + a_N^N E_{N,c1}(w,t-u-v))]dvdu\\
&-\int_{u=0}^{t}(a_0^N E_0 + E_{1,c3}(w,u) + a_2^N E_{2,c3}(w,u) + ... + a_N^N E_{N,c3}(w,u))\\
&\int_{v=0}^{t-u}[(a_0^N E_0 + E_{1,c1}(0,v) + a_2^N E_{2,c1}(0,v) + ... + a_N^N E_{N,c1}(0,v)))\\
&(a_0^N E_0 + E_{1,c2}(b,t-u-v) + a_2^N E_{2,c2}(b,t-u-v) + ... + a_N^N E_{N,c2}(b,t-u-v)\\
&-(a_0^N E_0 + E_{1,c2}(0,v) + a_2^N E_{2,c2}(0,v) + ... + a_N^N E_{N,c2}(0,v))\\
&(a_0^N E_0 + E_{1,c1}(b,t-u-v) + a_2^N E_{2,c1}(b,t-u-v) + ... + a_N^N E_{N,c1}(b,t-u-v))]dvdu\\
&+\tilde{r}_N\left(t;\{a_0^N, a_2^N, a_3^N, ..., a_N^N\}\right),\ t \geq 0
\end{aligned} \tag{5.15}
$$

In Eq. (5.15), all the variables are known except the N undetermined coefficients $\{a_0^N, a_2^N, a_3^N, ..., a_N^N\}$. A nonlinear least-squares method based on residual $\tilde{r}_N\left(t;\{a_0^N, a_2^N, a_3^N, ..., a_N^N\}\right)$ can be used for estimating the N undetermined coefficients $\{a_0^N, a_2^N, a_3^N, ..., a_N^N\}$. The least-squares method is formulated as

$$
\begin{aligned}
&\tilde{r}_N\left(t_i;\{a_0^N, a_2^N, a_3^N, ..., a_N^N\}\right) \\
&= \int_{u=0}^{t_i} (a_0^N E_0 + E_{1,c3}(0,u) + a_2^N E_{2,c3}(0,u) + ... + a_N^N E_{N,c3}(0,u)) \\
&\int_{v=0}^{t_i-u} [(a_0^N E_0 + E_{1,c1}(b,v) + a_2^N E_{2,c1}(b,v) + ... + a_N^N E_{N,c1}(b,v)) \\
&(a_0^N E_0 + E_{1,c2}(w,t_i-u-v) + a_2^N E_{2,c2}(w,t_i-u-v) + ... + a_N^N E_{N,c2}(w,t_i-u-v)) \\
&-(a_0^N E_0 + E_{1,c2}(b,v) + a_2^N E_{2,c2}(b,v) + ... + a_N^N E_{N,c2}(b,v)) \\
&\ (a_0^N E_0 + E_{1,c1}(w,t_i-u-v) + a_2^N E_{2,c1}(w,t_i-u-v) + ... + a_N^N E_{N,c1}(w,t_i-u-v))]dvdu \\
&-\{\int_{u=0}^{t_i} (a_0^N E_0 + E_{1,c3}(b,u) + a_2^N E_{2,c3}(b,u) + ... + a_N^N E_{N,c3}(b,u)) \\
&\int_{v=0}^{t_i-u} [(a_0^N E_0 + E_{1,c1}(0,v) + a_2^N E_{2,c1}(0,v) + ... + a_N^N E_{N,c1}(0,v)) \\
&(a_0^N E_0 + E_{1,c2}(w,t_i-u-v) + a_2^N E_{2,c2}(w,t_i-u-v) + ... + a_N^N E_{N,c2}(w,t_i-u-v)) \\
&-(a_0^N E_0 + E_{1,c2}(0,v) + a_2^N E_{2,c2}(0,v) + ... + a_N^N E_{N,c2}(0,v)) \\
&(a_0^N E_0 + E_{1,c1}(w,t_i-u-v) + a_2^N E_{2,c1}(w,t_i-u-v) + ... + a_N^N E_{N,c1}(w,t_i-u-v))]dvdu \\
&-\int_{u=0}^{t_i} (a_0^N E_0 + E_{1,c3}(w,u) + a_2^N E_{2,c3}(w,u) + ... + a_N^N E_{N,c3}(w,u)) \\
&\int_{v=0}^{t_i-u} [(a_0^N E_0 + E_{1,c1}(0,v) + a_2^N E_{2,c1}(0,v) + ... + a_N^N E_{N,c1}(0,v))) \\
&(a_0^N E_0 + E_{1,c2}(b,t_i-u-v) + a_2^N E_{2,c2}(b,t_i-u-v) + ... + a_N^N E_{N,c2}(b,t_i-u-v) \\
&-(a_0^N E_0 + E_{1,c2}(0,v) + a_2^N E_{2,c2}(0,v) + ... + a_N^N E_{N,c2}(0,v)) \\
&(a_0^N E_0 + E_{1,c1}(b,t_i-u-v) + a_2^N E_{2,c1}(b,t_i-u-v) + ... + a_N^N E_{N,c1}(b,t_i-u-v))]dvdu\}
\end{aligned}
$$

$$
i = 1, 2, \ldots, M \qquad (5.16)
$$

where $\{t_i\}_{i=1}^{M}$ denotes the discrete sampling time, and M is the number of data points in the discretized temporal domain beyond the initial condition. The sum of the squares of $\tilde{r}_N\left(t_i;\{a_0^N, a_2^N, a_3^N, ..., a_N^N\}\right)$ can be formed as

$$
R_N\left(\{a_0^N, a_2^N, \ldots, a_N^N\}\right) = \sum_{i=1}^{M} \tilde{r}_N^{\,2}\left(t_i; \{a_0^N, a_2^N, a_3^N, \ldots, a_N^N\}\right)
$$

$$
= \sum_{i=1}^{M} \left(\begin{array}{l}
\int_{u=0}^{t_i} (a_0^N E_0 + E_{1,c3}(0,u) + a_2^N E_{2,c3}(0,u) + \ldots + a_N^N E_{N,c3}(0,u)) \\
\int_{v=0}^{t_i - u} [(a_0^N E_0 + E_{1,c1}(b,v) + a_2^N E_{2,c1}(b,v) + \ldots + a_N^N E_{N,c1}(b,v)) \\
(a_0^N E_0 + E_{1,c2}(w, t_i - u - v) + a_2^N E_{2,c2}(w, t_i - u - v) + \ldots + a_N^N E_{N,c2}(w, t_i - u - v)) \\
-(a_0^N E_0 + E_{1,c2}(b,v) + a_2^N E_{2,c2}(b,v) + \ldots + a_N^N E_{N,c2}(b,v)) \\
\quad (a_0^N E_0 + E_{1,c1}(w, t_i - u - v) + a_2^N E_{2,c1}(w, t_i - u - v) + \ldots + a_N^N E_{N,c1}(w, t_i - u - v))]dvdu \\
-\{\int_{u=0}^{t_i} (a_0^N E_0 + E_{1,c3}(b,u) + a_2^N E_{2,c3}(b,u) + \ldots + a_N^N E_{N,c3}(b,u)) \\
\int_{v=0}^{t_i - u} [(a_0^N E_0 + E_{1,c1}(0,v) + a_2^N E_{2,c1}(0,v) + \ldots + a_N^N E_{N,c1}(0,v)) \\
(a_0^N E_0 + E_{1,c2}(w, t_i - u - v) + a_2^N E_{2,c2}(w, t_i - u - v) + \ldots + a_N^N E_{N,c2}(w, t_i - u - v)) \\
-(a_0^N E_0 + E_{1,c2}(0,v) + a_2^N E_{2,c2}(0,v) + \ldots + a_N^N E_{N,c2}(0,v)) \\
(a_0^N E_0 + E_{1,c1}(w, t_i - u - v) + a_2^N E_{2,c1}(w, t_i - u - v) + \ldots + a_N^N E_{N,c1}(w, t_i - u - v))]dvdu \\
-\int_{u=0}^{t_i} (a_0^N E_0 + E_{1,c3}(w,u) + a_2^N E_{2,c3}(w,u) + \ldots + a_N^N E_{N,c3}(w,u)) \\
\int_{v=0}^{t_i - u} [(a_0^N E_0 + E_{1,c1}(0,v) + a_2^N E_{2,c1}(0,v) + \ldots + a_N^N E_{N,c1}(0,v))) \\
(a_0^N E_0 + E_{1,c2}(b, t_i - u - v) + a_2^N E_{2,c2}(b, t_i - u - v) + \ldots + a_N^N E_{N,c2}(b, t_i - u - v) \\
-(a_0^N E_0 + E_{1,c2}(0,v) + a_2^N E_{2,c2}(0,v) + \ldots + a_N^N E_{N,c2}(0,v)) \\
(a_0^N E_0 + E_{1,c1}(b, t_i - u - v) + a_2^N E_{2,c1}(b, t_i - u - v) + \ldots + a_N^N E_{N,c1}(b, t_i - u - v))]dvdu\}
\end{array} \right)^2
$$

$$
i = 1, 2, \ldots, M \qquad (5.17)
$$

Next, we formally minimize, with respect to each undetermined coefficient in the set, through

$$
\frac{\partial R_N}{\partial a_n^N}(\{a_0^N, a_2^N, a_3^N, \ldots, a_N^N\}) = 0, \quad n = 0, 2, 3, \ldots, N \qquad (5.18)
$$

Equation (5.18) forms a closed system of nonlinear equations involving N undetermined coefficients. To solve the N nonlinear system of equations for obtaining the N unknown coefficients, an appropriate numerical method can be used. After the N undetermined coefficients $\{a_0^N, a_2^N, a_3^N, \ldots, a_N^N\}$ are obtained, one can return to Eq. (5.14c) for the inverse heat conduction analysis. Two well-defined calibration tests are used in Eq. (5.14c) using the calculated coefficients $\{a_0^N, a_2^N, a_3^N, ..., a_N^N\}$ for predicting the transformed front surface temperature $\phi_r(0, t)$. Equation (5.14c) is a Volterra integral equation of the first kind for $\phi_r(0, t)$ which is ill-posed [67, 68]. A future-time method [47] is now introduced for stabilizing the first kind Volterra integral equation for the predicted surface temperature given in Eq. (5.14c). The implementation of the future-time [47] and numerical methods for predicting the transformed front surface temperature $\phi_r(0, t)$ is discussed in Section 5.3.

5.3 Regularization and numerical methods

For notational convenience, the implementation of the future-time method [3, 47, 64] and numerical method for estimating the transformed front surface temperature in reconstruction test denoted as $\phi_r(0, t)$ is illustrated by the calibration integral equation in the compact form given in Eqs. (5.11). Let's re-write the Eqs. (5.11) herein as

$$\int_{u=0}^{t} \phi_r(0,u) K(t-u) du = F(t), \quad t \geq 0 \tag{5.19a}$$

where the forcing function $F(t)$ and the convolution kernel $K(t-u)$ are defined as

$$\begin{aligned} F(t) = &\int_{u=0}^{t} \phi_r(b,u) \int_{v=0}^{t-u} \left(\phi_{c1}(0,v)\phi_{c2}(w,t-u-v) - \phi_{c2}(0,v)\phi_{c1}(w,t-u-v)\right) dv du \\ &- \int_{u=0}^{t} \phi_r(w,u) \int_{v=0}^{t-u} \left(\phi_{c1}(0,v)\phi_{c2}(b,t-u-v) - \phi_{c2}(0,v)\phi_{c1}(b,t-u-v)\right) dv du, \quad t \geq 0 \end{aligned} \tag{5.19b}$$

$$K(t-u) = \int_{v=0}^{t-u} \left(\phi_{c1}(b,v)\phi_{c2}(w,t-u-v) - \phi_{c2}(b,v)\phi_{c1}(w,t-u-v)\right) dv, \quad (t-u) \geq 0 \tag{5.19c}$$

Following the same procedure outlined in Section 4.3, the desired transformed front surface temperature prediction $\phi_{r,\gamma_m}(0,t)$ can be expressed as

$$\phi_{r,\gamma_m}(0,t_i)=\frac{F(t_i+\gamma_m)-\sum_{j=1}^{i-1}\phi_{r,\gamma_m}(0,t_j)\int_{u=t_{j-1}}^{t_j}K(b,t_i+\gamma_m-u)du}{\int_{u=t_i-1}^{t_i}K(b,t_i+\gamma_m-u)du+\int_{u=0}^{\gamma_m}K(b,\gamma_m-u)du},$$

$$i = 1, 2, \ldots, M - mM_f \quad (5.20)$$

Equation (5.20) shows that the discrete values of the predicted transformed front surface temperature prediction $\phi_{r,\gamma_m}(0,t_i)$ are calculated by time marching. The future-time parameter is chosen as $\gamma \to \gamma_m = mM_f\Delta t$ where m is a positive integer, and Δt is given as $\Delta t = t_{max}/M$. Here, M is the number of data in the discretized time domain beyond the initial condition, and M_f is a convenient multiplying factor that allows for computational flexibility.

5.4 Phase plane and cross-correlation analyses for estimating the optimal future-time parameter

Following Chapter 3, a phase plane and cross-correlation analyses based on surface temperature and surface temperature rate are applied for estimating the optimal future-time parameter. Again, the phase plane is obtained by plotting the discrete surface temperature rate, dT/dt in the y-axis against the surface temperature, T in the x-axis. The surface temperature cross-correlation coefficient is given as [56, 75, 76]

$$R_T(T_{r,\gamma_m},T_{r,\gamma_{m+1}})=\frac{\sum_{i=1}^{M-PM_f}T_{r,\gamma_m}(0,t_i)T_{r,\gamma_{m+1}}(0,t_i)}{\sqrt{\sum_{i=1}^{M-PM_f}\left(T_{r,\gamma_m}(0,t_i)\right)^2\sum_{i=1}^{M-PM_f}\left(T_{r,\gamma_{m+1}}(0,t_i)\right)^2}},$$

$$i=1,2,\ldots,M-PM_f;\ m=p,\ p+1,\ldots,p-1+P \qquad (5.21a)$$

while the surface temperature rate cross-correlation coefficient is given as [56, 75, 76]

$$R_{\dot{T}}(\dot{T}_{r,\gamma_m}, \dot{T}_{r,\gamma_{m+1}}) = \frac{\sum_{i=1}^{M-PM_f} \dot{T}_{r,\gamma_m}(0,t_i)\dot{T}_{r,\gamma_{m+1}}(0,t_i)}{\sqrt{\sum_{i=1}^{M-PM_f}\left(\dot{T}_{r,\gamma_m}(0,t_i)\right)^2 \sum_{i=1}^{M-PM_f}\left(\dot{T}_{r,\gamma_{m+1}}(0,t_i)\right)^2}},$$

$$i = 1, 2, \ldots, M - PM_f; m = p, p+1, \ldots, p-1+P \qquad (5.21b)$$

where $\gamma_m = mM_f\Delta t$ (s), $m = p, p+1, \ldots, p-1+P$, p is the 1st m value and P is the number of values in γ spectrum. Here, $M_f\,\Delta t$ is the stepping time for forming a finite set of predictions since Δt is the sampling time.

5.5 Results

5.5.1 Data collection for inverse simulation

Numerical simulation is called upon for generating artificial data for the inverse analysis. To do this, a direct nonlinear heat conduction problem is solved based on given auxiliary conditions. This allows for in-depth probe data to be synthesized. The schematic for the one-dimensional heat conduction problem with two in-depth thermocouples is displayed in Fig. A-5.1. The thickness of the one-dimensional slab is L. In a physical context, let an idealized thin film thermocouple be placed at $x = 0$. Two in-depth thermocouples are located at $x = b$ and $x = w$, respectively. The front ($x = 0$) and back ($x = L$) surfaces of the slab are subjected to heat fluxes denoted by $q_0''(t)$ and $q_L''(t)$, respectively. The imposed heat fluxes $q_0''(t)$ and $q_L''(t)$ can be composed of various heat transfer modes involving conduction, convection, radiation. For the present context, the conductive (net) heat fluxes at front and back surfaces are given by $q''(0,t) = q_0''(t)$ and $q''(L,t) = q_L''(t)$. The host material for the one-dimensional slab for simulation is stainless steel 304. The thermophysical properties of the stainless steel 304 [80], as well as the geometrical properties for the simulation, are given in Table A-5.2. Figures A-5.2a-c display the temperature-dependent thermal conductivity, $k(T)$, specific heat, $c(T)$ and thermal diffusivity, $\alpha(T) = k(T)/(\rho c(T))$ over a large temperature range. In order to emulate nonlinear effects in a surface heating experiment, the simulation covers a large temperature range. The numerical simulations presented in this chapter are performed using MATLAB R2016a on a Lenovo Thinkpad T530 laptop.

The two-probe calibration equation is used in situations where the back surface boundary condition influences the overall heat transfer or when the back surface boundary condition changes drastically between the calibration campaign and reconstruction test. The estimated thermal penetration time from the front to the back surface based on room temperature evaluated properties is 2 seconds. The simulations provided in this study run to 60 seconds indicating that the back surface boundary condition influences the system. In this context, three calibration tests denoted as "c1", "c2" and "c3" are required for estimating the undetermined coefficients $\{a_0^N, a_2^N, a_3^N, ..., a_N^N\}$ in Eq. (5.15). The calculated coefficients $\{a_0^N, a_2^N, a_3^N, ..., a_N^N\}$ together with the data from calibration test 1 ("c1"), test 2 ("c2") and in-depth thermocouple data in the reconstruction test are incorporated into Eq. (5.14c) for the inverse analysis to verify the two-probe surface temperature prediction approach. In calibration test 1, the front and back surface heat fluxes are fixed at constant values denoted as $q''_{0,c1,\max}$ and $q''_{L,c1,\max}$. In calibration test 2, the front surface heat flux is $q''_{0,c2,\max}$ at $t \in [0, t_{\max}/2]$ s and $q''_{0,c2,\max}/2$ at $t \in (t_{\max}/2, t_{\max}]$ s while the back surface boundary condition is idealized as adiabatic. In calibration test 3, the front surface heat flux is $q''_{0,c3,\max}$ at $t \in [0, t_{\max}/5]$ s and $q''_{0,c3,\max}/2$ at $t \in (t_{\max}/5, t_{\max}]$ s while the back surface boundary condition is a constant value at $q''_{L,c3,\max}$. The front surface heat flux in the reconstruction test is a double Gaussian function defined as

$$q''_s(t) = q''(0,t) = q''_{r,\max}\left(e^{-\frac{(t-\beta_1)^2}{\sigma_1^2}} + 0.75e^{-\frac{(t-\beta_2)^2}{\sigma_2^2}}\right),\ t \in [0, t_{\max}] \tag{5.22}$$

while the back surface heat flux in the reconstruction test is a linear function from 0 to $-q''_{L,r,\max}$ at $t \in [0, t_{\max}]$ s. The values for the parameters, β_1, β_2, σ_1, σ_2 are given in Table A-5.2. The imposed front and back surface heat fluxes for the calibration tests "c1", "c2", "c3" and the reconstruction test "r" are shown in Figs. A-5.3a, b. An implicit finite difference method, using a one-time step lag evaluation of the thermophysical properties, is applied for numerically solving the direct heat conduction problems. The transient temperature responses at $x = 0$, b, w and L in the calibration tests "c1", "c2", "c3" and the reconstruction test "r" are obtained and displayed in Figs. A-5.4a-d. The convergence of the implicit finite difference method has been verified and shown by plotting the positional temperature at $x = b$, $T_r(b, t_i)$ in the reconstruction test obtained by $(\Delta x, \Delta t)$ and $(\Delta x/2, \Delta t/2)$, respectively. The convergence plot is displayed in Fig. A-5.5. The maximum relative difference between $T_r(b, t_i)$ obtained by $(\Delta x, \Delta t)$ and $(\Delta x/2, \Delta t/2)$ is 0.0662%. In this chapter, all data generated are obtained by the proposed finite difference method with the temporal and spatial widths given by $(\Delta x, \Delta t)$.

Artificial noise is added to the positional front surface temperatures in the three calibration tests as well as the positional temperatures at $x = b$ and $x = w$ obtained by the finite difference method in the three calibration tests and the reconstruction test. Noisy data for surface temperature and in-depth temperatures are generated through

$$T_{noise,c}(0,t_i) = T_c(0,t_i)(1+\varepsilon_q r_{i,j}),\ \ t_i = i\Delta t,\, i = 0, 1, \dots, M \tag{5.23a}$$

$$T_{tc,c}(b,t_i) = T_c(b,t_i)(1+\varepsilon_T r_{i,j}),\ \ t_i = i\Delta t,\, i = 0, 1, \dots, M \tag{5.23b}$$

$$T_{tc,c}(w,t_i) = T_c(w,t_i)(1+\varepsilon_T r_{i,j}),\ \ t_i = i\Delta t,\, i = 0, 1, \dots, M \tag{5.23c}$$

$$T_{tc,r}(b,t_i) = T_r(b,t_i)(1+\varepsilon_T r_{i,j}),\ \ t_i = i\Delta t,\, i = 0, 1, \dots, M \tag{5.23d}$$

$$T_{tc,r}(w,t_i) = T_r(w,t_i)(1+\varepsilon_T r_{i,j}),\ \ t_i = i\Delta t,\, i = 0, 1, \dots, M \tag{5.23e}$$

where ε_q and ε_T denote noise factors, subscript "c" denotes the three calibration tests in general, and $r_{i,j}$, i = 0, 1, … , M are random numbers drawn from the interval [-1,1] obtained by the MATLAB command "2(*rand*-0.5)" for each noise addition case of temperature (subscript "j" is used to denote these cases). Equations (5.23a-e) are used to independently generate noisy data sets for all tests. The values for noise factors ε_q and ε_T are given in Table A-5.2. The uncorrupted positional and noise added temperature data at x = 0, b and w in the calibration tests 1, 2, 3 and at x = b and w in the reconstruction test are displayed in Figs. A-5.6a-d, respectively. The values for noise factors ε_q and ε_T are set as 0.01 which implies 1% relative noise. All parameters used for the numerical simulation are listed in Table A-5.2.

5.5.2 Inverse simulation using noiseless data

In this section, the noiseless front surface and in-depth (x = b and x = w) temperatures in the three calibration tests, as well as the noiseless in-depth temperature in the reconstruction test, are used for verifying the proposed numerical procedure for the two-probe surface temperature calibration integral equation method. In this context, the positional temperatures displayed in Figs. A-5.4a-d are used as noiseless "thermocouple" data for the simulation. Using noiseless data permits evaluating the numerical methods without considering the instability effects introduced by noise.

To begin, the undetermined expansion coefficients $\{a_0^N, a_2^N, a_3^N, ..., a_N^N\}$ in Eq. (5.15) are estimated by the nonlinear least-squares method discussed in Section 5.2. The noiseless "thermocouple" data (positional temperature at x = 0, b and w obtained by the implicit finite difference method) in the three calibration tests are denoted as $T_{c1}(0, t_i)$, $T_{c2}(0, t_i)$, $T_{c3}(0, t_i)$, $T_{c1}(b, t_i)$, $T_{c2}(b, t_i)$, $T_{c3}(b, t_i)$, $T_{c1}(w, t_i)$, $T_{c2}(w, t_i)$ and $T_{c3}(w, t_i)$, $t_i = i\Delta t$, $i = 1, 2, \dots, M$. These data are then substituted into Eq. (5.15). The positional temperatures and noiseless thermocouple temperatures are assumed identical implying that sensor delay and attenuation effects are not considered in the numerical simulation. The chosen sampling frequency is 50 Hz which indicates Δt = 0.02 s. Next, the discrete residual function $\tilde{r}_N\left(t_i; \{a_0^N, a_2^N, a_3^N, ..., a_N^N\}\right)$, $i = 1, 2, \dots, M$ in Eq. (5.16) is obtained using a trapezoidal integration rule [79]. The undetermined coefficients $\{a_0^N, a_2^N, a_3^N, ..., a_N^N\}$ are symbolically calculated by the MATLAB function "*lsqnonlin*". An initial guess for the undetermined coefficients $\{a_0^N, a_2^N, a_3^N, ..., a_N^N\}$ is required for the MATLAB command "*lsqnonlin*". The trivial value of 0 is used as the initial guess for all undetermined coefficients.

The optimal choice for the number of the undetermined coefficients N needs to be chosen in some manner. In addition, after determining the coefficients $\{a_0^N, a_2^N, a_3^N, ..., a_N^N\}$ by the least-squares method, the balance of Eq. (5.15) needs to be verified. The left-hand side and first term on the right-hand side of Eq. (5.15) as a function of discrete time $t_i = i\Delta t$, i = 1, 2, … , M can be plotted in the same figure. The discrete version of Eq. (5.15) can be expressed as

$$G_{LHS,N}(t_i) = G_{RHS,N}(t_i) + \tilde{r}_N\left(t_i; \{a_0^N, a_2^N, a_3^N, ..., a_N^N\}\right), \qquad t_i = i\Delta t, \quad i = 1, 2, \ldots, M$$

(5.24a) where

$$\begin{aligned}
&G_{LHS,N}(t_i) \\
&= \int_{u=0}^{t} (a_0^N E_0 + E_{1,c3}(0,u) + a_2^N E_{2,c3}(0,u) + ... + a_N^N E_{N,c3}(0,u)) \\
&\int_{v=0}^{t-u} [(a_0^N E_0 + E_{1,c1}(b,v) + a_2^N E_{2,c1}(b,v) + ... + a_N^N E_{N,c1}(b,v)) \\
&(a_0^N E_0 + E_{1,c2}(w,t-u-v) + a_2^N E_{2,c2}(w,t-u-v) + ... + a_N^N E_{N,c2}(w,t-u-v)) \\
&-(a_0^N E_0 + E_{1,c2}(b,v) + a_2^N E_{2,c2}(b,v) + ... + a_N^N E_{N,c2}(b,v)) \\
&\quad (a_0^N E_0 + E_{1,c1}(w,t-u-v) + a_2^N E_{2,c1}(w,t-u-v) + ... + a_N^N E_{N,c1}(w,t-u-v))] dv du
\end{aligned}$$

$$i = 1, 2, \ldots, M \quad (5.24b)$$

and

$$
\begin{aligned}
&G_{RHS,\,N}(t_i) \\
&= \int_{u=0}^{t} (a_0^N E_0 + E_{1,\,c3}(b,u) + a_2^N E_{2,\,c3}(b,u) + ... + a_N^N E_{N,\,c3}(b,u)) \\
&\int_{v=0}^{t-u} [(a_0^N E_0 + E_{1,\,c1}(0,v) + a_2^N E_{2,\,c1}(0,v) + ... + a_N^N E_{N,\,c1}(0,v)) \\
&(a_0^N E_0 + E_{1,\,c2}(w,t-u-v) + a_2^N E_{2,\,c2}(w,t-u-v) + ... + a_N^N E_{N,\,c2}(w,t-u-v)) \\
&-(a_0^N E_0 + E_{1,\,c2}(0,v) + a_2^N E_{2,\,c2}(0,v) + ... + a_N^N E_{N,\,c2}(0,v)) \\
&(a_0^N E_0 + E_{1,\,c1}(w,t-u-v) + a_2^N E_{2,\,c1}(w,t-u-v) + ... + a_N^N E_{N,\,c1}(w,t-u-v))]dvdu \\
&-\int_{u=0}^{t} (a_0^N E_0 + E_{1,\,c3}(w,u) + a_2^N E_{2,\,c3}(w,u) + ... + a_N^N E_{N,\,c3}(w,u)) \\
&\int_{v=0}^{t-u} [(a_0^N E_0 + E_{1,\,c1}(0,v) + a_2^N E_{2,\,c1}(0,v) + ... + a_N^N E_{N,\,c1}(0,v))) \\
&(a_0^N E_0 + E_{1,\,c2}(b,t-u-v) + a_2^N E_{2,\,c2}(b,t-u-v) + ... + a_N^N E_{N,\,c2}(b,t-u-v) \\
&-(a_0^N E_0 + E_{1,\,c2}(0,v) + a_2^N E_{2,\,c2}(0,v) + ... + a_N^N E_{N,\,c2}(0,v)) \\
&(a_0^N E_0 + E_{1,\,c1}(b,t-u-v) + a_2^N E_{2,\,c1}(b,t-u-v) + ... + a_N^N E_{N,\,c1}(b,t-u-v))]dvdu
\end{aligned}
$$

$i = 1, 2, \ldots, M$ (5.24c)

The balance can be visualized by plotting $G_{\mathrm{LHS},\,\mathrm{N}}(t_i)$ and $G_{\mathrm{RHS},\,\mathrm{N}}(t_i)$ over time. This effectively illustrates the smallness of the residual $\tilde{r}_N\left(t_i;\{a_0^N, a_2^N, a_3^N, ..., a_N^N\}\right)$ given in Eq. (5.24a).

To illustrate, let us begin by using a 6th order (N = 6) Chebyshev expansion. The undetermined coefficients $\{a_0^6, a_2^6, a_3^6, ..., a_6^6\}$ are calculated by the least-squares method and listed in column 2 of Table A-5.3. Figure A-5.7a displays $G_{\mathrm{LHS},\,6}(t_i)$ and $G_{\mathrm{RHS},\,6}(t_i)$ as defined in Eqs. (5.24b, c) when N = 6. In Fig. A-5.7a, the discrepancy between $G_{\mathrm{LHS},\,6}(t_i)$ and $G_{\mathrm{RHS},\,6}(t_i)$ can be observed. This imbalance implies that the 6th order truncation for the Chebyshev expansion is a poor choice for representing the transformed variable $\phi(T)$. Next, consider a 5th order (N = 5) Chebyshev expansion. A time sequential study using subsets of the total available data in the time interval $t \in [0, t_{\max}]$ is performed for demonstrating the stability of the coefficients [96]. The times 54s, 48s, 42s as well as the total data collection time t_{max} = 60s are used in the sequential study for checking whether the expansion coefficients calculated by the least-squares method replicate. Table A-5.4 provides the calculated expansion coefficients $\{a_0^5, a_2^5, a_3^5, \ldots, a_5^5\}$ based on the data collection times 60s, 54s, 48s, and 42s. As shown in Table A-5.4, sequential consistency of the calculated expansion coefficients $\{a_0^5, a_2^5, a_3^5, \ldots, a_5^5\}$ is achieved based on different data collection times. Figure A-5.7b illustrates the balance verification between $G_{\mathrm{LHS},\,5}(t_i)$ and $G_{\mathrm{RHS},\,5}(t_i)$ is obtained. Figure A-5.8 displays the transformed variable $\phi(T)$ as a function of temperature defined in Eq. (5.13a) in the temperature range [293.15, 1400] K using the calculated coefficients $\{a_0^5, a_2^5, a_3^5, \ldots, a_5^5\}$ as listed in column 4 of Table A-5.3. Based on the discussion above, the 5$^{\text{th}}$ order (N = 5) Chebyshev expansion is chosen for representing $\phi(T)$ as defined in Eq. (5.13a) in this section. The corresponding coefficients $\{a_0^5, a_2^5, a_3^5, \ldots, a_5^5\}$ are listed in column 3 of Table A-5.3.

The transformed front surface temperature in the reconstruction test $\phi_r(T)$ can now be estimated using Eq. (5.20). The calibration tests are designated as c1 and c2 and their corresponding imposed front and back surface heat fluxes are displayed in Fig. A-5.3a. These two cases are chosen as the calibration tests for the inverse study. The imposed front and back surface heat fluxes in the reconstruction test are shown in Fig. A-5.3b. Following the procedure previously discussed, the transformed front surface temperature prediction $\phi_{r,\gamma_m}(0, t_i)$ can be calculated by Eq. (5.20) for each fixed future-time parameter γ_m. A numerical root-finder is applied for obtaining the surface temperature at x = 0 in the reconstruction test denoted as $T_{r,\gamma_m}(0,t_i)$ using $\phi_{r,\gamma_m}(0,t_i)$, $t_i = i\Delta t$, i = 0, 1, … , $M - mM_f$ through Eq. (5.12) and Eqs. (5.13a, b). More specifically, common order terms in the Chebyshev expansion shown in Eq. (5.13a) are collected by the calculated coefficients $\{a_0^N, a_2^N, a_3^N, ..., a_N^N\}$ with $a_1^N = 1$ for forming a monomial based polynomial on the order of the predicted mapped surface temperature denoted as $T^*_{r,\gamma_m}(0,t_i)$, $t_i = i\Delta t$, i = 0, 1, … , $M - mM_f$. The MATLAB function "*roots*" for finding roots of monomial based polynomials is applied for calculating $T^*_{r,\gamma_m}(0,t_i)$, $t_i = i\Delta t$, i = 0, 1, … , $M - mM_f$. Multiple roots including complex numbers can be observed. The unfavorable roots are eliminated by setting the limit range of roots as $T^*_{r,\gamma_m}(0,t_i) \in [-1,1]$. In the end, the surface temperature in the reconstruction test denoted as $T_{r,\gamma_m}(0,t_i)$ can be obtained by inverting $T^*_{r,\gamma_m}(0,t_i)$, $t_i = i\Delta t$, i = 0, 1, … , $M - mM_f$, per Eq. (5.12).

Figure A-5.9 displays a comparison between the surface temperature prediction $T_{r,\gamma_m}(0,t_i)$ using the nonlinear model discussed in this chapter and the surface temperature prediction $T_{r,\gamma_m}(0,t_i)$ based on the linear two-probe calibration integral equation given in Eq. (5.2). The future-time parameter used for both the nonlinear and the linear models is γ_m = 0.6 s. By comparing to the exact surface temperature $T_r(0, t)$, the standard derivation of the surface temperature prediction $T_{r,\gamma_m}(0,t_i)$ by using the linear model and the nonlinear model are 6.87 K and 4.74 K, respectively. This indicates the standard derivation of the surface temperature prediction decreases 31% by using the nonlinear model instead of the linear model. Figure A-5.10 illustrates a comparison of the absolute error between surface temperature prediction $T_{r,\gamma_m}(0,t_i)$ by the nonlinear model and the linear model when γ_m = 0.6 s. The two-probe surface heat flux prediction results [97] display more distinction between nonlinear and linear model than the two-probe surface temperature problem. For the two-probe surface temperature estimation, the nonlinear model will produce significantly better surface temperature predictions than the linear model for some aerospace materials possessing highly temperature-dependent thermophysical properties.

In this section, a feasible numerical method for resolving the nonlinear inverse heat conduction problem has been demonstrated for the two-probe surface temperature estimation problem based on noiseless data.

5.5.3 Inverse simulation using noisy data

In this section, noise is added to the front surface temperature in the three calibration tests $T_{tc,c1}(0,t_i)$, $T_{tc,c2}(0,t_i)$, $T_{tc,c3}(0,t_i)$ as shown in Figs. A-5.6a-c. Figures A-5.6a-d display the noisy in-depth "thermocouple" data $\{T_{tc,c1}(b, t_i), T_{tc,c1}(w, t_i)\}$, $\{T_{tc,c2}(b, t_i), T_{tc,c2}(w, t_i)\}$, $\{T_{tc,c3}(b, t_i), T_{tc,c3}(w, t_i)\}$, $\{T_{tc,r}(b, t_i), T_{tc,r}(w, t_i)\}$ that are used in the numerical simulation. Surface temperature phase plane and cross-correlation analyses per Eqs. (5.21a, b) are applied for estimating the optimal future-time parameter, γ_{opt}. Table A-5.5 lists the numerically calculated expansion coefficients $\{a_0^N, a_2^N, a_3^N, ..., a_N^N\}$ for various N based on noisy data that are acquired using a 50 Hz sampling frequency. Figure A-5.11 shows the imbalance between $G_{\mathrm{LHS},\,6}(t_i)$ and $G_{\mathrm{RHS},\,6}(t_i)$ in the presence of noisy data and

$\{a_0^6, a_2^6, a_3^6, \ldots, a_6^6\}$ are listed in column 2 of Table A-5.5. This displayed imbalance implies that the 6th order truncation is a poor choice for the Chebyshev expansion and therefore it is removed from further consideration. Next, consider a 5th order (N = 5) Chebyshev expansion. Table A-5.6 show the sequential time study for the calculated expansion coefficients $\{a_0^N, a_2^N, a_3^N, \ldots, a_N^N\}$ when N = 5. In this case, sequential stability is achieved. Figure A-5.12 displays the balance between $G_{\mathrm{LHS},\,5}(t_i)$ and $G_{\mathrm{RHS},\,5}(t_i)$ as defined by Eqs. (5.24b, c) by using noisy data and the coefficients $\{a_0^5, a_2^5, a_3^5, a_4^5, a_5^5\}$ as listed in column 3 of Table A-5.5. Therefore, the 5th order (N = 5) Chebyshev expansion and its corresponding expansion coefficients $\{a_0^5, a_2^5, a_3^5, a_4^5, a_5^5\}$ are used in this section for representing the transformed variable $\phi(T)$ defined in Eq. (5.13a). Figure A-5.13 shows the transformed variable $\phi(T)$ as a function of temperature defined in Eq. (5.13a) in the temperature range [293.15, 1400] K.

The front surface temperature in the reconstruction test can be estimated by the procedure discussed in Section 5.3 with a chosen future-time parameter γ leading to the approximation $T_{r,\gamma}(0,t)$. A spectrum of future-time parameters γ_m's are developed and the phase plane and cross-correlation analyses discussed in Section 5.4 are applied for estimating the optimal future-time parameter γ_{opt}. Figure A-5.14a shows the predicted surface temperature rate $\dot{T}_{r,\gamma_m}(0,t_i)$ and predicted surface temperature $T_{r,\gamma_m}(0,t_i)$ phase plane when $\gamma_m = M_f\, m\Delta t$ for m = 9, 10, … , 16, M_f = 5, Δt =0.02 s while Fig. A-5.14b displays a zoomed in version of Fig. A-5.14a with m = 9, 10, … , 16.

In Fig. A-5.14a, a random pattern is observed for small γ's ($\gamma < 1.0$ s). As the future-time parameter γ_m increases to 1.4 s, randomness is substantially reduced and the corresponding phase plane exhibits a distinctive pattern. The onset of a pattern defines the transition region where the balance between stability and accuracy is achieved in the surface temperature prediction. In Fig. A-5.14b, one can qualitatively see that the onset of a pattern occurs in the interval $\gamma \in [1.5, 1.6]\ \mathrm{s}$. Highly smoothed surface temperature rate and surface temperature predictions are observed when $\gamma \in [1.5, 1.6]\ \mathrm{s}$. In order to recover small temporal changes in the predicted surface temperature, it is favorable to retain as many high-frequency components in the signal. Therefore, surface temperature predictions using $\gamma \in [1.5, 1.6]\ \mathrm{s}$ or greater are removed from further consideration due to over-smoothing. The surface temperature rate and surface temperature phase plane in Figs. A-5.14a, b provide the initial qualitative perspective for extracting the optimal future-time parameter.

Figure A-5.15 illustrates the cross-correlation coefficients phase plane. This phase plane is defined in terms of the surface temperature cross-correlation coefficient $R_T(T_{r,\gamma_m}, T_{r,\gamma_{m+1}})$ and surface temperature rate cross-correlation coefficient $R_{\dot{T}}(\dot{T}_{r,\gamma_m}, \dot{T}_{r,\gamma_{m+1}})$ as given in Eqs. (5.21a, b). Three defined regions (unstable, transition and over-smoothed) that are discussed in the Figs. A-5.14a, b are described in an alternative way in Fig. A-5.16. In Fig. A-5.16, γ pairs (0.9, 1.0) s to (1.5, 1.6) s are defined. Small values of $R_T(T_{r,\gamma_m}, T_{r,\gamma_{m+1}})$ and $R_{\dot{T}}(\dot{T}_{r,\gamma_m}, \dot{T}_{r,\gamma_{m+1}})$ equate to highly random or uncorrelated predictions. As γ increases to 1.5,

$R_{\dot{T}}(\dot{T}_{r,\gamma_m}, \dot{T}_{r,\gamma_{m+1}})$ climbs toward unity. Unity on the $R_T(T_{r,\gamma_m}, T_{r,\gamma_{m+1}})$ is more readily available or desirable than $R_{\dot{T}}(\dot{T}_{r,\gamma_m}, \dot{T}_{r,\gamma_{m+1}})$. As previously noted, approaching unity on the vertical axis should be physically avoided as numerical differentiation is a roughening operation. Hence, it makes no sense to expect or desire unity. In this study, γ = 1.4s is chosen as the γ pair (1.4, 1.5) s lies closest to the experienced-based, cut-off line. This choice of γ_{opt} = 1.4s retains sufficient high-frequency content in the signal that balances stability and accuracy. The cut-off line could also be placed at $R_{\dot{T}}(\dot{T}_{r,\gamma_m}, \dot{T}_{r,\gamma_{m+1}})$ as indicated by experiments. Figure A-5.16 displays the predicted surface temperature, $T_{r,\gamma_m}(0,t_i)$ over the future-time spectrum $\gamma_m = M_f\, m\Delta t$, m = 9 – 16, M_f = 5, Δt =0.02 s. Figure A-5.17 compares the surface temperature, $T_{r,\gamma}(0,t_i)$ to the exact $T_r(0,t)$ when γ_{opt} = 1.4 s. Highly favorable results are produced in light of the significant amount of noise contained in the surface temperatures and the "thermocouple" data for the calibration tests (Figs. A-5.6a-c) and in the "thermocouple" data for the reconstruction test (Fig. A-5.6d). It is worth noting that the two-probe calibration integral equation method developed in this chapter not only works for predicting the front surface temperature in case of back surface cooling but also works in case of back surface heating.

5.6 Conclusions

In this chapter, a nonlinear two-probe calibration integral equation method (CIEM) is proposed and numerically verified for resolving a nonlinear inverse heat conduction problem requiring the resolution of the surface temperature having a time-varying back surface boundary condition. Phase plane and cross-correlation analyses are employed for estimating the optimal future-time parameter from a spectrum of chosen values. Numerical simulations using stainless steel as host material yield excellent surface temperature predictions.

Chapter 6: Concluding Remarks and Future Works

In this dissertation, one-probe and two-probe calibration integral equations are developed for resolving nonlinear inverse heat conduction problems involving the reconstruction of the surface temperature and net surface heat flux. The calibration integral equation method is a "parameter free" approach that does not require the specification of sensor locations, sensor parameters and temperature-dependent thermophysical properties of the host material. Phase plane and cross-correlation analyses have been verified as an effective metric for estimating the optimal regularization parameter for both the "parameter free" and the "parameter required" methods. Several new findings have been developed and reported that will impact the inverse heat conduction community.

6.1 Concluding remarks

Chapter 2 demonstrates a space marching method for resolving the surface temperature and net surface heat flux in a nonlinear inverse heat conduction problem. A low-pass Gauss filter is introduced for filtering the noisy in-depth "thermocouple" data. This filter contains a parameter called the "cut-off frequency". The cut-off frequency is the regularization parameter for this study. Numerical results indicate the robustness of the Gauss filter and the feasibility of the phase plane and cross-correlation analyses for extracting the optimum cut-off frequency.

Chapter 3 describes the development of a one-probe "parameter free" inverse heat conduction approach for resolving the surface temperature in a one-dimensional geometry where the host material possesses temperature-dependent thermophysical properties. The calibration integral equation method (CIEM) framework is extended to accommodate such a physical formulation. The formulation and numerical procedure are clearly described indicating the merit of the method. This procedure includes numerical implementation, regularization and the optimal determination of truncation order of the applied first Chebyshev expansion for approximating the property transform function as well as the value of regularization parameter (future-time parameter). This preliminary chapter focused on the situation where the back surface boundary condition remained adiabatic for both the calibration and reconstruction tests. The highly favorable results from this study motivated the generalizations described in Chapters 4 and 5 where the constraint of adiabatic back surface boundary condition is removed. Chapters 4 and 5 describe the reconstruction of the surface temperature and net heat flux, respectively, in the context of nonlinear two-probe inverse heat conduction problems. A clear and new methodology is described in these chapters. The major contributions of this dissertation are:

1) Developed and expanded phase plane and cross-correlation analyses for estimating regularization parameters in both "parameter required" and "parameter free" techniques for inverse heat conduction problems.
2) Introduced a well-conditioned expansion required for representing the property transform function, ϕ. The Chebyshev expansion of the first kind substantially reduces ill-conditioning effects in the least-squares procedure described in Chapters 3-5.
3) Proposed and demonstrated the use of sequential time studies for identifying the optimal truncation order of the Chebyshev expansion used for representing the transform function, ϕ in the linearization process.

4) Developed an effective numerical code in MATLAB for resolving the nonlinear least-squares problems needed for determining the expansion coefficients in the Chebyshev expansion.
5) Generalized the calibration integral equation method to two-probe studies involving nonlinear inverse heat conduction.

6.2 Future works

This dissertation focused on model development for a "parameter free" inverse heat conduction method based on calibration principles. Additionally, some constraints were imposed that should be relaxed for a large class of problems. Furthermore, experimental studies for validating the proposed calibration method should be performed and reported in future publications. The suggestions for future research are list below:

1) Remove the present assumption $\alpha(T) \rightarrow \alpha_0$ (see Eq. (3.5)) and form the next level of approximation and analysis.
2) Study non-traditional bases functions for representing the property transform function (example: radial basis function).
3) Develop analysis for uncertainty propagation.
4) Develop a small sample, rapid turn around experimental platform for surface heat flux and temperature reconstruction studies. This would be useful for both "parameter required" and "parameter free" methods. Instrumentation and sources would be of calibration quality. This would require incorporating experimental design concepts in the source evaluation.
5) Experimentally validate the proposed space marching method (Chapter 2) and the

calibration integral equation approach (Chapters 3-5) using a variety of engineering and aerospace materials at elevated temperatures.

6) Further verify the effectiveness of the phase plane and cross-correlation analyses as a general statistical tool for determining optimal regularization parameters when using different techniques for resolving inverse heat conduction problems (for example, TSVD).

List of References

[1] J.V. Beck, B. Blackwell, C.R.S. Clair Jr, Inverse Heat Conduction: Ill-Posed Problems, John Wiley & Sons, New York, 1985.

[2] J. Frankel, B. Elkins, M. Keyhani, Rate-based sensing concepts for heat flux and property estimation; and, transition detection, in: 16th AIAA/DLR/DGLR International Space Planes and Hypersonic Systems and Technologies Conference, Bremen, Germany, 2009, pp. 7303.

[3] J.I. Frankel, M. Keyhani, B.E. Elkins, Surface heat flux prediction through physics-based calibration, part 1: theory, J. Thermophys Heat Transfer, 27(2) (2013) 189-205.

[4] K.A. Woodbury, Effect of thermocouple sensor dynamics on surface heat flux predictions obtained via inverse heat transfer analysis, Int. J. Heat Mass Transfer, 33(12) (1990) 2641-2649.

[5] F.K. Lu, Marren, D, Advanced Hypersonic Test Facilities, American Institute of Aeronautics and Astronautics, Inc., Reston, Virginia, 2002.

[6] V.A. Figueroa, J.T. Nakos, J.E. Murphy, Uncertainty analysis of heat flux measurements estimated using one-dimensional inverse heat conduction program, Sandia Report, SAND2005-0039. Sandia National Laboratory, New Mexico, 2005.

[7] M.R. Golriz, B. Sundén, A method for temperature measurements in circulating fluidized bed combustors, Exp. Therm Fluid Sci., 9(3) (1994) 274-282.

[8] M. Heitor, A. Moreira, Thermocouples and sample probes for combustion studies, Prog. Energy Combust. Sci., 19(3) (1993) 259-278.

[9] D. Meresse, S. Harmand, M. Siroux, M. Watremez, L. Dubar, Experimental disc heat flux identification on a reduced scale braking system using the inverse heat conduction method, Appl. Therm. Eng., 48 (2012) 202-210.

[10] Y.-C. Yang, W.-L. Chen, A nonlinear inverse problem in estimating the heat flux of the disc in a disc brake system, Appl. Therm. Eng., 31(14) (2011) 2439-2448.

[11] T.K.G. Howse, R. Kent, H. Rawson, Determination of glass-mould heat fluxes from mould temperature measurements, Glass Technol., 12(4) (1971).

[12] S.G. Chen, C.I. Weng, J.M. Lin, Inverse estimation of transient temperature distribution in the end quenching test, J. Mater. Process. Technol., 86(1-3) (1999) 257-263.

[13] D. France, T. Chiang, Analytic solution to inverse heat conduction problems with periodicity, J. Heat Transfer, 102(3) (1980) 579-581.

[14] B.S. Elkins, Challenges for the accurate determination of the surface thermal condition via in-depth sensor data, Ph.D. Dissertation, The University of Tennessee at Knoxville, 2011.

[15] O. Burggraf, An exact solution of the inverse problem in heat conduction theory and applications, J. Heat Transfer, 86(3) (1964) 373-380.

[16] A.S. Carasso, Space marching difference schemes in the nonlinear inverse heat conduction problem, Inverse Prob., 8(1) (1992) 25-43.

[17] A.S. Carasso, Slowly divergent space marching schemes in the inverse heat conduction problem, Numer. Heat Transfer, Part B, 23(1) (1993) 111-126.

[18] N. Dsouza, Numerical solution of one-dimensional inverse transient heat conduction by finite difference method, in: ASME Winter Annual Meeting, Houston, Texas, 1975.

[19] R. Hills, E. Hensel Jr, One-dimensional nonlinear inverse heat conduction technique, Numer. Heat Transfer, Part A, 10(4) (1986) 369-393.

[20] J. Taler, A new space marching method for solving inverse heat conduction problems, Forsch. Ingenieurwes., 64(11) (1999) 296-306.

[21] J. Beck, Calculation of surface heat flux from an internal temperature history, ASME paper, 62 (1962).

[22] J. Beck, B. Blackwell, A. Haji-Sheikh, Comparison of some inverse heat conduction methods using experimental data, Int. J. Heat Mass Transfer, 39(17) (1996) 3649-3657.

[23] J.V. Beck, Filter solutions for the nonlinear inverse heat conduction problem, Inverse Prob. Sci. Eng., 16(1) (2008) 3-20.

[24] B.S. Elkins, M. Keyhani, J. Frankel, Global time method for inverse heat conduction problem, Inverse Prob. Sci. Eng., 20(5) (2012) 651-664.

[25] M. Prud'Homme, T.H. Nguyen, Fourier analysis of conjugate gradient method applied to inverse heat conduction problems, Int. J. Heat Mass Transfer, 42(24) (1999) 4447-4460.

[26] J.H. Zhou, Y.W. Zhang, J.K. Chen, Z.C. Feng, Inverse heat conduction using measured back surface temperature and heat flux, J. Thermophys Heat Transfer, 24(1) (2010) 95-103.

[27] M. Monde, Analytical method in inverse heat transfer problem using Laplace transform technique, Int. J. Heat Mass Transfer, 43(21) (2000) 3965-3975.

[28] M. Monde, H. Arima, W. Liu, Y. Mitutake, J.A. Hammad, An analytical solution for two-dimensional inverse heat conduction problems using Laplace transform, Int. J. Heat Mass Transfer, 46(12) (2003) 2135-2148 (10.1016/s0017-9310(02)00510-0).

[29] D. Lesnic, L. Elliott, D.B. Ingham, Application of the boundary element method to inverse heat conduction problems, Int. J. Heat Mass Transfer, 39(7) (1996) 1503-1517.

[30] R. Pasquetti, C. Leniliot, Boundary element approach for inverse heat-conduction problems - application to a bidimensional transient numerical experiment, Numer. Heat Transfer, Part B, 20(2) (1991) 169-189.

[31] O. Alifanov, Solution of an inverse problem of heat conduction by iteration methods, J. Eng. Phys. Thermophys., 26(4) (1974) 471-476.

[32] B. Blackwell, J.V. Beck, A technique for uncertainty analysis for inverse heat conduction problems, Int. J. Heat Mass Transfer, 53(4) (2010) 753-759.

[33] N. Al-Khalidy, Analysis of boundary inverse heat conduction problems using space marching with Savitzky-Gollay digital filter, Int. Commun. Heat Mass Transfer, 26(2) (1999) 199-208 (10.1016/s0735-1933(99)00006-8).

[34] J. Taler, P. Duda, Solution of non-linear inverse heat conduction problems using the method of lines, Heat Mass Transfer, 37(2-3) (2001) 147-155.

[35] J. Plewa, B. Elkins, M. Keyhani, J. Frankel, Heat transfer analysis via rate based sensors, in: 50th AIAA Aerospace Sciences Meeting including the New Horizons Forum and Aerospace Exposition, Nashville, TN, 2012, pp. 810.

[36] J. Frankel, M. Keyhani, K. Taira, In-phase error estimation of experimental data and optimal first derivatives, AIAA Journal, 42(5) (2004) 1017-1024.

[37] A.M. Osman, K.J. Dowding, J.V. Beck, Numerical solution of the general two-dimensional inverse heat conduction problem (IHCP), J. Heat Transf.-Trans. ASME, 119(1) (1997) 38-45 (10.1115/1.2824098).
[38] B.S. Elkins, M. Huang, J.I. Frankel, Higher-time derivative of in-depth temperature sensors for aerospace heat transfer, Int. J. Therm. Sci., 52 (2012) 31-39.
[39] J.I. Frankel, Regularization of inverse heat conduction by combination of rate sensor analysis and analytic continuation, J. Eng. Math., 57(2) (2007) 181-198.
[40] J.V. Beck, K.J. Arnold, Parameter Estimation in Engineering and Science, John Wiley & Sons, New York, 1977.
[41] K. Levenberg, A method for the solution of certain non-linear problems in least squares, Q. Appl. Math., 2(2) (1944) 164-168.
[42] M.N. Ozisik, H.R.B. Orlande, Inverse Heat Transfer: Fundamentals and Applications, Taylor & Francis, New York, 2000.
[43] S. Rouquette, J. Guo, P. Le Masson, Estimation of the parameters of a Gaussian heat source by the Levenberg–Marquardt method: application to the electron beam welding, Int. J. Therm. Sci., 46(2) (2007) 128-138.
[44] A.N. Tikhonov, V.Y. Arsenin, Solutions of Ill-Posed Problems, V. H. Winston and Sons, New York, 1977.
[45] J.M.G. Cabeza, J.A.M. García, A.C. Rodríguez, A sequential algorithm of inverse heat conduction problems using singular value decomposition, Int. J. Therm. Sci., 44(3) (2005) 235-244.
[46] J. Shenefelt, R. Luck, R. Taylor, J. Berry, Solution to inverse heat conduction problems employing singular value decomposition and model-reduction, Int. J. Heat Mass Transfer, 45(1) (2002) 67-74.
[47] P.K. Lamm, A survey of regularization methods for first-kind Volterra equations, in: D. Colton, H.W. Engl, A. Louis, J.R. McLaughlin, W. Rundell (Eds.) Surveys on solution methods for inverse problems, Springer, New York, 2000, pp. 53-82.
[48] B.S. Elkins, M. Keyhani, J.I. Frankel, Surface heat flux prediction through physics-based calibration, part 2: experimental validation, J. Thermophys Heat Transfer, 27(2) (2013) 206-216.
[49] V.A. Morozov, Methods for Solving Incorrectly Posed Problems, Springer-Verlag, New York, 2012.
[50] H.W. Engl, M. Hanke, A. Neubauer, Regularization of Inverse Problems, Springer Science & Business Media, Dordrecht, The Netherlands, 1996.
[51] M. Hanke, Limitations of the L-curve method in ill-posed problems, BIT Numer. Math., 36(2) (1996) 287-301.
[52] P.C. Hansen, Analysis of discrete ill-posed problems by means of the L-curve, SIAM Rev., 34(4) (1992) 561-580.
[53] P.C. Hansen, D.P. O'Leary, The use of the L-curve in the regularization of discrete ill-posed problems, SIAM J. Sci. Comput., 14(6) (1993) 1487-1503.
[54] H.C. Chen, J.I. Frankel, M. Keyhani, Nonlinear inverse heat conduction: digital filtered space marching with phase-plane and cross-correlation analysis, Numer. Heat Transfer, Part B, 72(2) (2017) 109-129.

[55] J.A.M. Garcia, J.M.G. Cabeza, A.C. Rodriguez, Two-dimensional non-linear inverse heat conduction problem based on the singular value decomposition, Int. J. Therm. Sci., 48(6) (2009) 1081-1093 (10.1016/j.ijthermalsci.2008.09.002).
[56] J. Frankel, M. Keyhani, Phase-plane and cross-correlation analysis for estimating optimal regularization in inverse heat conduction, J. Thermophys Heat Transfer, 28(3) (2014) 542-548.
[57] J.-L. Battaglia, O. Cois, L. Puigsegur, A. Oustaloup, Solving an inverse heat conduction problem using a non-integer identified model, Int. J. Heat Mass Transfer, 44(14) (2001) 2671-2680.
[58] J.L. Gardarein, J.L. Battaglia, S. Loehle, Heat flux sensor calibration using noninteger system identification: Theory, experiment, and error analysis, Rev. Sci. Instrum., 80(2) (2009) 025103.
[59] S. Loehle, J.L. Battaglia, J.C. Batsale, F. Bourserau, D. Conte, P. Jullien, B. van Ootegem, J. Couzi, J.P. Lasserre, Ieee, Estimation of high heat flux in supersonic plasma flows, in: IECON 2006 - 32nd Annual Conference on IEEE Industrial Electronics, Vols 1-11, IEEE, New York, 2006, pp. 3806-3813.
[60] S. Loehle, J.L. Battaglia, J.C. Batsale, O. Enouf, J. Dubard, J.R. Filtz, Characterization of a heat flux sensor using short pulse laser calibration, Rev. Sci. Instrum., 78(5) (2007) 053501.
[61] S. Loehle, J.L. Battaglia, P. Jullien, B. van Ootegem, J. Couzi, J.P. Lasserre, Improvement of high heat flux measurement using a null-point calorimeter, J. Spacecr. Rockets, 45(1) (2008) 76-81.
[62] S. Loehle, J.I. Frankel, Physical insight into system identification parameters applied to inverse heat conduction problems, J. Thermophys Heat Transfer, 29(3) (2015) 467-472.
[63] K.B. Oldham, J. Spanier, The Fractional Calculus: Theory and Applications of Differentiation and Integration to Arbitrary Order, Dover, New York, 2002.
[64] H.C. Chen, J.I. Frankel, M. Keyhani, Two-dimensional formulation for inverse heat conduction problems by the calibration integral equation method (CIEM), Appl. Math. Modell., 40(13-14) (2016) 6588-6603.
[65] J.I. Frankel, M. Keyhani, Nonlinear inverse calibration heat conduction through property physics, J. Thermophys Heat Transfer, 28(2) (2014) 203-217.
[66] J.I. Frankel, M. Keyhani, Theoretical development of a new surface heat flux calibration method for thin-film resistive temperature gauges and co-axial thermocouples, Shock Waves, 23(2) (2013) 177-188.
[67] P. Linz, Analytical and Numerical Methods for Volterra Equations, SIAM, Philadelphia, PA, 1985.
[68] R. Kress, Linear Integral Equations, Third Edition, Springer, New York, 2014.
[69] J.I. Frankel, M. Keyhani, Calibration integral equation method for two-probe inverse heat conduction analysis, J. Thermophys Heat Transfer, 28(3) (2014) 548-553.
[70] Y.Y. Chen, J.I. Frankel, M. Keyhani, A new front surface heat flux calibration method for a 1-D nonlinear thermal system with a time-varying back boundary condition, J. Eng. Math., 105(1) (2017) 157-187.

[71] A.S. Pande, Investigation of the One-Probe and Two-Probe Calibration Integral Equation Methods Using Experimental Data, M.S. Thesis, University of Tennessee, 2013.
[72] Y.Y. Chen, J.I. Frankel, M. Keyhani, A new nonlinear surface heat flux calibration method based on Kirchhoff transformation and rescaling principles, Inverse Prob. Sci. Eng., 22(8) (2014) 1394-1421.
[73] J. Myrick, M. Keyhani, J. Frankel, Inverse prediction of temperature through time rescaling of high-temperature experimental data, J Therm Sci Eng Appl, 8(4) (2016) 041005.
[74] J. Myrick, M. Keyhani, J. Frankel, Determination of surface heat flux and temperature using in-depth temperature data–Experimental verification, Int. J. Heat Mass Transfer, 111 (2017) 982-998.
[75] J.I. Frankel, H.C. Chen, M. Keyhani, New step response formulation for inverse heat conduction, J. Thermophys Heat Transfer, (2017) (DOI: 10.2514/1.T5067).
[76] J.I. Frankel, M. Keyhani, Cross correlation and inverse heat conduction by a calibration method, J. Thermophys Heat Transfer, (2017) (DOI: 10.2514/1.T5059).
[77] J.I. Frankel, M. Keyhani, Moving low-pass Gauss filter with automatically defined influence region for diffusive studies, J. Thermophys Heat Transfer, 26(1) (2012) 176-181.
[78] W.L. Briggs, V.E. Henson, The DFT: an Owners' Manual for the Discrete Fourier Transform, SIAM, Philadelphia, PA, 1995.
[79] W.H. Press, S.A. Teukolsky, W.T. Vetterling, B.P. Flannery, Numerical Recipes: the Art of Scientific Computing, Third Edition, Cambridge University Press, New York, 2007.
[80] D.P. Bentz, K. Prasad, Thermal Performance of Fire Resistive Materials: I. Characterization with Respect to Thermal Performance Models, in, US Department of Commerce, Technology Administration, National Institute of Standards and Technology, 2007.
[81] J.I. Frankel, M. Keyhani, A global time treatment for inverse heat conduction problems, J. Heat Transf.-Trans. ASME, 119(4) (1997) 673-683 (10.1115/1.2824171).
[82] R.W. Truitt, Fundamentals of Aerodynamic Heating, The Ronlad Press Company, New York, 1960.
[83] J. Frankel, S. Allison, D. Beshears, Design of phosphor thermometry system for transient high heat flux surface thermometry, in: 58th International Instrumentation Symposium, San Diego, CA, June, 2012, pp. 4-8.
[84] Y. Chen, Calibration and Rescaling Principles for Nonlinear Inverse Heat Conduction and Parameter Estimation Problems, Ph.D. Dissertation, The University of Tennessee at Knoxville, 2015.
[85] M.N. Ozisik, Heat Conduction, John Wiley & Sons, New York, 1980.
[86] M. Abramowitz, I.A. Stegun, Handbook of Mathematical Functions: with Formulas, Graphs, and Mathematical Tables, Dover Publications Inc., New York, 1972.
[87] J.P. Boyd, Chebyshev and Fourier Spectral Methods, Dover, New York, 2001.

[88] L.C. Andrews, Special Functions of Mathematics for Engineers, Second Edition, McGraw-Hill, New York, 1992.
[89] G. Sansone, Orthogonal Functions, Dover, New York, 1991.
[90] B. Carnahan, H.A. Luther, J.O. Wilkes, Applied Numerical Methods, John Wiley & Sons, New York, 1969.
[91] E. Cheney, D. Kincaid, Numerical Mathematics and Computing, Second Edition, Brooks/Cole Publishing Company, Monterey, California, 1985.
[92] C.F. Gerald, P.O. Wheatley, Applied Numerical Analysis, Fifth Edition, Addison-Wesley Publishing Company, Reading, MA, 1994.
[93] H.T. Davis, Introduction to Nonlinear Differential and Integral Equations, Dover, New York, 1962.
[94] M.N. Ozisik, Heat conduction, Second Edition, John Wiley & Sons, 1993.
[95] Thermocouple Tolerances (Reference Junction at 0°C), in.
[96] H.C. Chen, J.I. Frankel, M. Keyhani, Nonlinear inverse heat conduction problem of surface temperature estimation by calibration integral equation method, Z. Angew. Math. Mech., (in review).
[97] H.C. Chen, J.I. Frankel, M. Keyhani, Two-probe calibration integral equation method for nonlinear inverse heat conduction problem of surface heat flux estimation, Int. J. Heat Mass Transfer, (in review).

Appendix

All the Figures and Tables

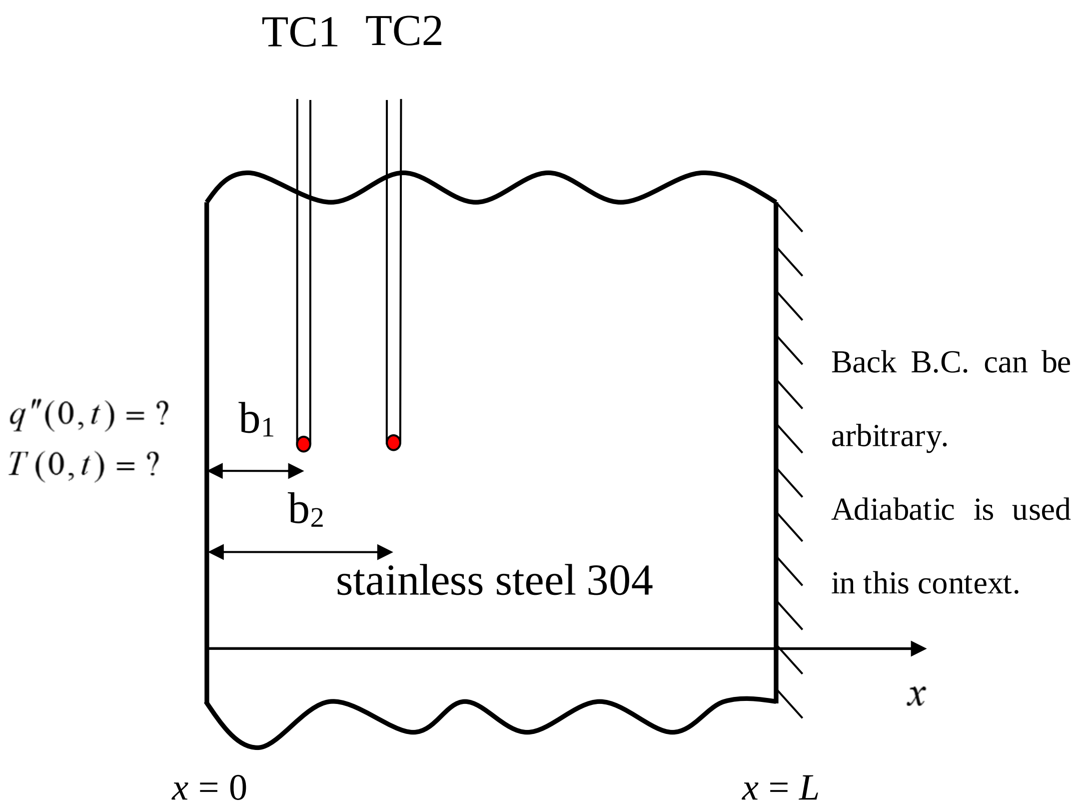

Fig. A-2.1 Schematic of the one-dimensional geometry with two in-depth TCs.

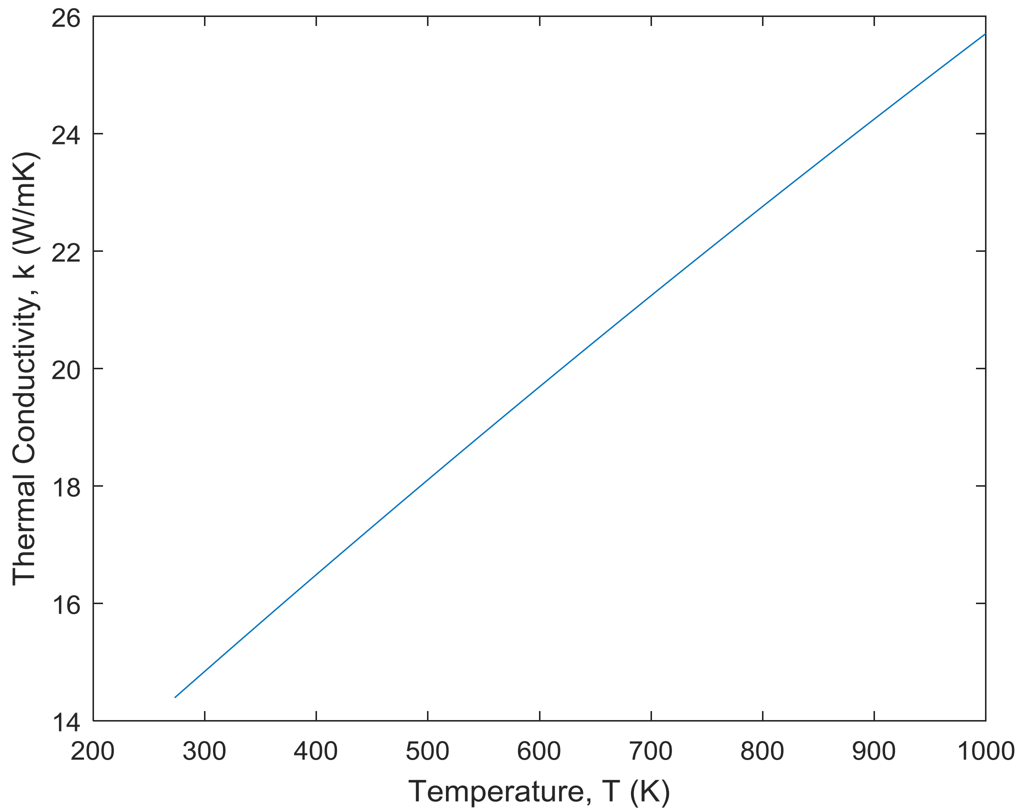

Fig. A-2.2a Thermal conductivity, $k(T)$ as a function of temperature for SS 304 [80].

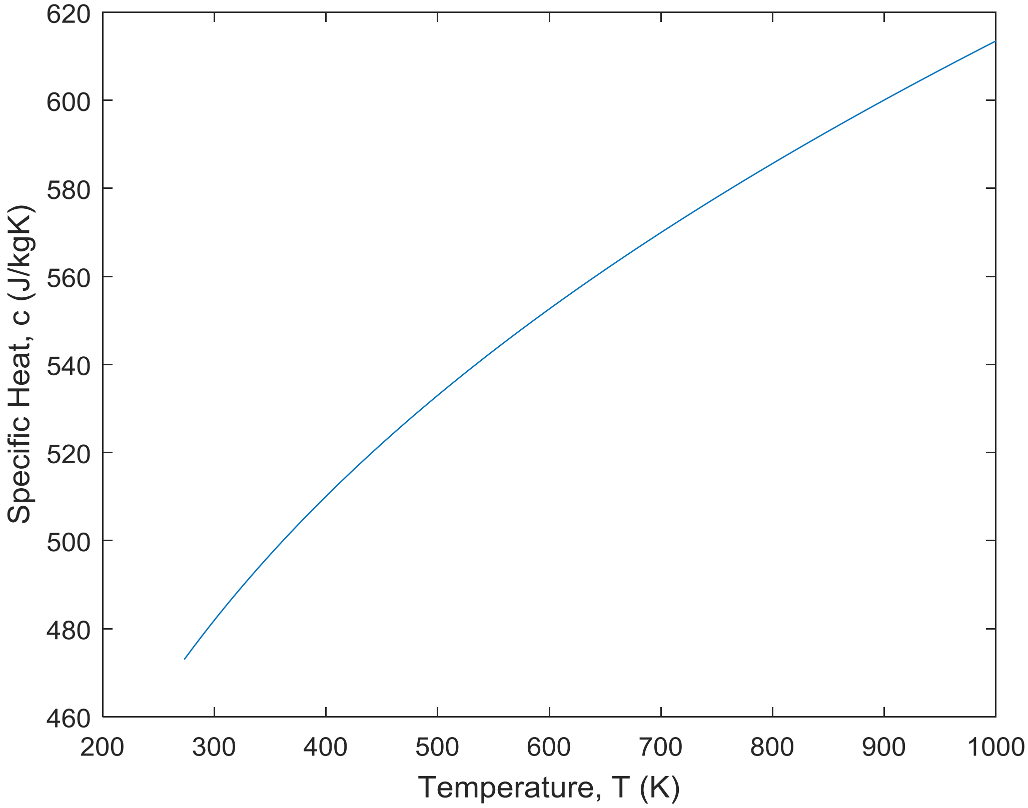

Fig. A-2.2b Specific heat, $c(T)$ as a function of temperature for SS 304 [80].

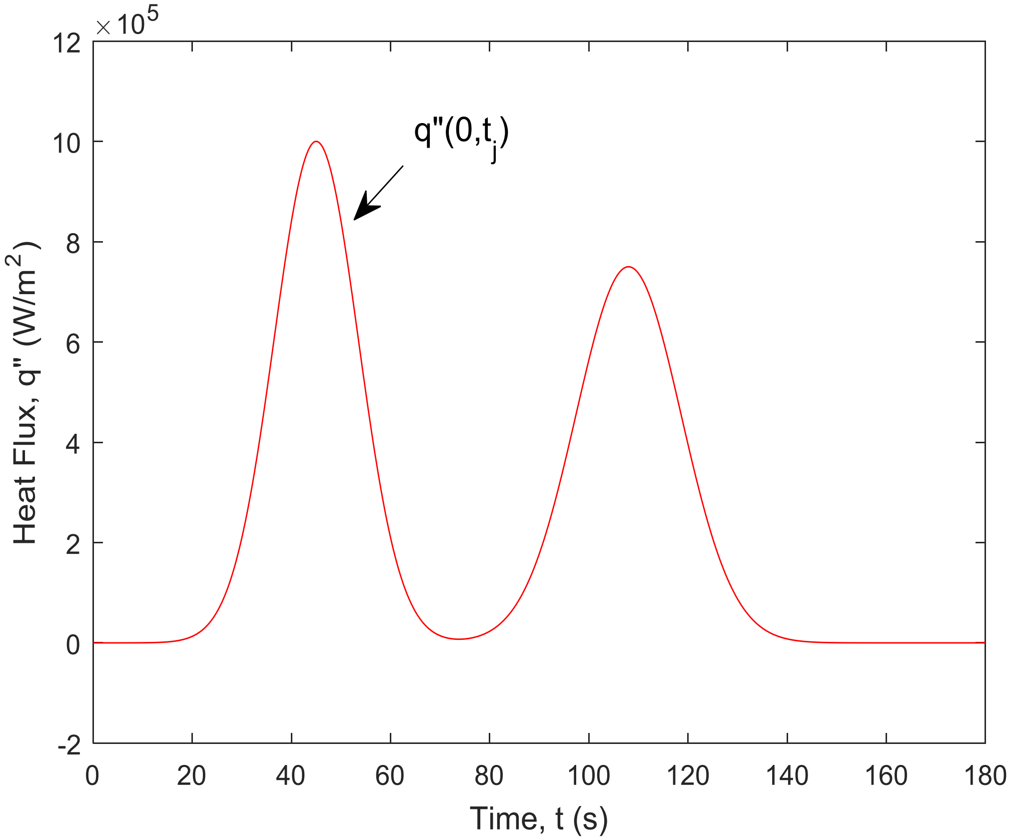

Fig. A-2.3 The exact surface heat flux $q''(0, t_j)$ to be reconstructed.

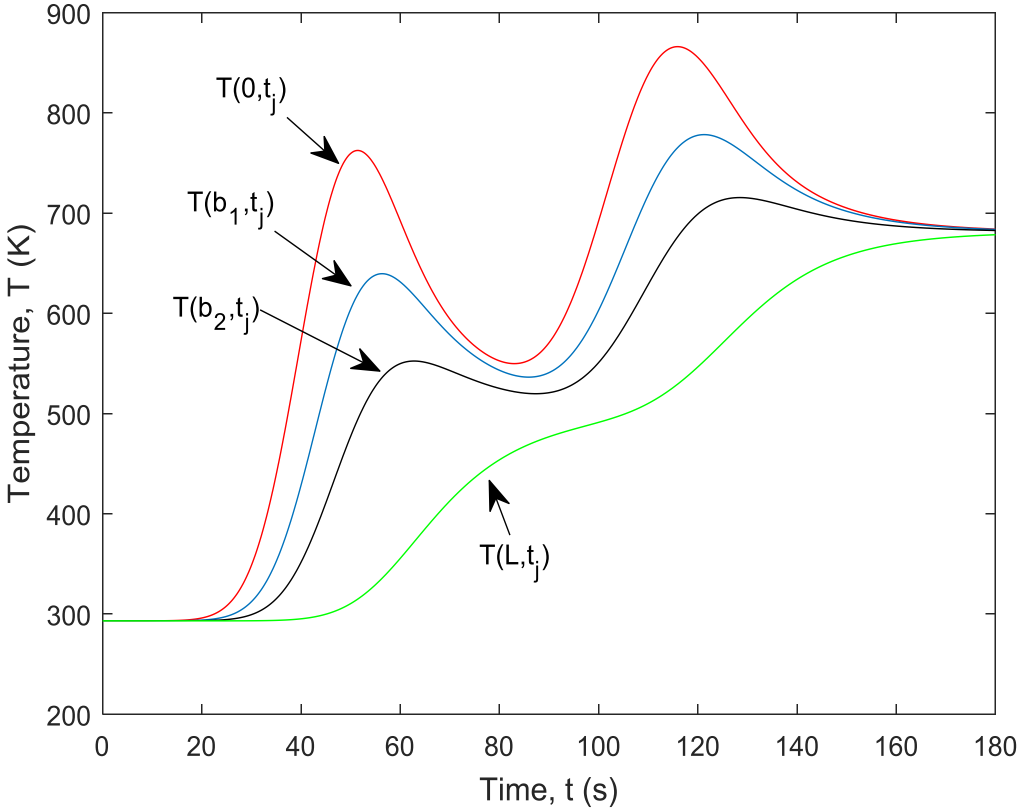

Fig. A-2.4 The surface temperature $T(0,\ t_j)$ to be reconstructed and the positional temperatures $T(b_1,\ t_j)$, $T(b_2,\ t_j)$ and $T(L,\ t_j)$ at $x = b_1$, b_2, and L, respectively ($b_1 = 4.2333\times10^{-3}$ m, $b_2 = 8.4667\times10^{-3}$ m, $L = 2.54\times10^{-2}$ m).

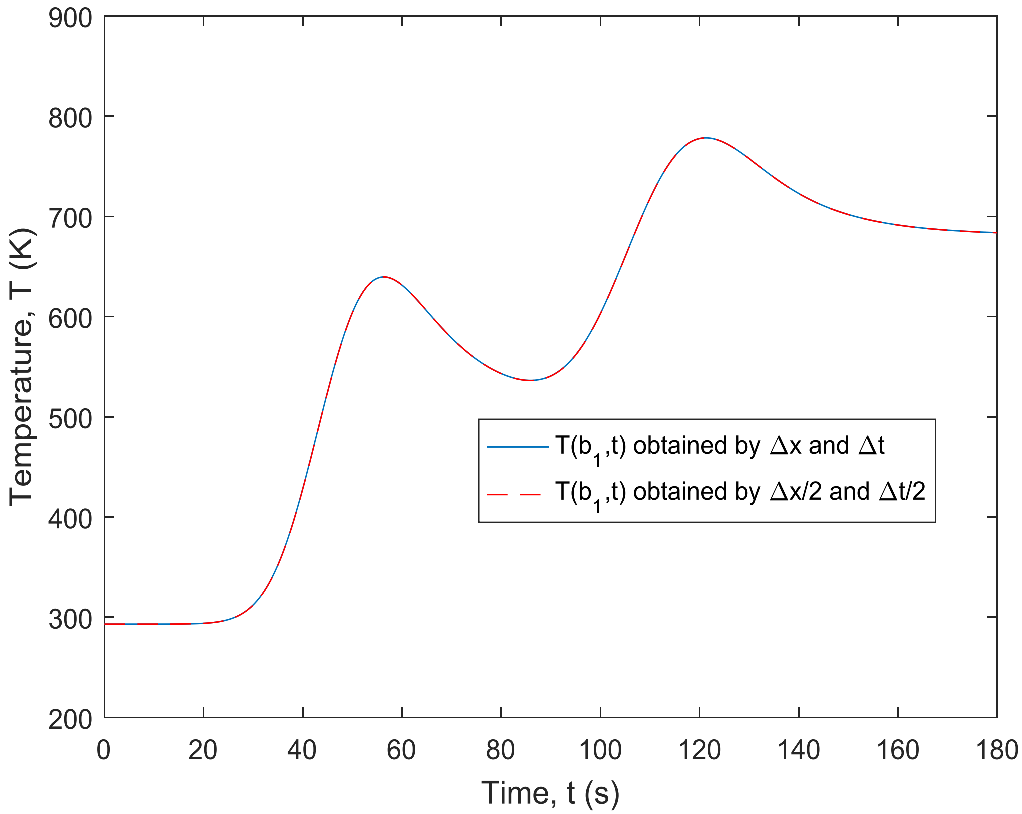

Fig. A-2.5 Convergence analysis by plotting $T(b_1, t_j)$ obtained by (Δx, Δt) and ($\Delta x/2$, $\Delta t/2$), respectively (Δx = 1.4111×10^{-4} m, Δt = 0.1 s).

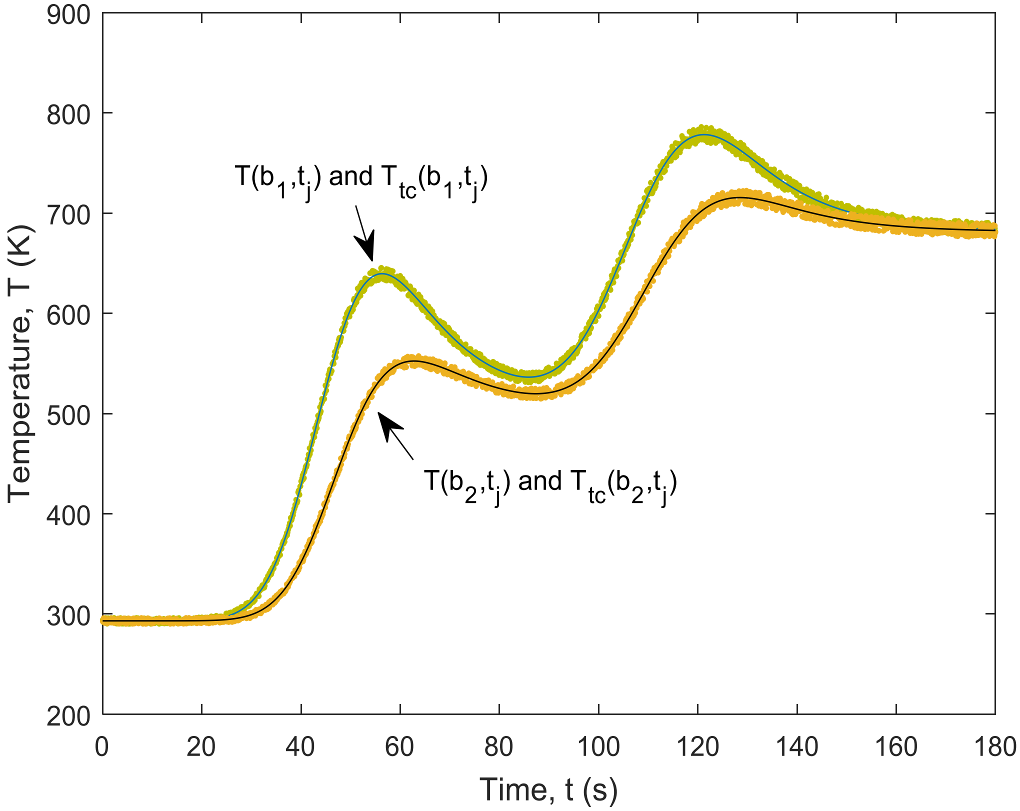

Fig. A-2.6 The positional temperatures at the thermocouple site $T(b_1, t_j)$ and $T(b_2, t_j)$ as well as the noisy "thermocouple" data $T_{tc}(b_1, t_j)$ and $T_{tc}(b_2, t_j)$.

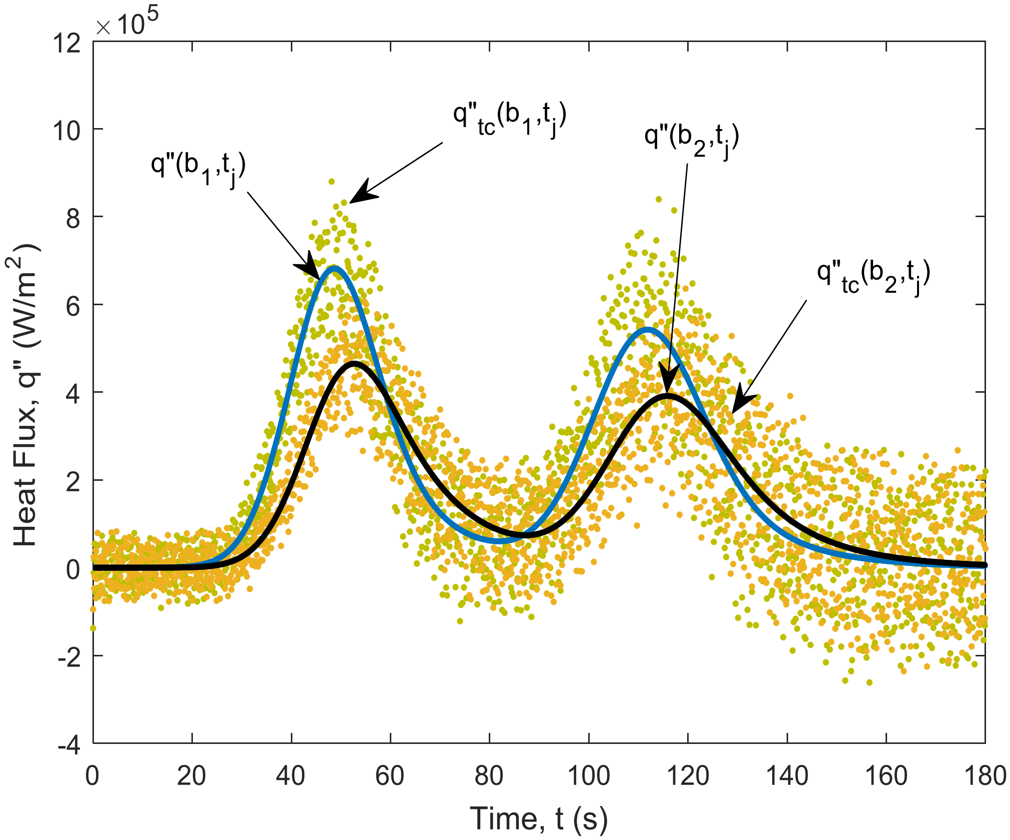

Fig. A-2.7 Comparison of numerically exact heat fluxes $q''(b_1, t_j)$, $q''(b_2, t_j)$ with heat fluxes $q''_{tc}(b_1, t_j)$, $q''_{tc}(b_2, t_j)$ resulting from the simulation of the direct problem in $x \in [b_1, b_2]$ using discrete "thermocouple" data.

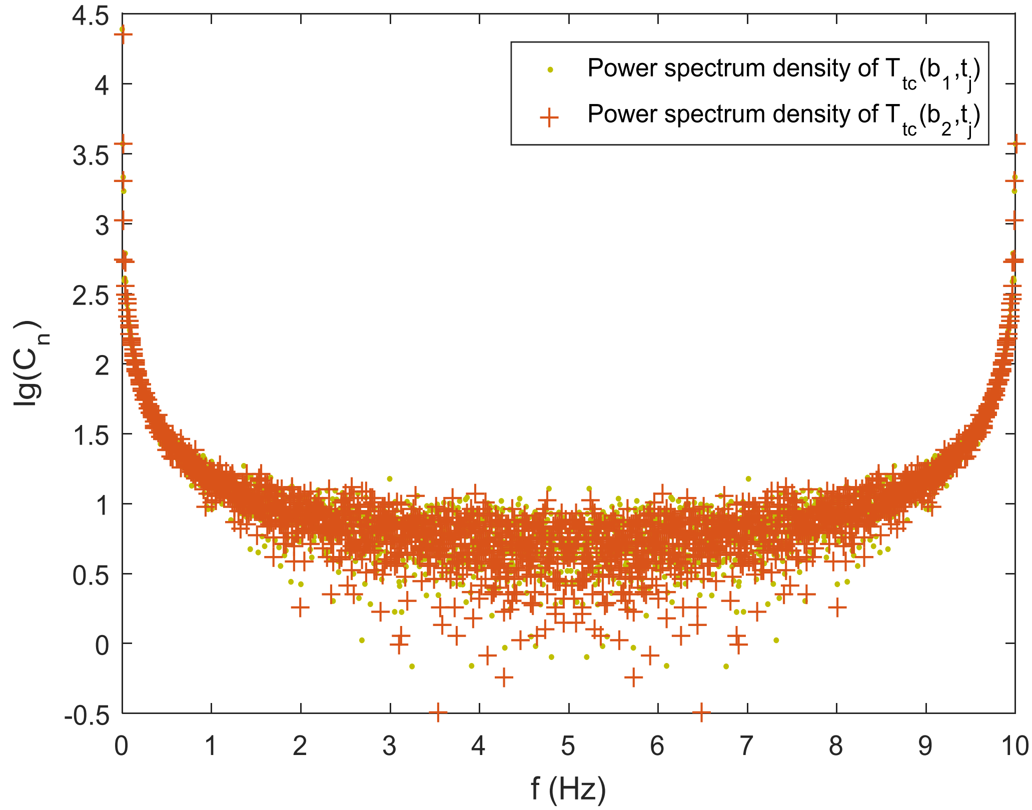

Fig. A-2.8a The power spectrum for “thermocouple” temperatures $T_{tc}(b_1, t_j)$ and $T_{tc}(b_2, t_j)$ in full f range.

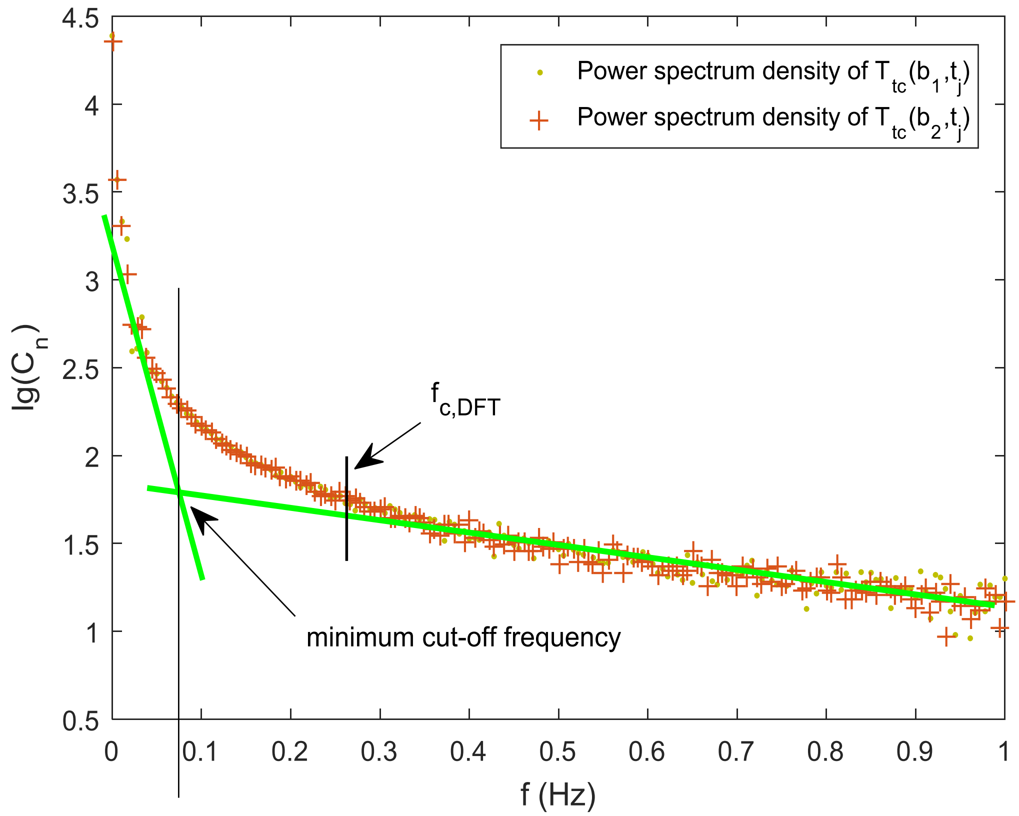

Fig. A-2.8b The power spectrums for "thermocouple" temperatures $T_{tc}(b_1, t_j)$ and $T_{tc}(b_2, t_j)$ in the range $f \in [0,1]$ Hz.

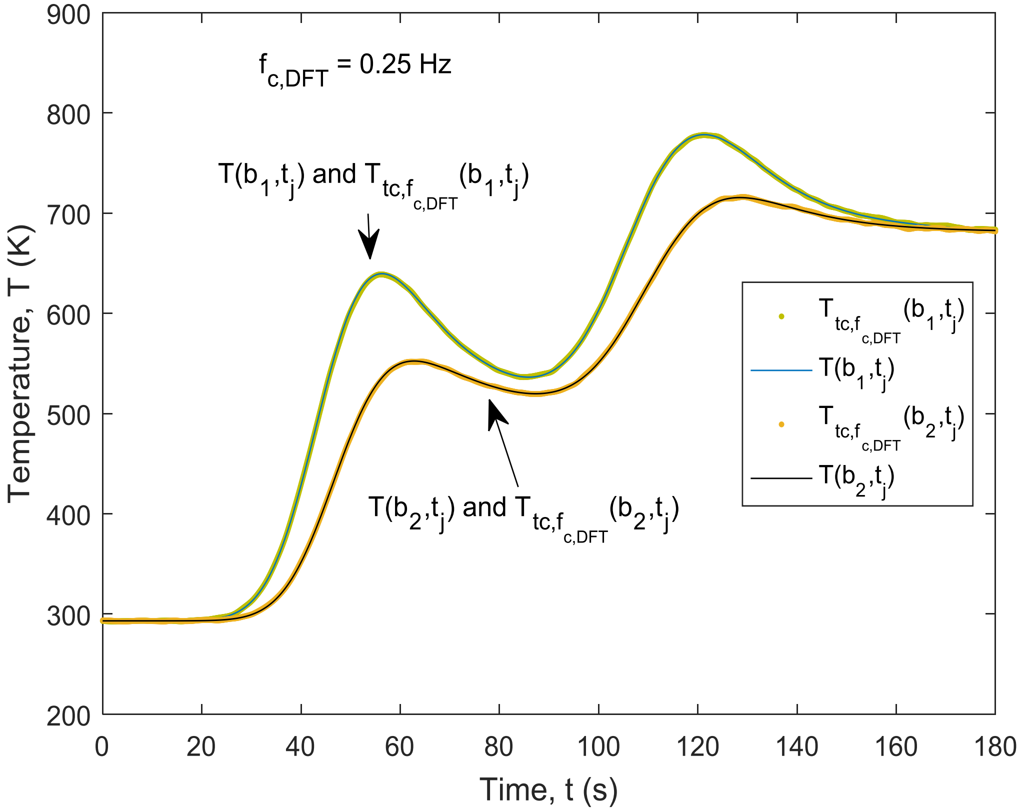

Fig. A-2.9 Comparison of positional temperatures $T(b_1, t_j)$, $T(b_2, t_j)$ and filtered "thermocouple" temperatures $T_{tc,f_{c,DFT}}(b_1,t_j)$, $T_{tc,f_{c,DFT}}(b_2,t_j)$.

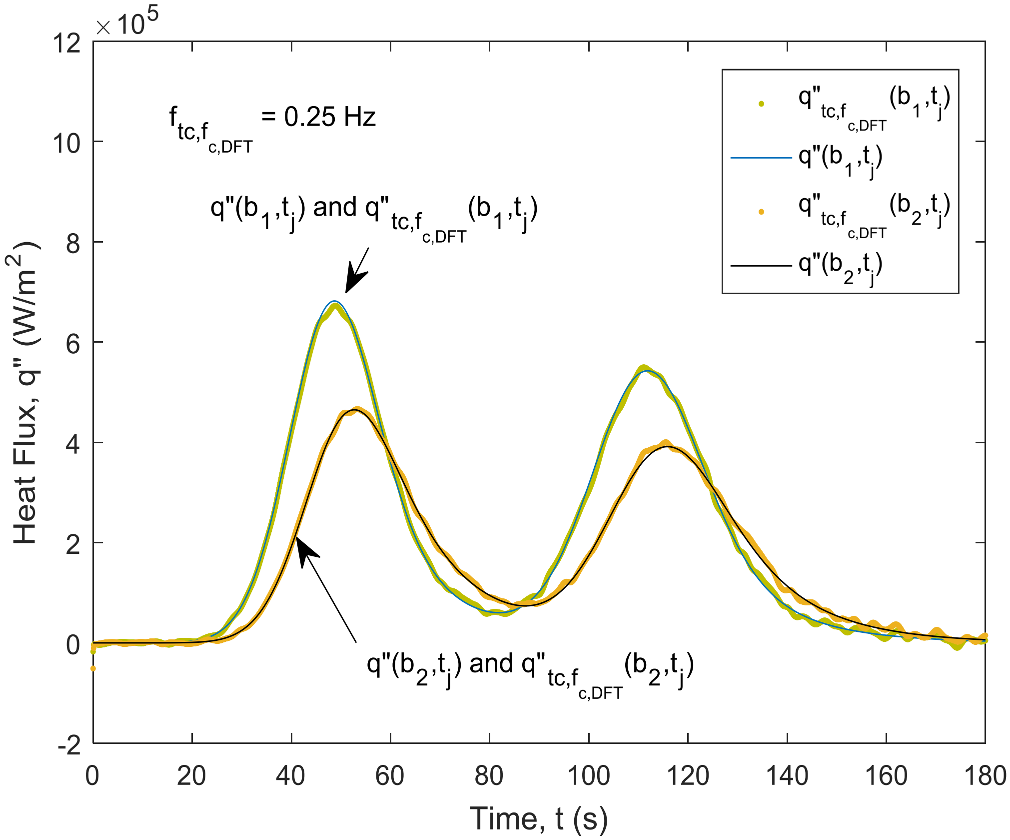

Fig. A-2.10 Comparison of exact heat fluxes $q''(b_1, t_j)$, $q''(b_2, t_j)$ and heat fluxes emanated from a simulation of the direct problem in $x \in [b_1, b_2]$ using filtered "thermocouple" data $q''_{tc,f_{c,DFT}}(b_1, t_j)$, ($f_{tc,DFT}$ = 0.25 Hz).

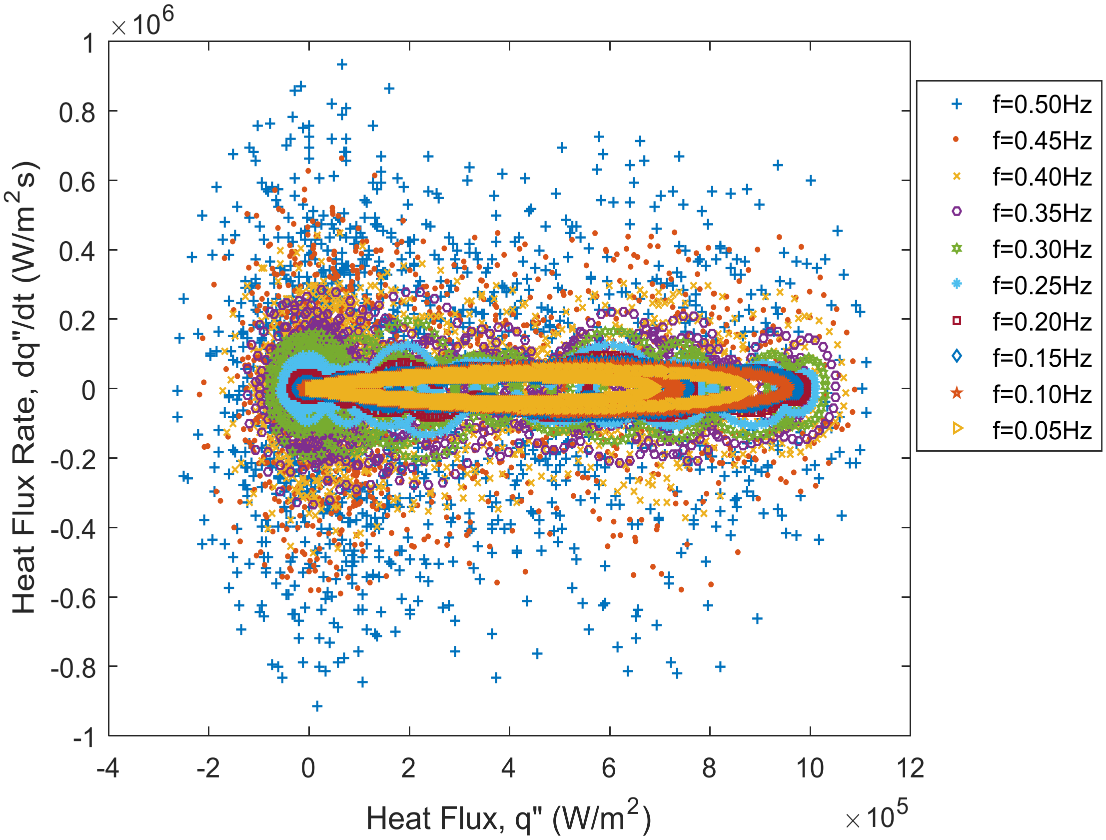

Fig. A-2.11a The predicted surface heat flux rate and heat flux phase planes for the indicated cut-off frequency spectrum "*f*".

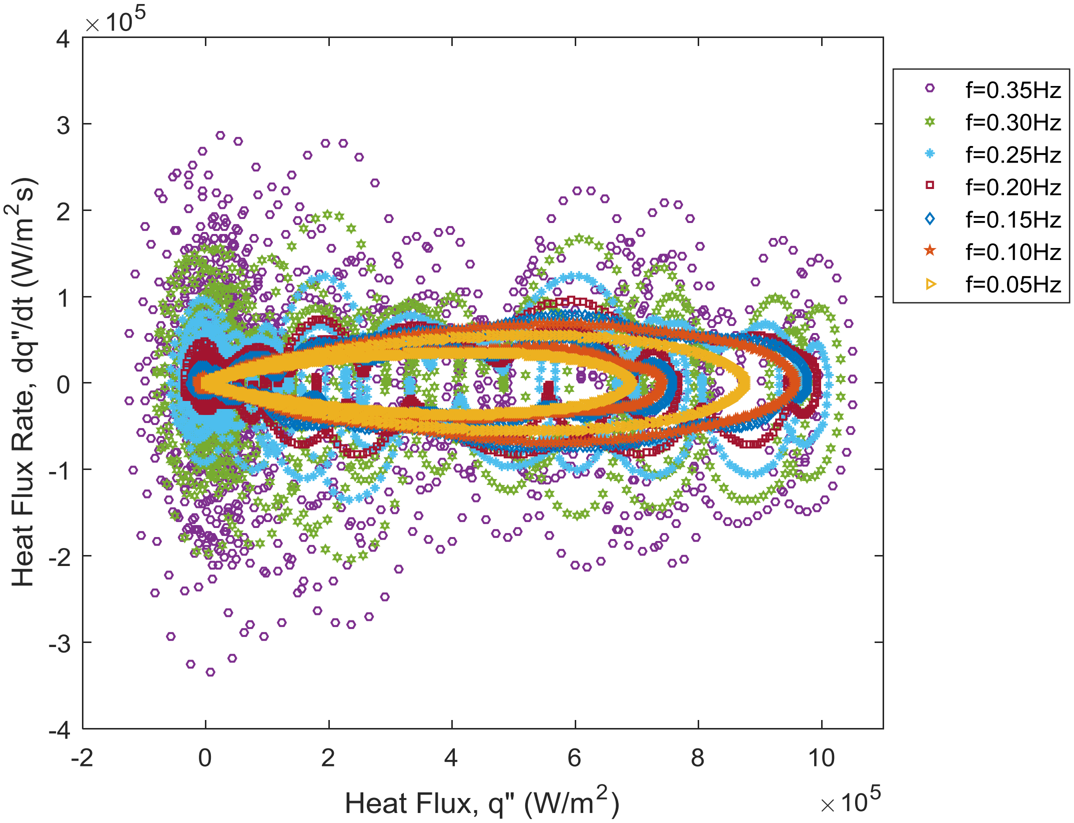

Fig. A-2.11b The predicted surface heat flux rate and heat flux phase planes for the indicated cut-off frequency spectrum “ *f* ” (zooming in and omitting *f* = 0.50, 0.45, 0.40 Hz of the Fig. A-2.11a).

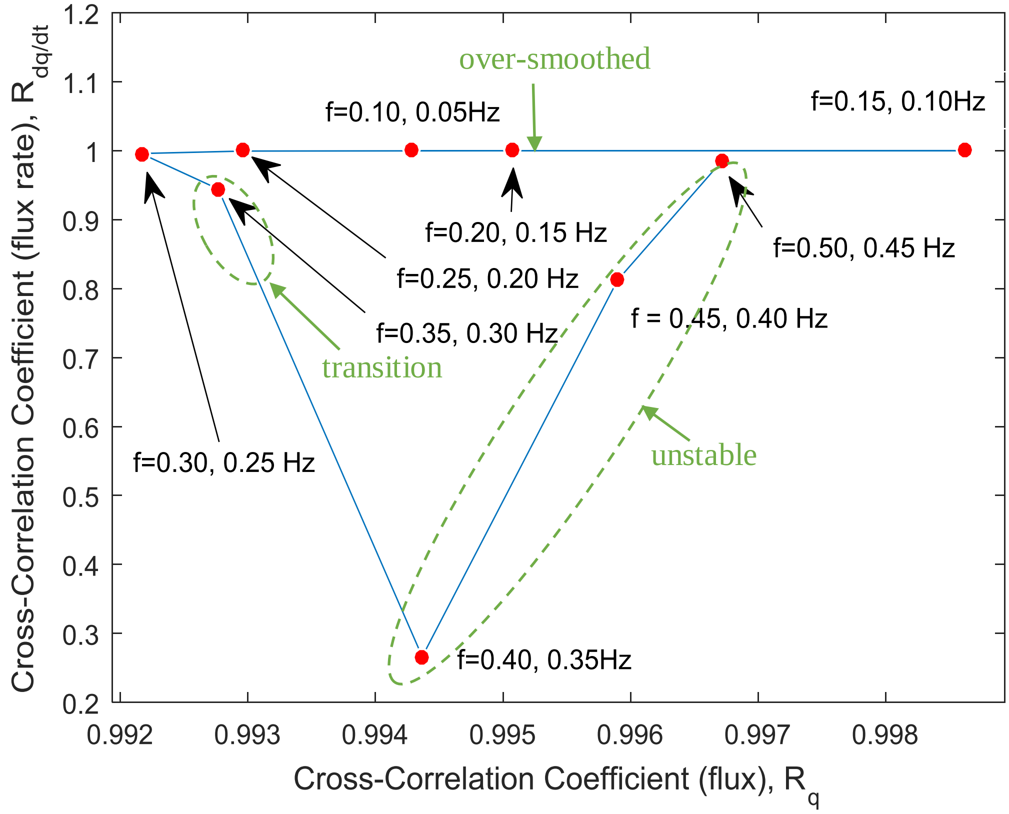

Fig. A-2.12a The predicted surface heat flux rate and heat flux cross-correlation coefficient phase planes for the indicated cut-off frequency "f" pairing when $N^* = 0$. Here, $R_{dq/dt} = R_{\dot{q}}(\dot{q}''_{f_n}, \dot{q}''_{f_{n+1}})$.

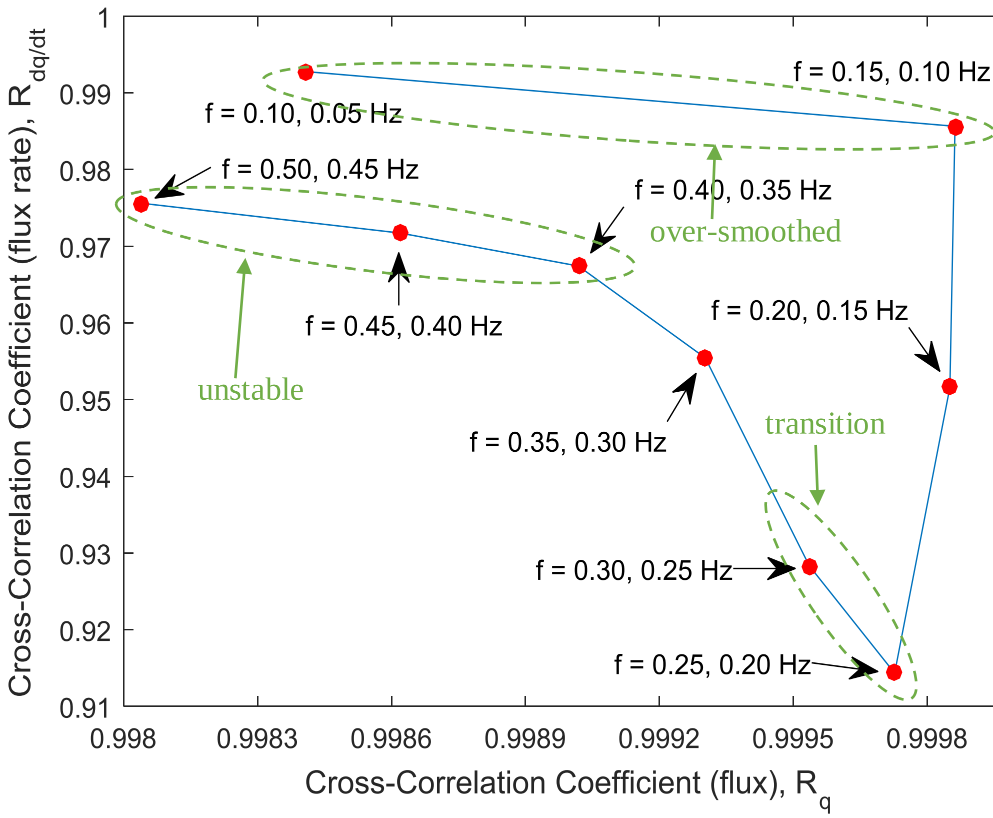

Fig. A-2.12b The predicted surface heat flux rate and heat flux cross-correlation coefficient phase planes for the indicated cut-off frequency " f " pairing when N^* = 20 (2 seconds). Here, $R_{dq/dt} = R_{\dot{q}}(\dot{q}''_{f_n}, \dot{q}''_{f_{n+1}})$.

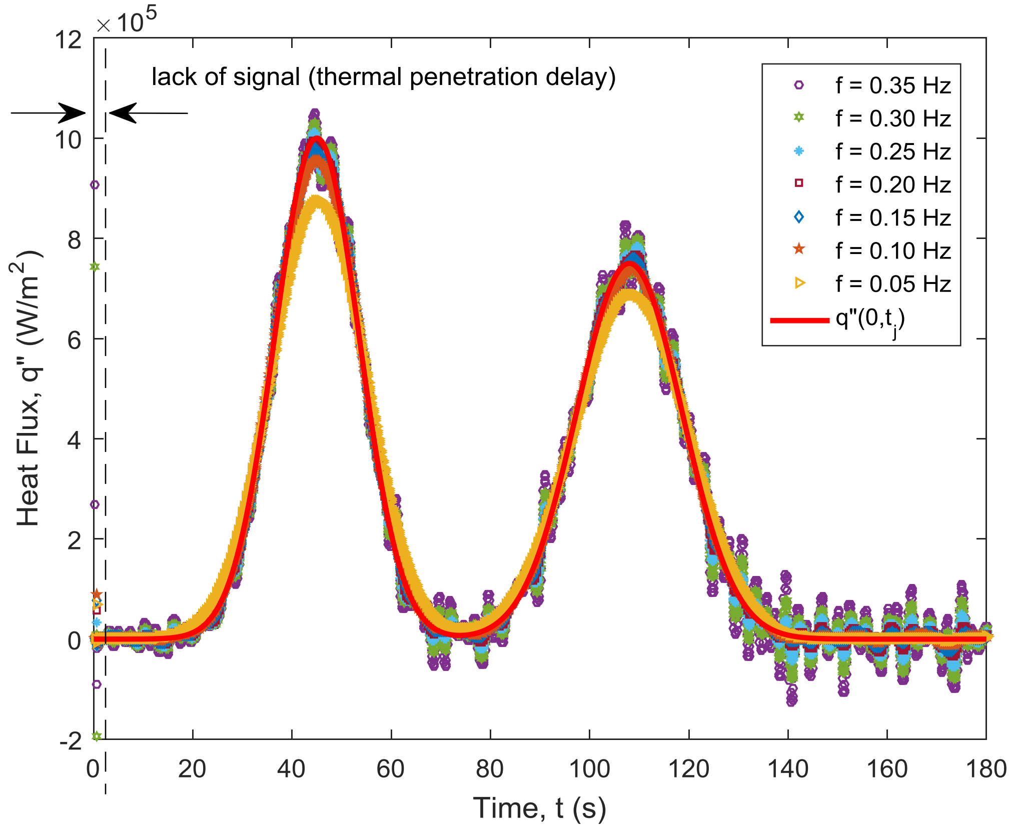

Fig. A-2.13 The surface heat flux predictions $q''_f(0,t_j)$ using f = 0.05, 0.10, 0.15, 0.20, 0.25, 0.30, 0.35 Hz and the exact surface heat flux $q''(0,t_j)$ (y axis scale is set from -20 to 120 W/cm^2).

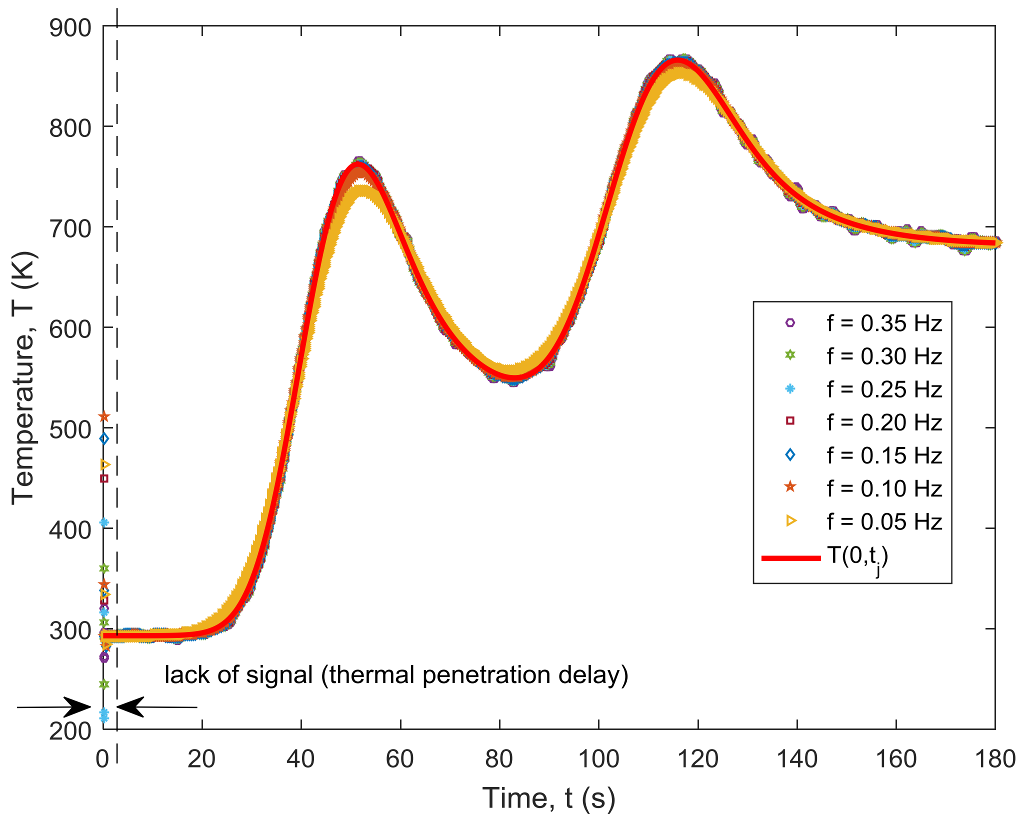

Fig. A-2.14 The surface temperature predictions $T_f(0, t_j)$ using f = 0.15, 0.20, 0.25, 0.30 Hz and the “exact” surface temperature $T(0, t_j)$ (y axis scale is set from 200 to 900 K).

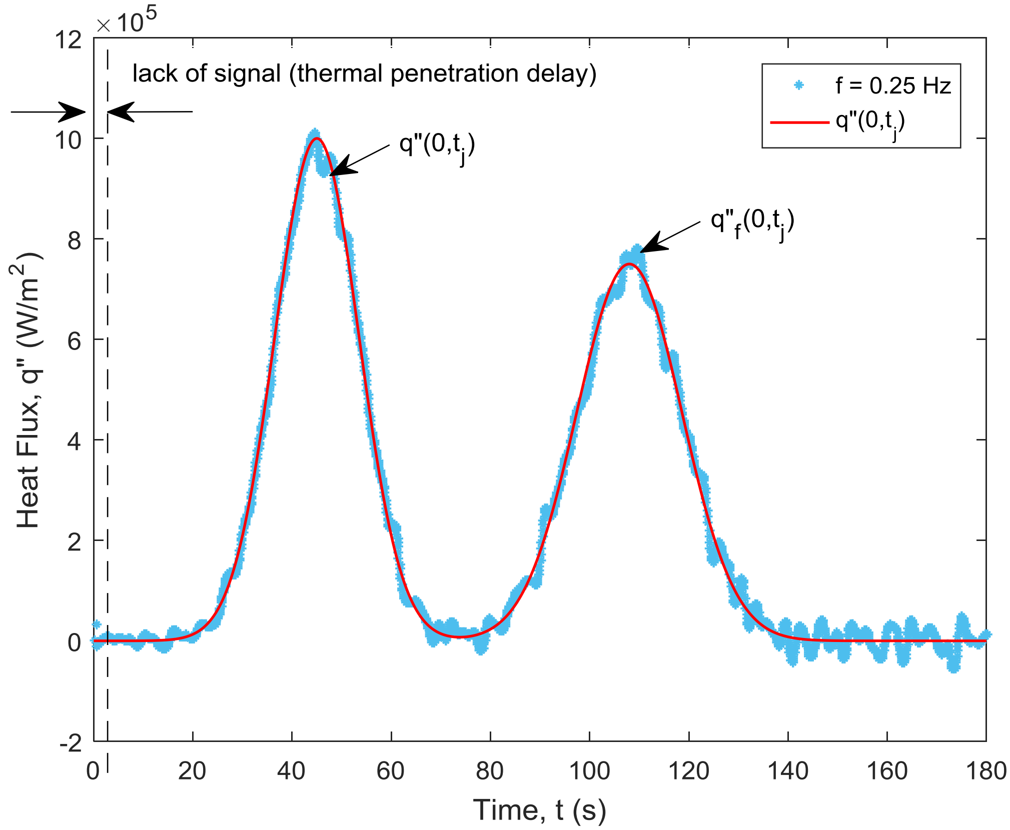

Fig. A-2.15 The predicted surface heat flux $q''_f(0,t_j)$ using f = 0.25 Hz and the exact surface heat flux $q''(0,t_j)$ (y-axis scale is set from -20 to 120 W/cm^2).

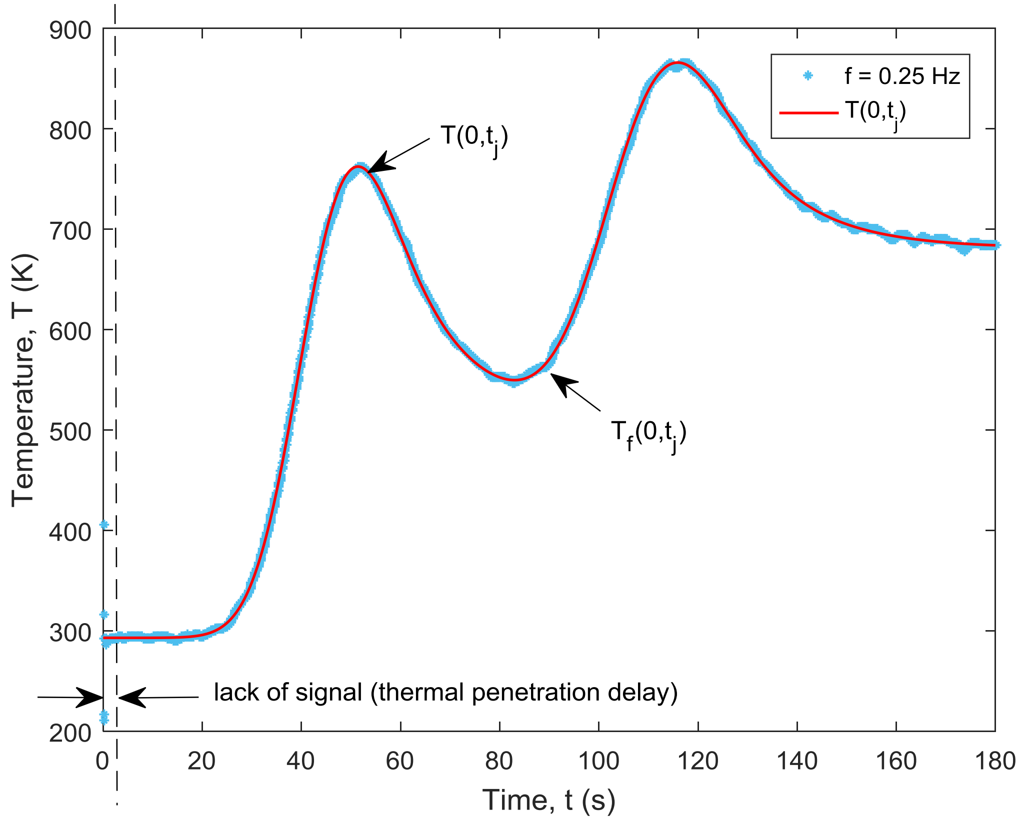

Fig. A-2.16 The predicted surface temperature $T_f(0, t_j)$ using $f = 0.25$ Hz and the exact surface temperature $T(0, t_j)$ (y-axis scale is set from 200 to 900 K).

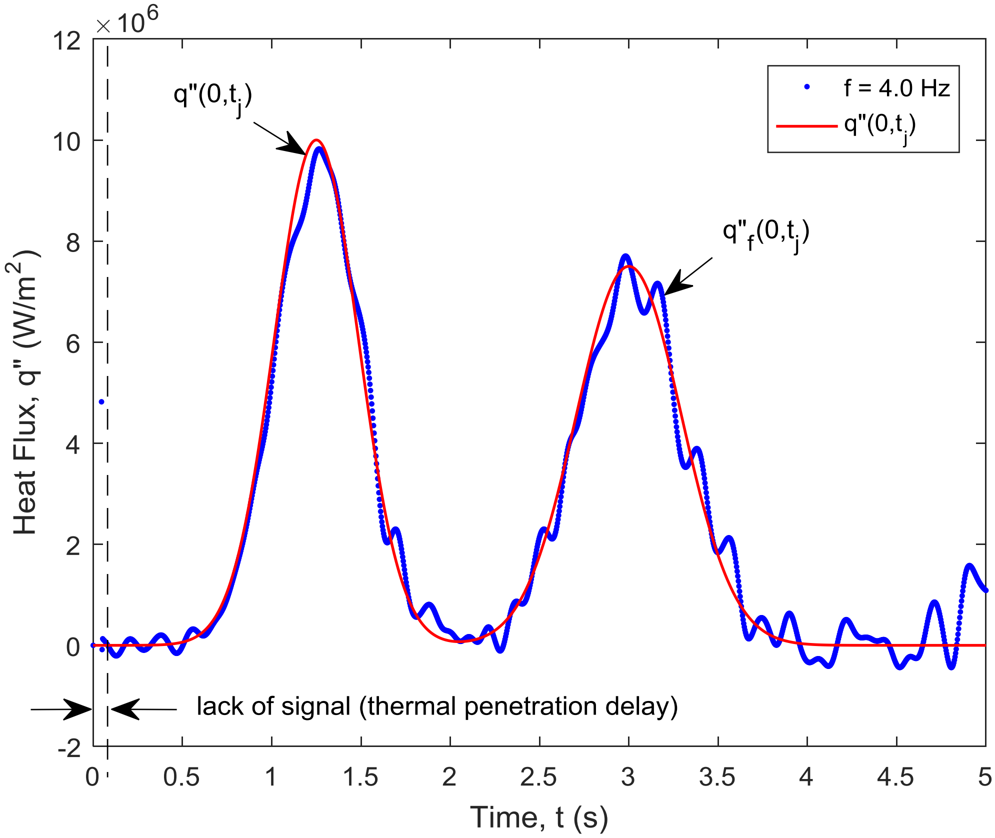

Fig. A-2.17 The predicted surface heat flux $q''_f(0,t_j)$ using f = 4.0 Hz and the exact surface heat flux $q''(0,t_j)$ (y-axis scale is set from -200 to 1200 W/cm^2).

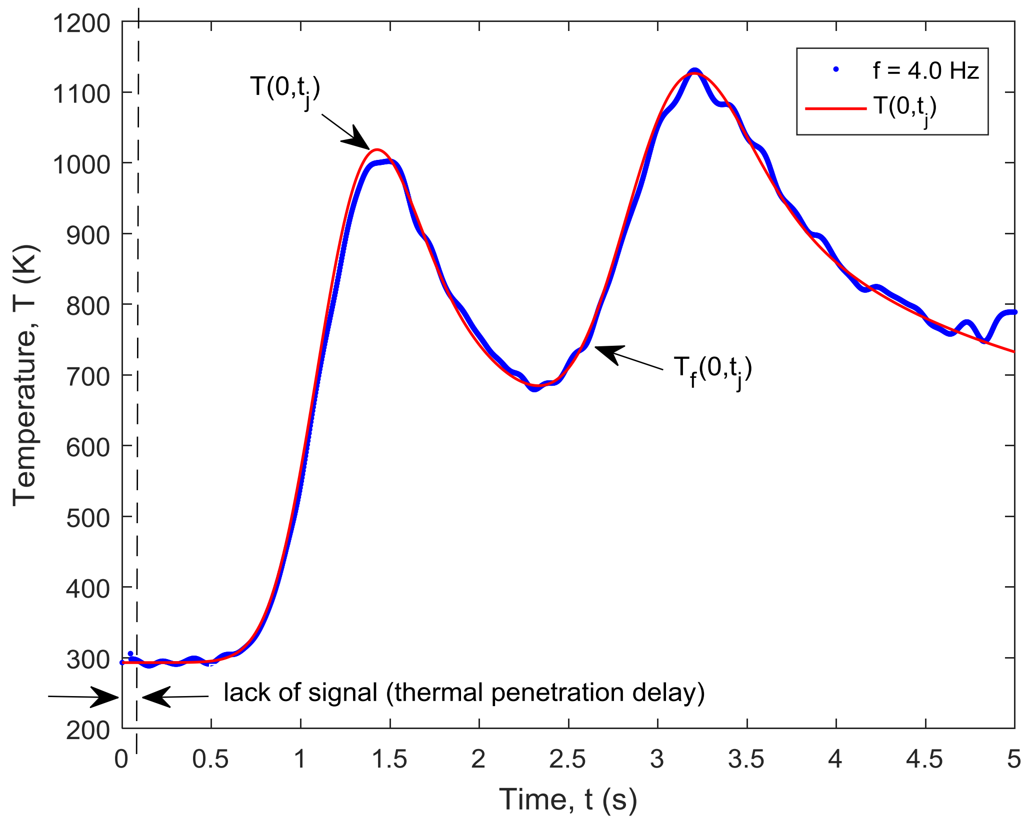

Fig. A-2.18 The predicted surface temperature $T_f(0,\ t_j)$ using f = 4.0 Hz and the exact surface temperature $T(0,\ t_j)$ (y-axis scale is set from 200 to 1200 K).

Table A-2.1 Thermophysical properties of stainless steel 304 [80] and parameters for the simulation.

Property	Value
b_1	4.2333×10^{-3} m
b_2	8.4667×10^{-3} m
c	$6.683+0.04906\times T+80.74\times\ln(T)$ J/(kg·K) [80]
$f_{c,\,DFT}$	0.25 Hz
$f_{sampling}$	10 Hz
k	$9.705+0.0176\times T-1.60\times10^{-6}\times T^{2}$ W/(m·K) [80]
L	2.54×10^{-2} m
M	30
N	1800
N^{*}	20
P	10
$q''_{\max}$	10^{6} W/m^{2}
$t_{\max}$	180 s
Δf	0.05 Hz
Δt	0.1 s
T_0	293.15 K
Δx	1.4111×10^{-4} m
ρ	7920 kg/m^{3} [80]

Table A-2.1 Continued

Property	Value
ε_T	0.01
β_1	$t_{\mathrm{max}}/4$ s
β_2	$0.6t_{\mathrm{max}}$ s
σ_1	$t_{\mathrm{max}}/15$ s
σ_2	$t_{\mathrm{max}}/12$ s

Table A-2.2 The parameters for the short time duration simulation.

Property	Value
b_1	2.1167×10^{-3} m
b_2	8.4667×10^{-3} m
$f_{sampling}$	300 Hz
L	2.54×10^{-2} m
M	16
N	1500
$q''_{\max}$	10^7 W/m^2
$t_{\max}$	5 s
Δt	3.3333×10^{-3} s
Δx	1.4111×10^{-4} m
ε_T	0.01
β_1	$t_{\max}/4$ s
β_2	$0.6t_{\max}$ s
σ_1	$t_{\max}/15$ s
σ_2	$t_{\max}/12$ s

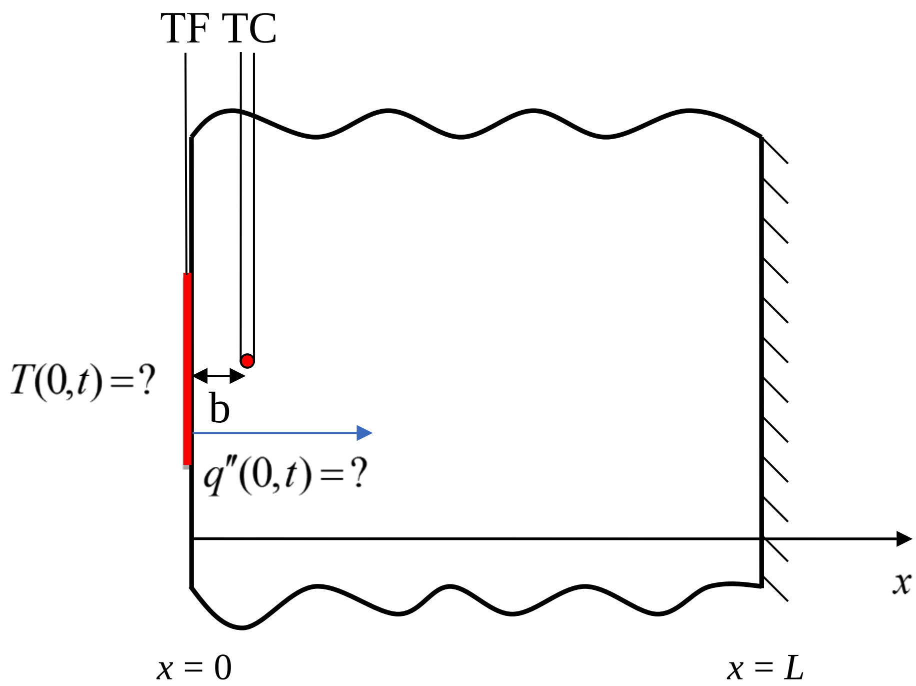

Fig. A-3.1 Schematic of one region, one-dimensional inverse heat conduction problem in a finite slab.

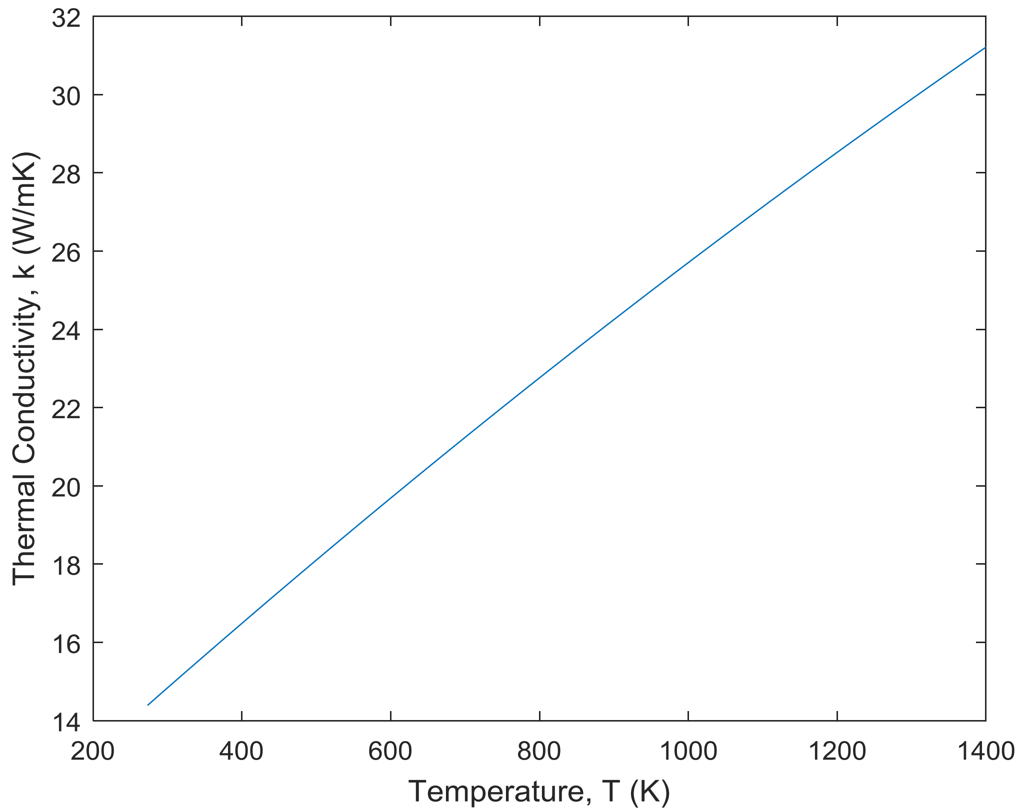

Fig. A-3.2a Thermal conductivity, $k(T)$ as a function of temperature for SS 304 [80].

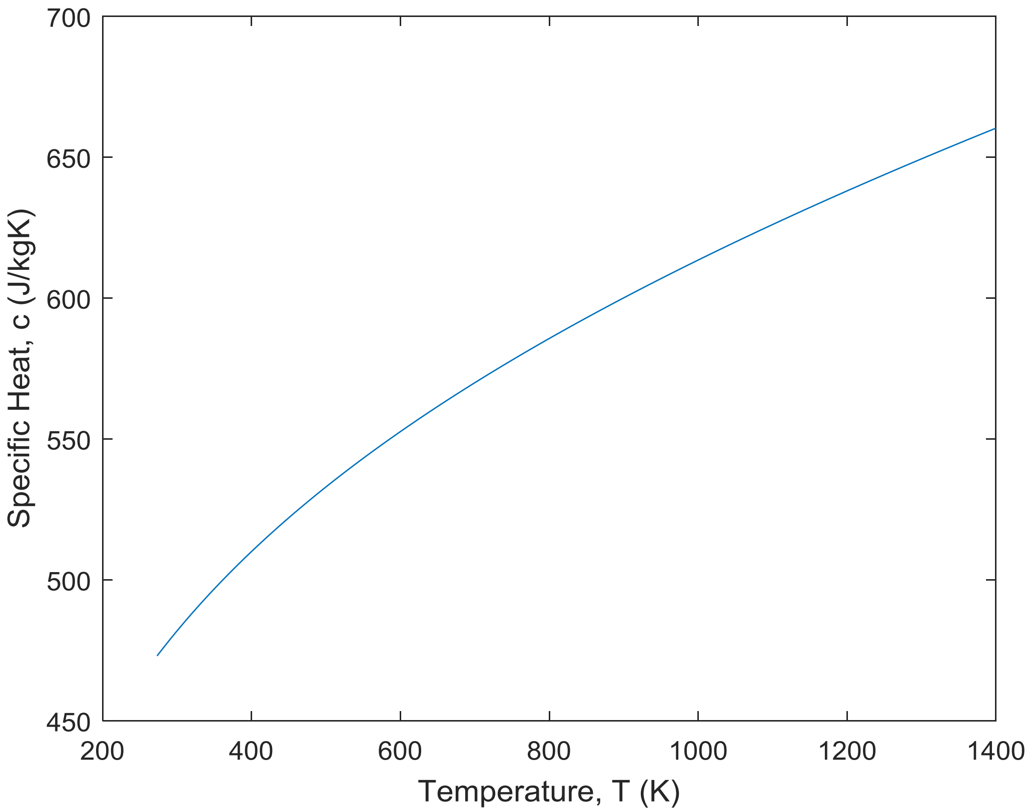

Fig. A-3.2b Specific heat, $c(T)$ as a function of temperature for SS 304 [80].

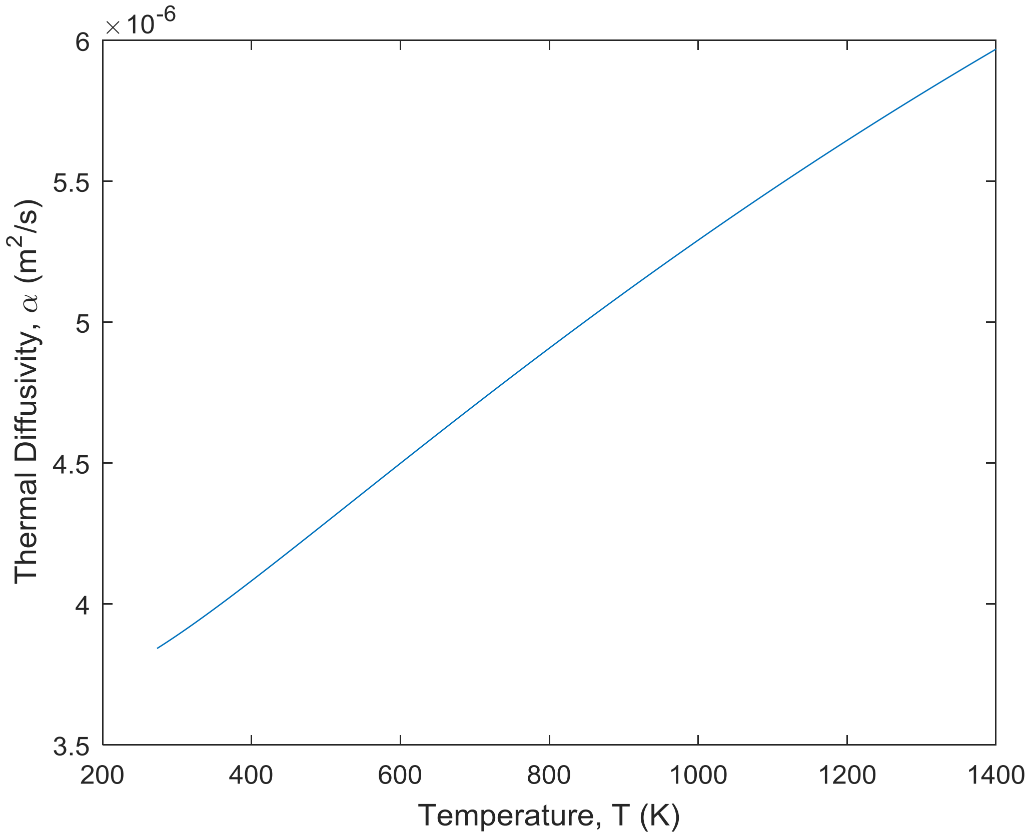

Fig. A-3.2c Thermal diffusivity, $\alpha(T)$ as a function of temperature for SS 304 [80].

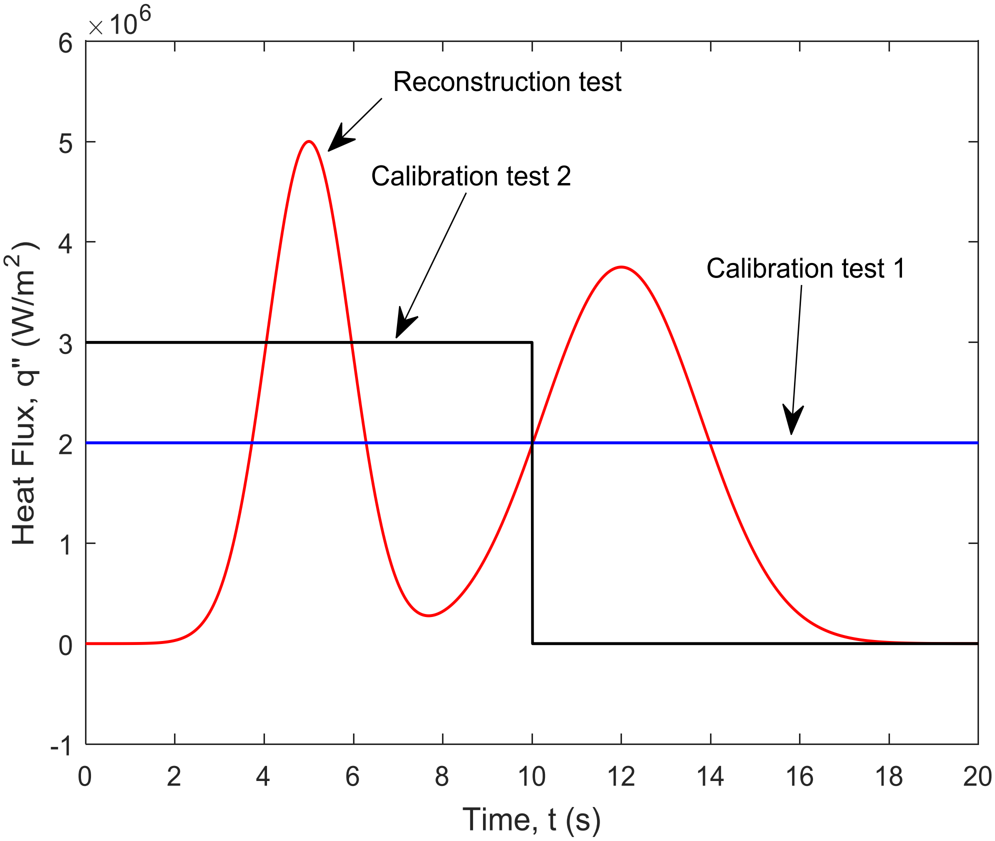

Fig. A-3.3 Surface heat fluxes provided in calibration test 1, $q''_{c1}(0,t)$, calibration test 2, $q''_{c2}(0,t)$ and reconstruction test, $q''_{r}(0,t)$.

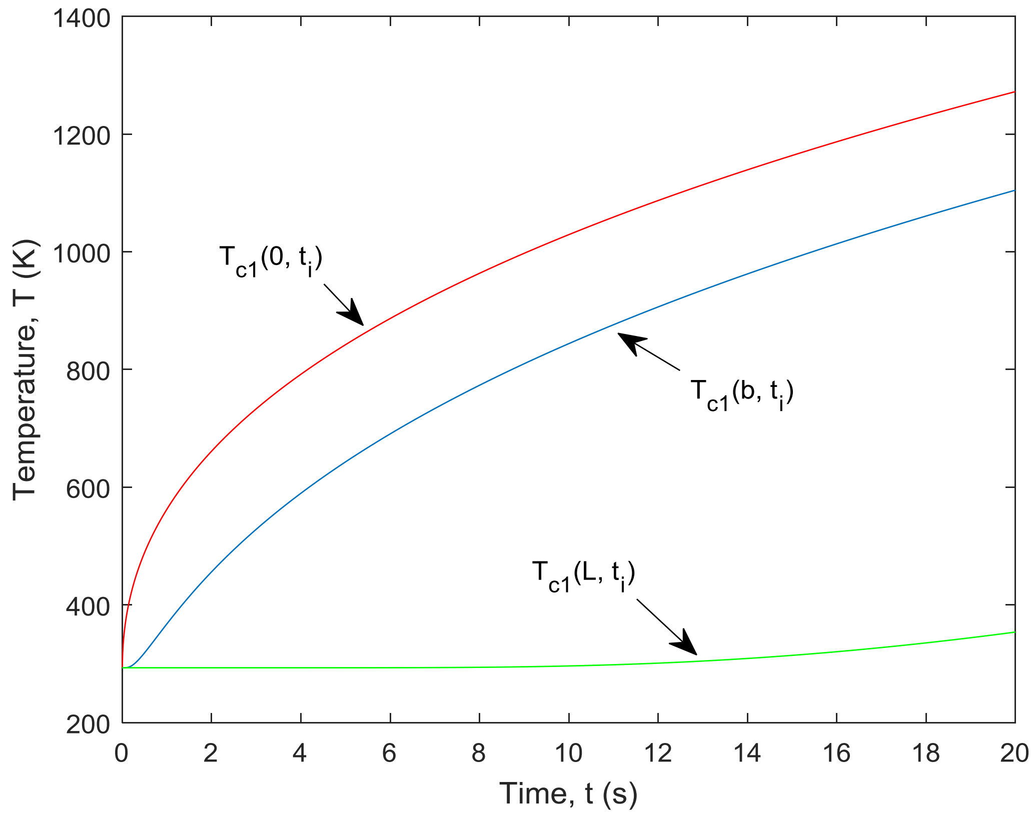

Fig. A-3.4a The positional temperatures at $x = 0$, $x = b$ and $x = L$ under the calibration test 1 obtained by the implicit finite difference scheme, $T_{c1}(0, t_i)$, $T_{c1}(b, t_i)$ and $T_{c1}(L, t_i)$, $t_i = i\Delta t$, $i = 1, 2, 3, \ldots, M$.

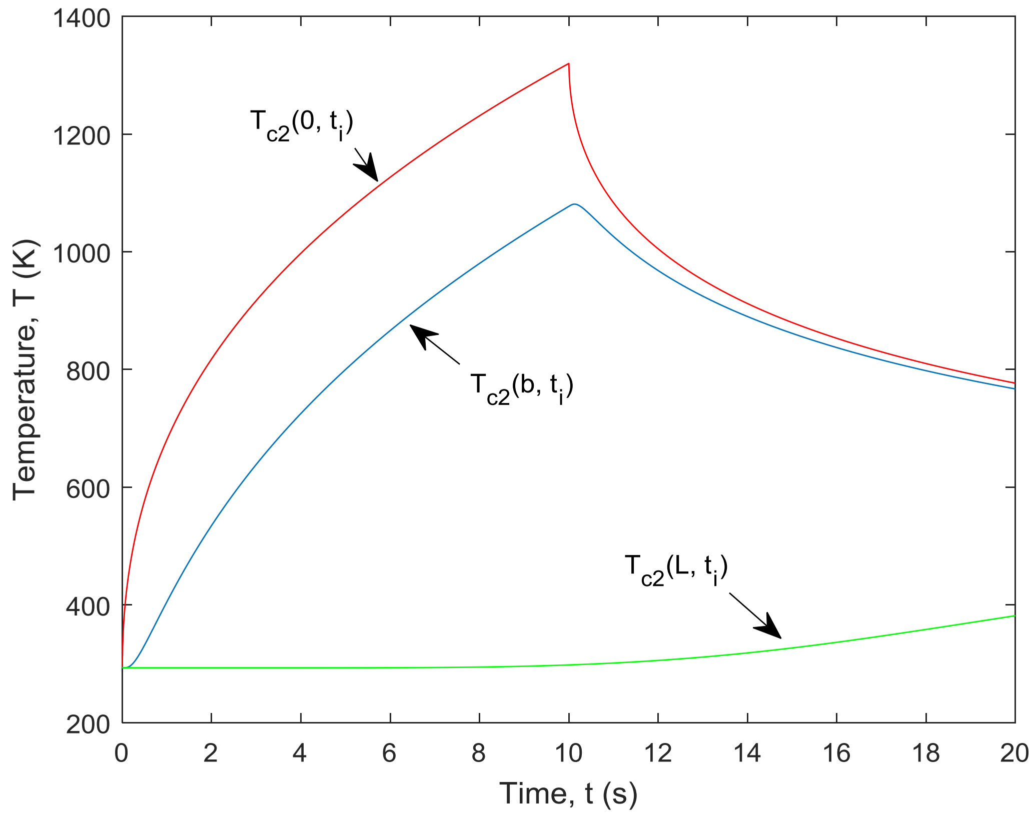

Fig. A-3.4b The positional temperatures at $x = 0$, $x = b$ and $x = L$ under the calibration test 2 obtained by the implicit finite difference scheme, $T_{c2}(0, t_i)$, $T_{c2}(b, t_i)$ and $T_{c2}(L, t_i)$, $t_i = i\Delta t$, $i = 1, 2, 3, \ldots, M$.

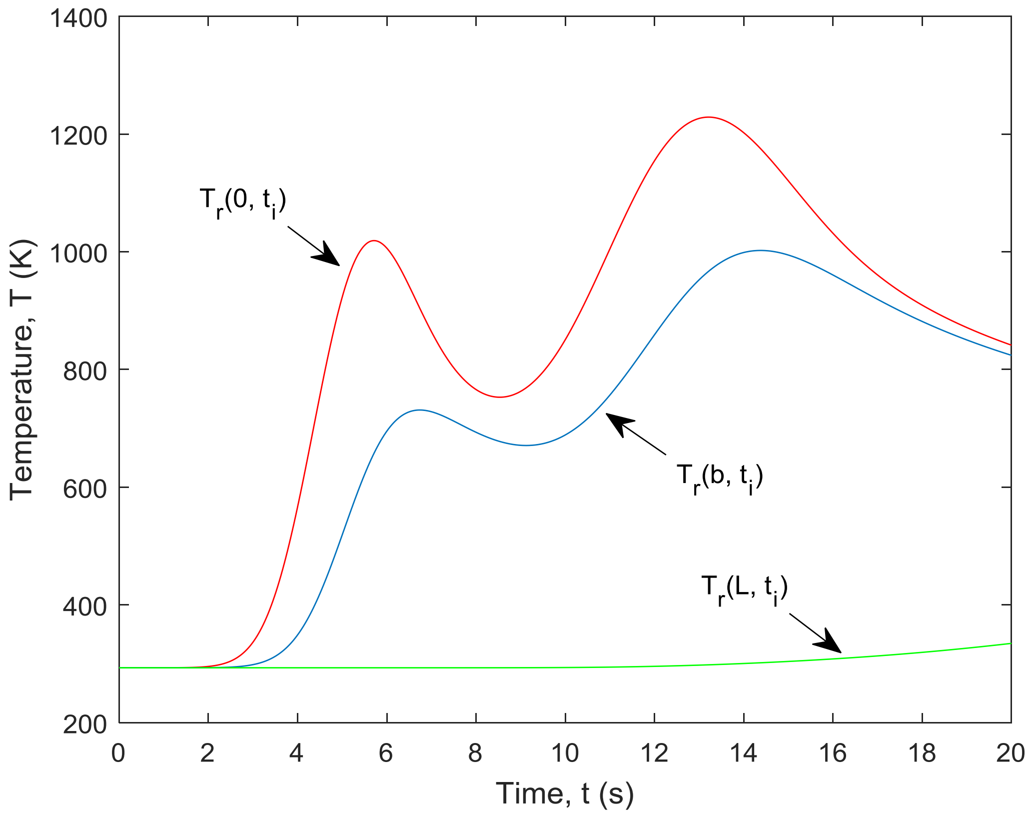

Fig. A-3.4c The positional temperatures at $x = 0$, $x = b$ and $x = L$ under the reconstruction test obtained by the implicit finite difference scheme, $T_r(0, t_i)$, $T_r(b, t_i)$ and $T_r(L, t_i)$, $t_i = i\Delta t$, $i = 1, 2, 3, \ldots, M$.

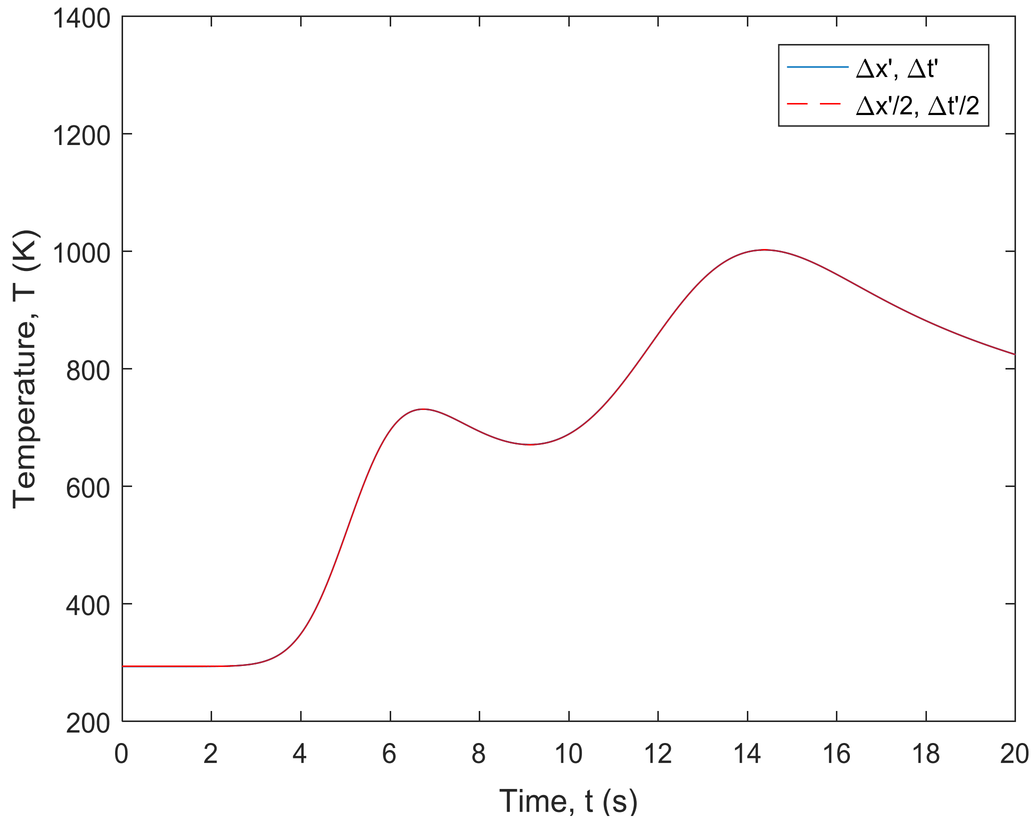

Fig. A-3.5 Convergence analysis by plotting $T(b, t_i)$ under reconstruction test obtained by the implicit finite difference scheme using spatial and temporal widths (Δx, Δt) and ($\Delta x/2$, $\Delta t/2$), respectively, where $\Delta x = 1.4111\times10^{-4}$ m, $\Delta t = 0.01$ s (from Table A-3.2).

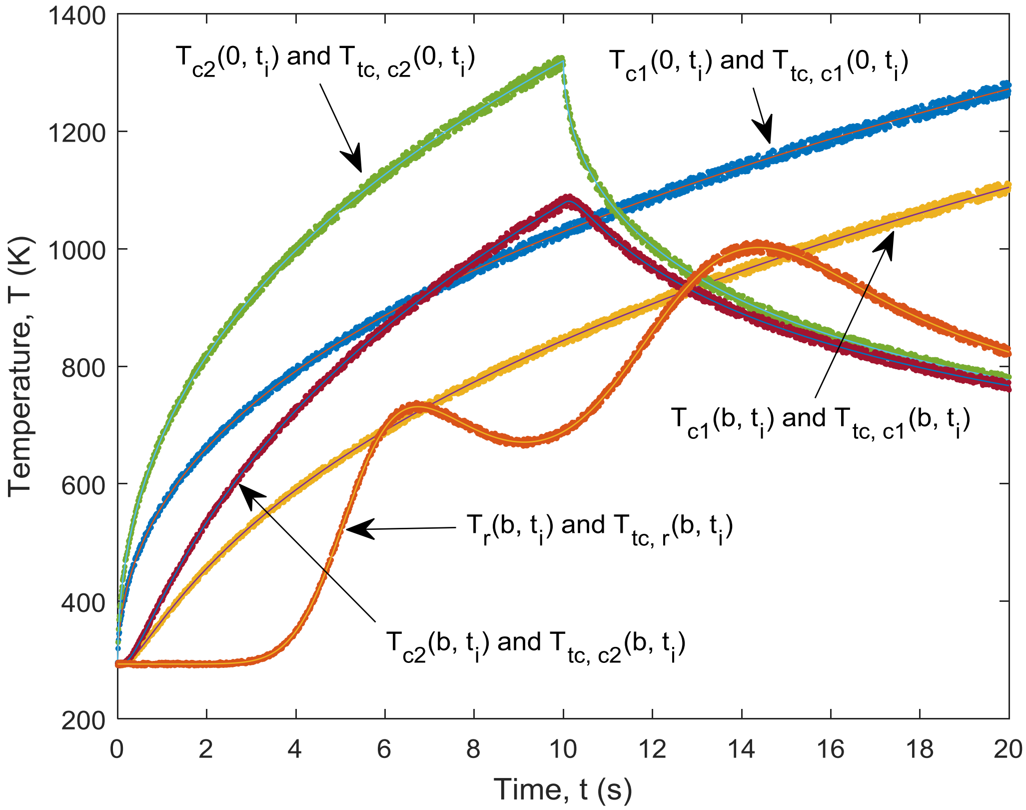

Fig. A-3.6 The positional temperatures $\{T_{c1}(0, t_i), T_{c1}(b, t_i)\}$, $\{T_{c2}(0, t_i), T_{c2}(b, t_i)\}$, $\{T_r(b, t_i)\}$ and noisy temperatures $\{T_{tc, c1}(0, t_i), T_{tc, c1}(b, t_i)\}$, $\{T_{tc, c2}(0, t_i), T_{tc, c2}(b, t_i)\}$, $\{T_{tc, r}(\mathrm{b}, t_i)\}$ under the calibration tests 1, 2 and reconstruction test, $t_i = i\Delta t$, $i = 1, 2, 3, \ldots, M$.

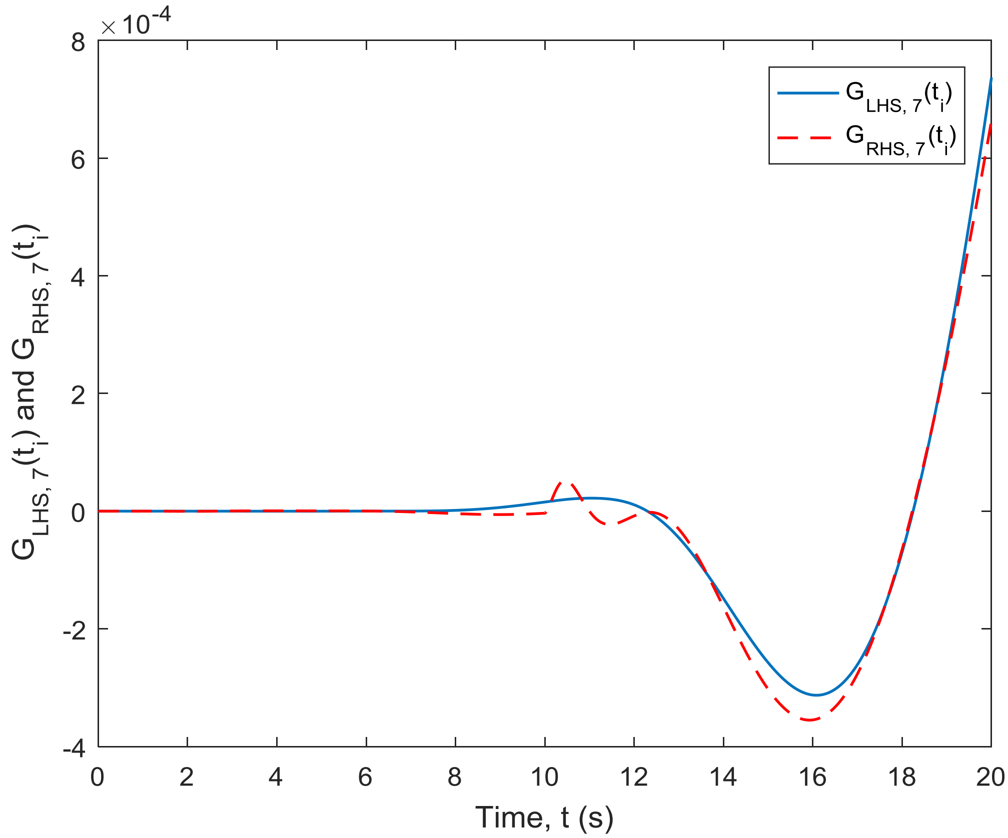

Fig. A-3.7 $G_{\mathrm{LHS},\,7}(t_i)$ and $G_{\mathrm{RHS},\,7}(t_i)$ defined in Eqs. (25b, c) by using noiseless temperatures at x = 0, b in calibration test 1 and test 2 denoted as $T_{c1}(0, t_i)$ and $T_{c1}(b, t_i)$, $T_{c2}(0, t_i)$ and $T_{c2}(b, t_i)$, $t_i = i\Delta t$, i = 1, 2, 3, … , M, and $\{a_0^7, a_2^7, a_3^7, \ldots, a_7^7\}$ listed in column 2 of Table A-3.3.

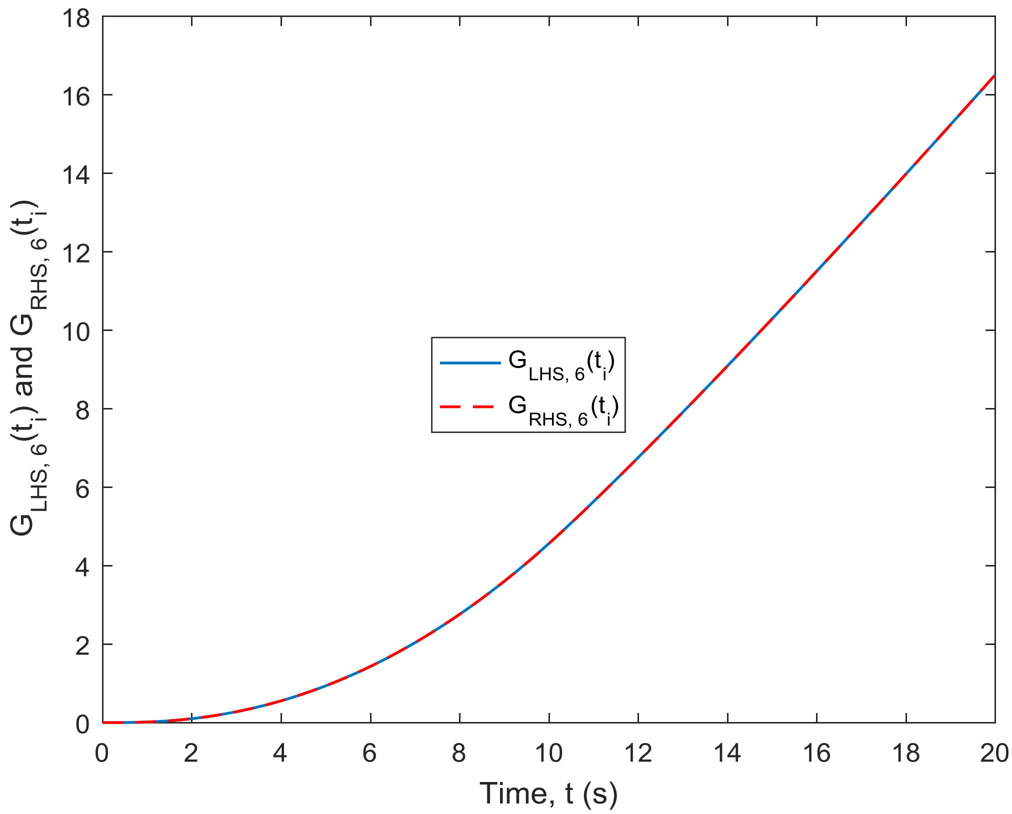

Fig. A-3.8 $G_{\mathrm{LHS},\,6}(t_i)$ and $G_{\mathrm{RHS},\,6}(t_i)$ defined in Eqs. (25b, c) by using noiseless temperatures at x = 0, b in calibration test 1 and test 2 denoted as $T_{c1}(0, t_i)$ and $T_{c1}(b, t_i)$, $T_{c2}(0, t_i)$ and $T_{c2}(b, t_i)$, $t_i = i\Delta t$, i = 1, 2, 3, … , M, and $\{a_0^6, a_2^6, a_3^6, \ldots, a_6^6\}$ obtained by noiseless data listed in column 3 of Table A-3.3.

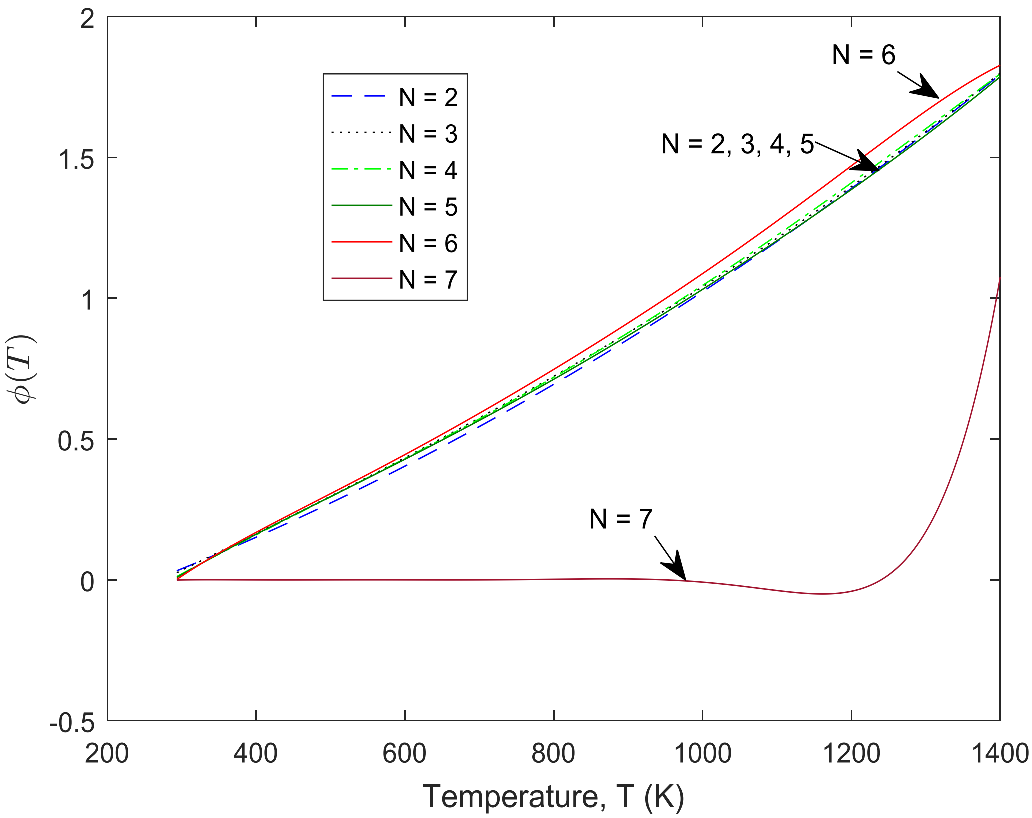

Fig. A-3.9 The transformed variable $\phi(T)$ as a function of temperature defined in Eq. (9) and Eqs. (10a, b) in the temperature range [293.15, 1400] K using the calculated coefficients $\{a_0^N, a_2^N, a_3^N, \ldots, a_N^N\}$ under six different N numbers (values are listed in Table A-3.3, noiseless data).

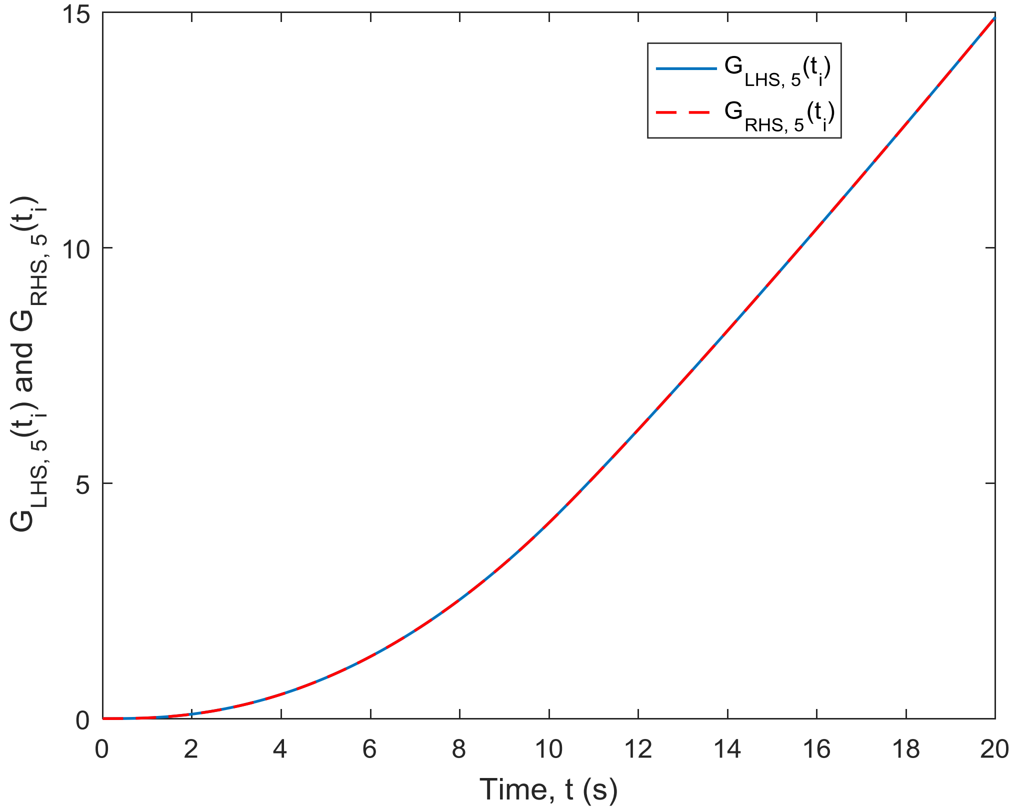

Fig. A-3.10 $G_{\mathrm{LHS},\ 5}(t_i)$ and $G_{\mathrm{RHS},\ 5}(t_i)$ defined in Eqs. (25b, c) by using noiseless temperatures at $x = 0$, b in calibration test 1 and test 2 denoted as $T_{c1}(0, t_i)$ and $T_{c1}(b, t_i)$, $T_{c2}(0, t_i)$ and $T_{c2}(b, t_i)$, $t_i = i\Delta t$, $i = 1, 2, 3, \ldots, M$, and $\{a_0^5, a_2^5, a_3^5, a_4^5, a_5^5\}$ obtained by noiseless data listed in column 4 of Table A-3.3.

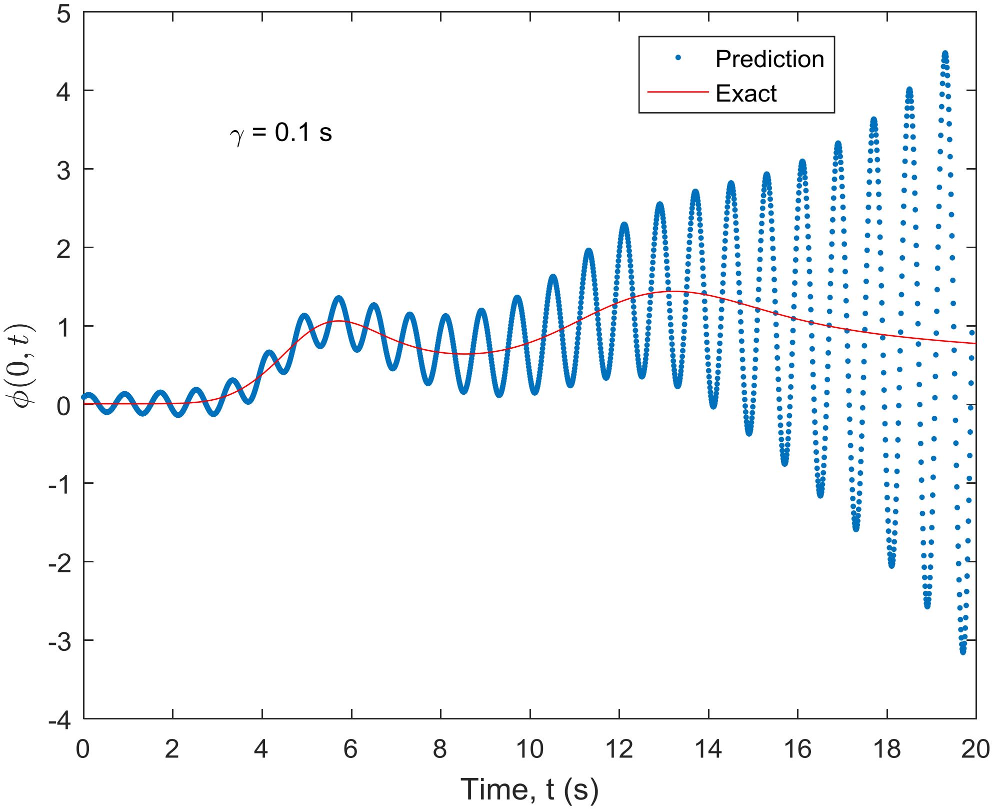

Fig. A-3.11a The exact transform variable $\phi_r(0, t_i)$ and the predicted transform variable in the reconstruction test $\phi_{r,\gamma_m}(0, t_i)$, using noiseless data $T_{c1}(0, t_i)$, $T_{c1}(b, t_i)$ and $T_r(b, t_i)$, and the calculated coefficients $\{a_0^5, a_2^5, a_3^5, a_4^5, a_5^5\}$ (listed in column 4 of Table A-3.3 (γ_m = 0.1 s).

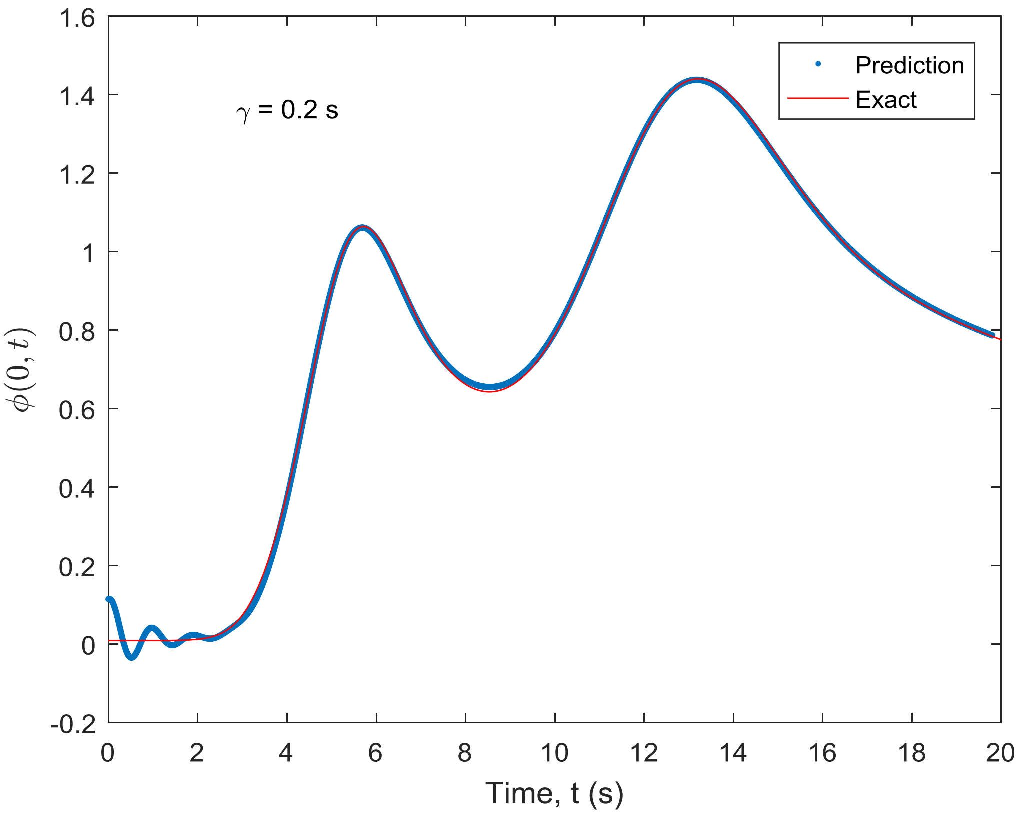

Fig. A-3.11b The exact transform variable $\phi_r(0,t_i)$ and the predicted transform variable in the reconstruction test $\phi_{r,\gamma_m}(0,t_i)$, using noiseless data $T_{c1}(0, t_i)$, $T_{c1}(b, t_i)$ and $T_r(b, t_i)$, and the calculated coefficients $\{a_0^5, a_2^5, a_3^5, a_4^5, a_5^5\}$ listed in column 4 of Table A-3.3 (γ_m = 0.2 s).

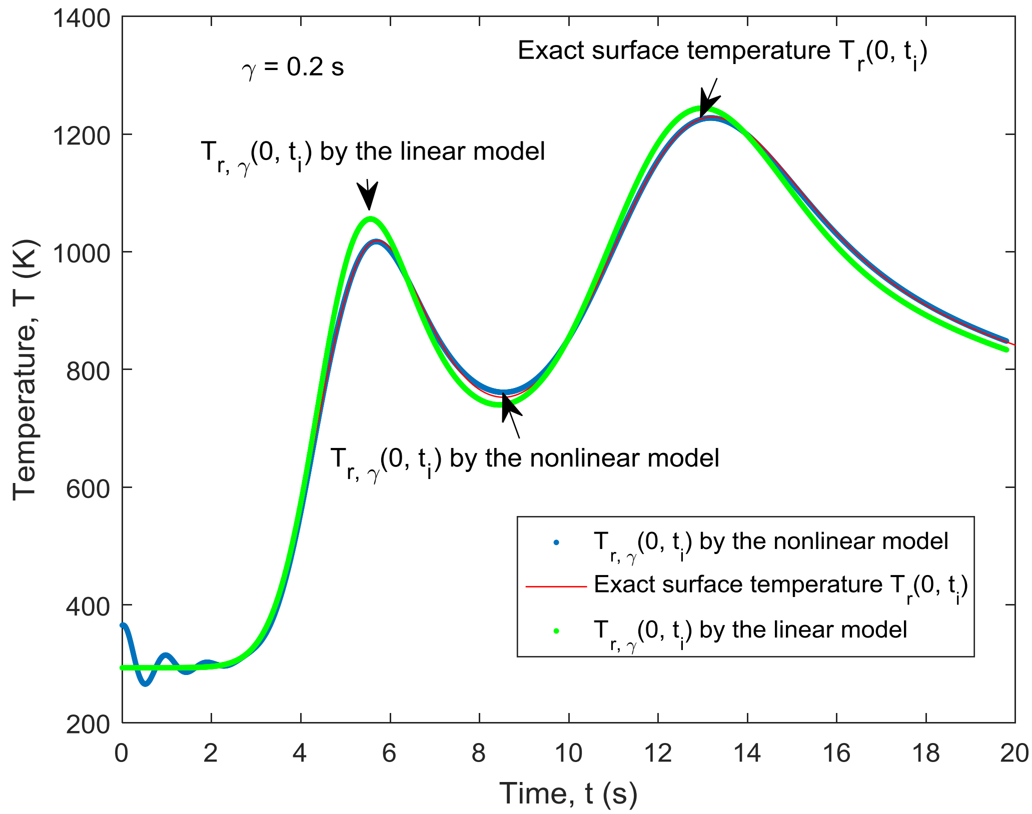

Fig. A-3.12 Comparison of the exact temperature $T_r(0,t_i)$, the corresponding predicted surface temperature $T_{r,\gamma_m}(0,t_i)$ to the predicted transform variable $\phi_{r,\gamma_m}(0,t_i)$ in Fig. A-3.11b (nonlinear model) and the predicted surface temperature $T_{r,\gamma_m}(0,t_i)$ using the linear temperature calibration integral equation given in Eq. (1) (noiseless data, γ_m = 0.2 s).

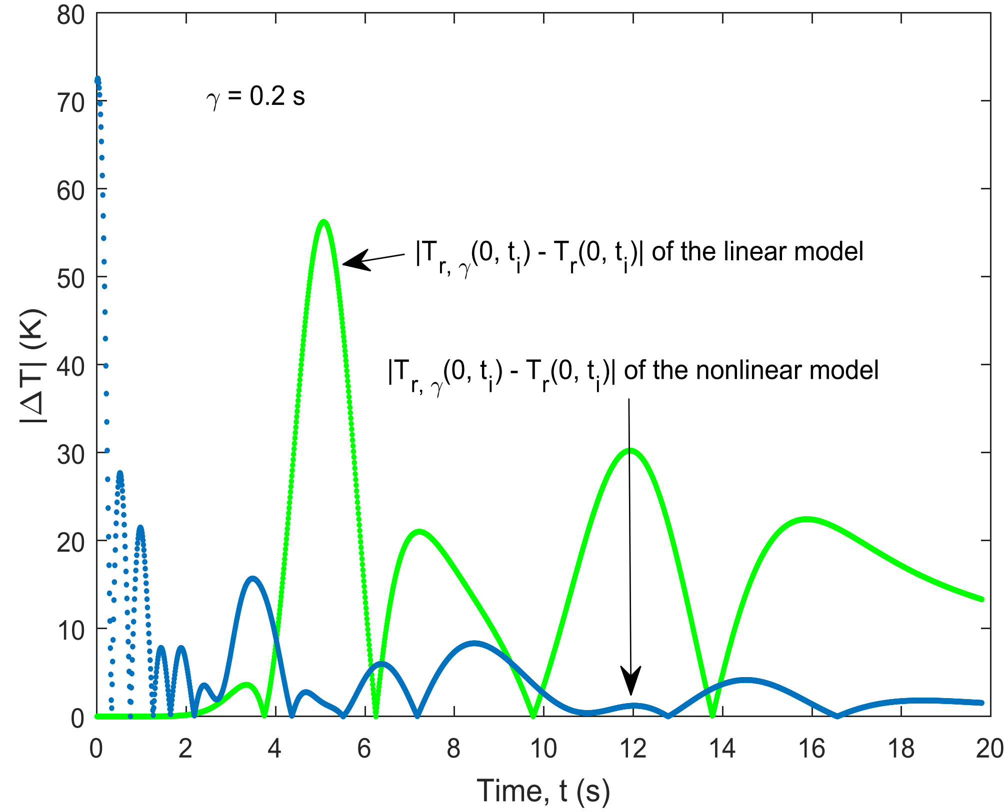

Fig. A-3.13 Comparison of the absolute error between surface temperature prediction $T_{r,\gamma_m}(0,t_i)$ by the nonlinear model and the linear model given in Eq. (1) (noiseless data, γ_m = 0.2 s).

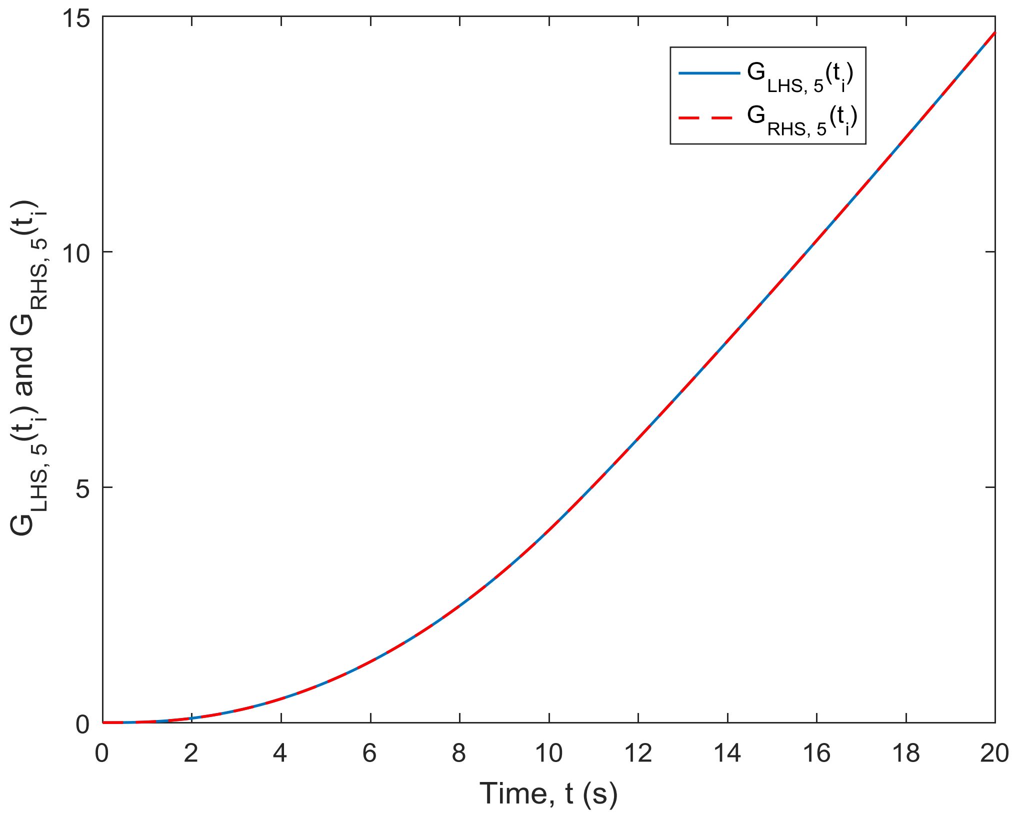

Fig. A-3.14 $G_{\mathrm{LHS},\,5}(t_i)$ and $G_{\mathrm{RHS},\,5}(t_i)$ defined in Eqs. (25b, c) by using $\{a_0^5, a_2^5, a_3^5, a_4^5, a_5^5\}$ listed in column 4 of Table A-3.6 (noisy data).

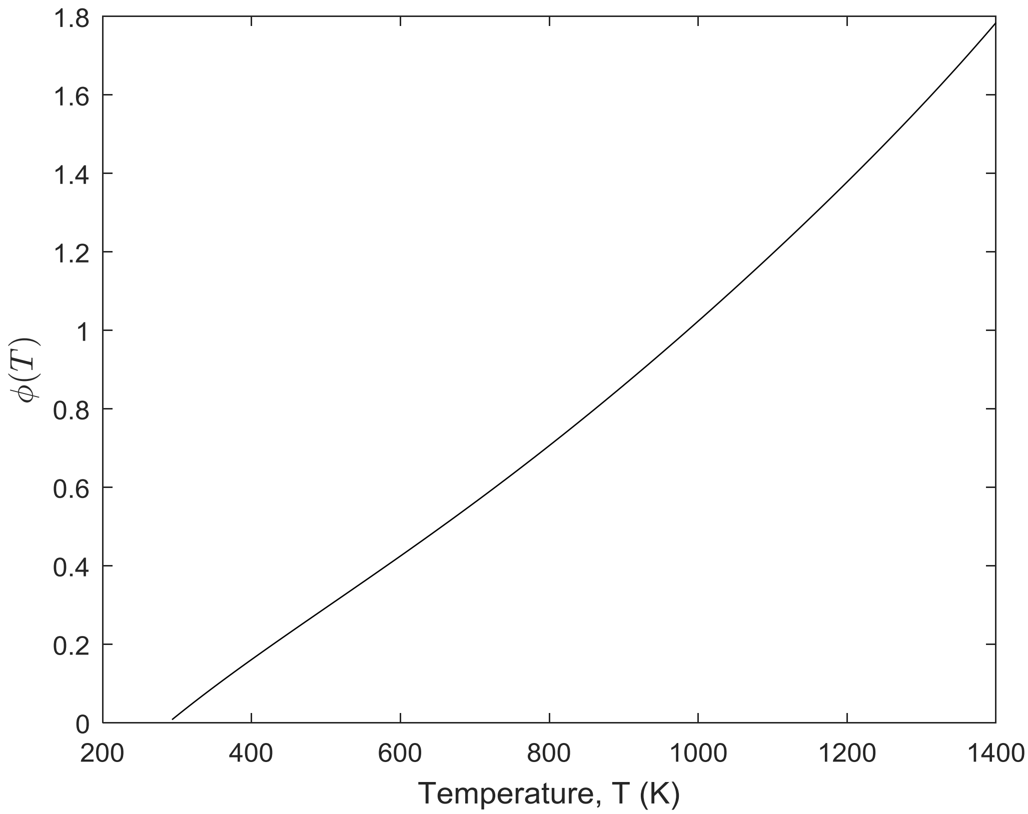

Fig. A-3.15 The transformed variable $\phi(T)$ as a function of temperature defined in Eq. (9) and Eqs. (10a, b) in the temperature range [293.15, 1400] K using the calculated coefficients $\{a_0^5, a_2^5, a_3^5, a_4^5, a_5^5\}$ listed in column 4 of Table A-3.6 (noisy data).

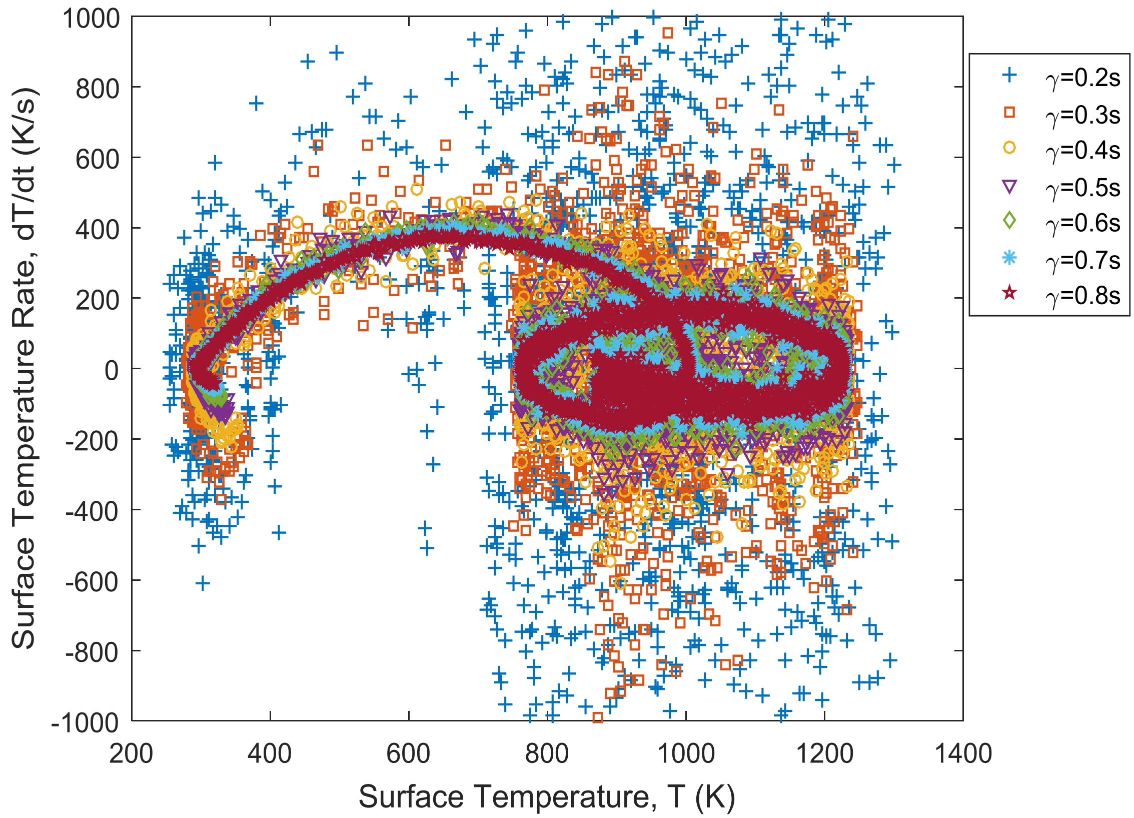

Fig. A-3.16a The predicted surface temperature and surface temperature rate phase planes for the future-time parameter spectrum γ = [0.2, 0.3, 0.4, 0.5, 0.6, 0.7, 0.8] s ($\{a_0^5, a_2^5, a_3^5, a_4^5, a_5^5\}$ listed in column 4 of Table A-3.6).

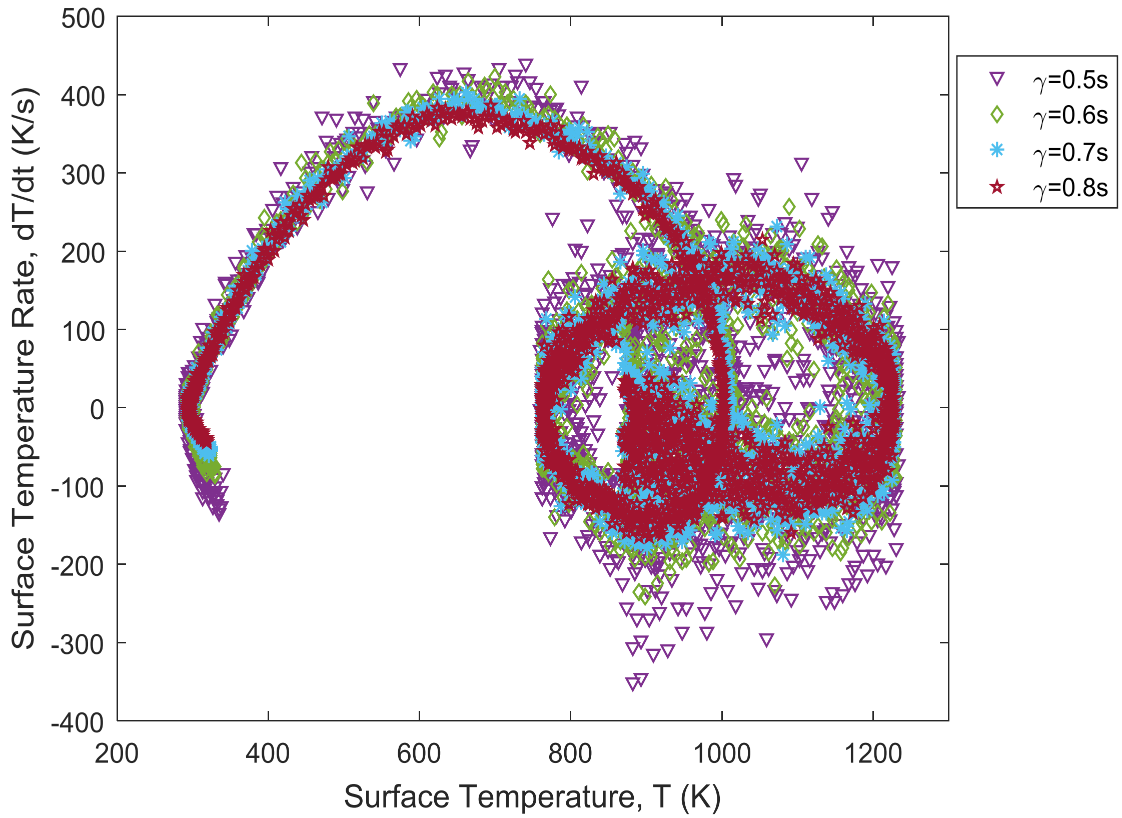

Fig. A-3.16b The predicted surface temperature and surface temperature rate phase planes for the future-time parameter spectrum γ = [0.5, 0.6, 0.7, 0.8] s ($\{a_0^5, a_2^5, a_3^5, a_4^5, a_5^5\}$ listed in column 4 of Table A-3.6).

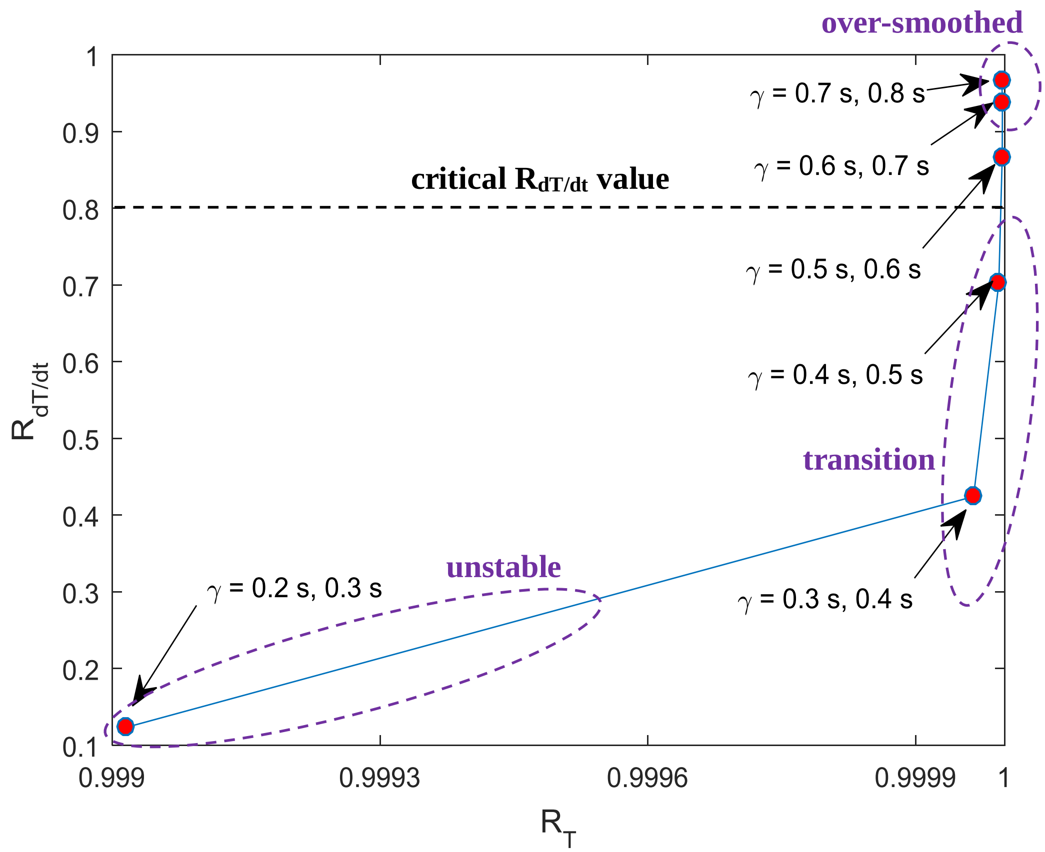

Fig. A-3.17 The predicted surface temperature rate and surface temperature cross-correlation coefficient phase planes for the for the future-time parameter spectrum γ = [0.2, 0.3, 0.4, 0.5, 0.6, 0.7, 0.8] s ($\{a_0^5, a_2^5, a_3^5, a_4^5, a_5^5\}$ listed in column 4 of Table A-3.6).

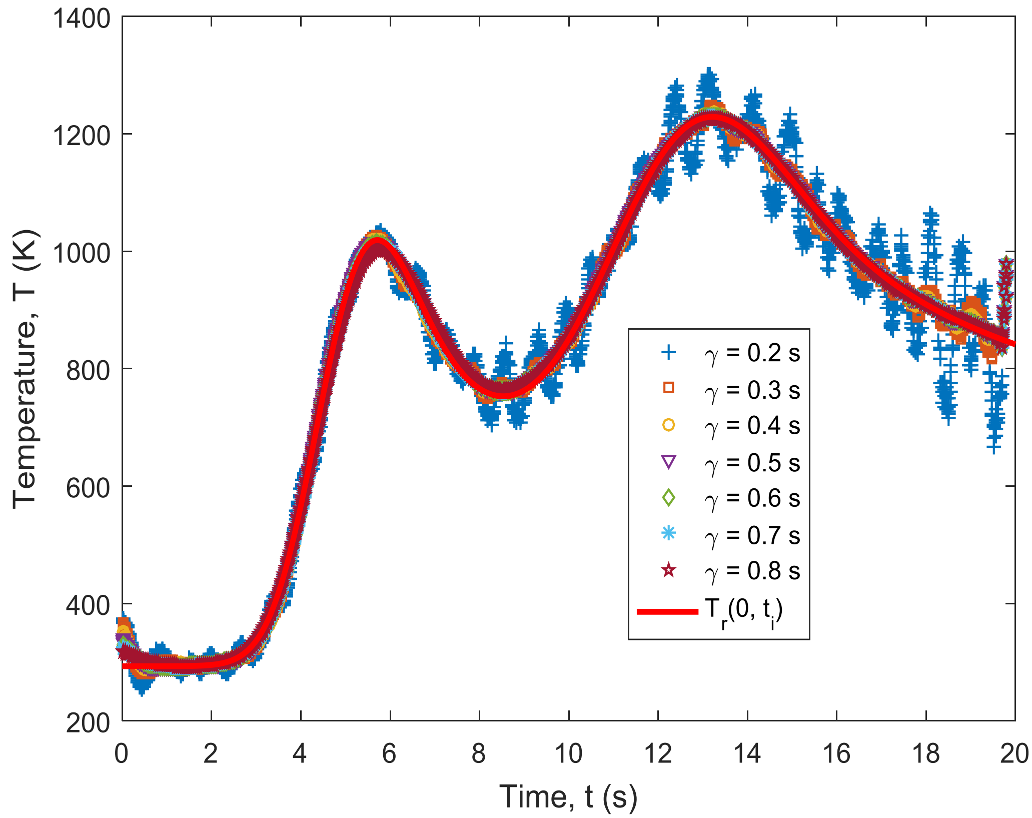

Fig. A-3.18 The exact surface temperature $T_r(0,t_i)$ and predicted surface temperature $T_{r,\gamma}(0,t_i)$ over a chosen future-time parameter spectrum γ = [0.2, 0.3, 0.4, 0.5, 0.6, 0.7, 0.8] s ($\{a_0^5, a_2^5, a_3^5, a_4^5, a_5^5\}$ listed in column 4 of Table A-3.6).

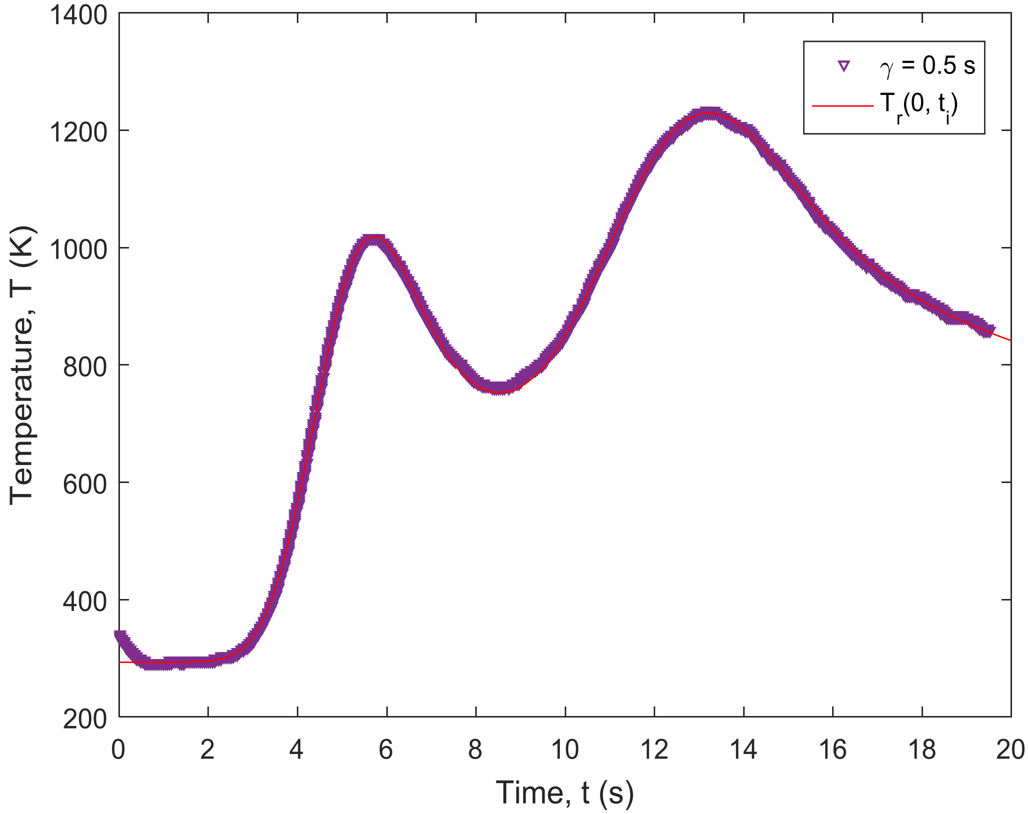

Fig. A-3.19 The exact surface temperature $T_r(0,t_i)$ and predicted surface temperature $T_{r,\gamma}(0,t_i)$ using future-time parameter γ = 0.5 s ($\{a_0^5, a_2^5, a_3^5, a_4^5, a_5^5\}$ listed in column 4 of Table A-3.6).

Table A-3.1 Some Chebyshev polynomials of the first kind [86] for mapped temperature as a variable.

E_n	Polynomial
E_0	1
E_1	T^*
E_2	$2T^{*2}-1$
E_3	$4T^{*3}-3T^*$
E_4	$8T^{*4}-8T^{*2}+1$
E_5	$16T^{*5}-20T^{*3}+5T^*$
E_6	$32T^{*6}-48T^{*4}+18T^{*2}-1$
E_7	$64T^{*7}-112T^{*5}+56T^{*3}-7T^*$

Table A-3.2 Thermophysical properties of stainless steel 304 [80] and parameters for the simulation.

Property	Value
b	2.54×10^{-3} m
c	$6.683+0.04906\times T+80.74\times\ln(T)$ J/(kg·K) [80]
$f_{sampling}$	100 Hz
k	$9.705+0.0176\times T-1.60\times10^{-6}\times T^2$ W/(m·K) [80]
L	2.54×10^{-2} m
M	2000
M_f	10
$q''_{c1,\max}$	2×10^6 W/m^2
$q''_{c2,\max}$	3×10^6 W/m^2
$q''_{r,\max}$	5×10^6 W/m^2
$t_{\max}$	20 s
Δt	0.01 s
T_0	293.15 K
T_L	273 K
T_U	1500 K
Δx	1.4111×10^{-4} m
ρ	7920 kg/m^3 [80]
ε_T	0.01

Table A-3.2 Continued

Property	Value
β_1	$t_{max}/4$ s
β_2	$0.6t_{max}$ s
σ_1	$t_{max}/15$ s
σ_2	$t_{max}/8$ s

Table A-3.3 Numerically calculated coefficients in the transformed variable $\phi(x, t)$ in Eq. (3.10) with $a_1^N \triangleq 1$ using noiseless data (t_{max} = 20 s).

Coefficients	$N = 7$	$N = 6$	$N = 5$	$N = 4$	$N = 3$	$N = 2$
a_0^N	0.5274	0.9411	0.9238	0.9285	0.9332	0.9215
a_2^N	0.8452	0.0273	0.0752	0.0649	0.0771	0.0895
a_3^N	0.6254	-0.0242	0.0158	0.0031	0.0109	N/A
a_4^N	0.3895	-0.0305	-0.0025	-0.0079	N/A	N/A
a_5^N	0.1932	-0.0079	0.0038	N/A	N/A	N/A
a_6^N	0.0681	-0.0062	N/A	N/A	N/A	N/A
a_7^N	0.0138	N/A	N/A	N/A	N/A	N/A

Table A-3.4 Sequential coefficient study for N = 6 using noiseless data collected up to 20s, 18s, 16s, and 14s, respectively.

Coefficients	t_{max} = 20 s	t'_{max} = 18 s	t'_{max} = 16 s	t'_{max} = 14 s
a_0^N	0.9411	0.5357	0.9480	0.9483
a_2^N	0.0273	0.8096	0.0238	0.0373
a_3^N	-0.0242	0.5486	-0.0237	-0.0064
a_4^N	-0.0305	0.2974	-0.0302	-0.0197
a_5^N	-0.0079	0.1150	-0.0086	-0.0038
a_6^N	-0.0062	0.0265	-0.0063	-0.0042

Table A-3.5 Sequential coefficient study for N = 5 using noiseless data collected up to 20s, 18s, 16s, and 14s, respectively.

Coefficients	t_{max} = 20 s	t'_{max} = 18 s	t'_{max} = 16 s	t'_{max} = 14 s
a_0^N	0.9238	0.9255	0.9309	0.9386
a_2^N	0.0752	0.0754	0.0721	0.0687
a_3^N	0.0158	0.0168	0.0170	0.0214
a_4^N	-0.0025	-0.0018	-0.0019	-0.0008
a_5^N	0.0038	0.0038	0.0033	0.0042

Table A-3.6 Numerically calculated coefficients in the transformed variable $\phi(x, t)$ in Eq. (3.10) with $a_1^N \triangleq 1$ using noisy data ($t_{\max}$ = 20 s).

Coefficients	$N = 7$	$N = 6$	$N = 5$	$N = 4$	$N = 3$	$N = 2$
a_0^N	0.5274	0.9265	0.9204	0.9254	0.9302	0.9168
a_2^N	0.8449	0.0631	0.0799	0.0608	0.0806	0.0949
a_3^N	0.6250	0.0043	0.0183	0.0046	0.0123	N/A
a_4^N	0.3891	-0.0117	-0.0019	-0.0077	N/A	N/A
a_5^N	0.1930	-0.0000	0.0041	N/A	N/A	N/A
a_6^N	0.0681	-0.0022	N/A	N/A	N/A	N/A
a_7^N	0.0139	N/A	N/A	N/A	N/A	N/A

Table A-3.7 Sequential coefficient study for $N = 6$ using noisy data collected up to 20s, 18s, 16s, and 14s, respectively.

Coefficients	t_{max} = 20 s	t'_{max} = 18 s	t'_{max} = 16 s	t'_{max} = 14 s
a_0^N	0.9265	0.5329	0.9356	0.9356
a_2^N	0.0631	0.8227	0.0550	0.0561
a_3^N	0.0043	0.5709	0.0010	0.0026
a_4^N	-0.0117	0.3188	-0.0141	-0.0132
a_5^N	-0.0000	0.1270	-0.0020	-0.0015
a_6^N	-0.0022	0.0302	-0.0030	-0.0028

Table A-3.8 Sequential coefficient study for $N = 5$ using noisy data collected up to 20s, 18s, 16s, and 14s, respectively.

Coefficients	t_{max} = 20 s	t'_{max} = 18 s	t'_{max} = 16 s	t'_{max} = 14 s
a_0^N	0.9204	0.9235	0.9276	0.9294
a_2^N	0.0799	0.0801	0.0777	0.0769
a_3^N	0.0183	0.0202	0.0202	0.0213
a_4^N	-0.0019	-0.0007	-0.0007	-0.0004
a_5^N	0.0041	0.0041	0.0037	0.0039

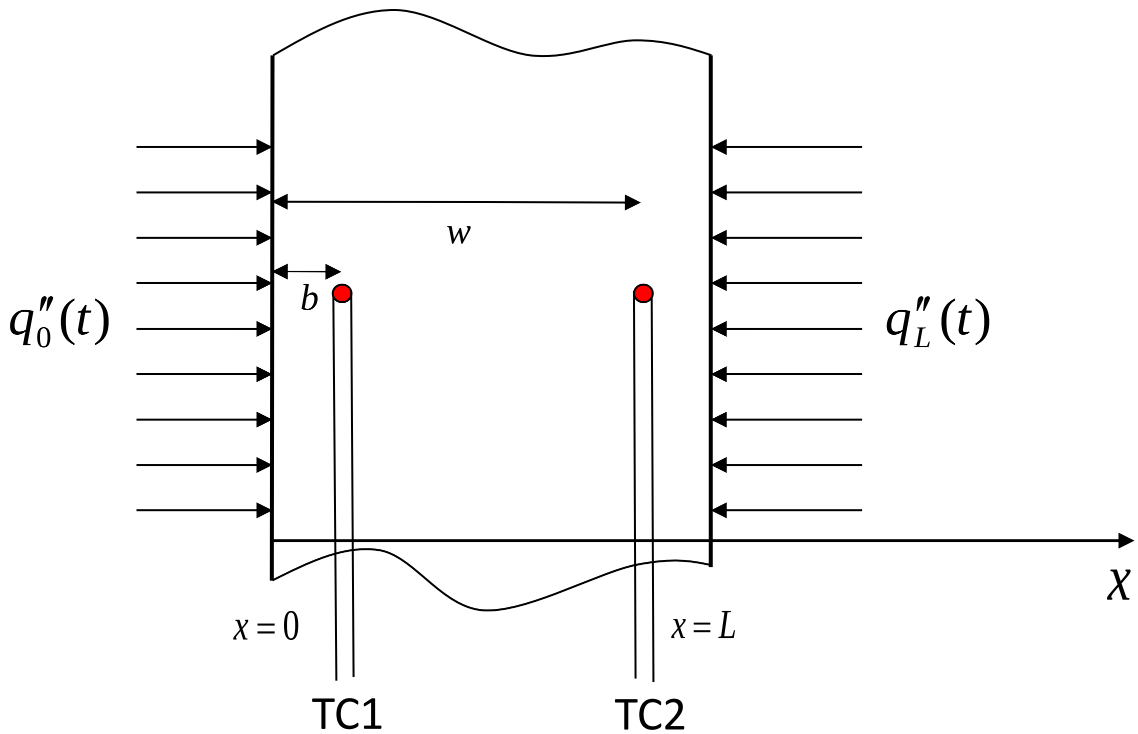

Fig. A-4.1 Schematic for one-dimensional heat conduction with two in-depth thermocouples.

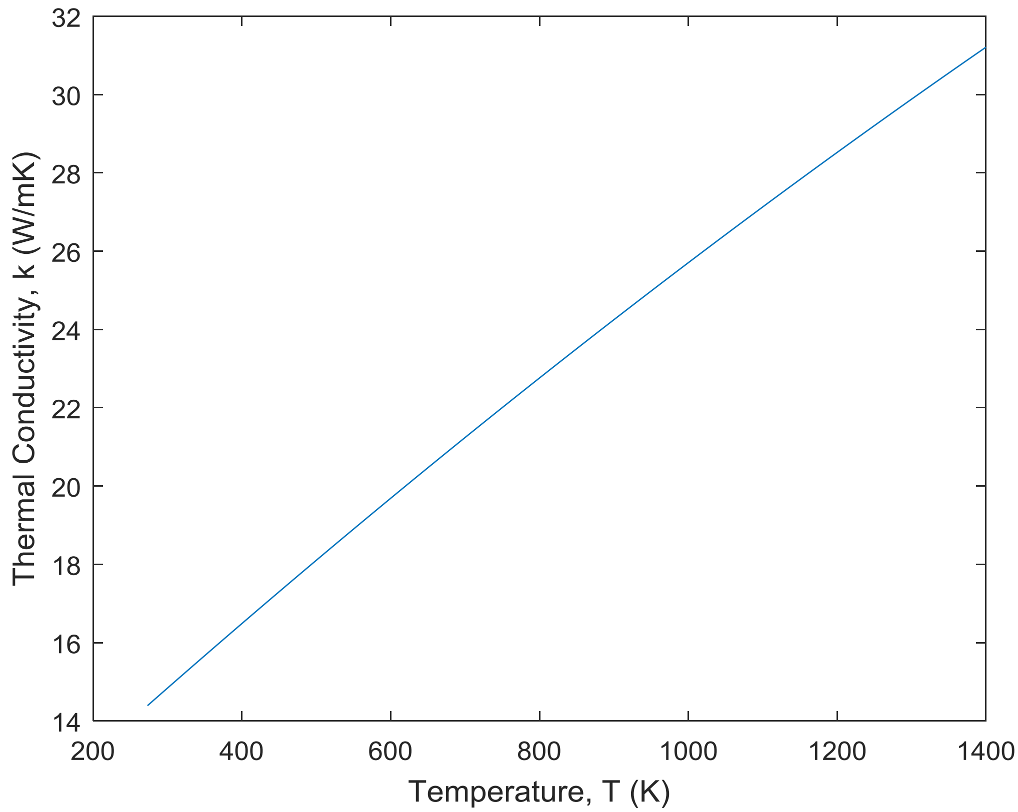

Fig. A-4.2a Thermal conductivity, $k(T)$ as a function of temperature for SS 304 [80].

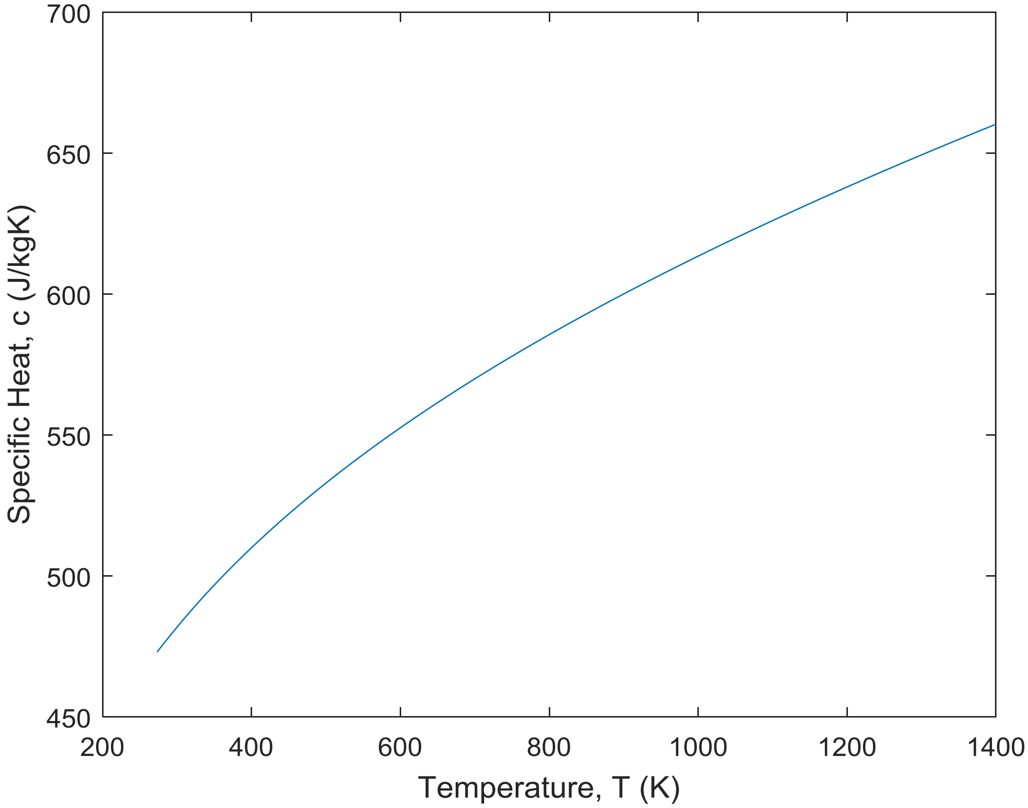

Fig. A-4.2b Specific heat, $c(T)$ as a function of temperature for SS 304 [80].

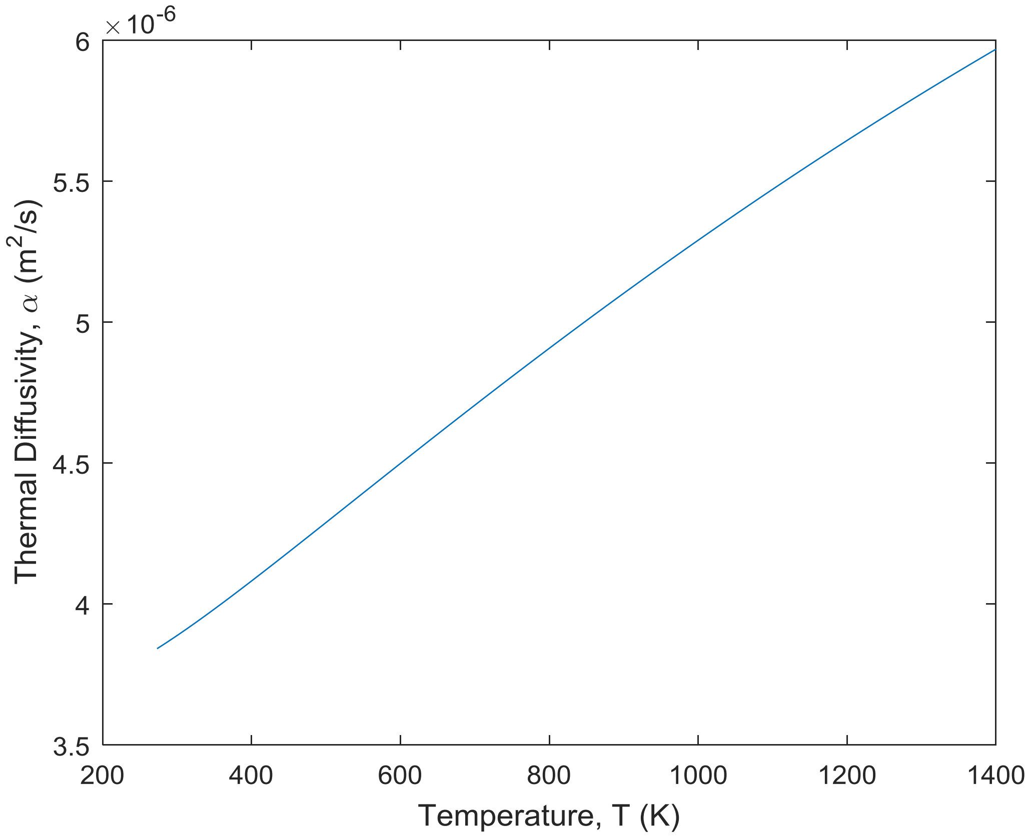

Fig. A-4.2c Thermal diffusivity, $\alpha(T)$ as a function of temperature for SS 304 [80].

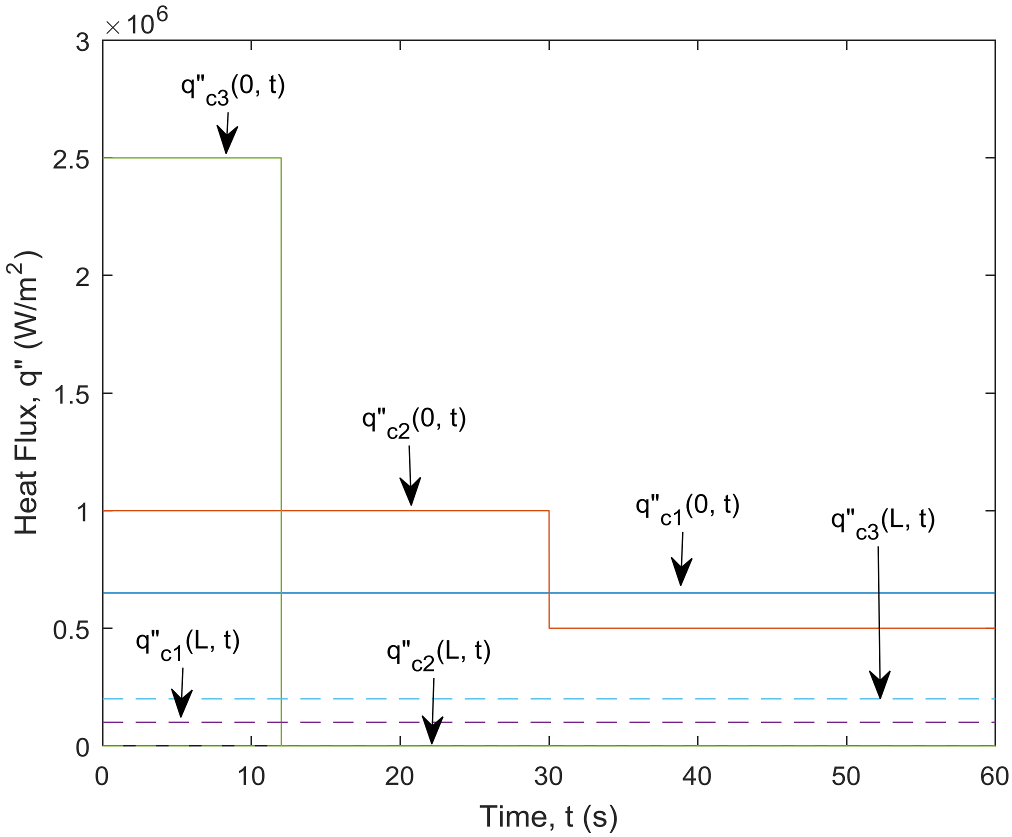

Fig. A-4.3a The imposed front surface heat fluxes $q''_{c1}(0,t), q''_{c2}(0,t), q''_{c3}(0,t)$, and back surface heat fluxes $q''_{c1}(L,t), q''_{c2}(L,t), q''_{c3}(L,t)$ in the calibration test 1, 2 and 3, respectively.

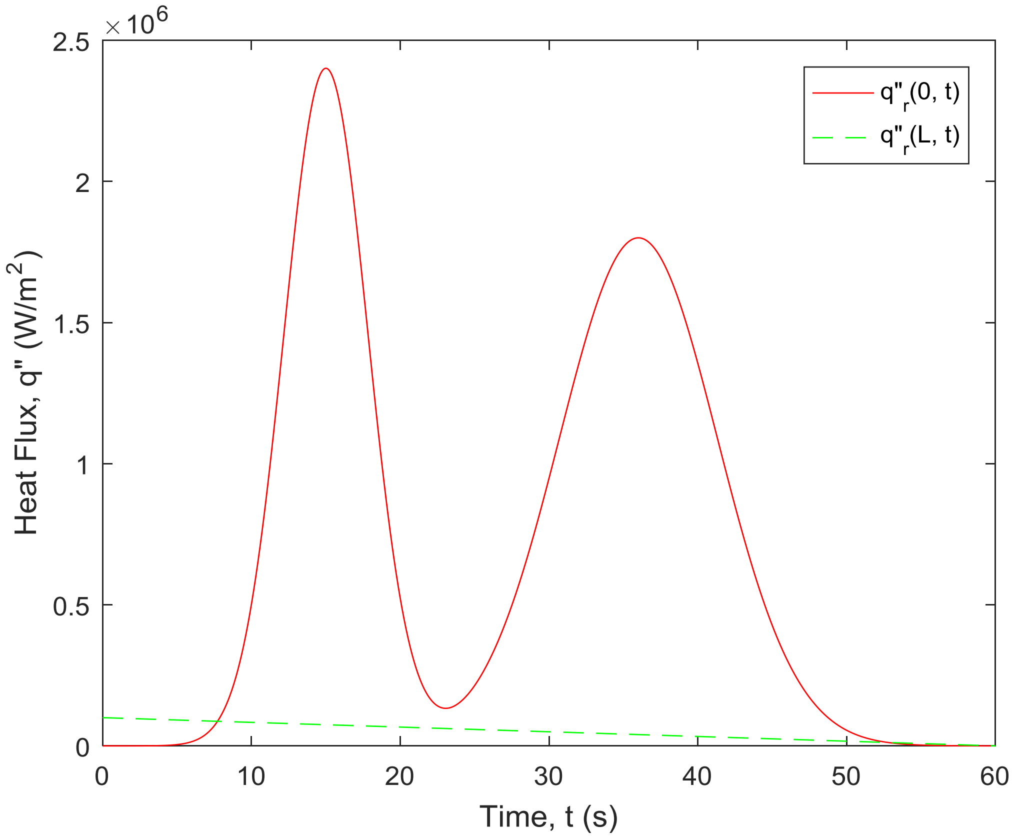

Fig. A-4.3b The imposed front surface heat flux $q_r''(0,t)$, and back surface heat flux $q_r''(L,t)$ in the reconstruction test.

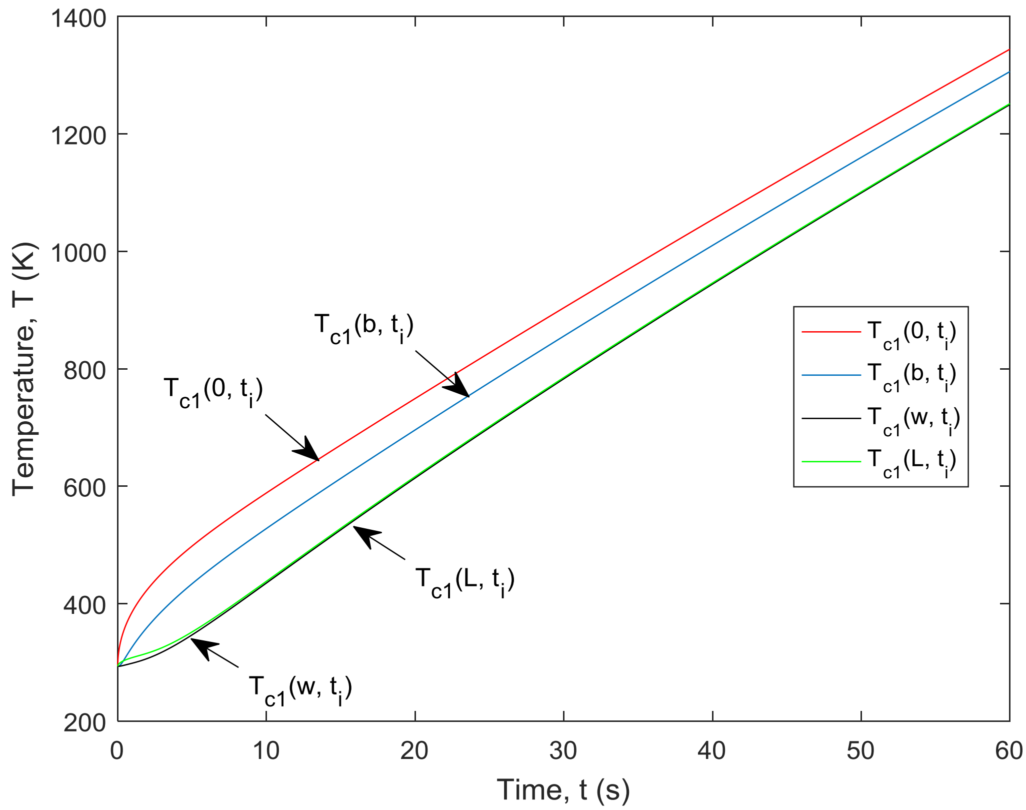

Fig. A-4.4a The positional temperature at x = 0, b, w, L denoted by $T_{c1}(0, t_i)$, $T_{c1}(b, t_i)$, $T_{c1}(w, t_i)$ and $T_{c1}(L, t_i)$ in the calibration test 1.

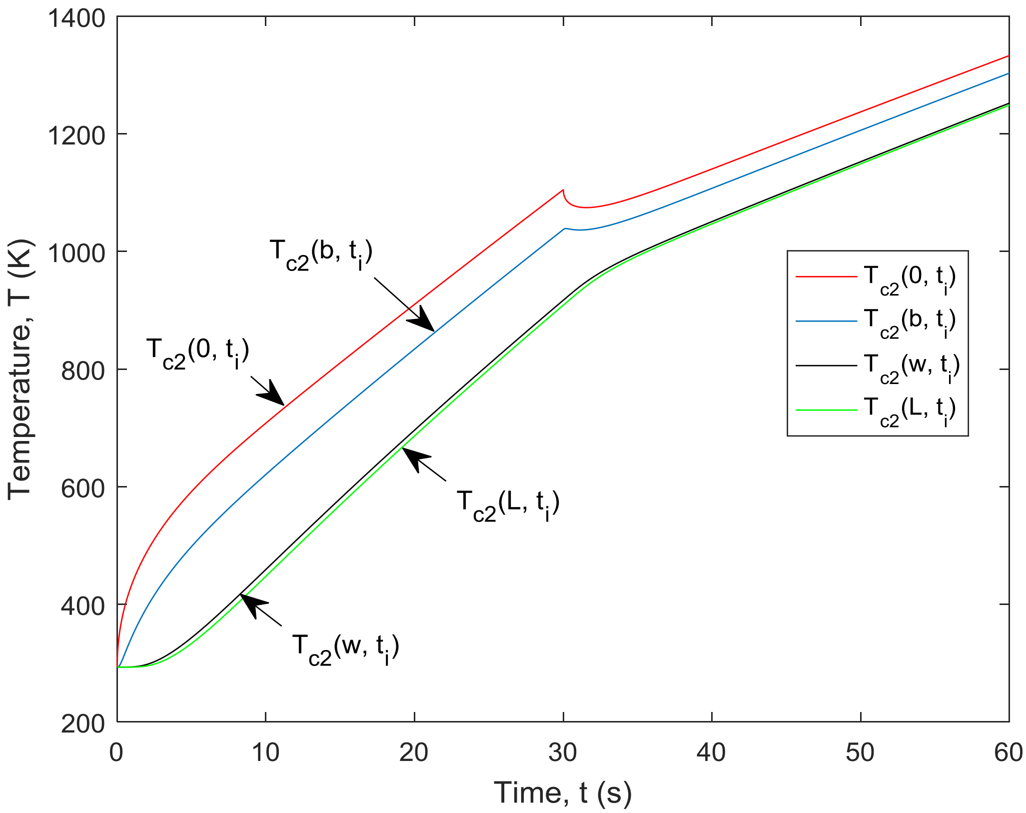

Fig. A-4.4b The positional temperature at x = 0, b, w, L denoted by $T_{c2}(0, t_i)$, $T_{c2}(b, t_i)$, $T_{c2}(w, t_i)$ and $T_{c2}(L, t_i)$ in the calibration test 2.

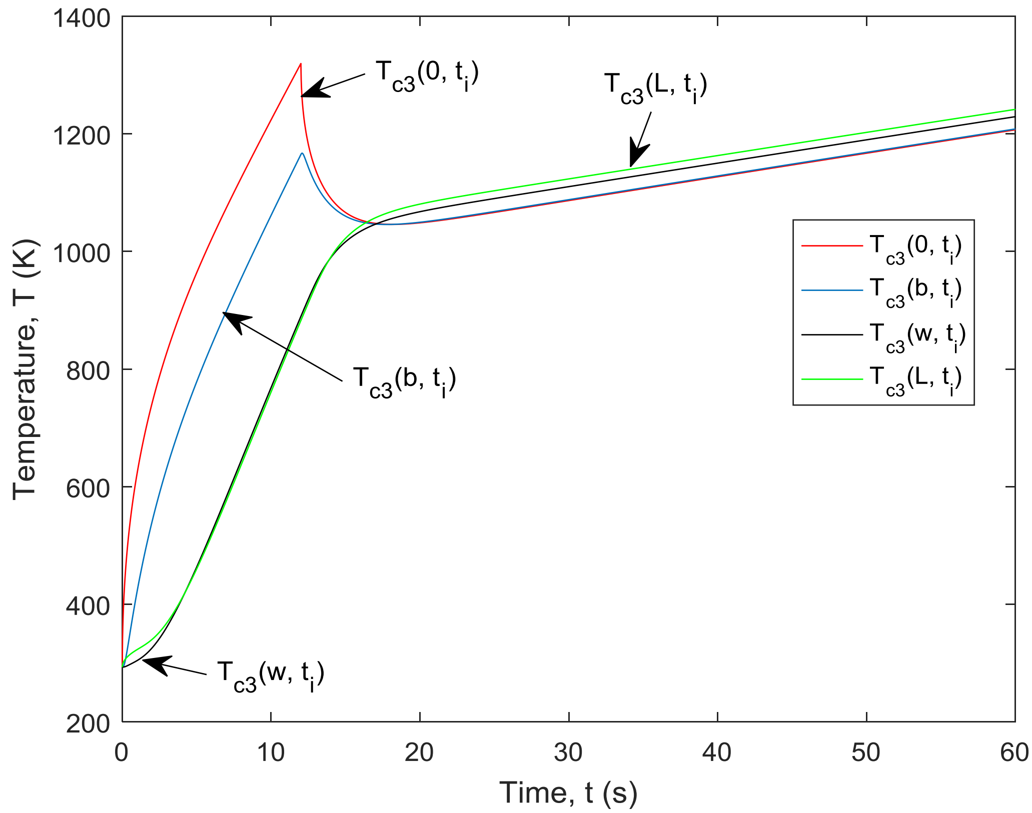

Fig. A-4.4c The positional temperature at x = 0, b, w, L denoted by $T_{c3}(0, t_i)$, $T_{c3}(b, t_i)$, $T_{c3}(w, t_i)$ and $T_{c3}(L, t_i)$ in the calibration test 3.

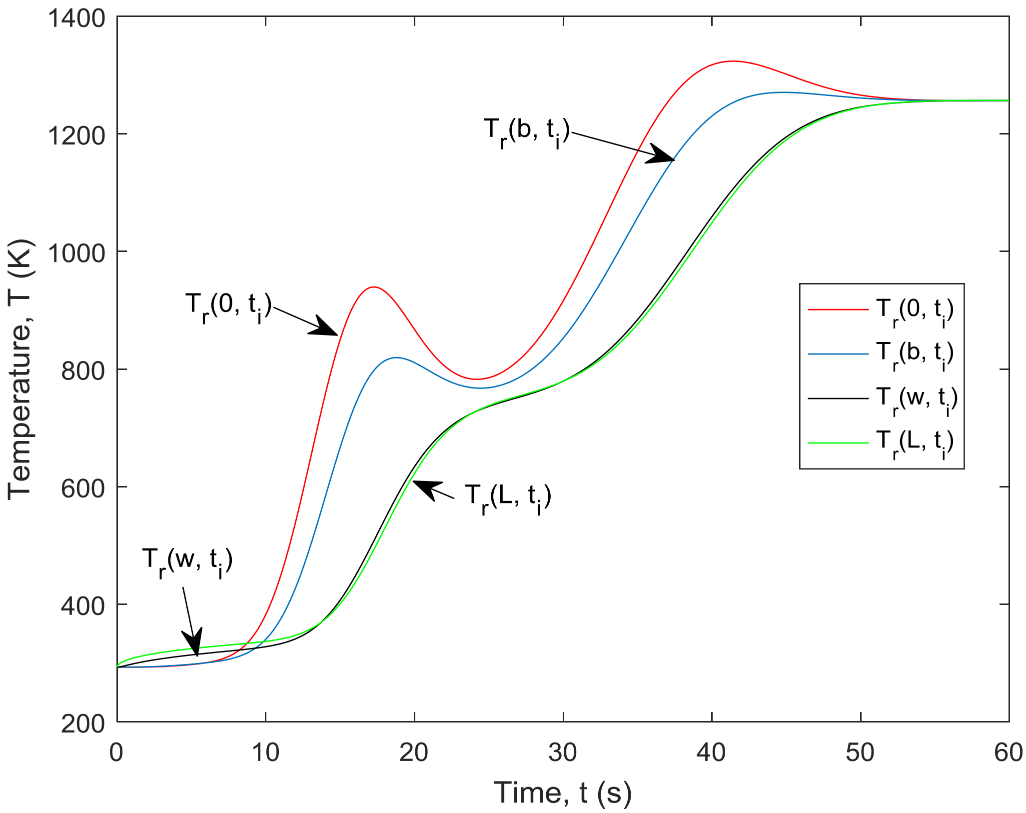

Fig. A-4.4d The positional temperature at $x = 0$, b, w, L denoted by $T_r(0, t_i)$, $T_r(b, t_i)$, $T_r(w, t_i)$ and $T_r(L, t_i)$ in the reconstruction test.

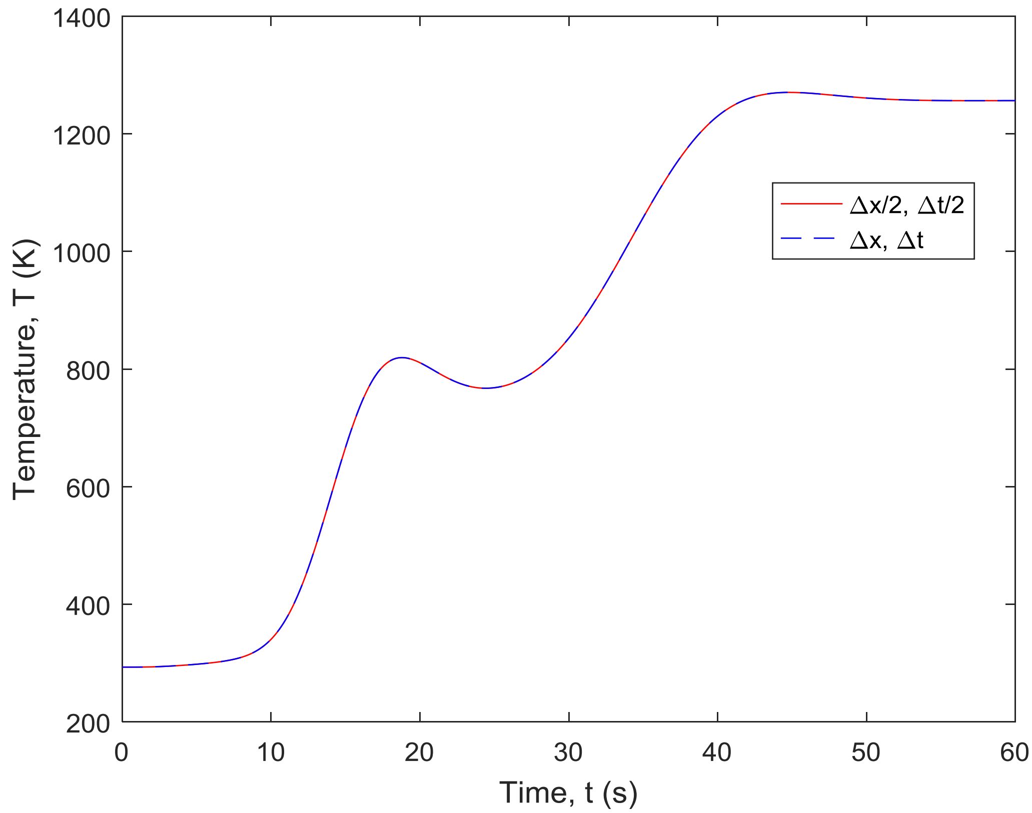

Fig. A-4.5 Convergence analysis of the implicit finite difference method by plotting the positional temperature at $x = b$, $T_r(b, t_i)$ in the reconstruction test obtained by (Δx, Δt) and ($\Delta x/2$, $\Delta t/2$), respectively.

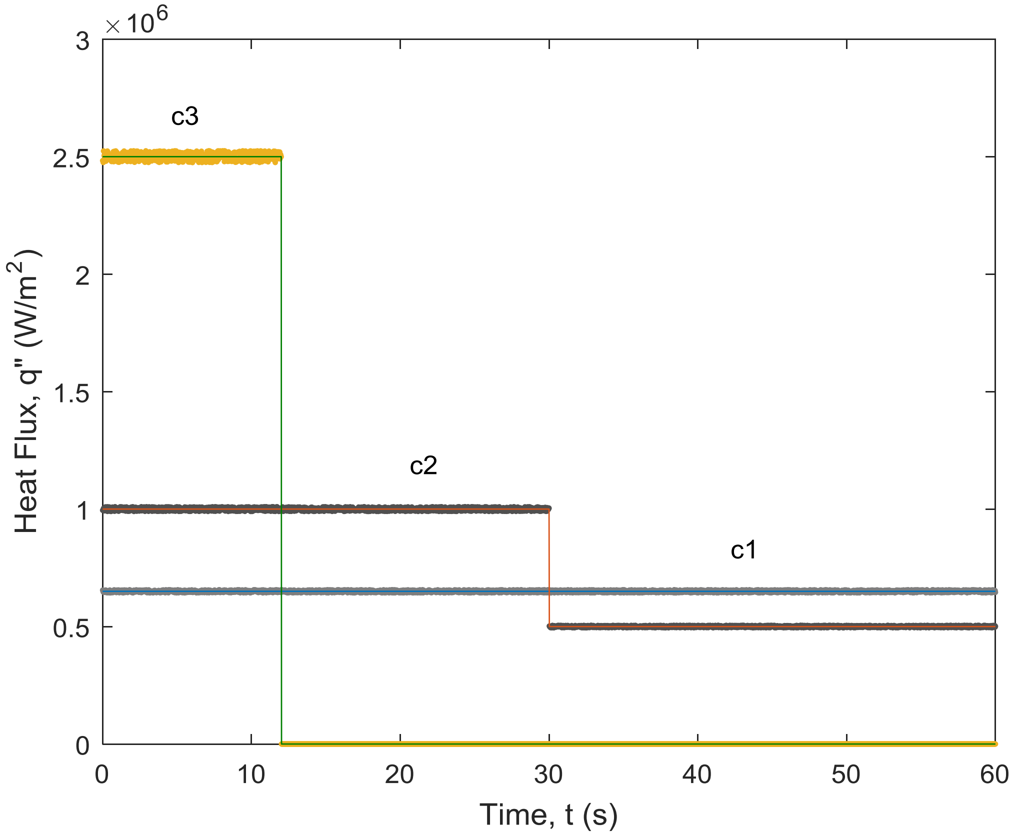

Fig. A-4.6 The exact imposed front surface heat fluxes $q''_{c1}(0,t)$, $q''_{c2}(0,t)$, $q''_{c3}(0,t)$ and noisy front surface heat fluxes $q''_{noise,c1}(0,t_i)$, $q''_{noise,c2}(0,t_i)$, $q''_{noise,c3}(0,t_i)$ for calibration tests 1, 2, 3.

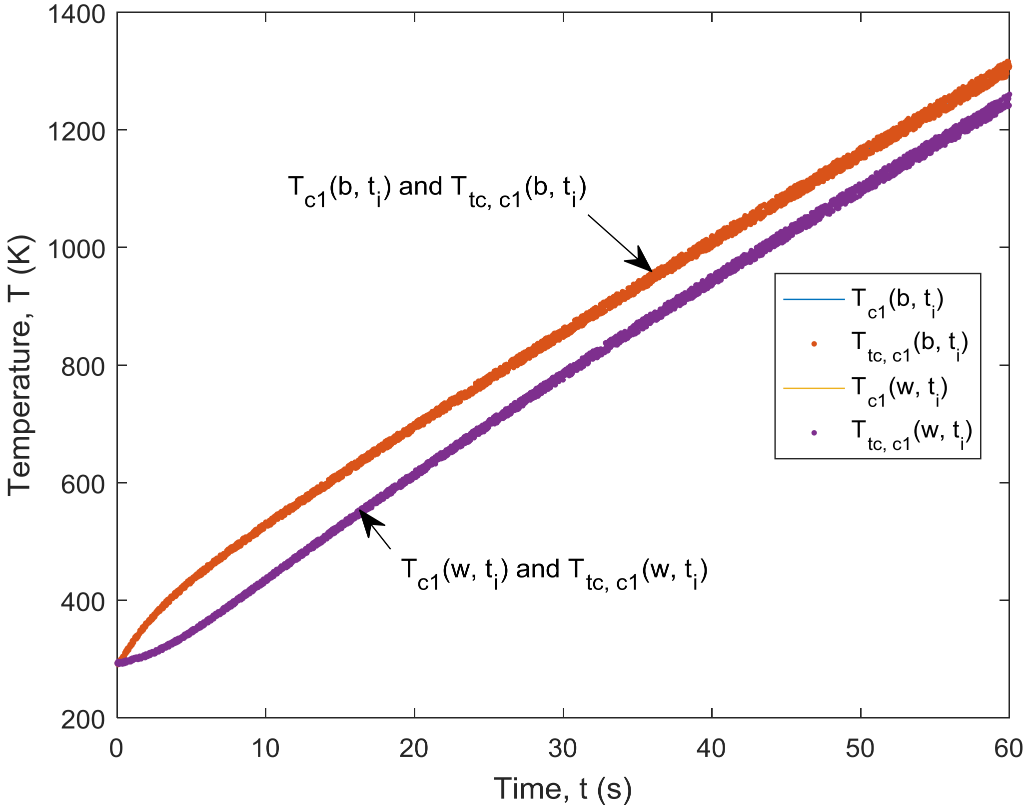

Fig. A-4.7a The positional temperature $T_{c1}(b, t_i)$, $T_{c1}(w, t_i)$ and emulated noisy "thermocouple" data $T_{tc, c1}(b, t_i)$, $T_{tc, c1}(w, t_i)$ for the calibration test 1, $t_i = i\Delta t$, $i = 1, 2, 3, \ldots, M$.

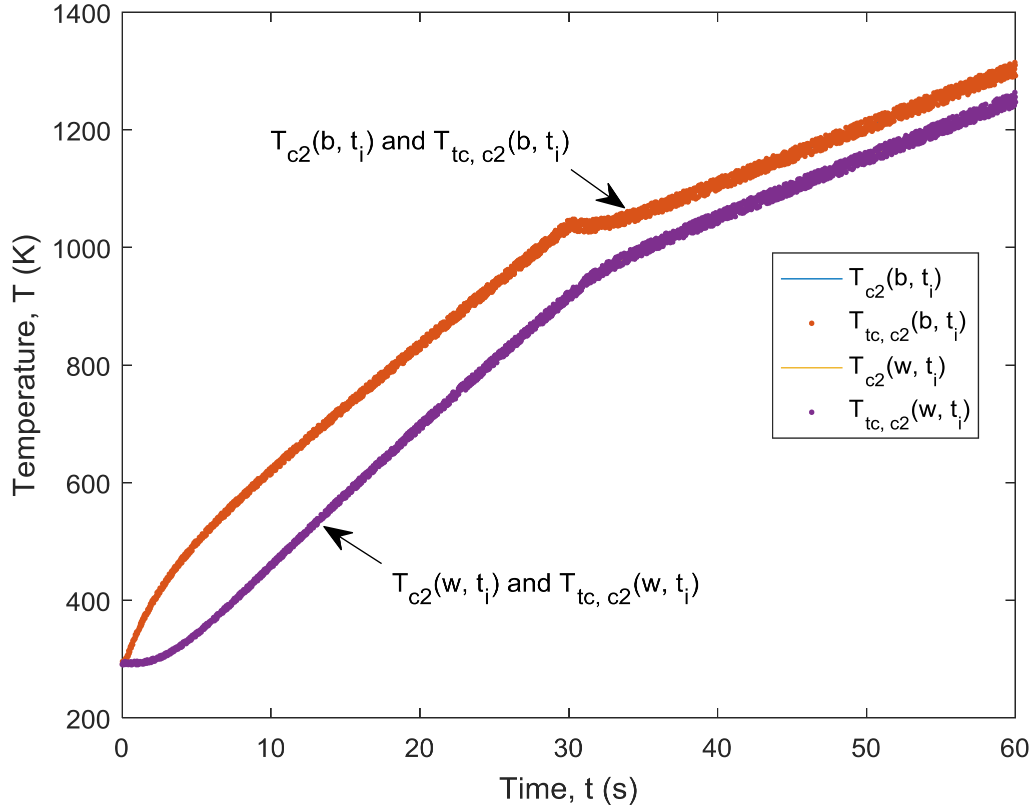

Fig. A-4.7b The positional temperature $T_{c2}(b, t_i)$, $T_{c2}(w, t_i)$ and emulated noisy "thermocouple" data $T_{tc,\,c2}(b, t_i)$, $T_{tc,\,c2}(w, t_i)$ for the calibration test 2, $t_i = i\Delta t$, $i = 1, 2, 3, \ldots, M$.

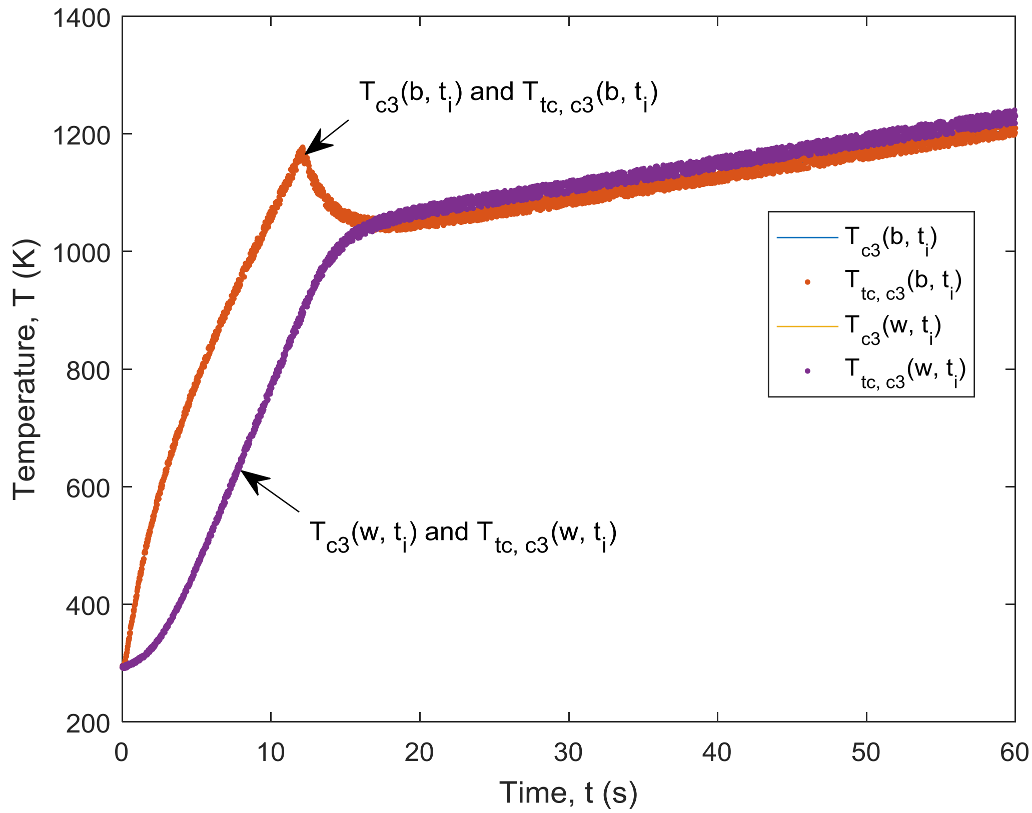

Fig. A-4.7c The positional temperature $T_{c3}(b, t_i)$, $T_{c3}(w, t_i)$ and emulated noisy "thermocouple" data $T_{tc,c3}(b, t_i)$, $T_{tc,c3}(w, t_i)$ for the calibration test 3, $t_i = i\Delta t$, $i = 1, 2, 3, \dots, M$.

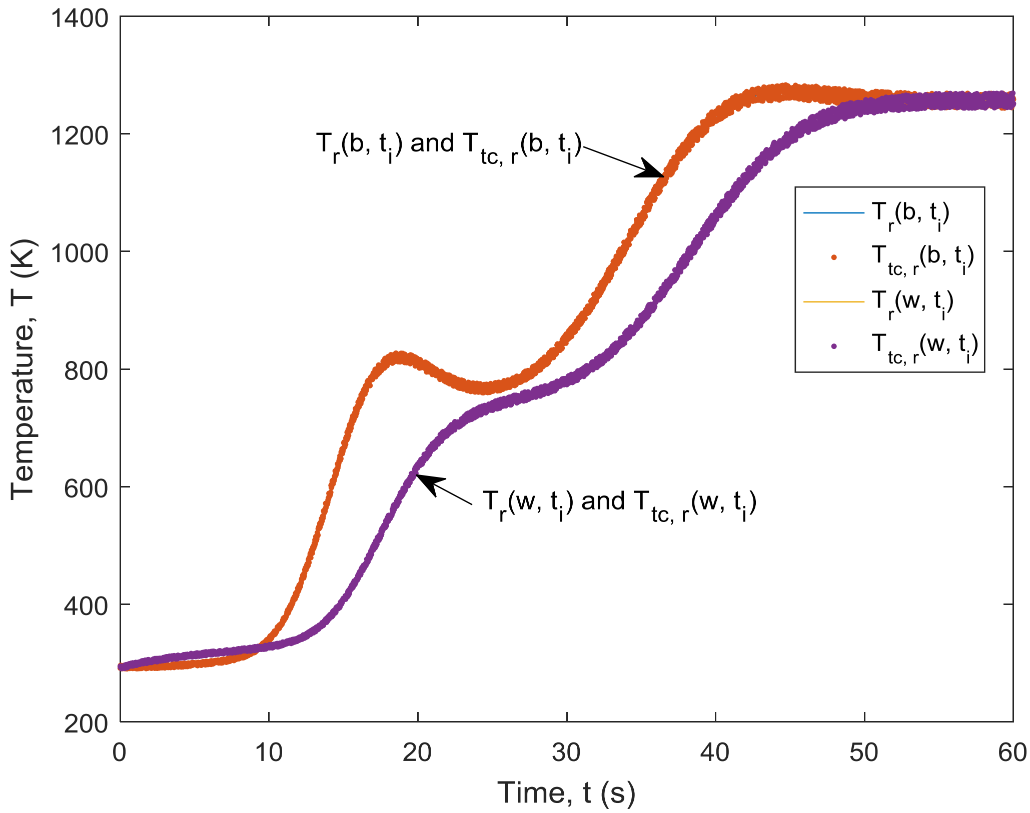

Fig. A-4.7d The positional temperature $T_r(b,\ t_i)$, $T_r(w,\ t_i)$ and emulated noisy "thermocouple" data $T_{tc,\,r}(b,\ t_i)$, $T_{tc,\,r}(w,\ t_i)$ for the reconstruction test, $t_i = i\Delta t$, $i = 1, 2, 3, \ldots, M$.

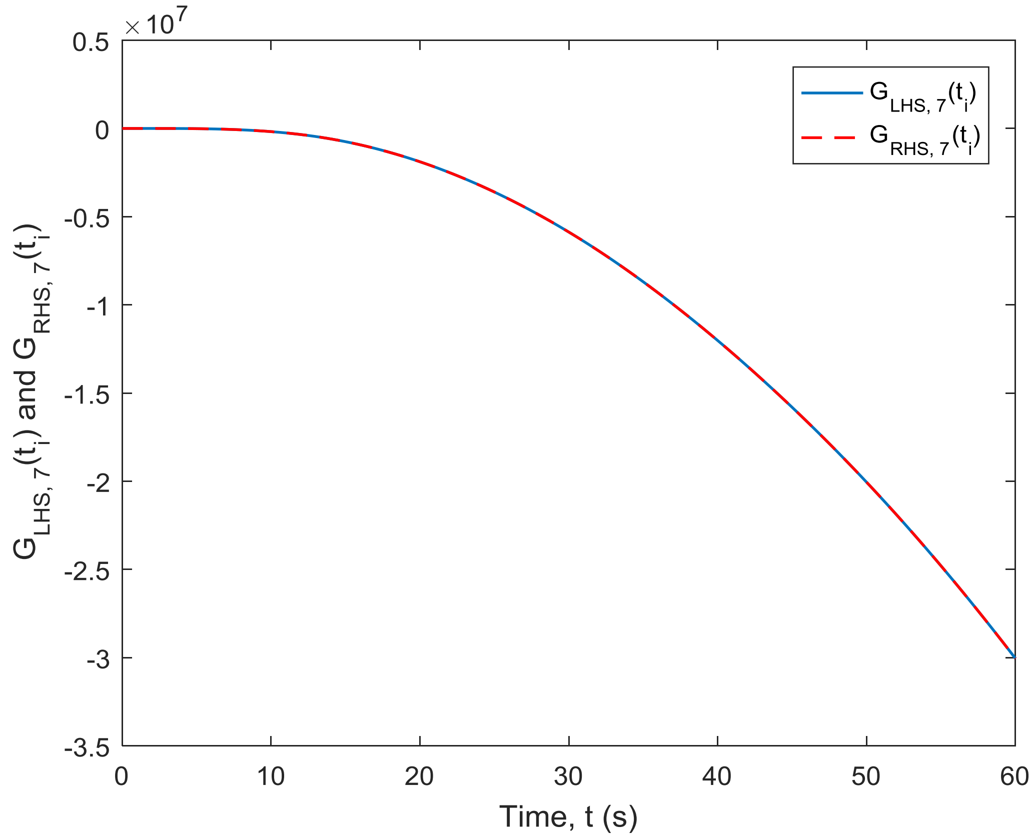

Fig. A-4.8a $G_{\mathrm{LHS},\,7}(t_i)$ and $G_{\mathrm{RHS},\,7}(t_i)$ defined in Eqs. (4.28b, c) by using noiseless data and $\{a_0^7, a_2^7, a_3^7, \ldots, a_7^7\}$ listed in column 2 of Table A-4.3.

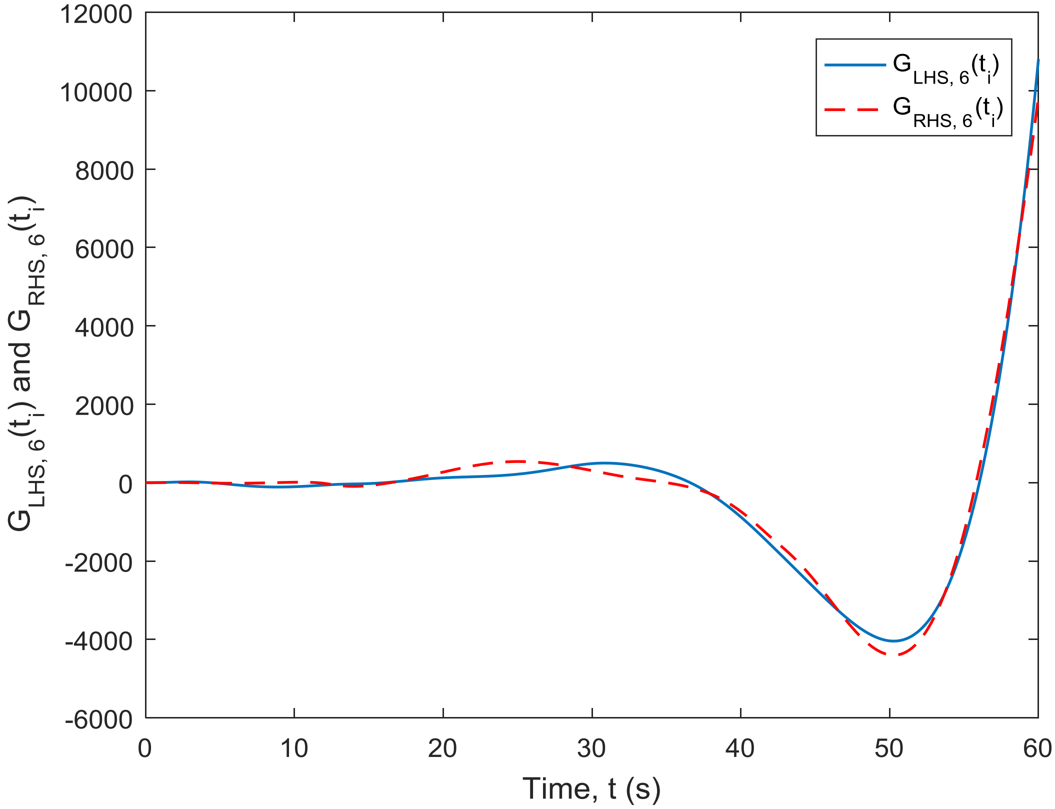

Fig. A-4.8b $G_{\mathrm{LHS},6}(t_i)$ and $G_{\mathrm{RHS},6}(t_i)$ defined in Eqs. (4.28b, c) by using noiseless data and $\{a_0^6, a_2^6, a_3^6, \ldots, a_6^6\}$ listed in column 3 of Table A-4.3.

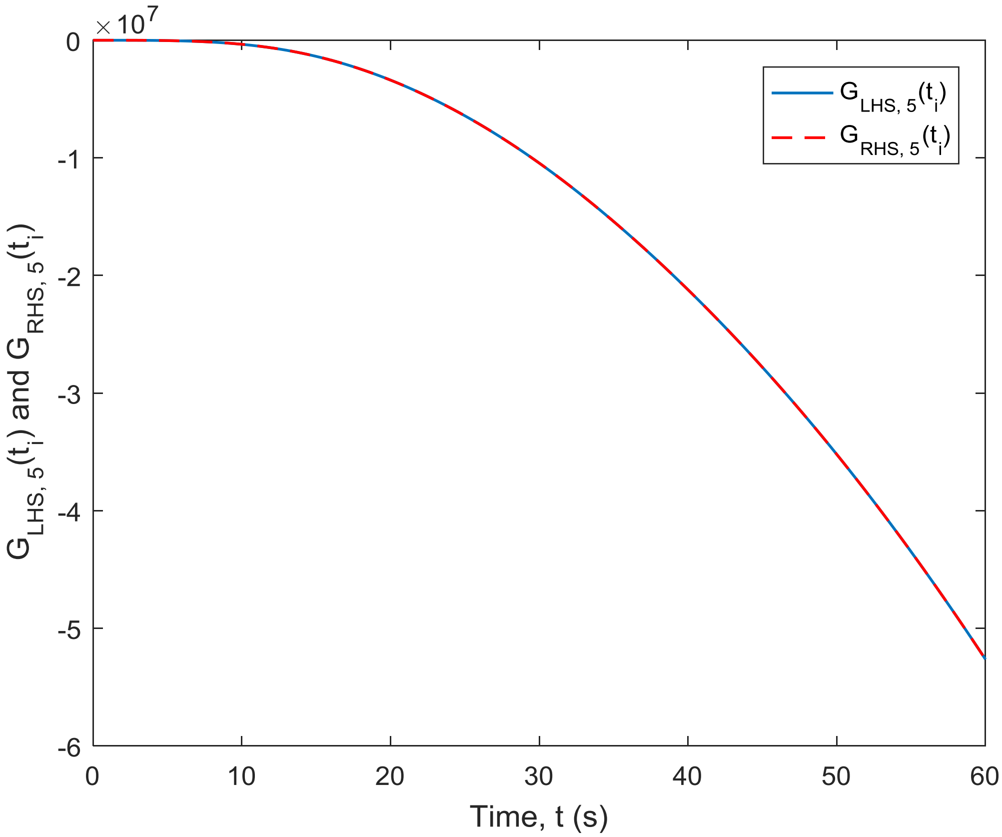

Fig. A-4.8c $G_{\text{LHS, }5}(t_i)$ and $G_{\text{RHS, }5}(t_i)$ defined in Eqs. (4.28b, c) by using noiseless data and $\{a_0^5, a_2^5, a_3^5, a_4^5, a_5^5\}$ listed in column 4 of Table A-4.3.

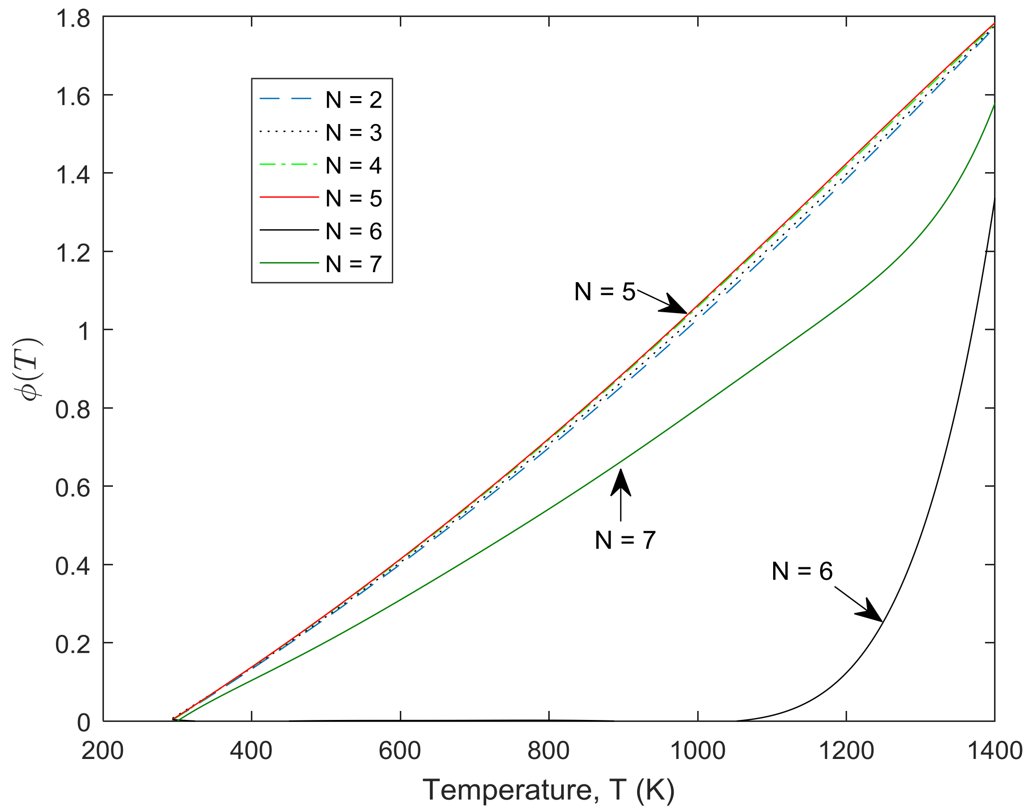

Fig. A-4.9 The transformed variable $\phi(T)$ as a function of temperature defined in Eq. (4.13a) in the temperature range [293.15, 1400] K using the calculated coefficients $\{a_0^N, a_2^N, a_3^N, \ldots, a_N^N\}$ under six different N numbers (coefficients are listed in Table A-4.3, noiseless data).

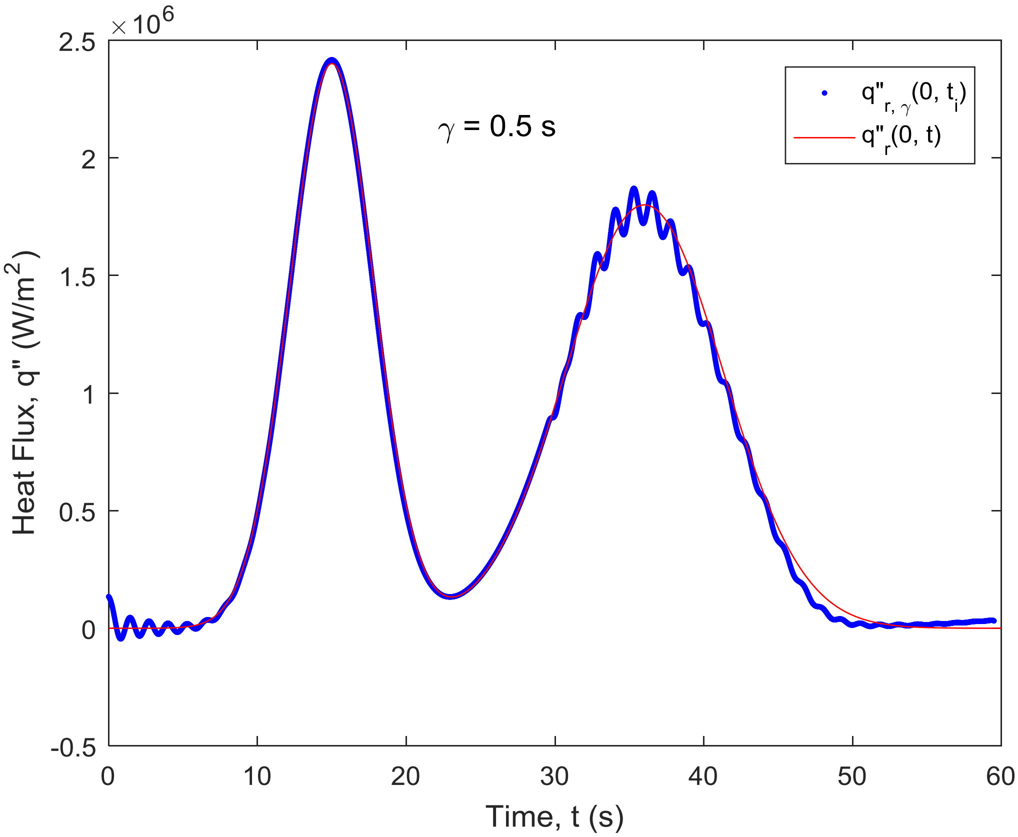

Fig. A-4.10a The exact front surface heat flux $q_r''(0,t)$ and the predicted front surface heat flux $q_{r,\gamma}''(0,t_i)$ in the reconstruction test, using noiseless data and the calculated expansion coefficients $\{a_0^5, a_2^5, a_3^5, a_4^5, a_5^5\}$ list in column 4 of Table A-4.3 (γ = 0.5 s).

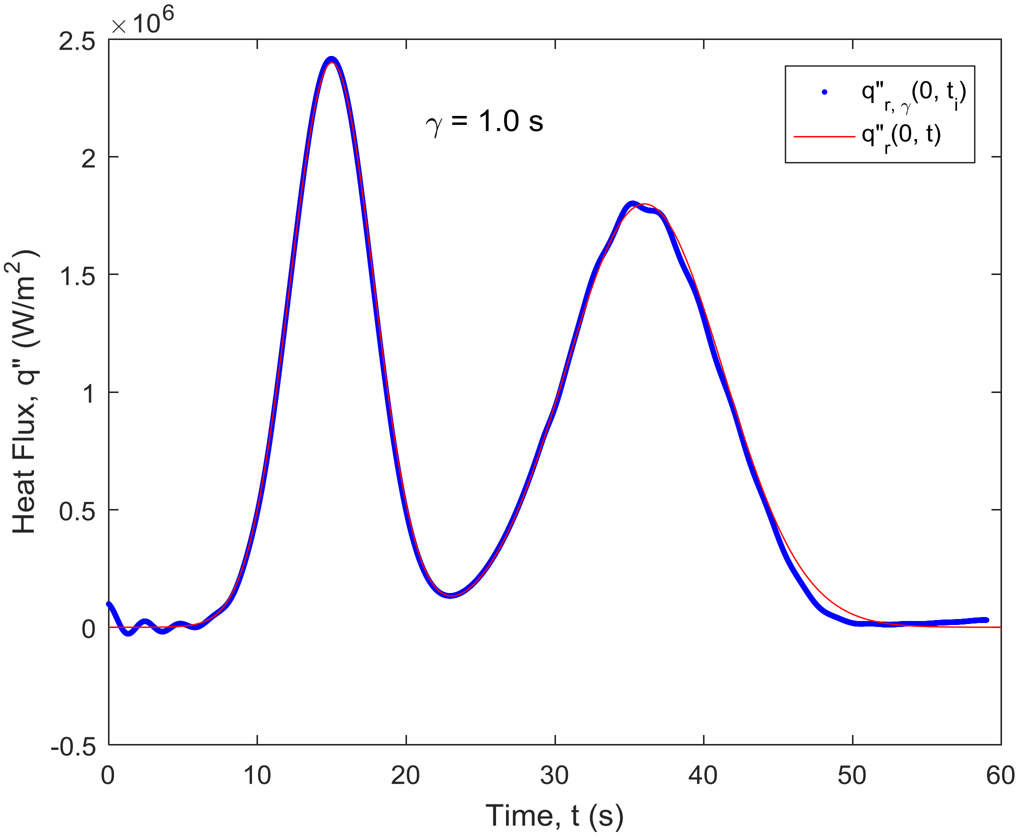

Fig. A-4.10b The exact front surface heat flux $q_r''(0,t)$ and the predicted front surface heat flux $q_{r,\gamma}''(0,t_i)$ in the reconstruction test, using noiseless data and the calculated expansion coefficients $\{a_0^5, a_2^5, a_3^5, a_4^5, a_5^5\}$ list in column 4 of Table A-4.3 (γ = 1.0 s).

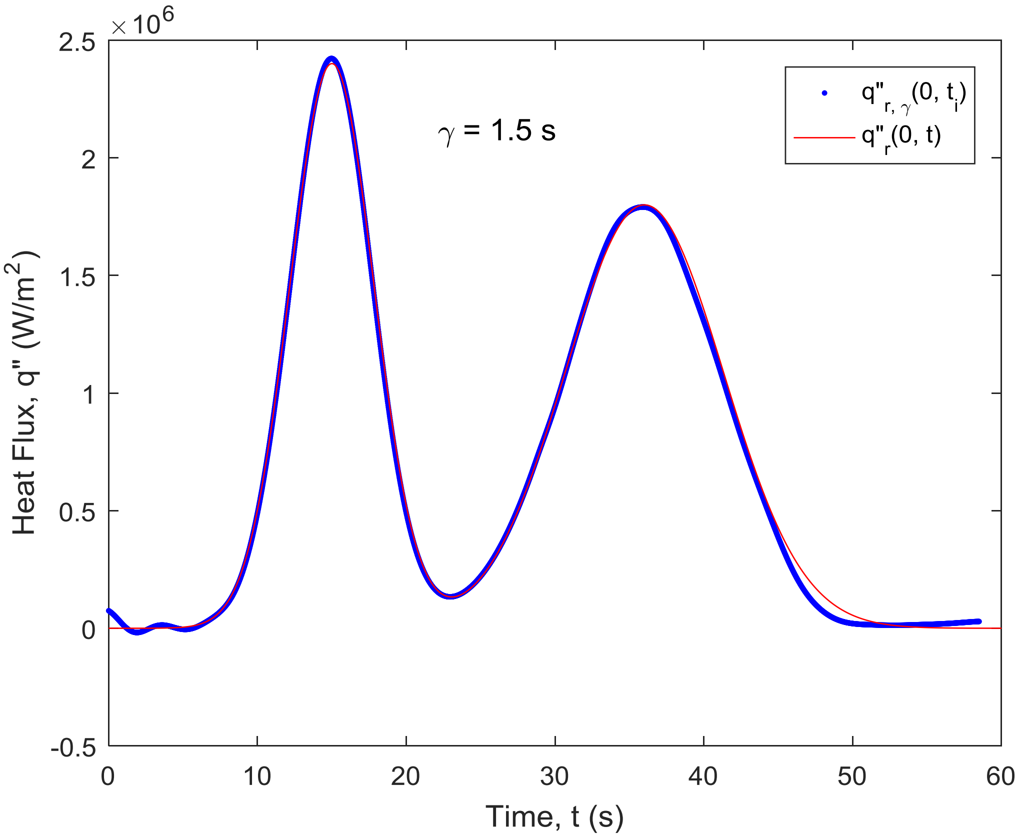

Fig. A-4.10c The exact front surface heat flux $q_r''(0,t)$ and the predicted front surface heat flux $q_{r,\gamma}''(0,t_i)$ in the reconstruction test, using noiseless data and the calculated expansion coefficients $\{a_0^5, a_2^5, a_3^5, a_4^5, a_5^5\}$ list in column 4 of Table A-4.3 (γ = 1.5 s).

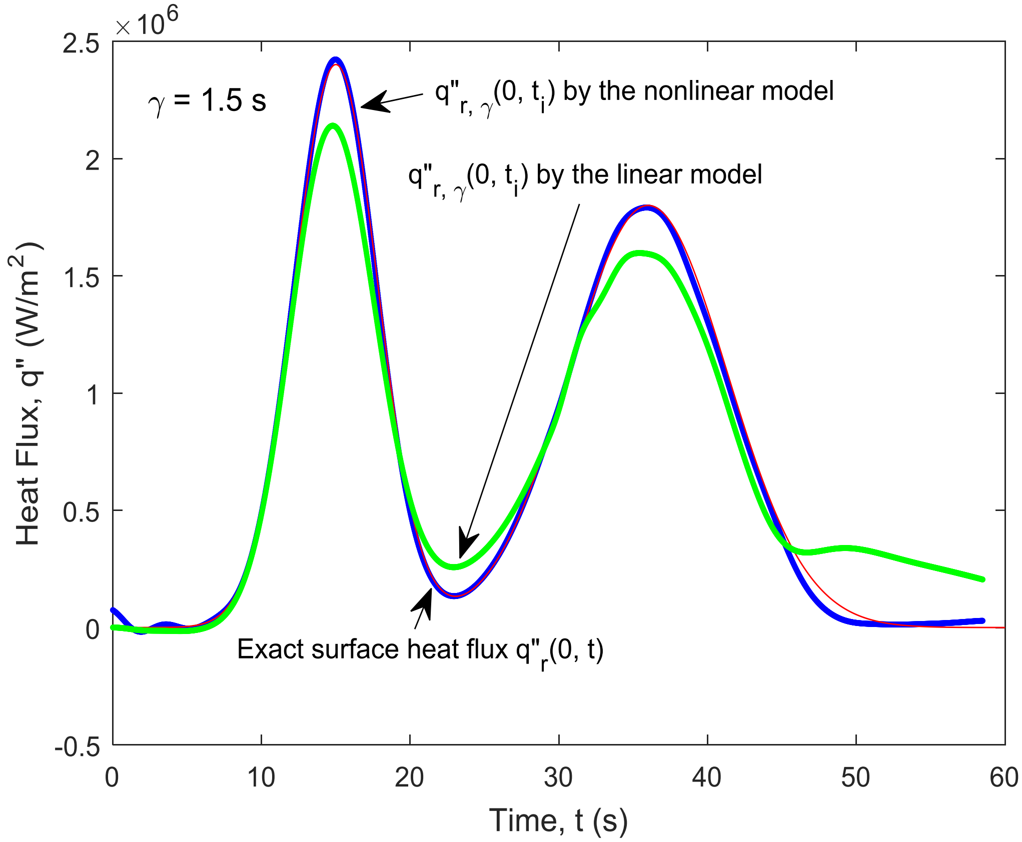

Fig. A-4.11 Comparison of the exact front surface heat flux $q''_r(0,t)$ and the predicted front surface heat flux $q''_{r,\gamma}(0,t_i)$ in Fig. A-4.10c (nonlinear model) and the predicted front surface heat flux $q''_{r,\gamma}(0,t_i)$ using the linear model given in Eq. (4.2) (noiseless data, γ = 1.5 s).

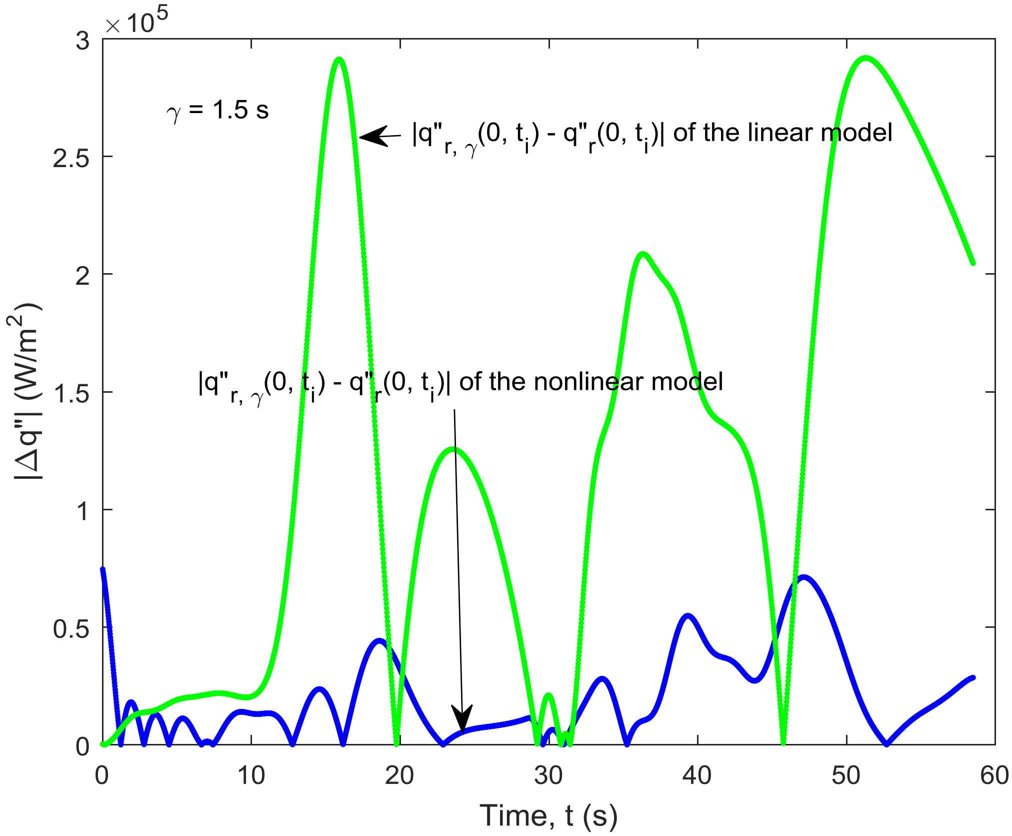

Fig. A-4.12 Comparison of the absolute error between surface heat flux prediction $q''_{r,\gamma}(0,t_i)$ by the nonlinear model and the linear model given in Eq. (4.2) (noiseless data, γ = 1.5 s).

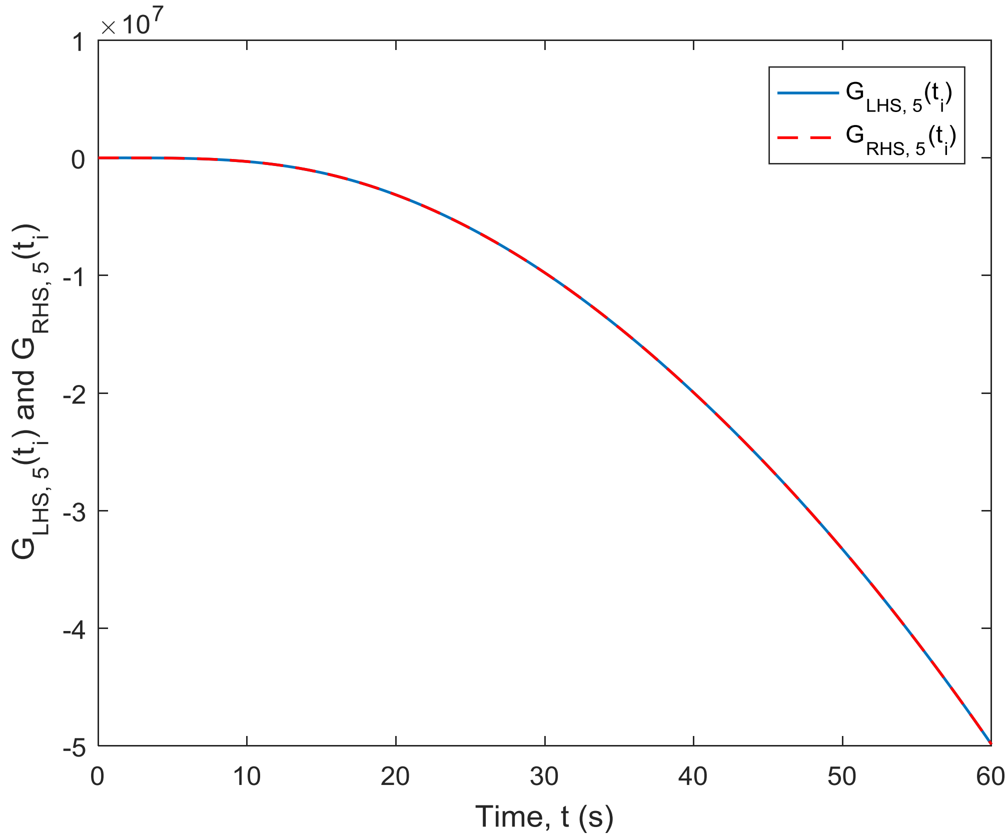

Fig. A-4.13 $G_{\mathrm{LHS},\,5}(t_i)$ and $G_{\mathrm{RHS},\,5}(t_i)$ defined in Eq. (4.28b, c) by using noisy data and $\{a_0^5, a_2^5, a_3^5, a_4^5, a_5^5\}$ listed in column 4 of Table A-4.6.

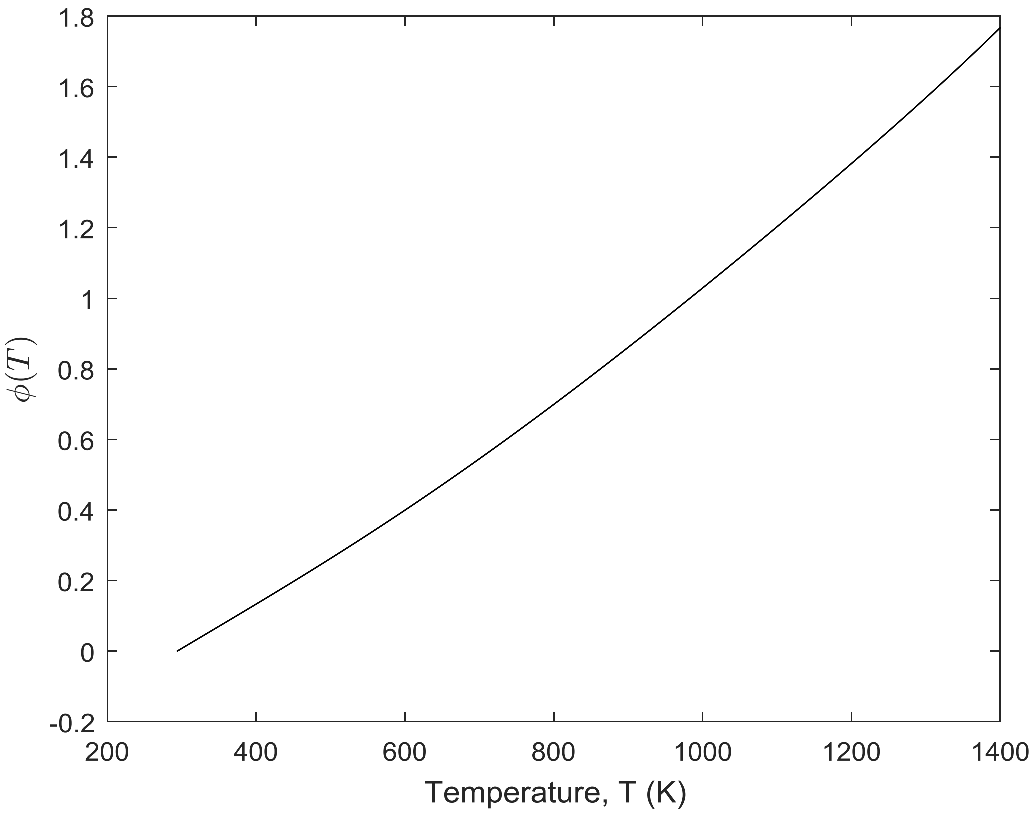

Fig. A-4.14 The transformed variable $\phi(T)$ as a function of temperature defined in Eq. (4.13a) in the temperature range [293.15, 1400] K using the calculated coefficients $\{a_0^5, a_2^5, a_3^5, a_4^5, a_5^5\}$ as listed in column 4 of Table A-4.6 (noisy data).

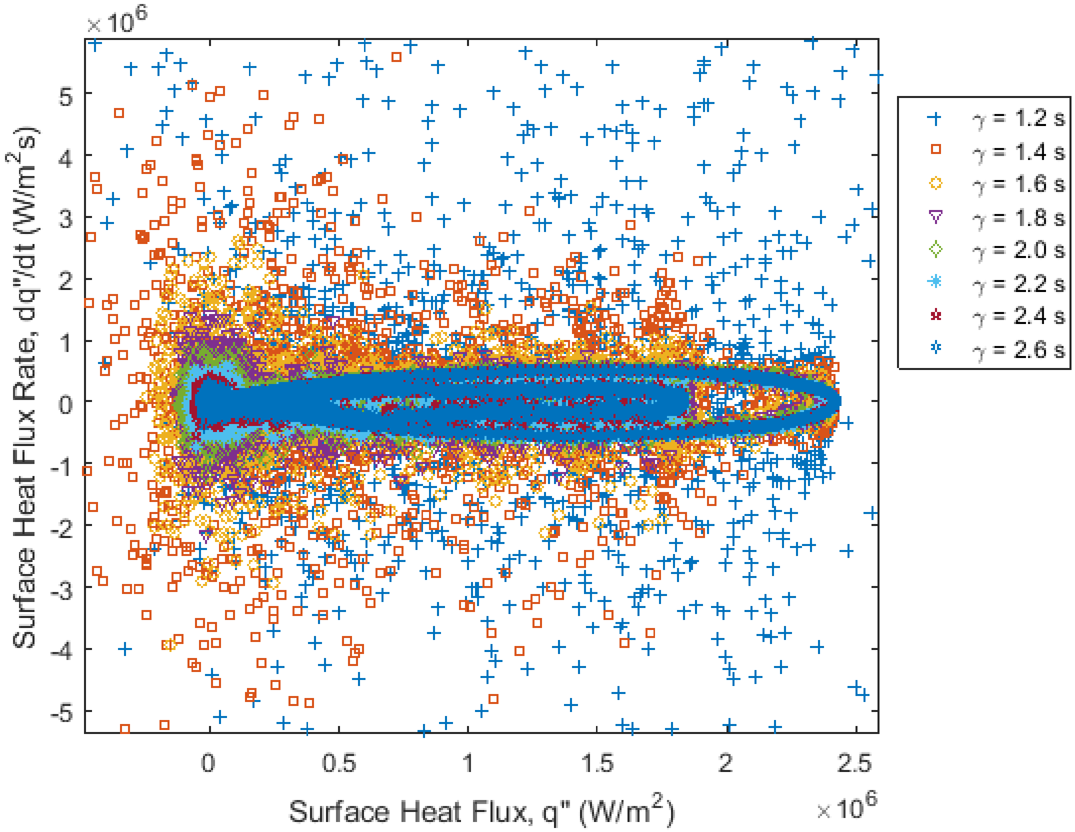

Fig. A-4.15a The predicted surface heat flux rate and surface heat flux phase planes for the future-time parameter spectrum γ = [1.2, 1.4, 1.6, 1.8, 2.0, 2.2, 2.4, 2.6] s ($\{a_0^5, a_2^5, a_3^5, a_4^5, a_5^5\}$ as listed in column 4 of Table A-4.6).

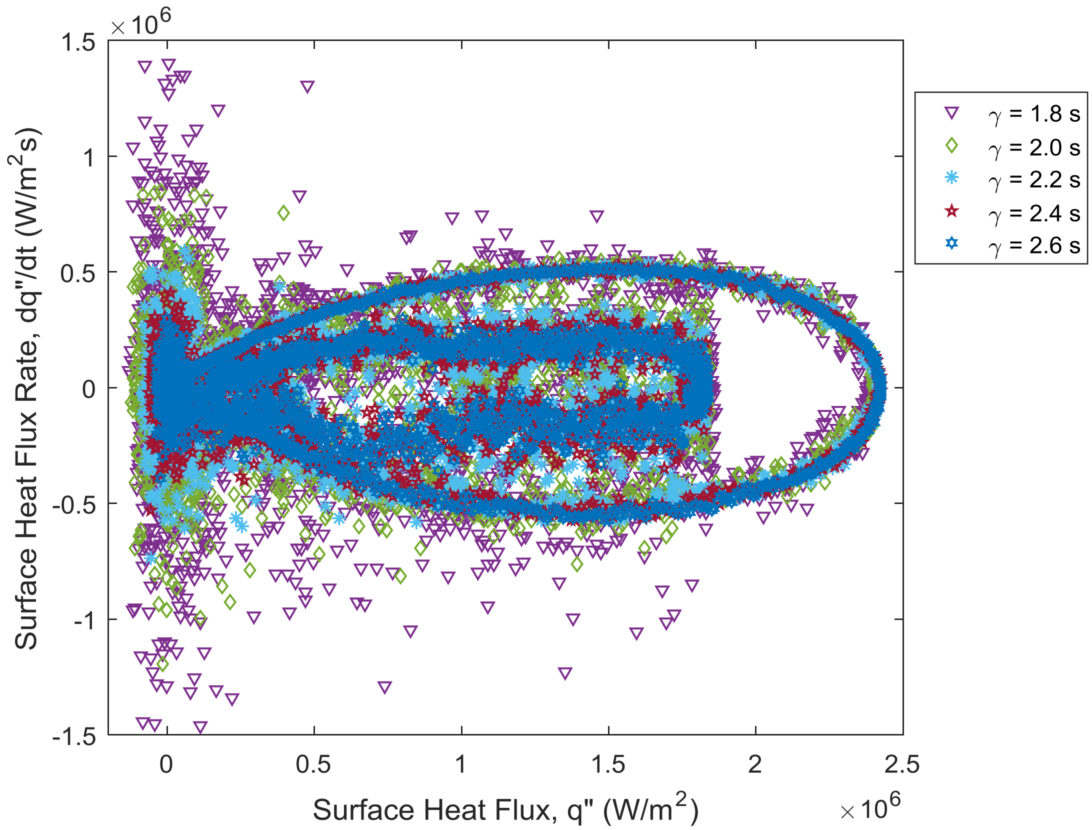

Fig. A-4.15b The predicted surface heat flux rate and surface heat flux phase planes for the future-time parameter spectrum γ = [1.8, 2.0, 2.2, 2.4, 2.6] s ($\{a_0^5, a_2^5, a_3^5, a_4^5, a_5^5\}$ as listed in column 4 of Table A-4.6).

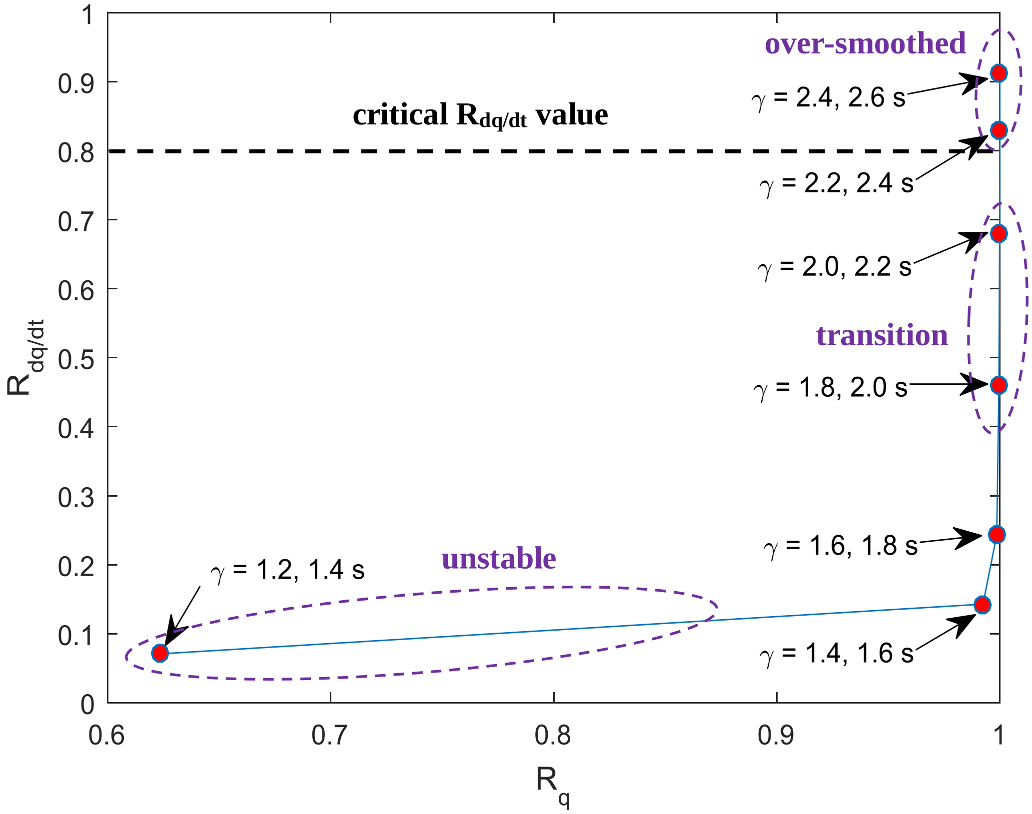

Fig. A-4.16 The predicted surface heat flux rate cross-correlation coefficient versus the surface heat flux cross-correlation coefficient for future-time parameter pairs.

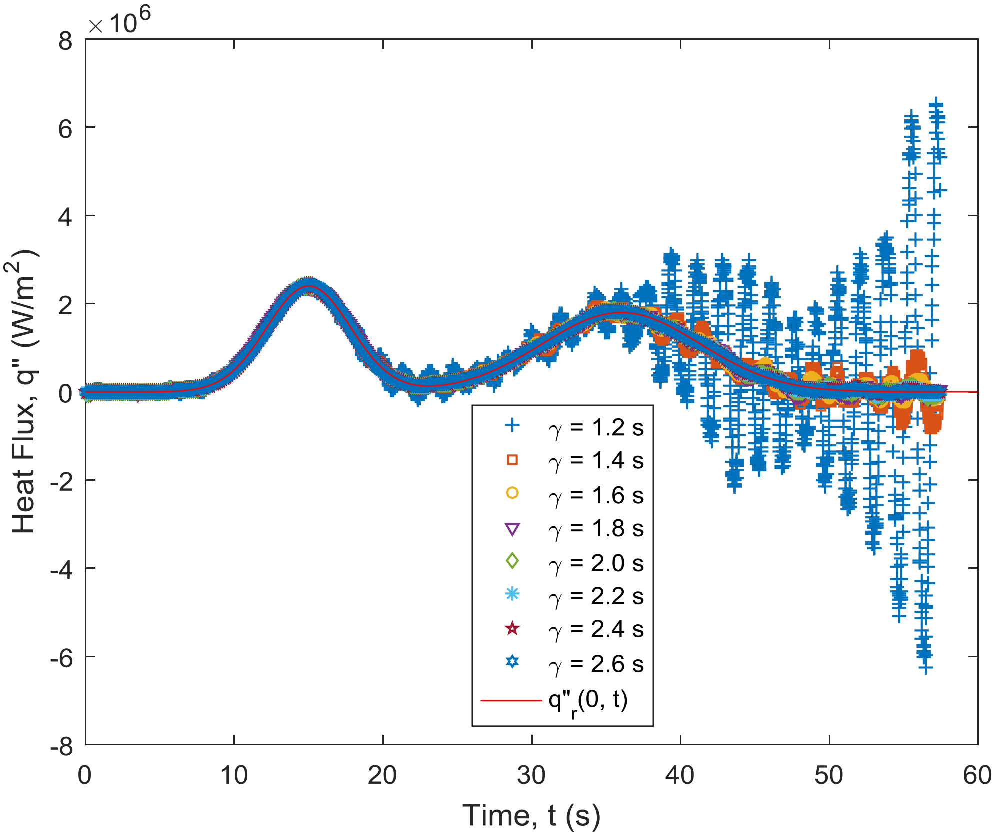

Fig. A-4.17 The exact surface heat flux $q''_r(0,t)$ and predicted surface heat flux $q''_{r,\gamma}(0,t_i)$ for the future-time parameter spectrum γ = [1.2, 1.4, 1.6, 1.8, 2.0, 2.2, 2.4, 2.6] s when N = 5.

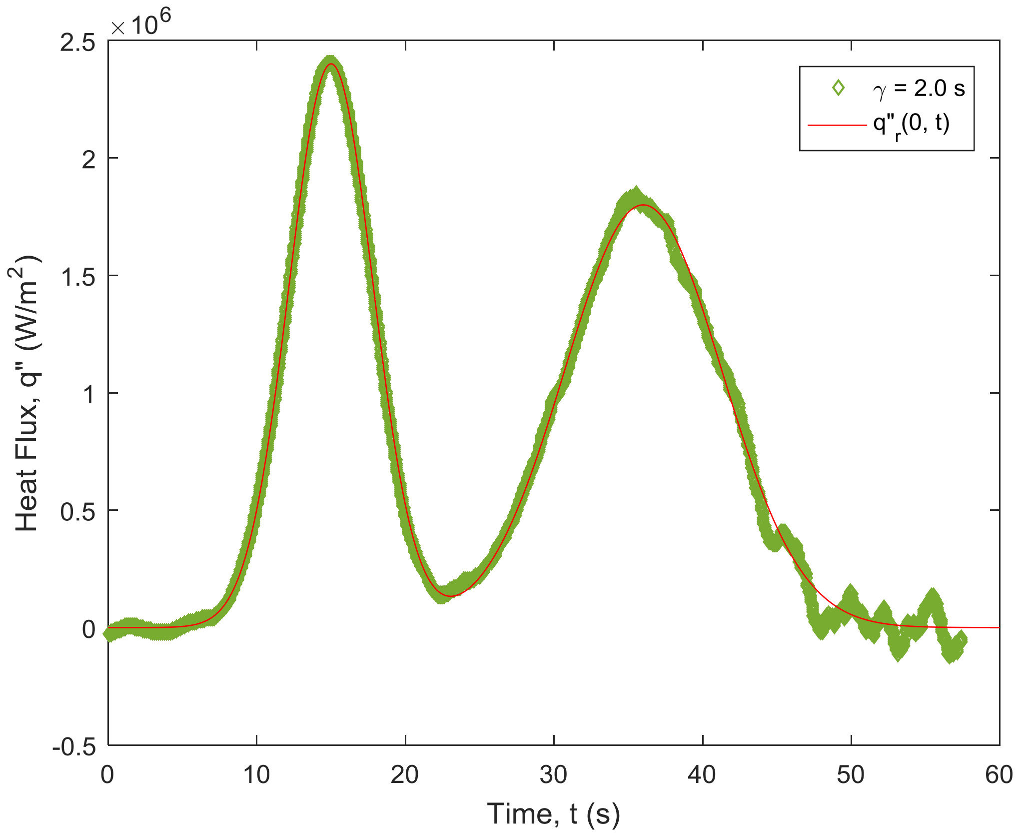

Fig. A-4.18 The exact surface heat flux $q''_r(0,t)$ and predicted surface heat flux $q''_{r,\gamma}(0,t_i)$ for the future-time parameter γ = 2.0 s (N = 5).

Table A-4.1 Several Chebyshev polynomials of the first kind [86] for mapped temperature as a variable.

E_n	Polynomial
E_0	1
E_1	T^*
E_2	$2T^{*2}-1$
E_3	$4T^{*3}-3T^*$
E_4	$8T^{*4}-8T^{*2}+1$
E_5	$16T^{*5}-20T^{*3}+5T^*$
E_6	$32T^{*6}-48T^{*4}+18T^{*2}-1$
E_7	$64T^{*7}-112T^{*5}+56T^{*3}-7T^*$

Table A-4.2 Thermophysical properties of stainless steel 304 [80] and parameters for the simulation.

Property	Value
b	2×10^{-3} m
c	$6.683+0.04906\times T+80.74\times\ln(T)$ J/(kg·K) [80]
$f_{sampling}$	50 Hz
k	$9.705+0.0176\times T-1.60\times10^{-6}\times T^2$ W/(m·K) [80]
L	1×10^{-2} m
M	3000
M_f	10
$q''_{0,c1,\max}$	6.5×10^{5} W/m^2
$q''_{L,c1,\max}$	1.0×10^{5} W/m^2
$q''_{0,c2,\max}$	1×10^{6} W/m^2
$q''_{L,c2,\max}$	0 W/m^2
$q''_{0,c3,\max}$	2.5×10^{6} W/m^2
$q''_{L,c3,\max}$	2.0×10^{5} W/m^2
$q''_{0,r,\max}$	2.4×10^{6} W/m^2
$q''_{L,r,\max}$	1.0×10^{5} W/m^2
$t_{\max}$	60 s
Δt	0.02 s

Table A-4.2 Continued

Property	Value
T_0	293.15 K
T_L	273 K
T_U	1500 K
w	8×10^{-3} m
Δx	5×10^{-5} m
ρ	7920 kg/m^3 [80]
ε_q	0.01
ε_T	0.01
β_1	$t_{max}/4$ s
β_2	$0.6t_{max}$ s
σ_1	$t_{max}/15$ s
σ_2	$t_{max}/8$ s

Table A-4.3 Numerically calculated coefficients in the transformed variable $\phi(x, t)$ in Eq. (4.13a) with $a_1^N \triangleq 1$ using noiseless data ($t_{\max}$ = 60 s).

Coefficients	N = 7	N = 6	N = 5	N = 4	N = 3	N = 2
a_0^N	0.8186	0.5455	0.9201	0.9179	0.9136	0.9076
a_2^N	0.2408	0.7731	0.0492	0.0516	0.0658	0.0712
a_3^N	0.1470	0.4902	-0.0143	-0.0118	-0.0040	N/A
a_4^N	0.0954	0.2484	-0.0054	-0.0043	N/A	N/A
a_5^N	0.0584	0.0894	-0.0010	N/A	N/A	N/A
a_6^N	0.0236	0.0209	N/A	N/A	N/A	N/A
a_7^N	0.0095	N/A	N/A	N/A	N/A	N/A

Table A-4.4 Sequential coefficient study for N = 7 using noiseless data collected up to 60s, 54s, 48s, and 42s, respectively.

Coefficients	t_{max} = 60 s	t'_{max} = 54 s	t'_{max} = 48 s	t'_{max} = 42 s
a_0^N	0.8186	0.5305	0.5674	0.5521
a_2^N	0.2408	0.8213	0.7470	0.7765
a_3^N	0.1470	0.5781	0.5211	0.5413
a_4^N	0.0954	0.3422	0.3082	0.3179
a_5^N	0.0584	0.1664	0.1493	0.1523
a_6^N	0.0236	0.0603	0.0534	0.0538
a_7^N	0.0095	0.0143	0.0122	0.0121

Table A-4.5 Sequential coefficient study for N = 5 using noiseless data collected up to 60s, 54s, 48s, and 42s, respectively.

Coefficients	t_{max} = 60 s	t'_{max} = 54 s	t'_{max} = 48 s	t'_{max} = 42 s
a_0^N	0.9201	0.9356	0.8595	0.8806
a_2^N	0.0492	0.0191	0.1554	0.1163
a_3^N	-0.0143	-0.0341	0.0611	0.0346
a_4^N	-0.0054	-0.0141	0.0280	0.0163
a_5^N	-0.0010	-0.0031	0.0110	0.0076

Table A-4.6 Numerically calculated coefficients in the transformed variable $\phi(x, t)$ in Eq. (4.13a) with $a_1^N \triangleq 1$ using noisy data ($t_{\max}$ = 60 s).

Coefficients	$N = 7$	$N = 6$	$N = 5$	$N = 4$	$N = 3$	$N = 2$
a_0^N	0.8483	0.9206	0.9065	0.9121	0.9128	0.9069
a_2^N	0.1800	0.0367	0.0700	0.0675	0.0650	0.0704
a_3^N	0.0950	-0.0228	0.0023	-0.0027	-0.0040	N/A
a_4^N	0.0604	-0.0146	0.0023	0.0008	N/A	N/A
a_5^N	0.0373	-0.0046	0.0029	N/A	N/A	N/A
a_6^N	0.0138	-0.0035	N/A	N/A	N/A	N/A
a_7^N	0.0056	N/A	N/A	N/A	N/A	N/A

Table A-4.7 Sequential coefficient study for $N = 7$ using noisy data collected up to 60s, 54s, 48s, and 42s, respectively.

Coefficients	$t_{max} = 60$ s	$t'_{max} = 54$ s	$t'_{max} = 48$ s	$t'_{max} = 42$ s
a_0^N	0.8483	0.5303	0.5702	0.5527
a_2^N	0.1800	0.8218	0.7414	0.7754
a_3^N	0.0950	0.5790	0.5171	0.5407
a_4^N	0.0604	0.3431	0.3060	0.3178
a_5^N	0.0373	0.1670	0.1484	0.1524
a_6^N	0.0138	0.0607	0.0531	0.0539
a_7^N	0.0056	0.0145	0.0121	0.0121

Table A-4.8 Sequential coefficient study for $N = 6$ using noisy data collected up to 60s, 54s, 48s, and 42s, respectively.

Coefficients	t_{max} = 60 s	t'_{max} = 54 s	t'_{max} = 48 s	t'_{max} = 42 s
a_0^N	0.9206	0.9405	0.6407	0.6370
a_2^N	0.0367	-0.0043	0.5918	0.5987
a_3^N	-0.0228	-0.0519	0.3737	0.3783
a_4^N	-0.0146	-0.0304	0.1961	0.1981
a_5^N	-0.0046	-0.0104	0.0754	0.0759
a_6^N	-0.0035	-0.0052	0.0177	0.0177

Table A-4.9 Sequential coefficient study for $N = 5$ using noisy data collected up to 60s, 54s, 48s, and 42s, respectively.

Coefficients	t_{max} = 60 s	t'_{max} = 54 s	t'_{max} = 48 s	t'_{max} = 42 s
a_0^N	0.9065	0.9152	0.8757	0.9072
a_2^N	0.0700	0.0534	0.1240	0.0654
a_3^N	0.0023	-0.0088	0.0406	0.0010
a_4^N	0.0023	-0.0026	0.0193	0.0019
a_5^N	0.0029	0.0016	0.0090	0.0041

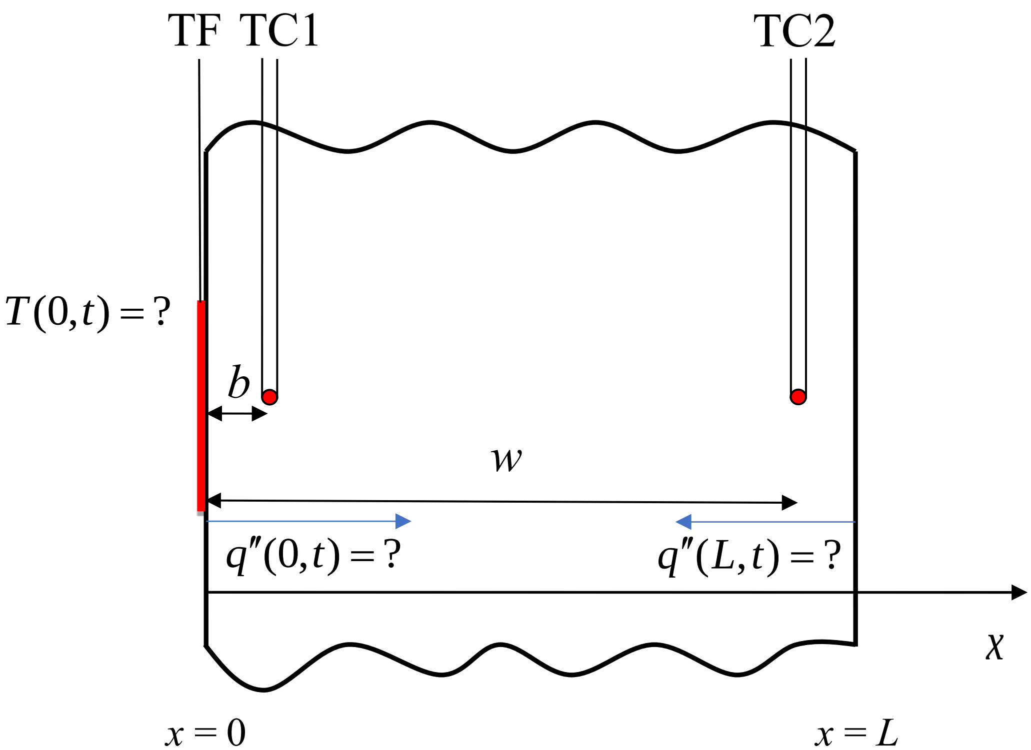

Fig. A-5.1 Schematic for one-dimensional heat conduction with one thin film (TF) thermocouple on the front surface and two in-depth thermocouples at $x = b$ and w.

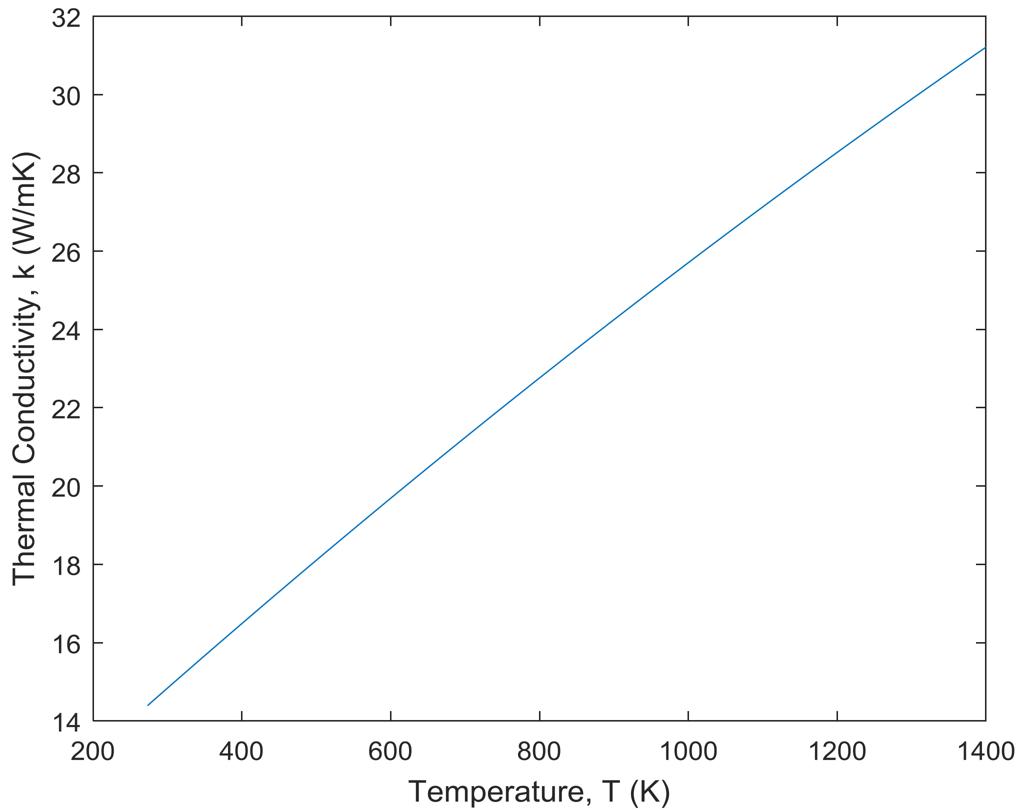

Fig. A-5.2a Thermal conductivity, $k(T)$ as a function of temperature for SS 304 [80].

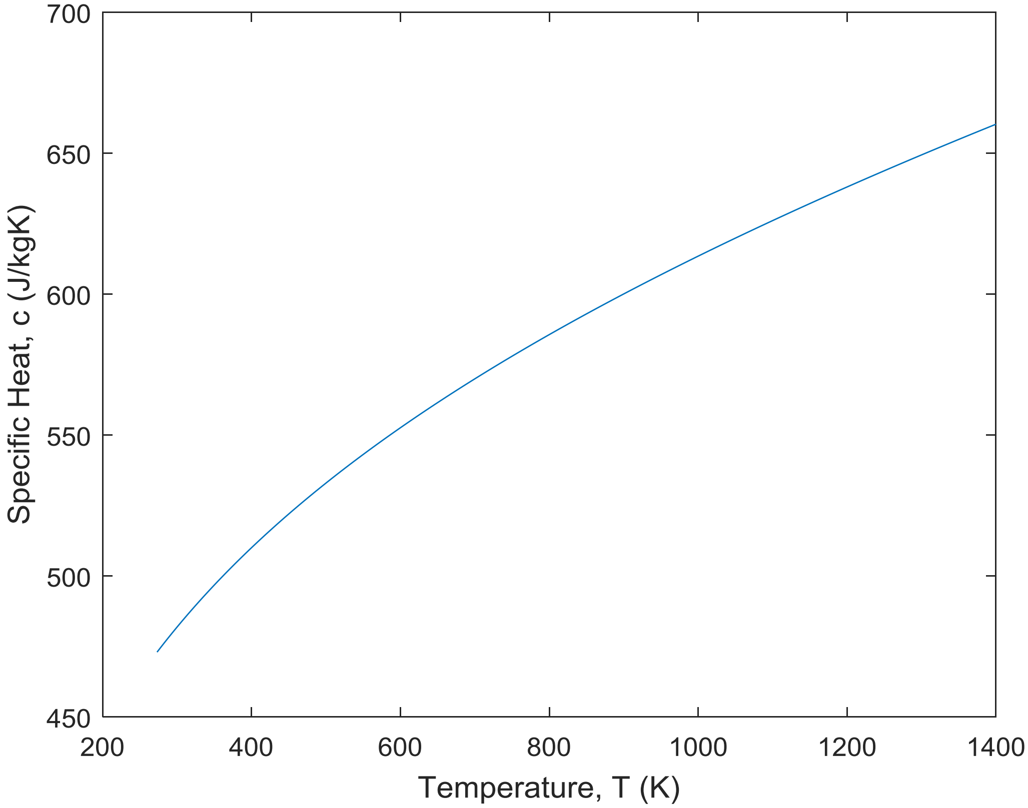

Fig. A-5.2b Specific heat, $c(T)$ as a function of temperature for SS 304 [80].

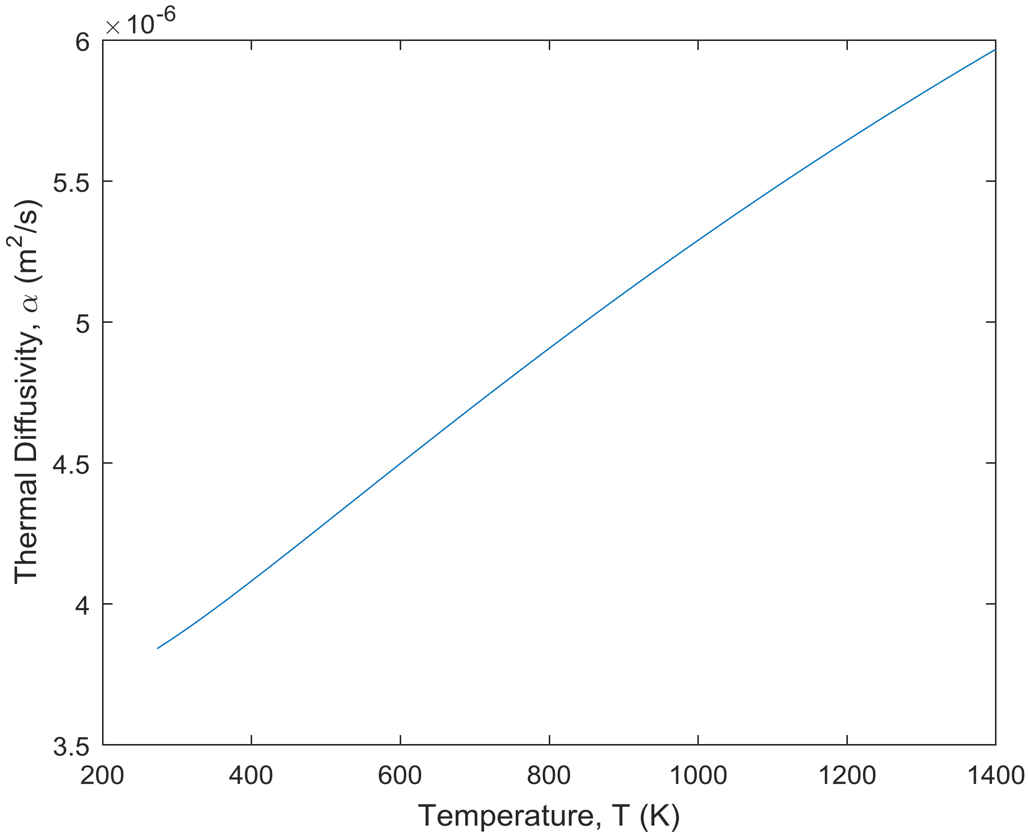

Fig. A-5.2c Thermal diffusivity, $\alpha(T)$ as a function of temperature for SS 304 [80].

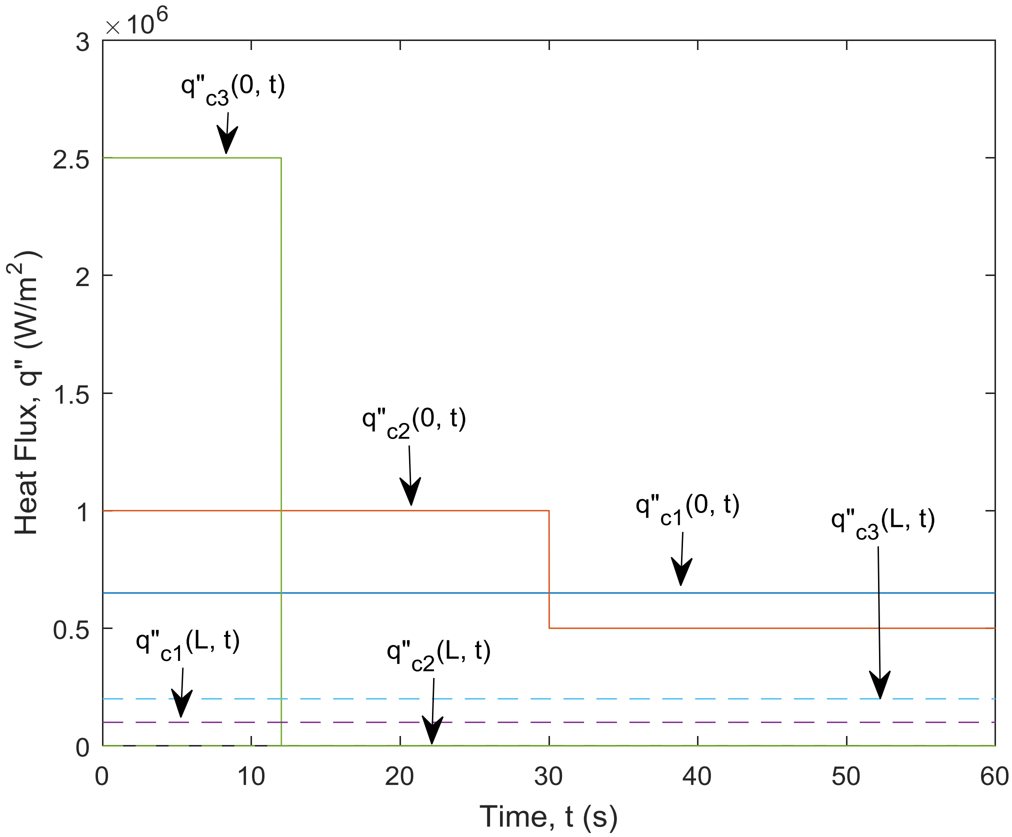

Fig. A-5.3a The imposed front surface heat fluxes $q''_{c1}(0,t), q''_{c2}(0,t), q''_{c3}(0,t)$, and back surface heat fluxes $q''_{c1}(L,t), q''_{c2}(L,t), q''_{c3}(L,t)$ in the calibration test 1, 2 and 3, respectively.

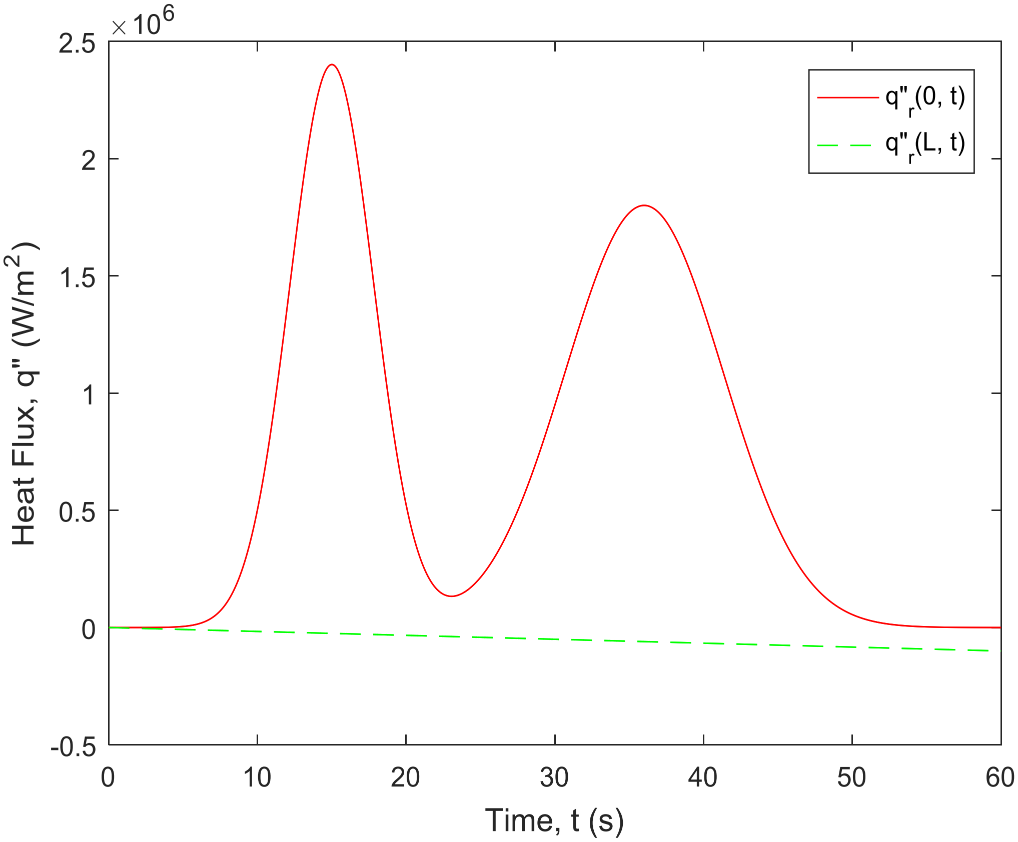

Fig. A-5.3b The imposed front surface heat flux $q_r''(0,t)$, and back surface heat flux $q_r''(L,t)$ in the reconstruction test.

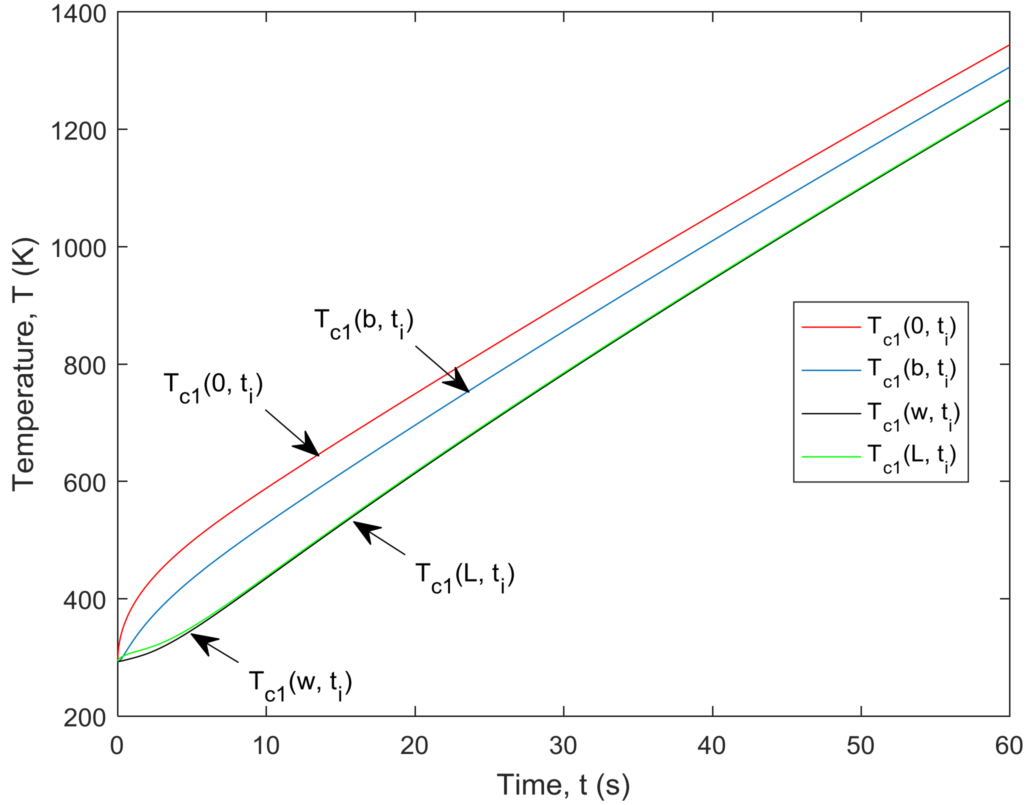

Fig. A-5.4a The positional temperature at x = 0, b, w, L denoted by $T_{c1}(0, t_i)$, $T_{c1}(b, t_i)$, $T_{c1}(w, t_i)$ and $T_{c1}(L, t_i)$ in the calibration test 1.

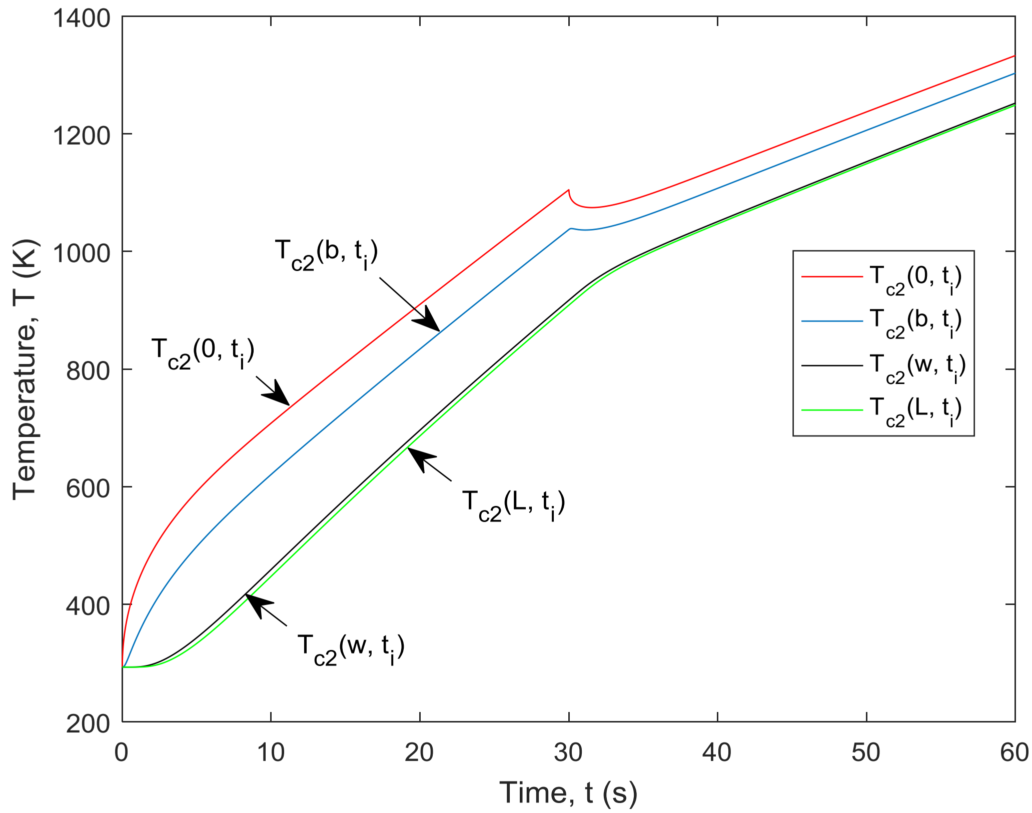

Fig. A-5.4b The positional temperature at x = 0, b, w, L denoted by $T_{c2}(0, t_i)$, $T_{c2}(b, t_i)$, $T_{c2}(w, t_i)$ and $T_{c2}(L, t_i)$ in the calibration test 2.

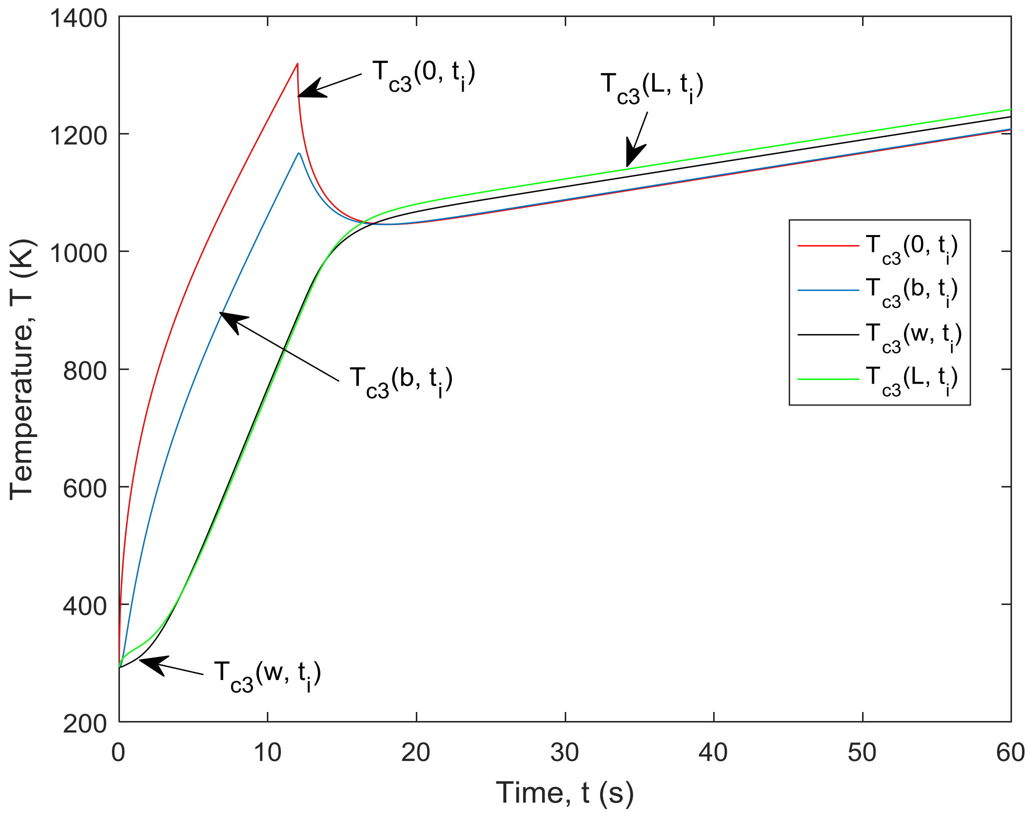

Fig. A-5.4c The positional temperature at $x = 0$, b, w, L denoted by $T_{c3}(0, t_i)$, $T_{c3}(b, t_i)$, $T_{c3}(w, t_i)$ and $T_{c3}(L, t_i)$ in the calibration test 3.

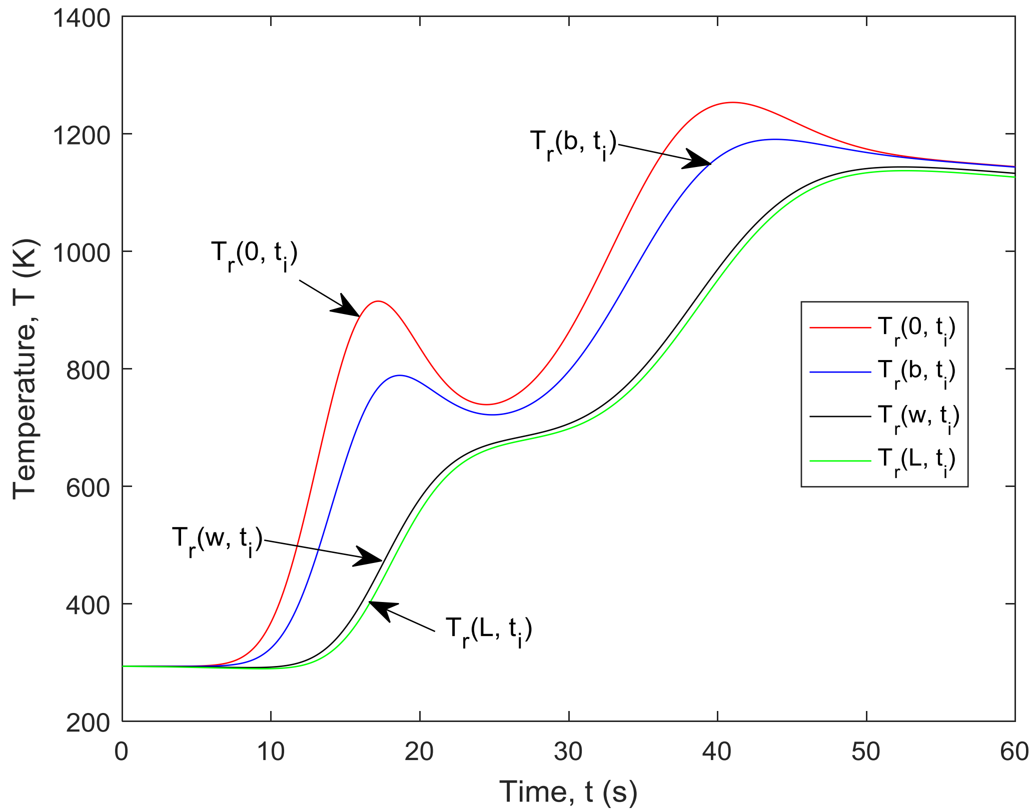

Fig. A-5.4d The positional temperature at x = 0, b, w, L denoted by $T_r(0, t_i)$, $T_r(b, t_i)$, $T_r(w, t_i)$ and $T_r(L, t_i)$ in the reconstruction test.

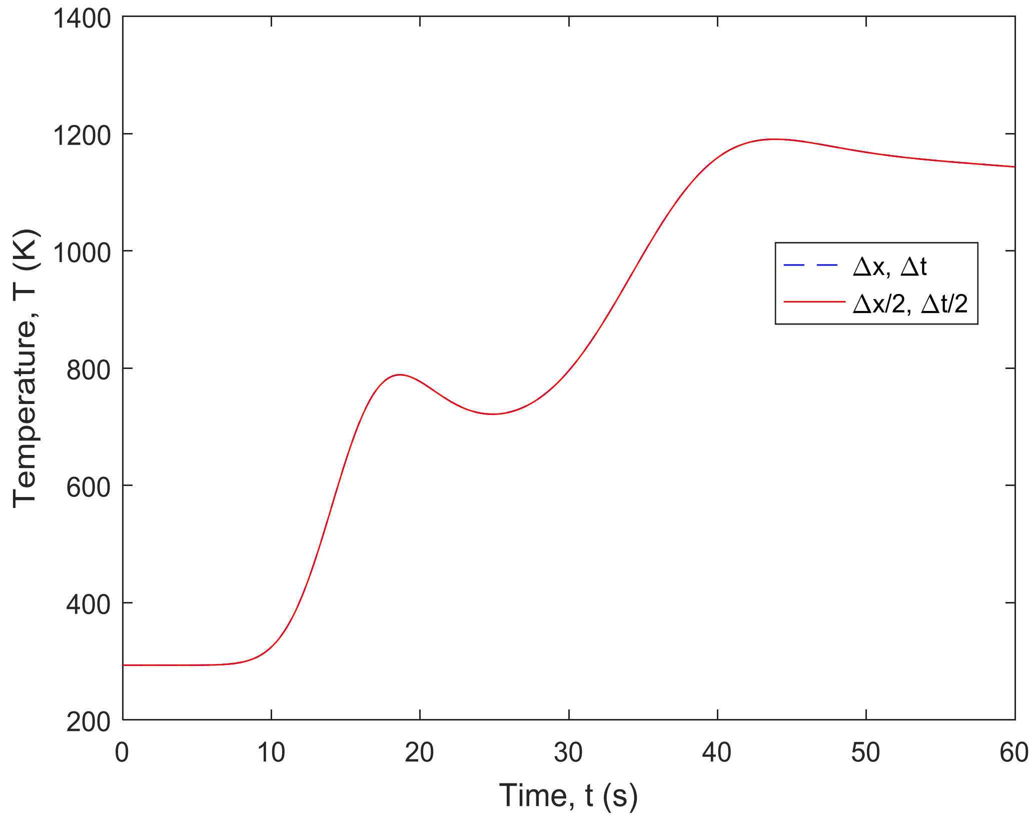

Fig. A-5.5 Convergence analysis of the implicit finite difference method by plotting the positional temperature at $x = b$, $T_r(b, t_i)$ in the reconstruction test obtained by (Δx, Δt) and ($\Delta x/2$, $\Delta t/2$), respectively.

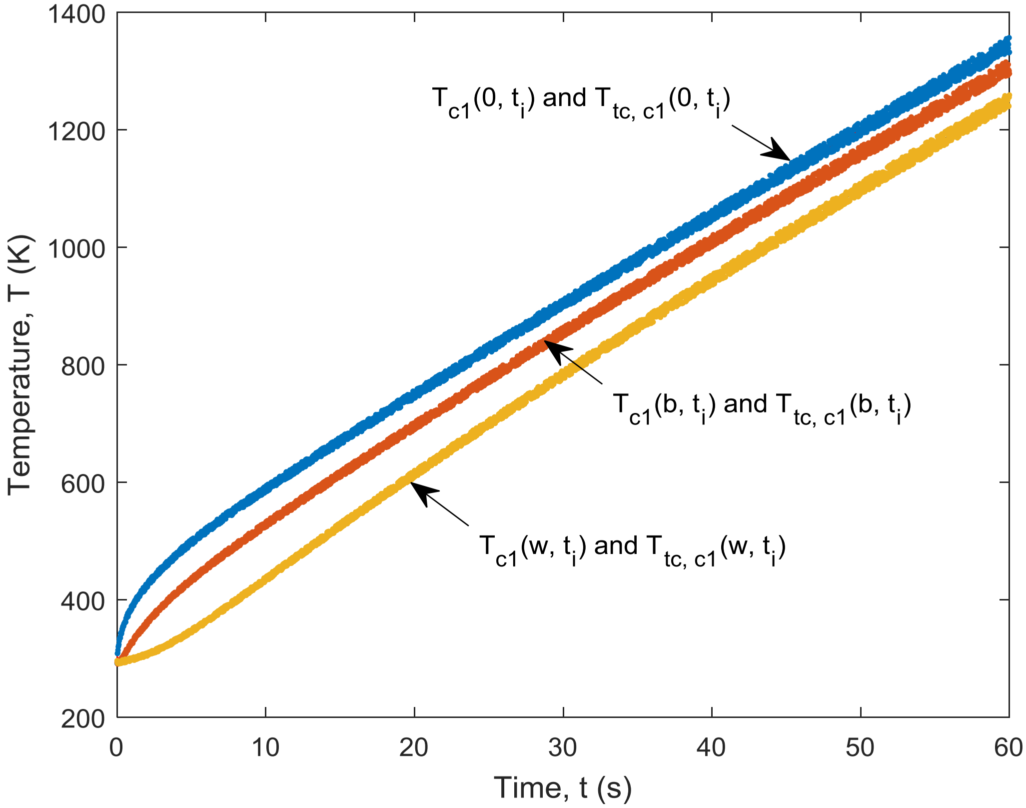

Fig. A-5.6a The positional temperature $T_{c1}(0, t_i)$, $T_{c1}(b, t_i)$, $T_{c1}(w, t_i)$ and emulated noisy "thermocouple" data $T_{tc,\,c1}(0, t_i)$, $T_{tc,\,c1}(b, t_i)$, $T_{tc,\,c1}(w, t_i)$ for the calibration test 1, $t_i = i\Delta t$, $i = 1, 2, 3, \ldots, M$.

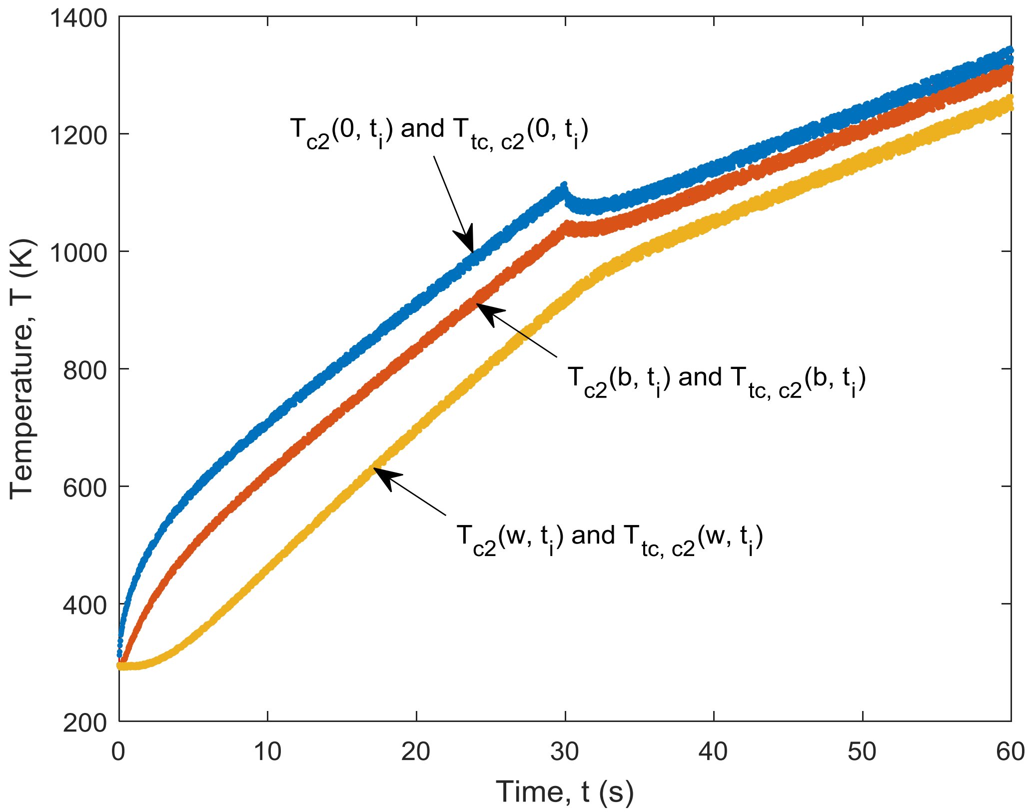

Fig. A-5.6b The positional temperature $T_{c2}(0, t_i)$, $T_{c2}(b, t_i)$, $T_{c2}(w, t_i)$ and emulated noisy "thermocouple" data $T_{tc,\, c2}(0, t_i)$, $T_{tc,\, c2}(b, t_i)$, $T_{tc,\, c2}(w, t_i)$ for the calibration test 1, $t_i = i\Delta t$, $i = 1, 2, 3, \ldots, M$.

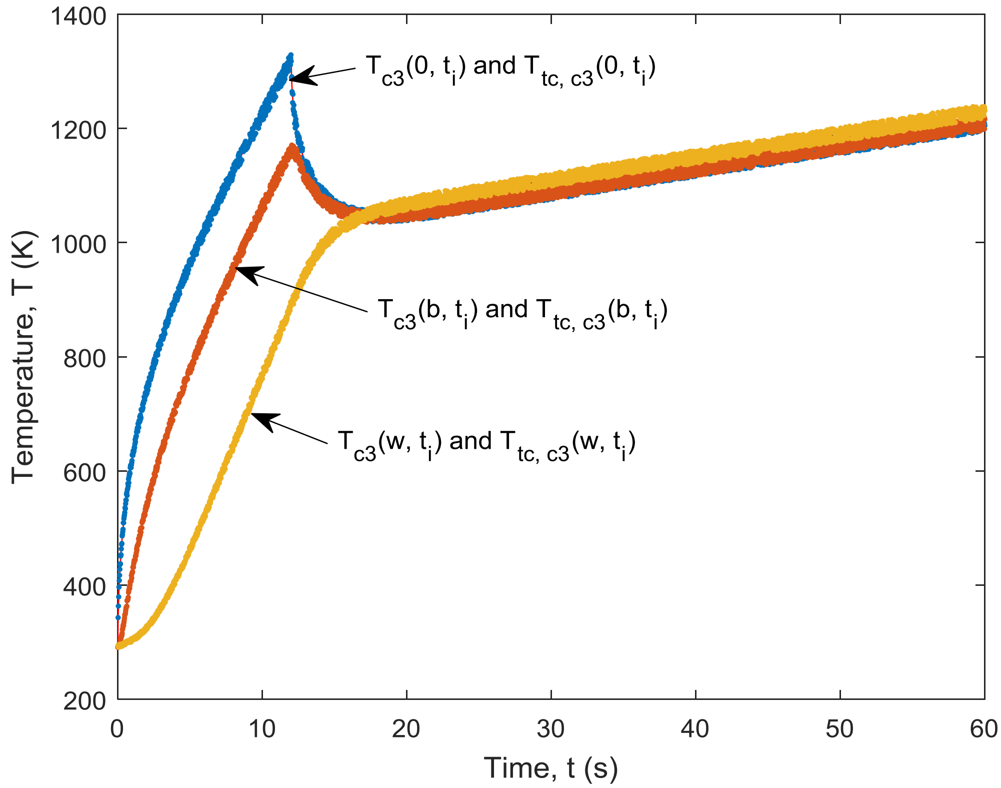

Fig. A-5.6c The positional temperature $T_{c3}(0, t_i)$, $T_{c3}(b, t_i)$, $T_{c3}(w, t_i)$ and emulated noisy "thermocouple" data $T_{tc,\,c3}(0, t_i)$, $T_{tc,\,c3}(b, t_i)$, $T_{tc,\,c3}(w, t_i)$ for the calibration test 1, $t_i = i\Delta t$, $i = 1, 2, 3, \ldots, M$.

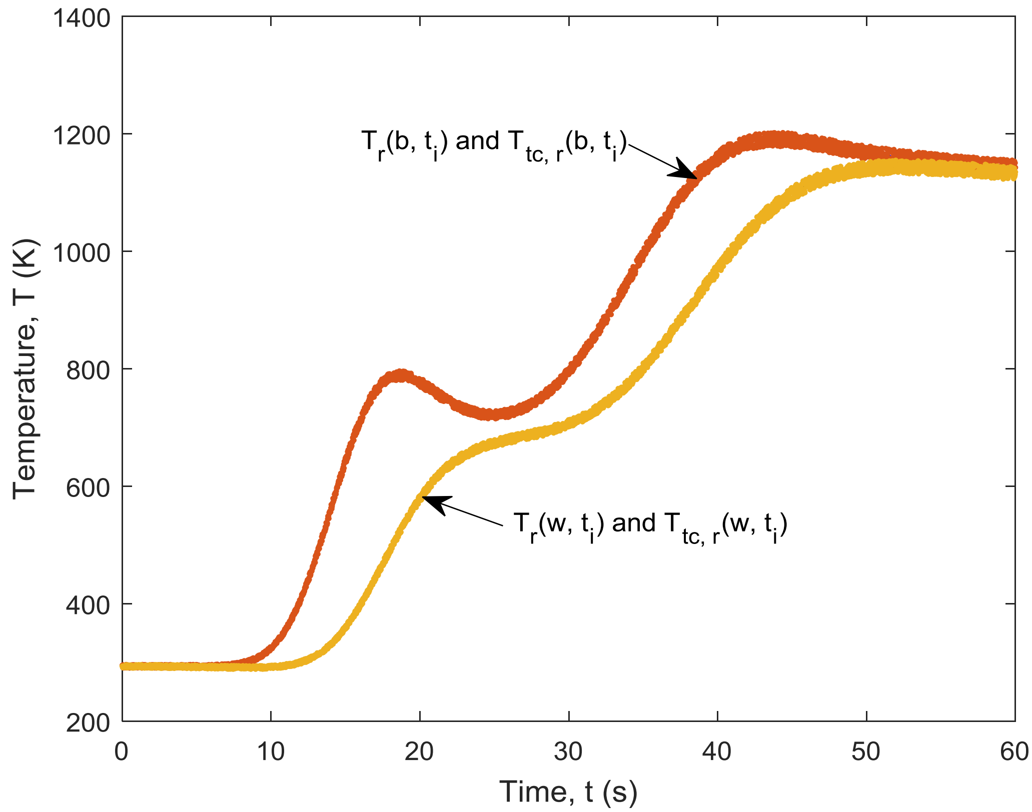

Fig. A-5.6d The positional temperature $T_r(b,\ t_i)$, $T_r(w,\ t_i)$ and emulated noisy "thermocouple" data $T_{tc,\,r}(b,\ t_i)$, $T_{tc,\,r}(w,\ t_i)$ for the calibration test 1, $t_i = i\Delta t$, $i = 1, 2, 3, \ldots, M$.

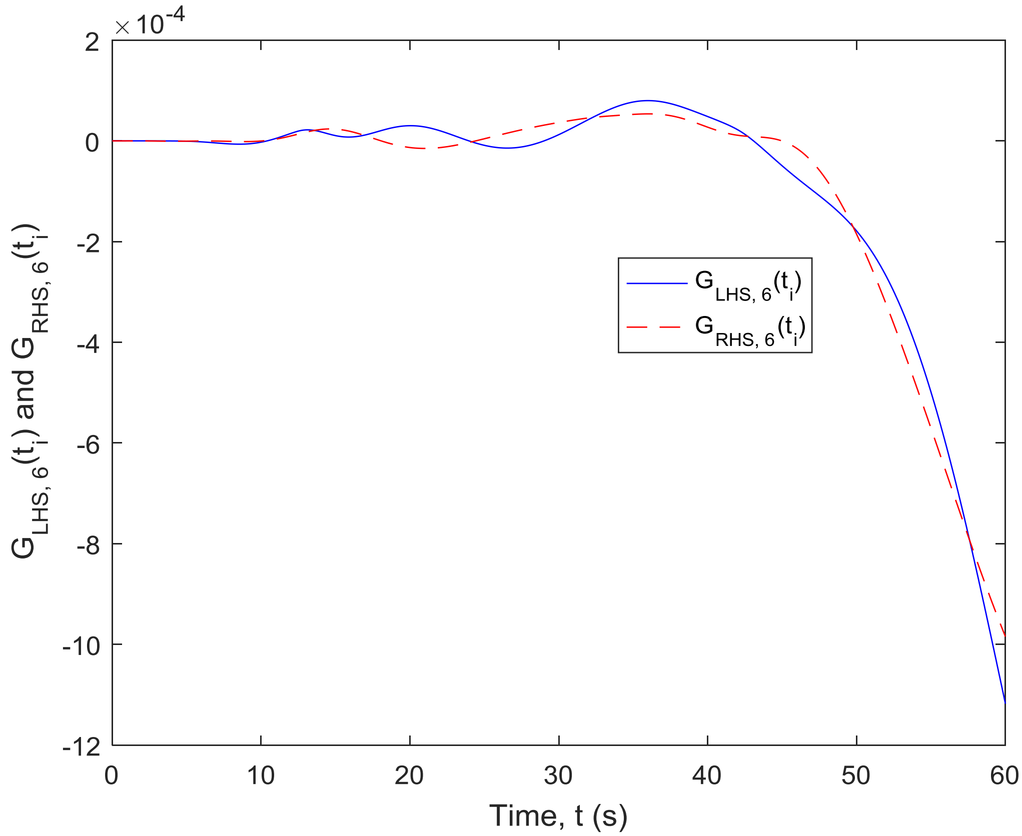

Fig. A-5.7a $G_{\mathrm{LHS},\,6}(t_i)$ and $G_{\mathrm{RHS},\,6}(t_i)$ defined in Eqs. (5.24b, c) by using noiseless data and $\{a_0^6, a_2^6, a_3^6, \ldots, a_6^6\}$ listed in column 2 of Table A-5.3.

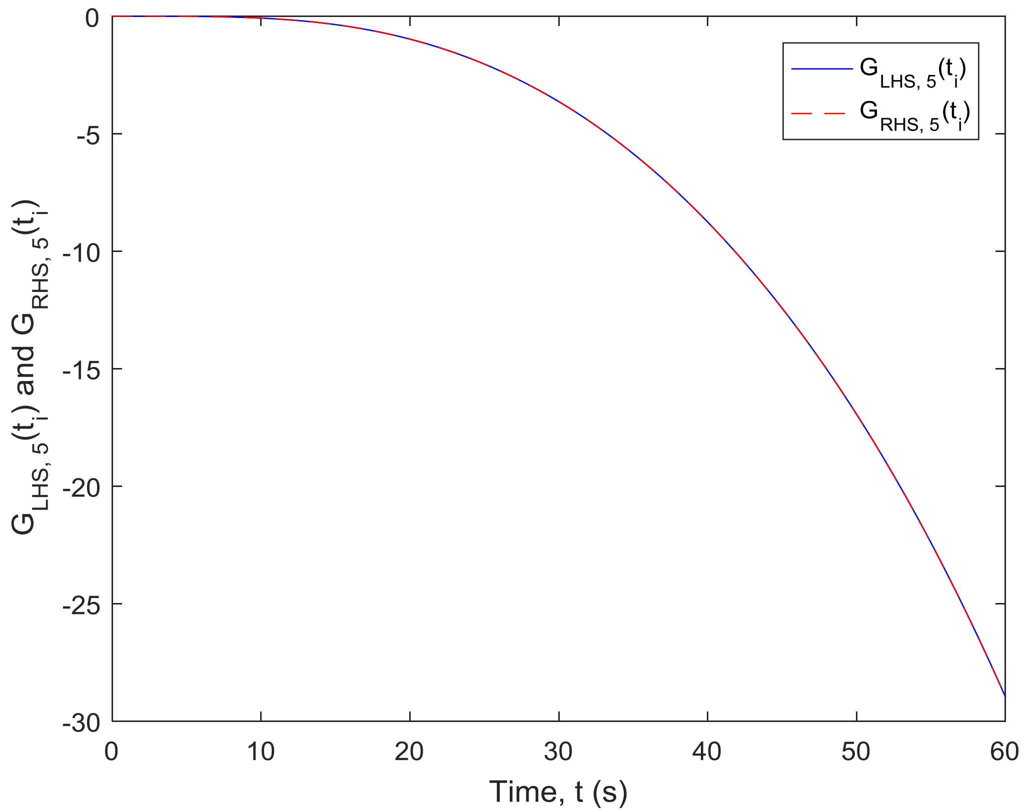

Fig. A-5.7b $G_{\mathrm{LHS},\,5}(t_i)$ and $G_{\mathrm{RHS},\,5}(t_i)$ defined in Eqs. (5.24b, c) by using noiseless data and $\{a_0^5, a_2^5, a_3^5, a_4^5, a_5^5\}$ listed in column 3 of Table A-5.3.

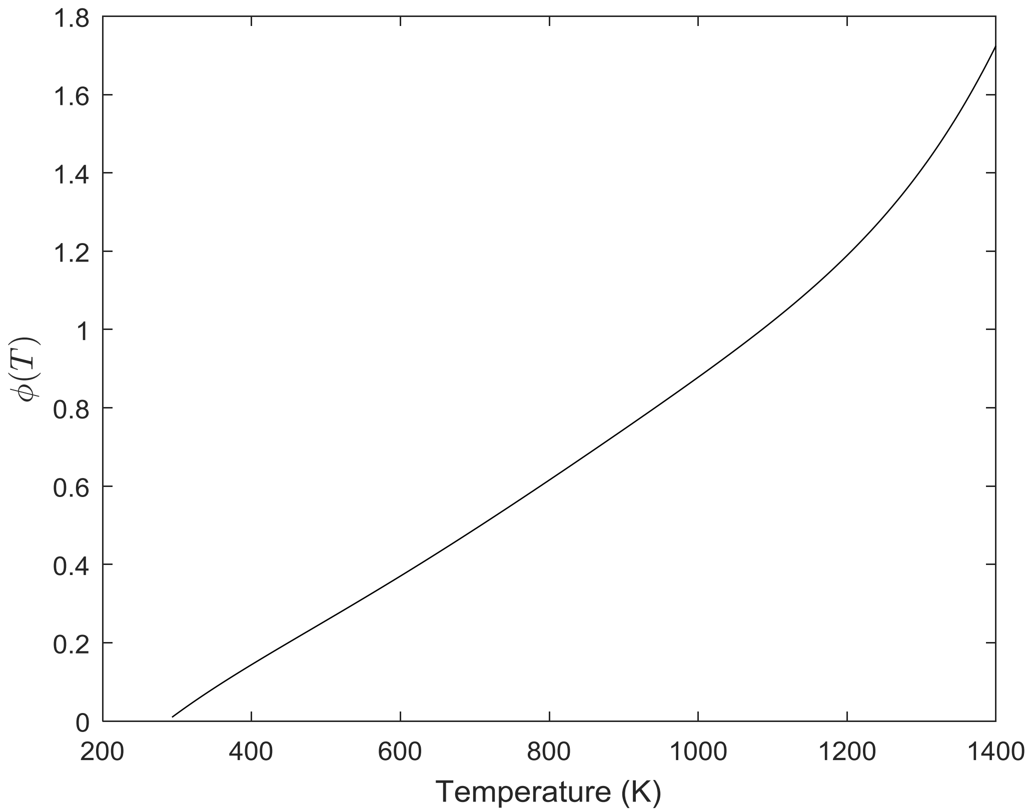

Fig. A-5.8 The transformed variable $\phi(T)$ as a function of temperature defined in Eq. (5.13a) in the temperature range [293.15, 1400] K using the calculated coefficients $\{a_0^5, a_2^5, a_3^5, a_4^5, a_5^5\}$ as listed in column 3 of Table A-5.3 (noiseless data).

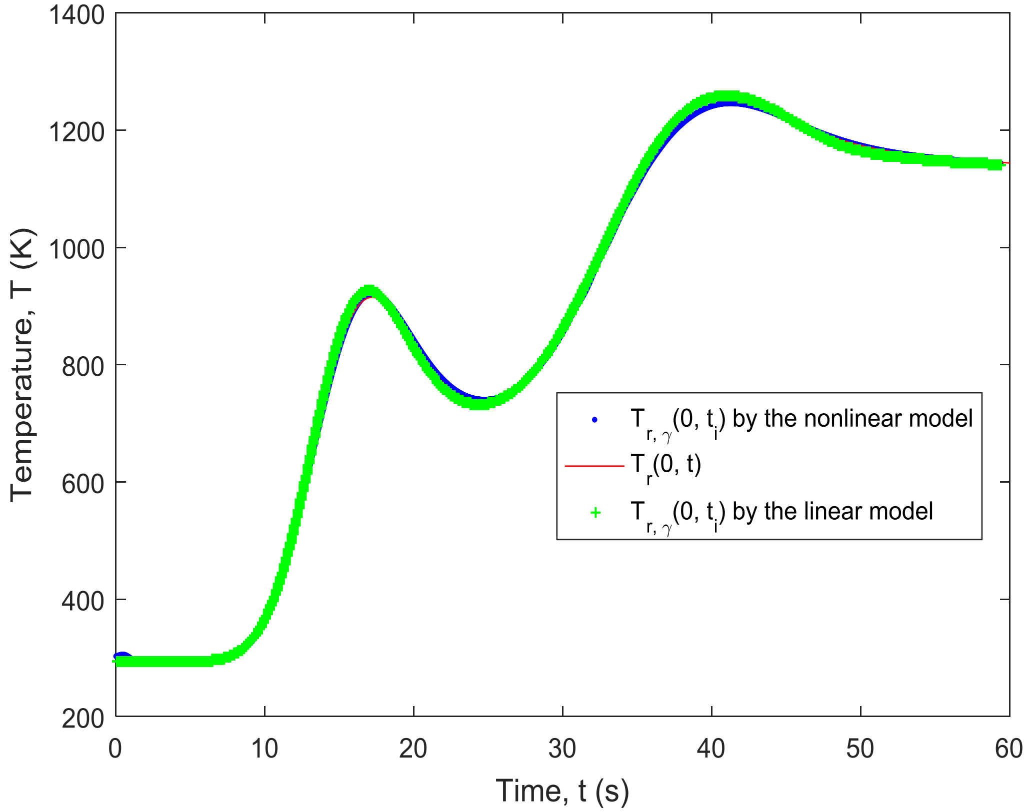

Fig. A-5.9 Comparison of the exact front surface temperature $T_r(0,t)$ and the predicted front surface temperature $T_{r,\gamma}(0,t_i)$ using the nonlinear model and the predicted front surface temperature using the linear model given in Eq. (5.2) (noiseless data, γ = 0.6 s).

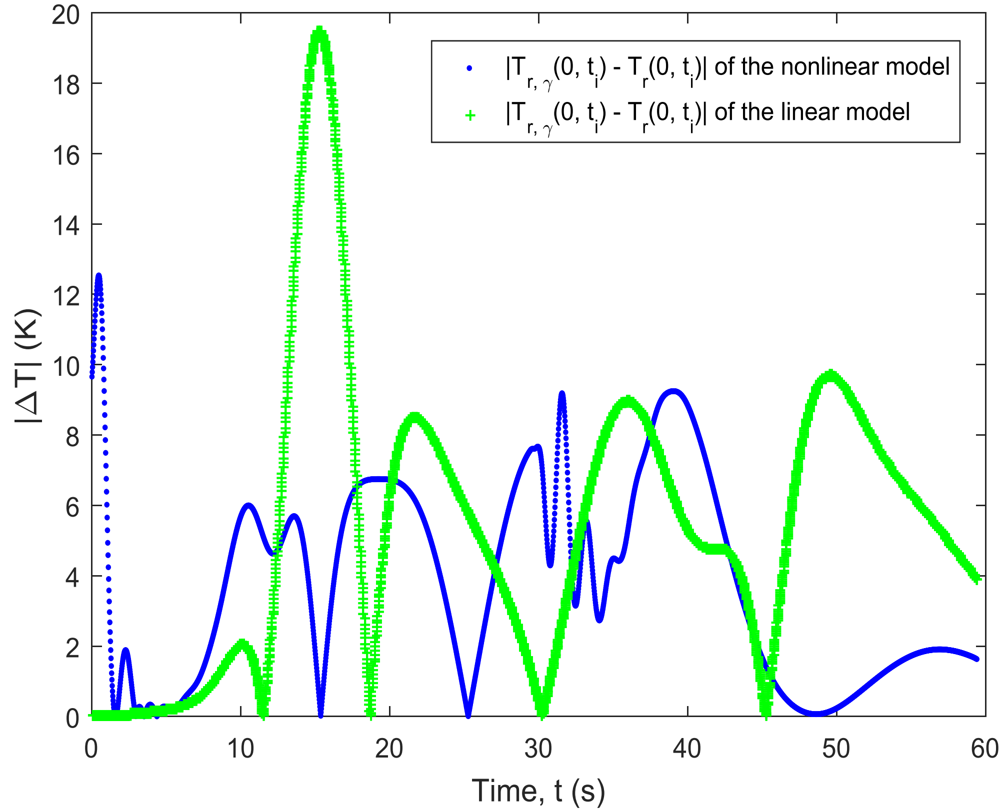

Fig. A-5.10 Comparison of the absolute error between surface temperature prediction by the nonlinear model and the linear model given in Eq. (5.2) (noiseless data, γ = 0.6 s).

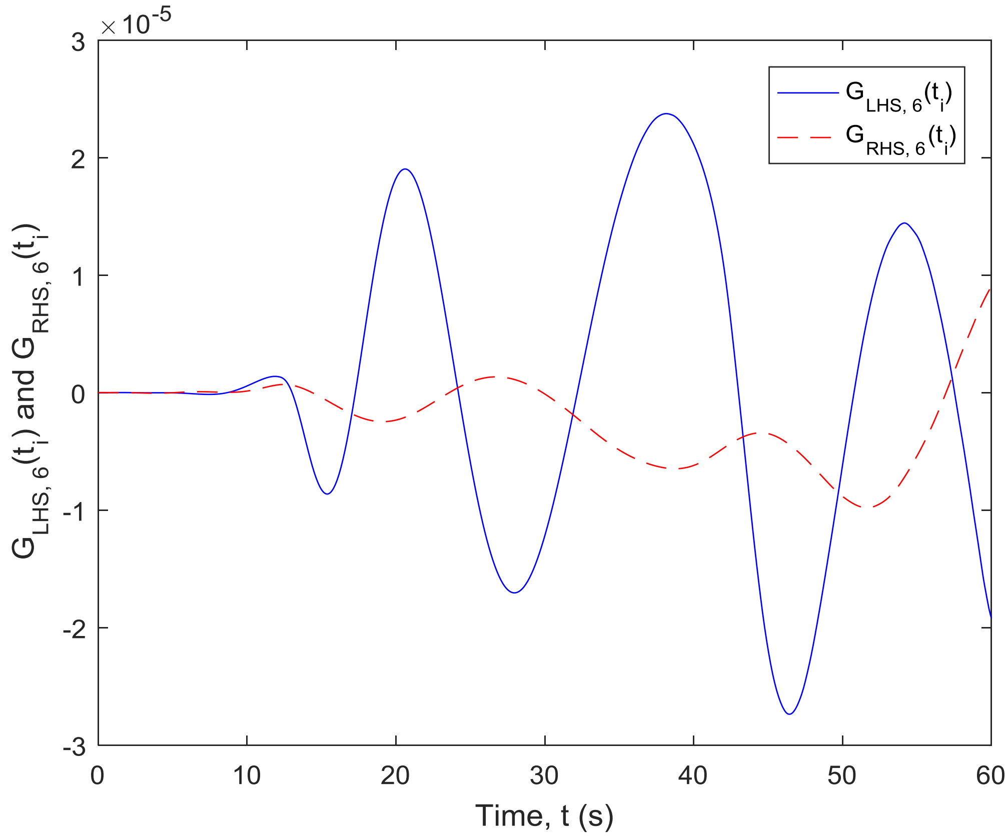

Fig. A-5.11 $G_{\mathrm{LHS},\,6}(t_i)$ and $G_{\mathrm{RHS},\,6}(t_i)$ defined in Eqs. (5.24b, c) by using noisy data and listed in column 2 of Table A-5.5.

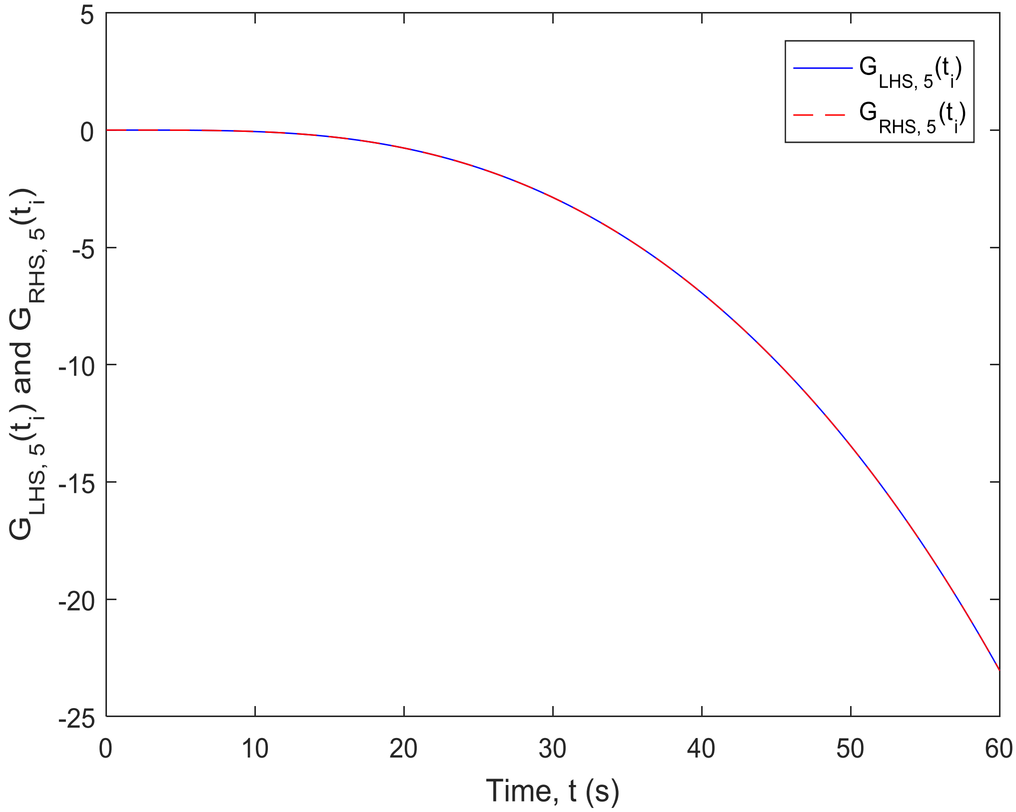

Fig. A-5.12 $G_{\mathrm{LHS},\,5}(t_i)$ and $G_{\mathrm{RHS},\,5}(t_i)$ defined in Eqs. (5.24b, c) by using noisy data and listed in column 3 of Table A-5.5.

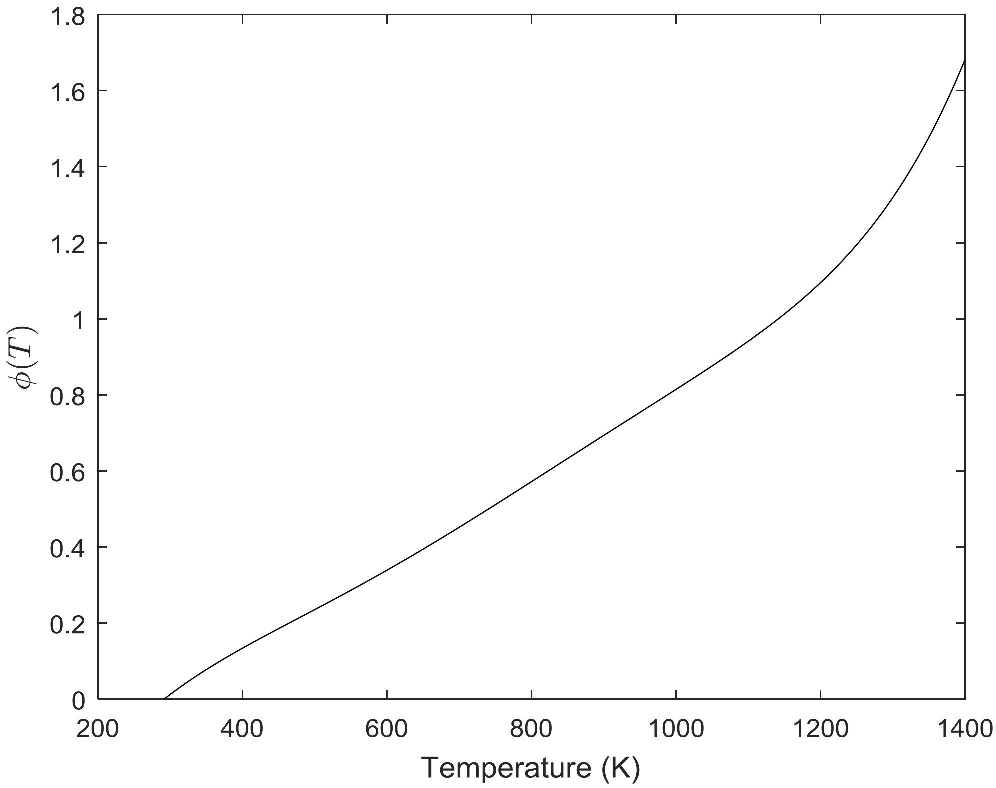

Fig. A-5.13 The transformed variable $\phi(T)$ as a function of temperature defined in Eq. (5.13a) in the temperature range [293.15, 1400] K using the calculated coefficients as listed in column 3 of Table A-5.5 (noisy data).

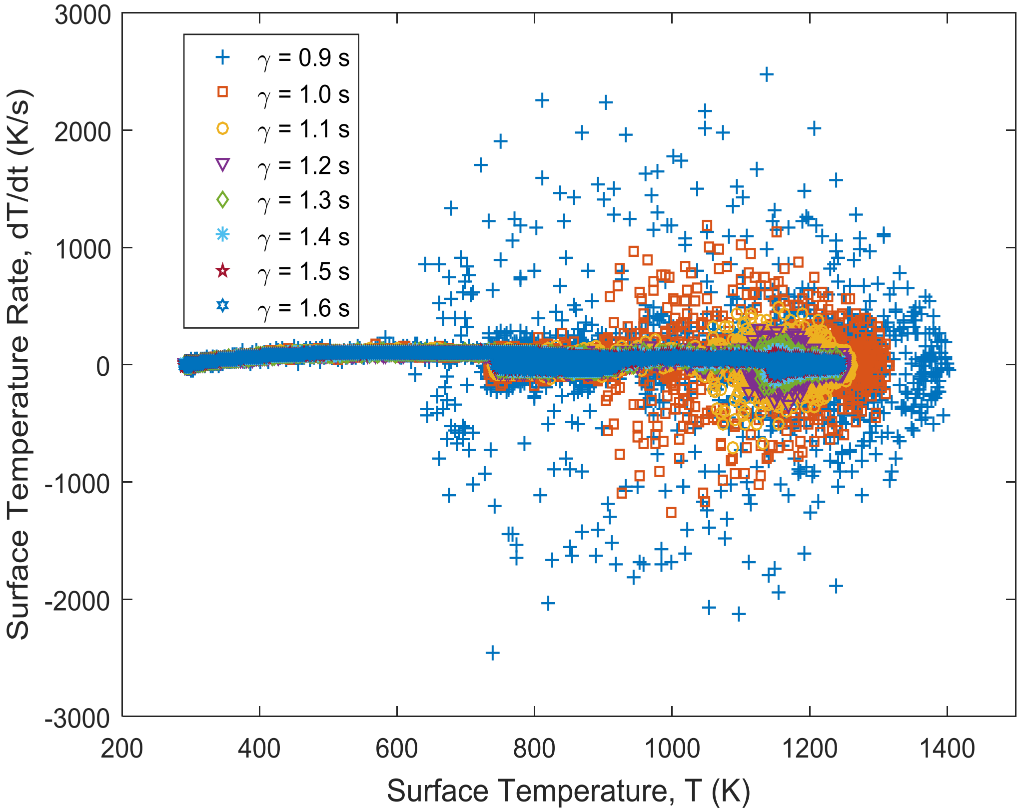

Fig. A-5.14a The predicted surface temperature rate and surface temperature phase planes for the future-time parameter spectrum γ = [0.9, 1.0, 1.1, 1.2, 1.3, 1.4, 1.5, 1.6] s (as listed in column 3 of Table A-5.5).

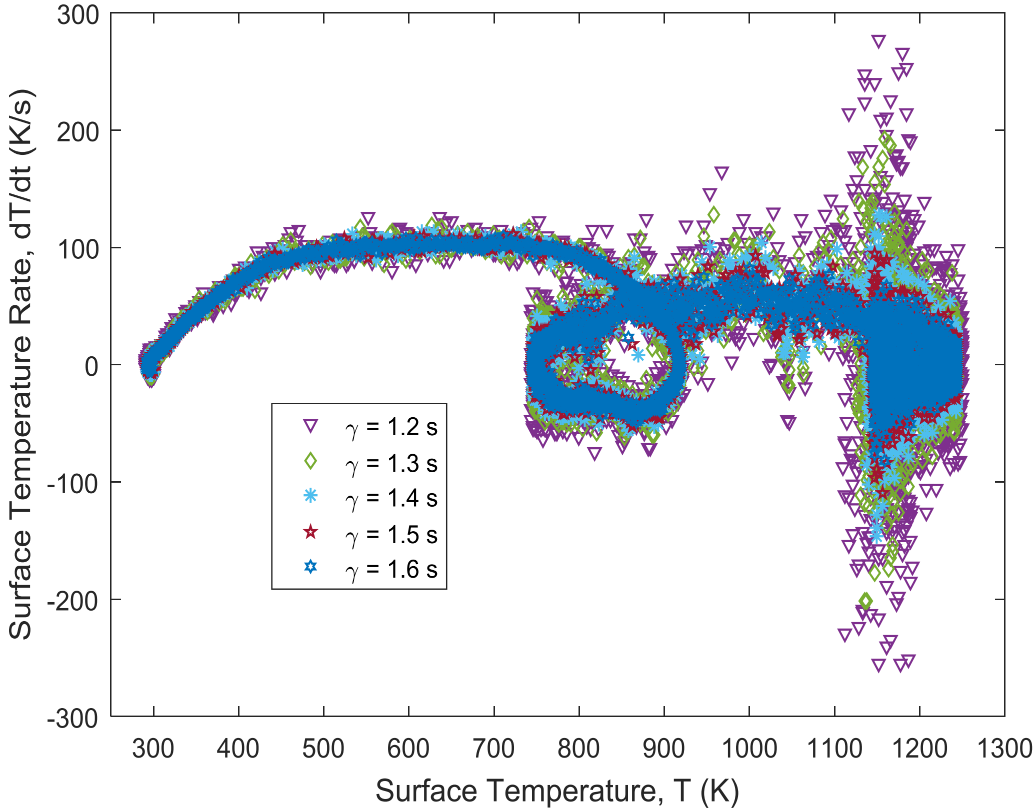

Fig. A-5.14b The predicted surface temperature rate and surface temperature phase planes for the future-time parameter spectrum γ = [1.2, 1.3, 1.4, 1.5, 1.6] s (as listed in column 3 of Table A-5.5).

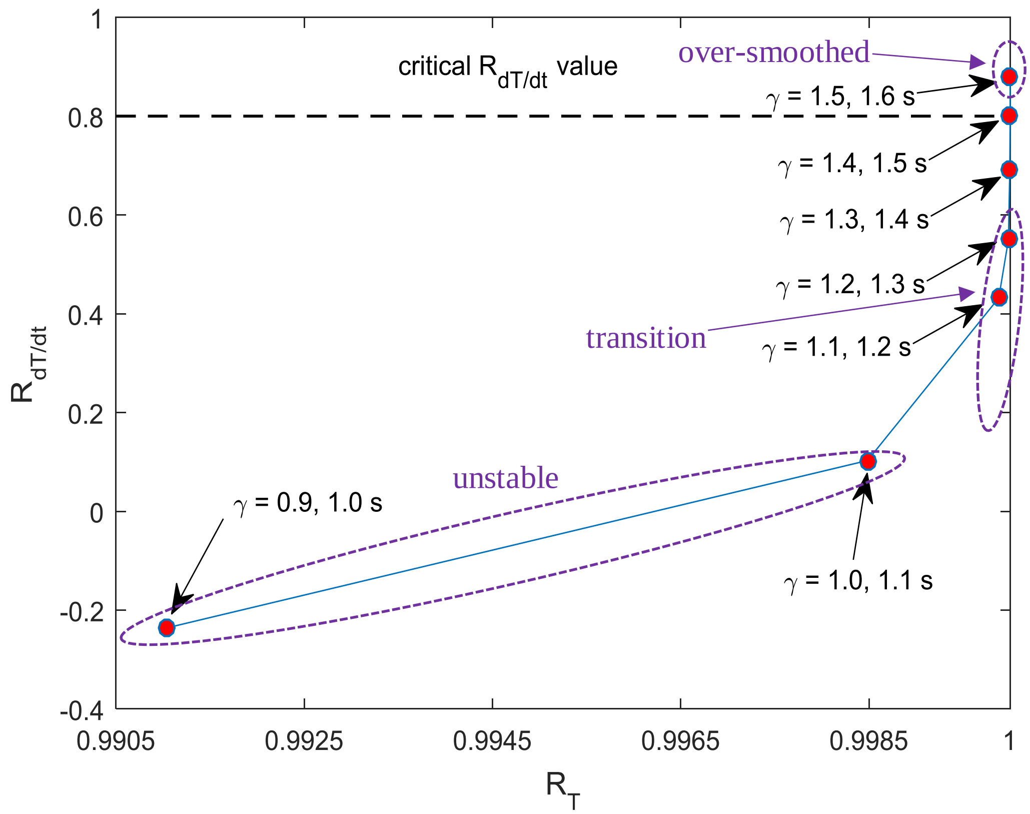

Fig. A-5.15 The predicted surface temperature rate cross-correlation coefficient versus the surface temperature cross-correlation coefficient for future-time parameter pairs.

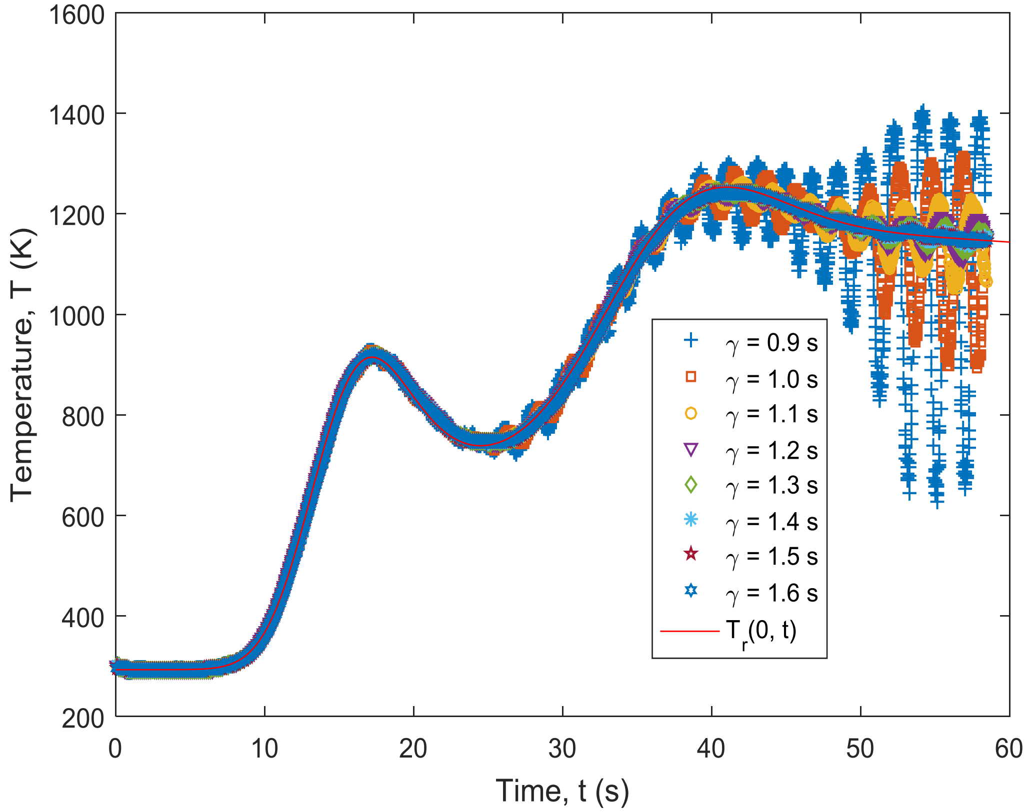

Fig. A-5.16 The exact surface temperature and predicted surface temperature for the future-time parameter spectrum γ = [0.9, 1.0, 1.1, 1.2, 1.3, 1.4, 1.5, 1.6] s when N = 5.

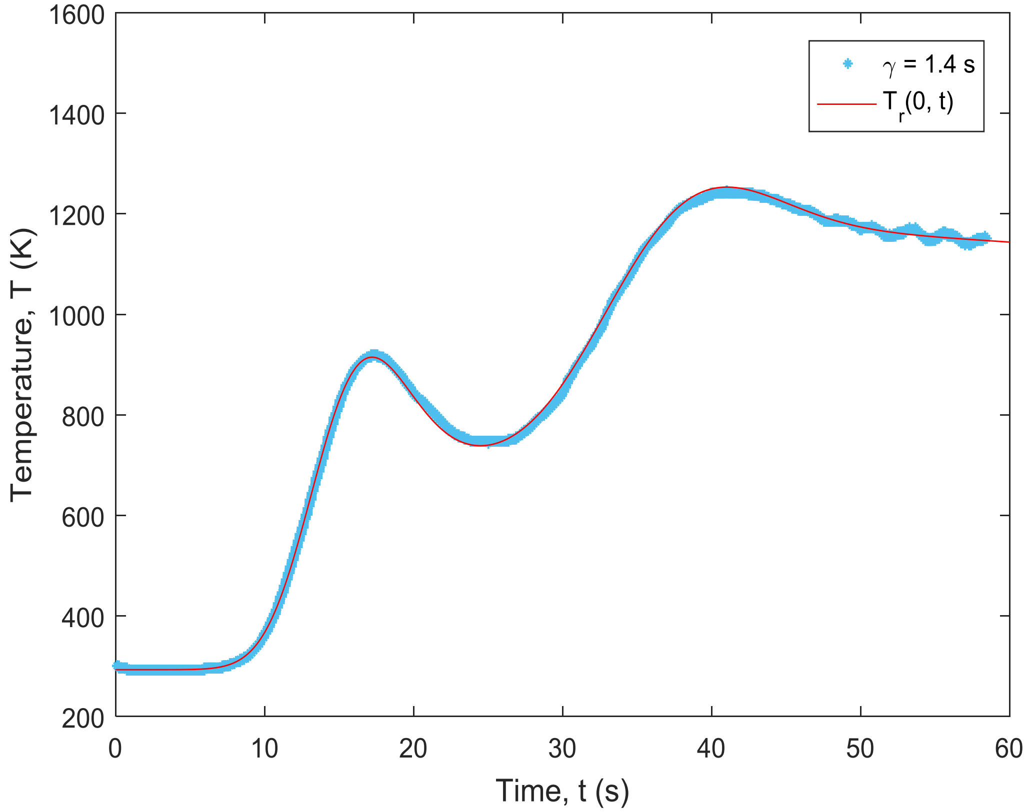

Fig. A-5.17 The exact surface temperature and predicted surface temperature for the future-time parameter spectrum γ = 1.4 s when N = 5.

Table A-5.1 Several Chebyshev polynomials of the first kind [86] for mapped temperature as a variable.

E_n	Polynomial
E_0	1
E_1	T^*
E_2	$2T^{*2}-1$
E_3	$4T^{*3}-3T^*$
E_4	$8T^{*4}-8T^{*2}+1$
E_5	$16T^{*5}-20T^{*3}+5T^*$
E_6	$32T^{*6}-48T^{*4}+18T^{*2}-1$
E_7	$64T^{*7}-112T^{*5}+56T^{*3}-7T^*$

Table A-5.2 Thermophysical properties of stainless steel 304 [80] and parameters for the simulation.

Property	Value
b	2×10^{-3} m
c	$6.683+0.04906\times T+80.74\times\ln(T)$ J/(kg·K) [80]
$f_{sampling}$	50 Hz
k	$9.705+0.0176\times T-1.60\times10^{-6}\times T^2$ W/(m·K) [80]
L	1×10^{-2} m
M	3000
M_f	5
$q''_{0,c1,\max}$	6.5×10^5 W/m^2
$q''_{L,c1,\max}$	1.0×10^5 W/m^2
$q''_{0,c2,\max}$	1×10^6 W/m^2
$q''_{L,c2,\max}$	0 W/m^2
$q''_{0,c3,\max}$	2.5×10^6 W/m^2
$q''_{L,c3,\max}$	2.0×10^5 W/m^2
$q''_{0,r,\max}$	2.4×10^6 W/m^2
$q''_{L,r,\max}$	1.0×10^5 W/m^2
$t_{\max}$	60 s
Δt	0.02 s

Table A-5.2 Continued

Property	Value
T_0	293.15 K
T_L	273
T_U	1500
w	8×10^{-3} m
Δx	5×10^{-5} m
ρ	7920 kg/m^3 [80]
ε_q	0.01
ε_T	0.01
β_1	$t_{\max}/4$ s
β_2	$0.6t_{\max}$ s
σ_1	$t_{\max}/15$ s
σ_2	$t_{\max}/8$ s

Table A-5.3 Numerically calculated coefficients in the transformed variable $\phi(x, t)$ in Eq. (5.13a) with $a_1^N \triangleq 1$ using noiseless data (t_{max} = 60 s).

Coefficients	$N = 6$	$N = 5$	$N = 4$	$N = 3$	$N = 2$
a_0^N	0.5442	0.8711	0.9011	0.6132	0.9008
a_2^N	0.8087	0.1814	0.1376	0.5112	0.1081
a_3^N	0.5805	0.0933	0.0510	0.1349	N/A
a_4^N	0.3660	0.0375	0.0137	N/A	N/A
a_5^N	0.1765	0.0161	N/A	N/A	N/A
a_6^N	0.0568	N/A	N/A	N/A	N/A

Table A-5.4 Sequential coefficient study for N = 5 using noiseless data collected up to 60s, 54s, 48s, 42s and 36s, respectively.

Coefficients	t_{max} = 60 s	t'_{max} = 54 s	t'_{max} = 48 s	t'_{max} = 42 s
a_0^N	0.8711	0.8630	0.8624	0.8638
a_2^N	0.1814	0.1980	0.1994	0.1956
a_3^N	0.0933	0.1096	0.1110	0.1068
a_4^N	0.0375	0.0468	0.0476	0.0453
a_5^N	0.0161	0.0206	0.0210	0.0200

Table A-5.5 Numerically calculated coefficients in the transformed variable $\phi(x, t)$ in Eq. (5.13a) with $a_1^N \triangleq 1$ using noisy data (t_{max} = 60 s).

Coefficients	N = 6	N = 5	N = 4	N = 3	N = 2
a_0^N	0.5376	0.8433	0.8942	0.6134	0.8920
a_2^N	0.8102	0.2261	0.1546	0.5108	0.1152
a_3^N	0.5560	0.1308	0.0608	0.1346	N/A
a_4^N	0.3137	0.0599	0.0214	N/A	N/A
a_5^N	0.1316	0.0273	N/A	N/A	N/A
a_6^N	0.0358	N/A	N/A	N/A	N/A

Table A-5.6 Sequential coefficient study for N = 5 using noisy data collected up to 60s, 54s, 48s, 42s and 36s, respectively.

Coefficients	t_{max} = 60 s	t'_{max} = 54 s	t'_{max} = 48 s	t'_{max} = 42 s
a_0^N	0.8433	0.8409	0.8459	0.9420
a_2^N	0.2261	0.2310	0.2182	0.0075
a_3^N	0.1308	0.1358	0.1218	-0.0954
a_4^N	0.0599	0.0627	0.0552	-0.0674
a_5^N	0.0273	0.0288	0.0252	-0.0336

Vita

Hongchu Chen was born in Pujiang, Zhejiang province, China on August 24, 1989. He attended Pujiang Middle School between August 2004 and June 2007. He began his undergraduate study in thermal energy and power engineering at Central South University in Changsha, Hunan in September 2007 and received a bachelor of engineering degree in June 2011. In Fall 2011, he enrolled in the graduate program in the Department of Mechanical, Aerospace and Biomedical Engineering at the University of Tennessee, Knoxville. His primary research focus involved many aspects of inverse heat conduction problems. His research involved theory, numerical simulation, experimental design, instrumentation and experimentation. He received his Master of Science degree in August 2013 under the supervision of Prof. Jay I. Frankel. Hongchu Chen continued his research by expanding the calibration integral equation method (CIEM) to a new class of inverse problems under the supervision of Prof. Jay I. Frankel. Concurrent to his Ph.D. dissertation studies, Hongchu Chen has been developing a new experimental test platform for investigating inverse heat conduction problems.